PHD

An investigation into the thin film deposition of binary oxide, ternary oxide and binary sulphide materials.

Thongchai, Prem

Award date:
2019

Awarding institution:
University of Bath

An investigation into the thin film deposition of binary oxide, ternary oxide and binary sulphide materials

Prem Thongchai

A thesis submitted for the degree of Doctor of Philosophy

University of Bath

Department of Chemistry

September 2018

COPYRIGHT

Contents

Acknowledgements vii

Declaration viii

Abstract ix

List of Abbreviations xi

List of Figures xiii

List of Tables xxv

List of Schemes xxxii

Chapter 1: Introduction 1

1.1 Thin film technology 2

1.2 Oxide materials 5

1.2.1 Binary metal oxide thin film materials 5

1.2.2 Ternary Metal Oxides (TMOs) 14

1.3 Metal sulphide materials 19

1.4 Combustion processing and metal nitrate salts 22

1.5 Thin film deposition techniques 26

1.5.1 Physical vapour deposition (PVD) 26

1.5.2 Chemical vapour deposition (CVD) 28

1.5.3 Chemical solution deposition (CSD) 31

1.5.4 Electrochemical deposition (ECD) 35

1.5.5 The consideration of thin film deposition technique selection 37

1.6 Aerosol-assisted chemical vapour deposition (AACVD) 39

1.6.1 Principles and Characteristics of the AACVD process 40

1.6.3 Thin film growth 43

1.6.4 The influence of the deposition conditions 45

1.7 Thesis outline 51

References 52

Chapter 2: Deposition of Binary oxide thin films 61

2.1 Binary oxide thin film depositions: Transition Metal oxides (TMOs) 62

2.1.1 Copper oxide thin film deposition 62

Conclusion 76

2.1.2 Nickel oxide thin film deposition 78

Conclusion 113

2.2 Binary oxide thin film deposition: Rare Earth oxides (REOs) 115

2.2.1 Lanthanum oxide thin film deposition 115

Conclusion 127

2.2.2. Praseodymium oxide thin films 129

Conclusion 138

References 140

Chapter 3: Deposition of Ternary oxide thin films 149

3.1 Introduction: Ternary oxide thin film deposition Lanthanum nickel oxide 150

3.2 Lanthanum nickel oxide thin film deposition by AACVD 151

3.2.1 Thermogravimetric analysis of the precursor mixtures 152

3.2.2 Appearance of deposited films 155

3.2.3 Crystallinity 155

3.2.4 Compositional analysis 160

3.2.5 Surface and cross-section morphology 162

3.3 Lanthanum nickel oxide thin film deposition by spin coating 169

3.3.1 Thermogravimetric analysis of the precursor components 170

3.3.2 Appearance of deposited films 171

3.3.3 Surface and cross-section morphology 172

3.3.4 Crystallinity 177

3.3.5 Compositional analysis 177

3.3.6 Optical properties 180

3.4 Lanthanum nickel oxide thin film deposition with various vol.% of acetic acid by spin coating 181

3.4.1 Thermogravimetric analysis of the precursor 182

3.4.2 Appearance of deposited films by using the LNR11 AA5-30 precursor systems. 182

3.4.3 Surface and cross-section morphology 183

3.4.4 Crystallinity 190

3.4.5 Compositional analysis 191

3.4.6 Optical properties 193

3.5 Single crystal complex from LNR11 precursor system in an acetic acid 195

3.5.1 Single crystal analysis 195

3.5.2 Thermogravimetric analysis of single crystal complex 199

3.6 Conclusions 200

3.6.1 Lanthanum nickel oxide by AACVD 200

3.6.2 Lanthanum nickel oxide by spin coating 200

3.6.3 Comparison of solution processing by the AACVD and spin coating techniques 201

3.6.4 Spray pyrolysis of precursor LNR11 202

References 206

Chapter 4: Deposition of zinc sulphide thin films 210

4.1 Introduction 211

4.1.1 Zinc xanthate complex precursors 212

4.1.2 Zinc thioureide complex precursors 214

4.2 Thermal analysis 216

4.3 ZnS thin film depositions 217

4.4 Appearance of deposited films 218

4.5 Crystallinity 220

4.6 Raman spectroscopy analysis 222

4.7 Compositional analysis 224
4.8 Surface and cross-section morphology 227
4.8.1 Surface morphology 227
4.8.2 Cross-section morphology 234
4.9 Optical properties 239
4.10 Conclusion 244
Reference 245
Chapter 5: Experimental 250
5.1 General experimental procedure 251
5.1.1 Chemicals and solvents 251
5.1.2 Substrate preparation 251
5.1.3 Aerosol Assisted Chemical Vapour Deposition (AACVD) procedure 252
5.1.4 Spin coating procedure 253
5.1.5 Thermogravimetric Analysis (TGA) 253
5.1.6 Powder X-ray Diffractometry (PXRD) 254
5.1.7 Atomic Force Microscopy (AFM) 254
5.1.8 UV-Visible Spectroscopy 254
5.1.9 Raman Spectroscopy Analysis 254
5.1.10 Scanning Electron Microscopy (SEM) 254
5.1.11 Energy-dispersive X-ray spectroscopy (EDS) 255
5.1.12 Single Crystal X-ray diffraction analysis 255
5.2 Experimental for Chapter 2 255
5.2.1 Copper thin film deposition 255
5.2.2 Nickel oxide thin film deposition 256
5.2.3 Lanthanum oxide thin film deposition 258
5.2.4 Praseodymium oxide thin film deposition 259
5.3 Experimental for Chapter 3 259

5.3.1 Lanthanum nickel oxide thin film deposition by using AACVD and hot-wall reactor.....259

5.3.2 Lanthanum nickel oxide thin film deposition by using AACVD and cold-wall reactor.....260

5.3.3 Lanthanum nickel oxide thin film deposition by using spin coating. 262

5.3.4 Lanthanum nickel oxide thin film deposition with various vol. % of an acetic acid by a spin coating technique. 262

5.3.5 Single crystal from lanthanum nitrate and nickel nitrate in an acetic acid solution.....263

5.4 Experimental for Chapter 4.....263

Chapter 6: Future work 266

6.1 Aerosol Assisted Chemical Vapour Deposition (AACVD).....267

6.2 Chapter 2: Deposition of Binary oxide thin films.....270

6.3 Chapter 3: Deposition of Ternary oxide thin films 271

6.4 Chapter 4: Deposition of Zinc sulphide thin films.....272

References.....274

Appendix.....275

Acknowledgements

First and foremost I would like to thank Professor Michael Hill and Dr Andrew Johnson. The guidance and support from them making my work and this thesis to achieve and complete. I am quite lucky to have them for good time in England.

A huge thank you goes to my Dad (Jhan Thonghchai) and Mum (Chumlonglak Thongchai) for their support throughout my life and also many thanks to my brothers. The encouragement from them always makes me be cheerful and stay strong.

I am so grateful to the Royal Thai Government to provide a full scholarship to me.

For all technical support, I would like to thank Dr. Gabriele Kociok-Köhn for the XRD analysis, Dr. Philip Fletcher for many great SEM images, Russel Barlow and Sarah Elkins for any conveniences in 1South store, Dave Elkins for his technical supports, Philip Jones for any repairs my glass tubes.

Many thanks to Dr David Stanton (Dave), Dr Jeff Hamilton (Jeff), Dr Andrew James Rushworth (Andrew), Dr Joseph Robert Thompson (Joe), Dr Ibrahim Yilmaz Ahmet (Ibbi), Jamie Parish, Peter Kubiak, Hannah Sullivan, Jerome Innocent, Emily Taylor and Michael Snook. It's quite difficult to describe what they are, but they can generated my happy time in Bath, a lot of laughs and smiles. Thank!!! Snakeeeee gang (+ Dr Andrew Johnson!!!).

I would like to thanks Dr Sam Cosham, Dr Anne-Frédérique Pecharman, Mathew Anker and Amanda Catherall for all help I have received.

A lot of thank to Hataikan Paradee, Pawitra Chiravirakul (P'Ta), Khloy Rawiwan, Pui aunt, Ice Phattranis, Knon Siwaraksa, Noon Naddaporn, Kim,Too (Yaya) Sukany, Pla Natthaya, Mick and the gang, and all Thai people which have been in my life here.

Last big thank to everything which I have been found and learn in Bath UK and they teach and treat me not only the knowledge from the PhD road but I do not know how to explain what I received from here. Thank you to raining and sunshine day. Thank you to winter and snow. Thank you to summer, colour change of tree and squirrel. And all most thank you to beautiful time here, BATH UK.

เปรม ทองชัย

Declaration

The work described in this thesis was conducted by the author at the University of Bath between October 2014 and October 2018. It represents the author's original and independent work, except where specific reference is made to the contrary. This thesis does not exceed the prescribed limit, including tables, references and appendices.

Abstract

Metal oxide and metal sulphide materials dominate a wide range of attractive properties and also to provide potential performances to various applications. There is a challenge to prepare these materials as a thin film with great quality and properties. Aerosol-assisted chemical vapour deposition (AACVD) is a promising technique to offer a desired thin film. The objective of this work is the preparation of the metal oxide and metal sulphide thin films via AACVD technique with single source precursor. The properties of deposited films were characterised.

Chapter 1: Introduction

The introduction provides an overview of the metal oxide and metal sulphide thin film materials. Various thin film fabrication techniques are indicated. AACVD technique is presented with key details.

Chapter 2: Deposition of Binary oxide thin films

This chapter describes and compares the binary oxide thin films from AACVD and spin coating technique. Simple metal nitrates were used as starting chemical to prepare a single source precursor for the thin film deposition. Copper oxide, nickel oxide, lanthanum oxide and praseodymium oxide thin film were deposited and investigated their morphology and properties. TGA, XRD, Uv-Vis, SEM, EDS and AFM were used to analyze the deposited films.

Chapter 3: Deposition of Ternary oxide thin films

This chapter focused on and attempt to deposit lanthanum nickel oxide thin films by using simple metal nitrates as precursor via AACVD and spin coating technique. The use of acetic acid was participated to improve the quality of the thin film deposition. The deposited films were investigated their morphology and properties via XRD, Raman, Uv-Vis, SEM, EDS and AFM.

Chapter 4: Deposition of Zinc sulphide thin film

This chapter demonstrated the deposition of a zinc sulphide thin film by using different single source precursor from $Zn(S_2COEt)_2$, 2-MePy[$Zn(S_2COEt)_2$] and $Zn[S=C(NMe)_2NCH(Me)_2]_2$. Thermal decomposition ability of these complexes was

analyzed by thermogravimetric analysis. AACVD was carried out to grow the ZnS films by the complex precursors. The morphology and properties of deposited films were characterized by XRD, Raman, Uv-Vis, SEM, EDS and AFM.

Chapter 5: Experimental

The general experimental procedures and the experimentals for chapter 2, 3 and 4 are described in this chapter.

Chapter 6: Future work

The interesting and further study to understand and develop a quality of thin film deposition via AACVD are presented in this chapter.

List of Abbreviations

AACVD	Aerosol-Assisted Chemical Vapour Deposition
AFM	Atomic Force Microscopy
ALD	Atomic Layer Deposition
ALE	Atomic Layer Epitaxy
AMO	Anti-bonding Molecular Orbital
AO	Atomic Orbital
APCVD	Atmospheric Pressure Chemical Vapour Deposition
BMO	Bonding Molecular Orbital
CBD	Chemical Bath Deposition
CMOS	Complementary Metal-Oxide-Semiconductor
CPU	Central Processing Unit
CSD	Chemical Solution Deposition
CVD	Chemical Vapour Deposition
DLICVD	Direct Liquid Injection Chemical Vapour Deposition
DRAM	Dynamic random-access memory
E_a	Activation energy
ECD	Electrochemical Deposition
EDS	Energy Dispersive [X-ray] Spectroscopy
E_F	Femi energy level
E_g	Energy band gap
eV	Electron Volt
FESEM	Field Emission Scanning Electron Microscopy
FTO	Fluorine-doped Tin Oxide
FWHM	Full-Width at Half-Maximum
ITO	Indium doped Tin Oxide
JCPDS	Joint Committee on Powder Diffraction Standards
LPCVD	Low-Pressure Chemical Vapour Deposition
MBE	Molecular Beam Epitaxial growth
MCFCs	Molten Carbonate Fuel Cells
Me	Metal atom
MIM	Metal-Insulator-Metal

MO	Molecular Orbital
MOCVD	Metal-Organic Chemical Vapour Deposition
MOSFETs	Metal-Oxide-Semiconductor Field-Effect Transistors
MPACVD	Microwave Plasma-Assisted Chemical Vapour Deposition
MPE	Mist Plasma Evaporation
n-type	Negative charge carrying semiconductor
PEMFCs	Polymer Electrolyte Membrane Fuel Cells
PLD	Pulsed Laser Deposition
p-type	Positive charge carrying semiconductor
PVD	Physical Vapour Deposition
PXRD	Powder X-ray Diffractometric
QDs	Quantum Dots
R	Rear earth
REMOs	Rare Earth Metal Oxides
RRAM	Resistive switching Random Access Memory
SEM	Scanning Electron Microscopy
SOFCs	Solid Oxide Fuel Cells
T_{ad}	Adiabatic flame temperature
TCOs	Transparent Conducting Oxides
TGA	Thermal Gravimetric Analysis
TMEDA	*N,N* tetramethylethylenediamine
TMOs	Transition Metal Oxides
TMS	Transition Metal Sulfides
UHCVD	Ultra-High Vacuum Chemical Vapour Deposition
UV	Ultraviolet
Vis	Visible
XRD	X-ray Diffraction

List of Figures

Chapter 1

Figure 1.1 ((a) Moore's law, the prediction of a number of transistors on an integrated circuit versus year.[1] (b) Intel 4004 in its package[4] (c) Intel® Core™ i9-8950HK.[5] 2

Figure 1.2 Illustration of thin film scale and other sizes of materials.[12] 4

Figure 1.3 The illustration of anti-bonding and bonding orbital which are formed by the in phase and out of phase combination of two s atomic orbitals..... 7

Figure 1.4 The diagram of molecular orbital energy level from the arrangement of numerous atoms. 8

Figure 1.5 Schematic illustration of the band structure of a solid. EF is the Fermi level which is the highest electronically occupied energy level, EC is the lowest energy level of the conduction band and EV is the highest energy level of the valence band. 9

Figure 1.6 Illustration of an intrinsic, n-type and p-type semiconductor. 10

Figure 1.7 Polymorphic crystal structures of the sesquioxides R_2O_3: (hexagonal) A-type, (monoclinic) B-type, (Cubic) C-type. The solid dots indicate the metal atoms. 11

Figure 1.8 Polymorphic transformation for the rare earth sesquioxides. 12

Figure 1.9 Representative fluorite-typed dioxide, RO_2. The solid dots indicate the metal atoms. 13

Figure 1.10 The relationship between the cubic fluorite-type dioxide (RO_2) and the cubic C-type sesquioxides (R_2O_3). 13

Figure 1.11 The major ternary structure families. 14

Figure 1.12 Crystal structure of a cubic ABO_3 perovskite. Orange spheres represent the A cation, blue spheres are B cations, and red spheres O anions. 14

Figure 1.13 Crystal structure of the ABO_4 scheelite-type structure. Example, 'A' atoms (blue sphere) can be Ca, Pb; 'B' atom (grey sphere) can be W, Mo and red spheres are oxygen atoms.[39] 15

Figure 1.14 Crystal structure of an AB_2O_4 spinel. ***Blue spheres*** represent A cations, ***green spheres*** B cations, and ***red sphere*** represent O anions.[46] 17

Figure 1.15 Crystal structure of the β-pyrochlore oxide KOs_2O_6. Corner-shared OsO_6 octahedra form a three-dimensional network, and the K atoms at the 8 site are located in the centre of the $Os_{12}O_{18}$ cage as shown in (b). The K atoms hypothetically form a diamond sublattice with a long K-K distance through the four channels of the $Os_{12}O_{18}$ cage along the (111) direction.[48] 18

Figure 1.16 a.) The diagram shows the comparison of the energetics between combustion and conventional processes b.) The three main components of the combustion system.[83] 23

Figure 1.17 Classifications of physical vapour deposition techniques.[94] 26

Figure 1.18 Basic steps involved in a PVD process.[94] 27

Figure 1.19 Schematic representation of the basic steps in the CVD process during thin film formation.[94,95] 28

Figure 1.20 Flow chart of typical chemical solution deposition routes.[98] 31

Figure 1.21 Illustration of the thermal treatment and crystallization process.[98] 35

Figure 1.22 Schematic diagram of the electrochemical deposition technique.[112,113] 36

Figure 1.23 SEM micrographs of nickel oxide thin films which are prepared by different techniques but at similar temperatures a.) PVD: RF reactive magnetron sputtering[114] b.) CVD: MOCVD[115] c.) CSD: Spin-coating[116] d.) ECD.[117] 38

Figure 1.24 Schematic diagram of the hot wall AACVD process used throughout this thesis and showing its major components. 40

Figure 1.25 Illustration of the precursor aerosol generation by the TSI aerosol generator 3076, pneumatic atomization system. 41

Figure 1.26 Schematic diagram of the basic AACVD reactor. (a) Cold-wall reactor (b) Hot-wall reactor. 43

Figure 1.27 Schematic representation of the thin film formation in the reaction chamber or reaction zone.[120–122] 44

Figure 1.28 The structure of thin film characteristics which are affected by (a) low enthalpy (b) high enthalpy (c) low or high enthalpy. 44

Figure 1.29 SEM images of AACVD-produced TiO_2 thin film on a glass substrate which were prepared by different precursors (a) titanium(IV) isopropoxide ($Ti(O'Pr)_4$)[123] (b) $Ti[OCH(CH_3)_2]_4$.[124] 46

Figure 1.30 SEM of TiO_2 as-deposited on steel by AACVD using various mixtures of carrier solvents, (a) ethanol 100%, (b) methanol 100%, (c) 10% methanol and 90% ethanol and (d) 25% methanol and 75% ethanol.[125] 47

Figure 1.31 SEM images of $ZnFe_2O_4$ thin films deposited on FTO substrates using optimum conditions of a deposition temperature of 450 °C and a deposition time of 35 min. (a) and (c) show surface the morphology and cross-section for the film deposited from a 0.1 M solution of (1) in methanol, whereas (b) and (d) show the same detail for a film deposited from 0.1 M solution of (1) in ethanol.[126] 48

Figure 1.32 SEM images of CdS thin films deposited from $[Cd(S_2CNCy_2)_2{\cdot}py]$ on FTO (a–c) and soda glass (d–f) at 350, 400, and 450 1C from THF solution.[127] 49

Figure 1.33 SEM images of Sb_2S_3 thin films deposited onto glass substrates at (a) 300 (b) 350 (c) and (d) 400 °C by AACVD from *tris*(thiobenzoato)antimony(III).[128] 50

Chapter 2

Figure 2.1 TGA curve of $Cu(NO_3)_2{\cdot}3H_2O$. 66

Figure 2.2 XRD patterns of deposited films of $Cu(NO_3)_2{\cdot}3H_2O$ prior to annealing using (a) ethanol or (b) methanol solvents. (c) is a XRD pattern of Pilkington SiCO glass. 68

Figure 2.3 XRD patterns of deposited films after annealing under air with the temperature range 300 – 600 °C and using (a) ethanol or (b) methanol as solvent. These peaks corresponding to monoclinic CuO, JCPDS No: 00-002-1040. 68

Figure 2.4 XRD patterns of AACVD deposited films from $Cu(NO_3)_2{\cdot}3H_2O$ by using (a) ethanol and (b) methanol as solvent at various deposition temperatures. These peaks corresponding to cubic Cu, JCPDS No: 01-085-1326. 72

Figure 2.5 The appearance of the deposited films with the deposition temperature at 600 °C and their SEM micrographs at 25,000x magnification using ethanol (a/b) and methanol (c/d), respectively. 73

Figure 2.6 The appearance of the films (a) as deposited at 300 °C and after annealing at different temperatures (b) 100°C (c) 150°C (d) 200°C (e) 250°C (f) 300°C (g) 400°C (h) 500°C (i) 600°C.....74

Figure 2.7 XRD patterns of the annealed films at different temperatures under an air atmosphere. Cu_2O (JCPDS No: 00-005-0667), CuO (JCPDS No: 00-041-0254). 75

Figure 2.8 Summary of copper/copper oxide transformations described in this section. 76

Figure 2.9 TGA curve of $Ni(NO_3)_2{\cdot}6H_2O$.....81

Figure 2.10 X-ray diffraction patterns for the annealed films prepared using (a) ethanol (b) methanol. These corresponding to cubic nickel oxide (NiO, JCPDS No: 00-004-0835).....83

Figure 2.11 XRD patterns of films deposited from $Ni(NO_3)_2{\cdot}6H_2O$ using (a) ethanol and (b) methanol as solvent at various deposition temperatures. These peaks corresponding to hexagonal nickel metal (JCPDS No: 00-045-1027).....85

Figure 2.12 The appearance of the films which were deposited at 600 °C by using (a) ethanol (b) methanol as solvent. 85

Figure 2.13 TGA curve of N1 N2 and N3.....87

Figure 2.14 XRD patterns of AACVD deposited films from the precursor systems (a) N1 (b) N2 and (c) N3 at various deposition temperatures. Red circles refer to hexagonal nickel (JCPDS No: 00-045-1027), blue circles refer to cubic nickel

(JCPDS No: 01-070-1849) and green circles refer to cubic nickel oxide (JCPDS No: 01-078-0423). 89

Figure 2.15 Surface morphologies of the nickel oxide films at a deposition temperature at 325 °C from the (a) NT (b) N2 and (c) N3 precursor systems and analysed by AFM. 91

Figure 2.16 AFM surface roughness of the deposited films from the N1, N2 and N3 precursor systems. Area measurement size 100 μm^2. 92

Figure 2.17 Transmittance spectra of the deposited films from the (a) N1 (b) N2 and (c) N3 precursor systems with deposition temperatures between 225 and 400 °C. (d) The deposited films at 325 °C from the N1, N2 and N3 precursor systems. 93

Figure 2.18 XRD patterns of films deposited using the N3 precursor system on (a) Pilkington SiCO glass and (b) FTO glass substrates. Green dots indicate cubic NiO (JCPDS No: 01-078-0423), blue dots indicate cubic Ni (JCPDS No: 01-070-1849), red dots indicate hexagonal nickel (JCPDS No: 00-045-1027), black dots indicate orthorombic Ni_3Sn_2 (JCPDS No: 00-006-0414) and yellow dots indicate orthorhombic NiF_2 (JCPDS No: 00-022-0749). 95

Figure 2.19 AFM surface roughness of the films deposited from the N3 precursor system on Pilkington and FTO glass. Area measurement size 100 μm^2 101

Figure 2.20 Comparable agglomeration of particles. SEM micrographs at 100,000x magnification of the films deposited at 325 °C (a) on Pilkington SiCO glass (b) FTO-coated glass. 102

Figure 2.21 SEM micrographs of the deposited film surface at 40,000x magnification from N3 precursor system at deposition temperature between 225 and 400 °C on Pilkington SiCO glass. 103

Chapter 3

Figure 3.1 TGA curve of LNR11 precursor system and a comparison with $La(NO_3)_3 \cdot 6H_2O$ and $Ni(NO_3)_2 \cdot 6H_2O$. 152

Figure 3.2 TGA curves of the LN R11 and LNA precursor systems. 153

Figure 3.3 Appearance of the deposited films following the deposition conditions in Table 3.3 at various deposition temperatures. 155

Figure 3.4 XRD patterns of (a) films deposited at different temperatures using the LNR11 precursor system and (b) testing the FTO glass performance. 159

Figure 3.5 EDS Mapping analysis of the film deposited from LNR11 precursor system at 450 °C on a FTO glass substrate. 161

Figure 3.6 EDS Mapping analysis of the film deposited from LNR11 precursor system at 500 °C on a FTO glass substrate. 161

Figure 3.7 SEM micrographs of samples prepared using the LNR11 precursor system on FTO glass with the deposition temperatures at (a) 250 °C, (b) 300 °C, (c) 350 °C, (d) 400 °C, (e) 450 °C and (f) 500 °C. 164

Figure 3.8 Cross-section SEM micrographs of samples prepared using the LNR11 precursor system on FTO glass with the deposition temperatures at (a) 250 °C, (b) 300 °C, (c) 350 °C, (d) 400 °C, (e) 450 °C and (f) 500 °C. 165

Figure 3.9 Cross-section SEM micrographs of samples (a) FTO glass, (b)-(c) E350 and (d)-(f) E500 166

Figure 3.10 AFM surface roughness of samples from the deposition conditions of Table 3.3 on FTO glass. Area measurement: 5 μm^2. 168

Figure 3.11 Comparison of the TGA curves of LN R11 and LNR11 AA5 precursor systems. 170

Figure 3.12 SEM micrographs of films from the LNR11 precursor system; (a) as-deposited film (b) annealed film at 600 °C at 100.0x magnification and (c) annealed film at 600 °C at 5000.0x magnification. 172

Figure 3.13 SEM micrographs of films from the LNR11-AA5 precursor system (a) as-deposited film and annealed films annealed at different temperatures: (b) 300 °C (c) 400 °C (d) 500 °C and (e) 600 °C. 173

Figure 3.14 Average surface roughness of the films deposited from the LNR11-AA5 precursor system with various annealing temperatures. Area measurement 25μm^2. 176

Figure 3.15 Cross-section SEM micrograph of the film annealed at 600 °C from the LNR11-AA5 precursor system. 176

Figure 3.16 XRD patterns of the as-deposited and annealed films using (a) LNR11-AA5 and (b) LNR11 precursor systems. (•) and (∇) Features corresponding to cubic $LaNiO_3$ (JCPDS: 00-033-0710) and monoclinic $La_2O_2CO_3$ (JCPDS: 00-048-1113), respectively. 177

Figure 3.17 Transmittance spectra of the films deposited from the LNR11 AA5 precursor system.....180

Figure 3.18 TGA curves of LNR11, LNR11-AA5, LNR11-A10, LNR11-AA15, LNR11-AA20 and LNR11-AA30 precursor systems. 182

Figure 3.19 FESEM micrographs of as-deposited and annealed films from LNR11-AA5, LNR11-AA10, LNR11-AA15, LNR11-AA20 and LNR11-AA30 precursor systems. 185

Figure 3.20 Average surface roughness of the as-deposited and annealed films from LNR11-AA5, LNR11-AA10, LNR11-AA15, LNR11-AA20 and LNR11-AA30 precursor systems. Area measurement 25μm^2. 188

Figure 3.21 Average thickness of the as-deposited and annealed films from LNR11-AA5, LNR11-AA10, LNR11-AA15, LNR11-AA20 and LNR11-AA30 precursor systems. 188

Figure 3.22 FESEM cross-section micrographs of the as-deposited and annealed films from LNR11-AA5, LNR11-AA10, LNR11-AA15, LNR11-AA20 and LNR11-AA30 precursor systems. 189

Figure 3.23 XRD patterns of the (a) as-deposited and (b) annealed films with different precursors containing varying vol.% of acetic acid. I=LNR11-AA5, II=LNR11-AA10, III=LNR11-AA15, IV=LNR11-AA20, V=LNR11-AA30. (♦) corresponding to cubic $LaNiO_3$ (JCPDS: 00-033-0710) and (∇) corresponding to monoclinic $La_2O_2CO_3$ phase (JCPDS: 00-048-1113). 190

Figure 3.24 Transmittance spectra of (a) as-deposited and (b) annealed films from LNR11-AA5, LNR11-AA10, LNR11-AA15, LNR11-AA20 and LNR11-AA30 precursor systems. 194

Figure 3.25 Reflectance spectra of (a) as-deposited films and (b) annealed films from LNR11-AA5, LNR11-AA10, LNR11-AA15, LNR11-AA20 and LNR11-AA30 precursor systems. 195

Figure 3.26 Single crystal structure of complex from lanthanum nitrate and nickel nitrate in an acetic acid. 196

Figure 3.27 (a) molecular structure of metal aquo complex (b) molecular structure from the experiment in this section. 197

Figure 3.28 TGA curve of single crystal complex from $La(NO_3)_3{\cdot}6H_2O$ and $Ni(NO_3)_2{\cdot}6H_2O$ in an acetic acid. 199

Figure 3.29 XRD patterns of the annealed films under difference atmosphere by (a) nitrogen and (b) air with annealing temperature at 500 and 600 °C. (♦) and (∇) Feature corresponding to cubic $LaNiO_3$ (JCPDS: 00-033-0710) and monoclinic $La_2O_2CO_3$ (JCPDS: 00-048-1113), respectively. 203

Chapter 4

Figure 4.1 Metal xanthate precursors used to deposit the ZnS thin film in this chapter. (a) $Zn(S_2COEt)_2$ (b) 2-MePy·$Zn(S_2COEt)_2$. 214

Figure 4.2 The binding modes of thioureide ligands. Inserted isothiocyanate is shown in red and the original metal amide nitrogen is designated as N'.[43,52] 215

Figure 4.3 Zn(isopropyl thioureide), $Zn(S{=}C(NMe)_2\ NCH(Me)_2)_2$. 216

Figure 4.4 TGA curves of **A:** $Zn(S_2COEt)_2$, **B:** 2-MePy·$Zn(S_2COEt)_2$ and **C:** $Zn(S{=}C(NMe)_2NCH(Me)_2)_2$. 216

Figure 4.5 XRD patterns of films deposited from (a) $Zn(S_2COEt)_2$ and (b) 2-MePy·$Zn(S_2COEt)_2$ and (c) $Zn(S{=}C(NMe)_2NCH(Me)_2)_2$ at various deposition temperatures. (∇: Cubic zinc blende ZnS, JCPDS: 03-065-0309), (●: Hexagonal wurtzite ZnS, JCPDS: 01-075-1534). 220

Figure 4.6 Raman spectra of films deposited from (a) $Zn(S_2COEt)_2$ (b) 2-MePy·$Zn(S_2COEt)_2$ (c) $Zn(S{=}C(NMe)_2NCH(Me)_2)_2$ at various deposition temperatures and (d) Pilkington SiCO glass. 222

Figure 4.7 FESEM micrographs of the film deposited from $Zn(S_2COEt)_2$ with the deposition temperature at (a) 150 °C (b) 200 °C. 229

Figure 4.8 FESEM micrographs of the film deposited from 2-MePy·$Zn(S_2COEt)_2$ with the deposition temperature at (a) 100 °C (b) 150 °C (c) 200 °C and (d) 250 °C. 229

Figure 4.9 FESEM micrographs of the film deposited from $Zn(S=C(NMe)_2NCH(Me)_2)_2$ with the deposition temperature at (a) 150 °C (b) 200 °C (c) 250 °C and (d) 300 °C. 230

Figure 4.10 AFM images of films deposited from $Zn(S_2COEt)_2$ with the deposition temperature at (a) 150 °C (b) 200 °C. 231

Figure 4.11 AFM images of films deposited from 2-MePy·$Zn(S_2COEt)_2$ with the deposition temperature at (a) 100 °C (b) 150 °C (c) 200 °C and (d) 250 °C. 232

Figure 4.12 AFM images of films deposited from $Zn(S=C(NMe)_2NCH(Me)_2)_2$ with the deposition temperature at (a) 150 °C (b) 200 °C (c) 250 °C and (d) 300 °C. 233

Figure 4.13 Cross-section micrographs of the film deposited from $Zn(S_2COEt)_2$ with the deposition temperature at (a) 150 °C (b) 200 °C. 234

Figure 4.14 Cross-section micrographs of the film deposited from 2-MePy·$Zn(S_2COEt)_2$ with the deposition temperature at (a) 100 °C (b) 150 °C (c) 200 °C and (d) 250 °C. 235

Figure 4.15 Cross-section micrographs of the film deposited from $Zn(S=C(NMe)_2NCH(Me)_2)_2$ with the deposition temperature at (a) 150 °C (b) 200 °C (c) 250 °C and (d) 300 °C. 235

Figure 4.16 Arrhenius plots; (a) the films deposited from 2-MePy·$Zn(S_2COEt)_2$ (b) the deposited films from $Zn(S=C(NMe)_2NCH(Me)_2)_2$. 238

Figure 4.17 Transmission spectra of the films deposited from the precursors (a) $Zn(S_2COEt)_2$, (b) 2-MePy·$Zn(S_2COEt)_2$ and (c) $Zn(S=C(NMe)_2NCH(Me)_2)_2$ with various deposition temperatures. (d) is a comparison graph of the films deposited $Zn(S_2COEt)_2$ **(A)**, 2-MePy·$Zn(S_2COEt)_2$ **(B)** and $Zn(S=C(NMe)_2NCH(Me)_2)_2$ **(C)** at 200 °C. 241

Figure 4.18 Band gaps of the films deposited from (a) $Zn(S_2COEt)_2$ **(A)** (b) 2-MePy·$Zn(S_2COEt)_2$ **(B)** and (c) $Zn(S{=}C(NMe)_2NCH(Me)_2)_2$ **(C)**. (d) is a comparison between the band gap values and the deposition temperatures of the films deposited from all three precursors. 242

Chapter 5

Figure 5.1 (a) Oxygen plasma cleaning equipment (b) sample substrates before and after oxygen plasma treatment with 10 and 20 min. 251

Figure 5.2 AACVD with the cold wall furnace reactor. 252

Figure 5.3 AACVD with the hot wall furnace reactor. 253

Figure 5.4 Aluminum foil was used to wrap the reactor during the deposition process to prevent light-induced decomposition. 265

Chapter 6

Figure 6.1 These samples are prepared with the different cooling rate. Those on the left in (a) and (b) were prepared with a rapid cooling rate and those on the right in (a) and (b) were prepared from a slow cooling rate. 268

Figure 6.2 Deposited films were prepared with the different type of nozzle. 268

Figure 6.3 Left is an insertion nozzle and right is sample resultant. 268

Figure 6.4 Different position of the heating plate for the cold wall reactor. 269

Figure 6.5 The deposition at 400 °C with the different deposition time. Left to right is 3, 5, 15 and 30 min. 269

Figure 6.6 The graphite supporter for the substrates. 269

Figure 6.7 Appearance of deposited film from copper nitrate and nickel nitrate with various ratios via AACVD technique. 270

Figure 6.8 XRD patterns of copper-nickel alloy thin film grown from simple metal nitrate precursor via the AACVD technique. 270

Figure 6.9 FESEM micrographs of the deposited film from 250 °C. 273

List of Tables

Chapter 1

Table 1.1 Examples of high technological devices which have thin films technology as a core component. 3

Table 1.2 Most common oxide crystal structures and examples.[13] 5

Table 1.3 Electronic properties of transition metal oxides of different types.[15] 6

Table 1.4 The examples materials of ABO_3 structure oxide.[16] 15

Table 1.5 Example of ABO_4 crystal structure oxides with their applications. 16

Table 1.6 Example materials of the AB_2O_4 structural family.[16,47] 17

Table 1.7 Some examples of other ternary oxide materials and their properties. 18

Table 1.8 Some of the typical unit cells of the most common sulphides of the transition metal.[54] 20

Table 1.9 Examples of transition metal sulphide materials and their properties and applications. 21

Table 1.10 Summary of the metal nitrate salts that have been used for thin film deposition. 25

Table 1.11 The advantages and disadvantages of the PVD technique.[94] 27

Table 1.12 The advantages and disadvantages of the CVD technique.[94–96] 29

Table 1.13 Summary of the types of CVD technique.[94–97] 30

Table 1.14 Examples of deposition methods based on the CSD technique. 32

Table 1.15 Considerations for thin film fabrication. 37

Chapter 2

Table 2.1 A summary of copper oxide material properties and their applications. 62

Table 2.2 Examples of copper oxide thin films which were deposited by different techniques and some of their properties. 64

Table 2.3 Deposition conditions for spin coating of $Cu(NO_3)_2 \cdot 3H_2O$. 67

Table 2.4 Crystallite size of the deposited films prepared using ethanol and methanol as solvent after annealing at various temperatures. 70

Table 2.5 Deposition conditions for AACVD of $Cu(NO_3)_2 \cdot 3H_2O$. 70

Table 2.6 The appearance of the deposited films by AACVD. 71

Table 2.7 Crystallite sizes of the AACVD deposited films fabricated by using ethanol and methanol as solvent. 73

Table 2.8 Annealing process conditions to study oxidation of the copper films. 74

Table 2.9 Comparison of the CuO crystallite size of the annealed films at 600 °C, deposited by either spin coating or AACVD. 76

Table 2.10 Examples of nickel oxide thin films (NiO) deposited by various techniques and some of their properties. 80

Table 2.11 Deposition conditions for spin coating of $Ni(NO_3)_2 \cdot 6H_2O$. 82

Table 2.12 Surface tension of the solvent.[57] 82

Table 2.13 Crystallite size of the deposited films prepared using ethanol and methanol as solvent after annealing. 83

Table 2.14 Deposition condition for AACVD of $Ni(NO_3)_2 \cdot 6H_2O$. 84

Table 2.15 Deposition conditions for nickel oxide thin film fabrication. 86

Table 2.16 The residual weight (%) from TGA curves and calculated weight for NiO from the N1, N2 and N3 precursor systems. 87

Table 2.17 Comparison of NiO crystallite size of films fabricated at 325 °C from the N1, N2 and N3 precursor systems. 88

Table 2.18 The appearance of the films deposited from the N1, N2 and N3 precursor systems at deposition temperatures between 225 and 400 °C. 90

Table 2.19 Deposition conditions for nickel oxide thin film fabrication from the N3 precursor system on FTO glass. 94

Table 2.20 Crystallite size of the deposited films on the Pilkington glass and FTO glass substrate. 96

Table 2.21 The surface morphology of the deposited films from the N3 precursor system at different deposition temperature using AFM on various substrate surfaces. 98

Table 2.22 The EDS analyses of the deposited films from the N3 precursor system on Pilkington SiCO glass substrates. Average atomic % from 3 measured areas. ..112

Table 2.23 The EDS data of the films deposited from the N3 precursor system on FTO glass substrates. Average atomic % from by measuring 3 areas. 113

Table 2.24 Summary of lanthanum oxide thin films (La_2O_3) deposited by different techniques and some of their properties. 117

Table 2.25 Deposition conditions for spin coating of $La(NO_3)_3{\cdot}6H_2O$. 121

Table 2.26 Deposition conditions for AACVD of $La(NO_3)_3{\cdot}6H_2O$. 123

Table 2.27 Summary of praseodymium oxide thin films which have been deposited by different techniques and some of their properties. 130

Table 2.28 Deposition conditions for spin coating of $Pr(NO_3)_3{\cdot}6H_2O$. 134

Table 2.29 Crystallite size of the deposited films on the Pilkington SiCO glass using ethanol and water as solvents. 135

Table 2.30 Deposition conditions for AACVD of $Pr(NO_3)_3{\cdot}6H_2O$. 136

Chapter 3

Table 3.1 List of precursor solution systems used in this chapter. 151

Table 3.2 Deposition conditions for of hot-wall AACVD of lanthanum nickel oxide thin films. 154

Table 3.3 Deposition conditions for AACVD of lanthanum nickel oxide thin film. 155

Table 3.4 Conditions of the FTO glass performance test and appearance of FTO glass after the process. 157

Table 3.5 Atomic % of elements on samples fabricated using the LNR11 precursor system at various deposition temperatures. 160

Table 3.6 Surface morphology of samples from the deposition conditions shown in Table 3.3 assessed by AFM on various substrate surfaces. 167

Table 3.7 Deposition conditions for spin coating of lanthanum nickel oxide thin film. 170

Table 3.8 Appearance of the deposited films from the LNR11 and LNR11-AA5 precursor systems. 171

Table 3.9 Conductivity of deposited films. 172

Table 3.10 Surface morphology of the as-deposited and annealed films from the LNR11 and LNR11-AA5 precursor systems at different annealing temperatures using AFM on various substrate surfaces. 174

Table 3.11 Summary of the EDS elemental analysis for films deposited onto Pilkington SiCO glass substrates from the LNR11-A55 precursor system after annealing under an air atmosphere. Average atomic % from 3 measured areas..... 179

Table 3.12 Summary of the ratio of La, Ni and O contents on the deposited films using EDS analysis. 180

Table 3.13 Deposition conditions for spin coating of lanthanum nickel oxide thin film. 181

Table 3.14 Appearance of the films from the LNR11 AA5-30 precursor systems. 183

Table 3.15 Conductivity of deposited films. 183

Table 3.16 Surface morphology of as-deposited and annealed films from LNR11-AA5, LNR11-AA10, LNR11-AA15, LNR11-AA20 and LNR11-AA30 precursor systems with and annealing temperature of 600 °C using AFM on various substrate surfaces. 186

Table 3.17 Crystallite size of annealed films. 191

Table 3.18 Summary of the EDS elemental analysis of as-deposited and annealed films from the LNR11-AA5, LNR11-AA10, LNR11-AA15, LNR11-AA20 and LNR11-AA30 precursor systems. Average atomic % from 3 measured areas.....192

Table 3.19 Atomic % ratio between La, Ni and O of the as-deposited and annealed films from all precursor systems. 193

Table 3.20 Selected bond lengths (Å) for complex from lanthanum nitrate and nickel nitrate in an acetic acid.....197

Table 3.21 Selected angles (Å) for complex from lanthanum nitrate and nickel nitrate in an acetic acid.....197

Table 3.22 Deposition conditions for spray pyrolysis of lanthanum nickel oxide thin films from the LNR11 precursor system.....202

Table 3.23 Appearances of the deposited films from the LNR11 precursor system via spray pyrolysis. 203

Table 3.24 Compositional analysis of the annealed film from annealing temperature of 600 °C under air atmosphere. 205

Chapter 4

Table 4.1 Examples of metal sulphide thin films from metal xanthate complex single source precursors.....212

Table 4.2 Examples of metal sulphide thin films from metal thioureide single source precursors. 215

Table 4.3 Deposition conditions used to deposit ZnS thin films.....217

Table 4.4 Appearance of all deposited films from $Zn(S_2COEt)_2$, 2-MePy·$Zn(S_2COEt)_2$ and $Zn(S{=}C(NMe)_2NCH(Me)_2)_2$ at various deposition temperatures. 219

Table 4.5 Estimated crystallite sizes of deposited films.....221

Table 4.6 Raman shifts of deposited thin films from $Zn(S_2COEt)_2$, 2-MePy·$Zn(S_2COEt)_2$ and $Zn(S{=}C(NMe)_2NCH(Me)_2)_2$ and their assignments. 223

Table 4.7 Summary of the EDS elemental analysis for ZnS films deposited onto Pilkington SiCO glass substrates from $Zn(S_2COEt)_2$ **(A)**, 2-MePy·$Zn(S_2COEt)_2$ **(B)** and $Zn(S=C(NMe)_2NCH(Me)_2)_2$ **(C)** at various deposition temperatures for 1 hour. Average atomic % from 3 measured areas.....226

Table 4.8 Summary of the ratio of Zn and S contents on the deposited films from $Zn(S_2COEt)_2$ **(A)**, 2-MePy·$Zn(S_2COEt)_2$ **(B)** and $Zn(S=C(NMe)_2NCH(Me)_2)_2$ **(C)** at different disposition temperatures.....227

Table 4.9 Average surface roughness of all deposited film $Zn(S_2COEt)_2$, 2-MePy·$Zn(S_2COEt)_2$ and $Zn(S=C(NMe)_2NCH(Me)_2)_2$ at various deposition temperature. Average atomic % from 3 measured areas.....230

Table 4.10 Average thickness for the film deposited from $Zn(S_2COEt)_2$ **(A)**, 2-MePy·$Zn(S_2COEt)_2$ **(B)** and $Zn(S=C(NMe)_2NCH(Me)_2)_2$ **(C)**. Average thickness from 3 measured areas. 234

Table 4.11 Average growth rate values for the film deposited from $Zn(S_2COEt)_2$ **(A)**, 2-MePy·$Zn(S_2COEt)_2$ **(B)** and $Zn(S=C(NMe)_2NCH(Me)_2)_2$ **(C)**.....236

Table 4.12 Activation energy values for the films deposited from 2-MePy·$Zn(S_2COEt)_2$ and $Zn(S=C(NMe)_2NCH(Me)_2)_2$.....238

Table 4.13 An overview of the band gap, film thickness, estimated crystallite size and roughness values of the films deposited from Zn(S2COEt)2, 2-MePy·Zn(S2COEt)2 and Zn(S=C(NMe)2NCH(Me)2)2 at various deposition temperatures. 243

Chapter 5

Table 5.1 Precursor recipes for the deposition of nickel oxide film and combustion processing technique. 257

Table 5.2 Summary of conditions for AACVD experiments to deposit lanthanum nickel oxide films via a hot wall reactor. 261

Table 5.3 Precursor recipes for the deposition in this section.....262

Table 5.4 Precursor recipes for the deposition in this section.....262

Table 5.5 Summary of the deposition conditions for ZnS thin film fabrication via AACVD. 265

Chapter 6

-

List of Schemes

Chapter 1

Scheme 1.1 Decomposition of a metal nitrate.[84] 23

Scheme 1.2 ZnO thin film preparation by the combustion synthesis.[83] 24

Chapter 2

Scheme 2.1 Decomposition of methanol.[22] 72

Chapter 3

-

Chapter 4

Scheme 4.1 Example of nickel sulphide (NiS) formation from a metal xanthate complex via the Chugaev elimination mechanism.[41] 213

Scheme 4.2 Typical synthetic routes of metal xanthates.[43] 213

Scheme 4.3 Synthesis of metal thioureide complexes.[43] 214

Chapter 5

-

Chapter 6

-

"PhD Doesn't Grow on Trees"

Chapter 1:

Introduction

1.1 Thin film technology

In 1965, Moore's law predicted that ***'the number of transistors on an integrated circuit will double around every two years'*** (Figure 1.1 (a)).[1] Around six years later, in 1971, Intel Corporation released the first 4-bit central processing unit (CPU) which was named ***'Intel 4004'***. It contained 2300 transistors on a 12 mm^2 integrated circuit, 4096 bytes of the memory and a 740 kHz CPU clock, (Figure 1.1 (b)).[2] Over the four decades since that time, the technology of the transistor has been developed and it is still moving forward in agreement with Moore's law. In April 2018, the Intel Corporation launched various types of new CPU to a global computer market. These CPUs were created under a new nanometer scale process with the special code name, the ***'Coffee Lake'***, which further improved performance. For example, a CPU with the code name Intel® Core™ i9-8950HK, (Figure 1.1 (c)), comprised more than 1.5 billion transistors on a 149 mm^2 integrated circuit and also obtained a maximum CPU clock at 4.8 GHz. That new technology processor increased the CPU performance through reduced power consumption, faster clock speed, as well as being smaller and more efficient than the original CPU in 1971. Furthermore, if the technology continues to improve in line with Moore's law, we will see the emergence of quantum transistors and further big jumps in the technology in the near future.[3]

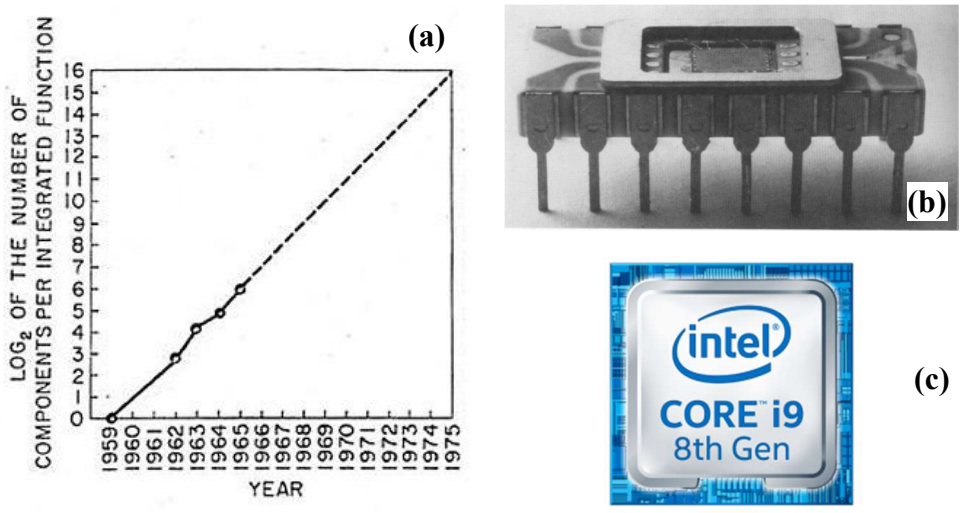

Figure 1.1 ((a) Moore's law, the prediction of a number of transistors on an integrated circuit versus year.[1] (b) Intel 4004 in its package[4] (c) Intel® Core™ i9-8950HK.[5]

The continued evolution of transistor technology offers incredible impacts to the world and improvement to the quality of human life. Indeed, '***thin film technology and material science'*** is the basis for many challenging technological developments. From the past until now thin film technology has been widely used in numerous fields such as communication, energy, medical and food. Some examples of applications which have used thin films as a part of the technology are illustrated in Table 1.1.

Table 1.1 Examples of high technological devices which have thin films technology as a core component.

Technology developments	Features
	The smartphone can generate electricity from sunlight by using its display screen. The display screen contains a thin film layer which has code name is '*Wysips Crystal layer'*. This smartphone is a prototype which was introduced by Kyocera Corporation in 2015.[6]
	The smart label is embedded into the packaging and provides detailed information about the product which that is useful for the customer. This label was launched by Thin Film Electronics company.[7]
	A thin-film solar cell is a device which is created by depositing one or multi-layers of photovoltaic materials on a polymer or glass substrate. Generally, the solar cell has an opaque or dark appearance. However, many researchers are trying to develop transparent solar cells because this feature can be applied to a house window to generate massive energy from nature.[8,9]

Technology developments	Features
	The biosensor chips which are shown in the picture were created by researchers from the Moscow Institute of Physics and Technology (MIPT). The sensor chips based on graphene, graphene oxide and carbon nanotube were prepared in the form of a thin film which can detect low concentrations of biological molecules such as RNA, DNA and proteins including antigens and viruses, (2015).[10]

A thin film can be defined as a material which obtains a thickness between the range of nanometer and a few of micrometres (Figure 1.2). As do many nanoscale materials, thin films provide a variety of outstanding or unique optical, electrical, magnetic, dielectric and optoelectronic properties in comparison to the bulk materials.[11] Moreover, the use of thin films devices provides other advantages such as a low consumption of materials in their production, reduced energy consumption in electronic devices and a lightweight construction to further reduce production costs.

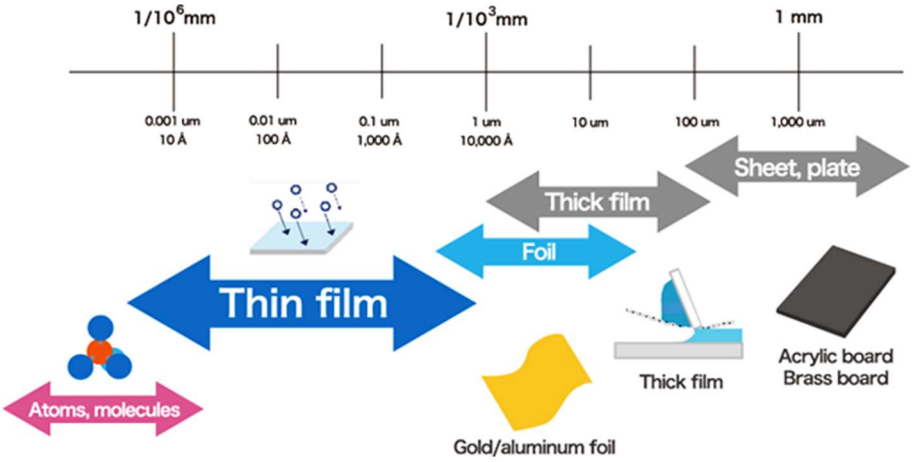

Figure 1.2 Illustration of thin film scale and other sizes of materials.[12]

From this context provided by modern device advances, this thesis is concerned with thin film fabrication with a particular focus on oxide and sulphide materials (their general characteristics and properties will be described in the following sections). The thesis is, thus concentrated not only on aspects of low-cost and environmentally friendly methods of fabrication but also explores the unique character and quality of the fabricated thin films.

1.2 Oxide materials

An oxide material is a substance that comprises atoms of oxygen and other elements in its chemical structure. Oxide materials comprise many different types of structure and present various properties that depend on the identity of the elements bonding with oxygen in the oxide structure. The common structures adopted by metal oxides are presented in Table 1.2 along with some examples of specific oxide materials.

Table 1.2 Most common oxide crystal structures and examples.[13]

Name	Examples
Rock salt	MgO, NiO, MnO, CoO, FeO
Fluorite	CeO_2, ZrO_2
Spinel	Al_2MgO_4, Fe_3O_4(Inverse)
Perovskite	$SrTiO_3$, $BiTiO_3$, $NaWO_3$
Wurtzite	ZnO, BeO
Rutile	TiO_2, RuO_2, SnO_2
Corundum	Al_2O_3, Fe_2O_3, Cr_2O_3, V_2O_3, Ti_2O_3

The variations in composition and structure adopted by materials in the oxide family and advantages provided by their thin film forms have led to intense worldwide interest in both industrial and academic laboratories. The fabrication of oxide thin films is challenging, however, and the most appropriate method to provide the necessary properties and proper morphology for particular application must be identified.

1.2.1 Binary metal oxide thin film materials

A binary metal oxide is a material which contains oxygen and one other element in its chemical formula. Generally, binary metal oxides appear with the most common stoichiometry of MO, MO_2, M_2O_3 and M_3O_4 (M = metal atom).[13] Oxide materials which are created from the transition metals and rare earth metals are well-known and are, thus, named as ***"Transition metal oxides (TMOs) and Rare earth metal oxides (REMOs)"***, respectively.

Transition Metal oxides (TMOs)

Transition metal oxides (TMOs) are the products from the reaction between a transition metal and oxygen. The unique nature of transition metals arises from an incomplete electron in d subshell. This feature leads to a wide range of oxidation states in their oxide materials. Typically, therefore, a single transition metal can form various types of TMO compounds and structures that provide varied unusual and useful properties.[14,15] Furthermore, vacancies, dislocations, grain boundaries and stacking faults provide material defects which affect and influence the a local oxygen bonding and lead to further fascinating properties of the oxides.[16] The physical properties and crystal structures of TMOs are thus largely dependent on their delocalized valence electrons. The electronic structure of TMOs dictate whether it presents a character as an insulator, semiconductor, metal or superconductor, (Table 1.3).[15] The well-known theory which can be used to describe the electronic behaviour of TMOs is ***"Band theory"***.

Table 1.3 Electronic properties of transition metal oxides of different types.[15]

Class of materials	Examples
Metals	
3*d* oxides	TiO, CrO_2
4*d* oxides	MoO_2, RuO_2
5*d* oxides	$ReO3$, A_xWO_3
Semiconductor or insulators	
3*d*	MnO, CoO, NiO, Fe_2O_3, Cr_2O_3
3*d* and 5*d*	MoO_3, WO_3, Nb_2O_5, Rh_2O_3
4*f*	Pr_2O_3, Pr_6O_{11}, PrO_2
Nonmetal (semiconductor)-to-metal transition	
3*d*	V_2O_3, VO_2, V_3O_5, V_4O_7, V_6O_{13}, Ti_2O_3, Ti_3O_5
4*d*	NbO_2
4*f*	EuO
Superconducting transition	TiO, $BaPb_{0.75}Bi_{0.25}O_3$, $LiTi_2O_4$, $YBa_2Cu_3O_7$

Band theory and Transition Metal oxides

Band theory focuses on the valence electrons which reside in the outermost shell of an atom and move around in a periodic lattice. The electrons orbit the atom with a wave-like behaviour. This behaviour can be described with a mathematic function which is

used to calculate the probability region or space in which an electron can be found; this region or space is called an ***'Atomic orbital, (AO)'***.

When an atomic orbital (AO) overlaps with another AO of the adjacent atom they can share the electron pairs together and a molecular orbital (MO) is formed. Bonding molecular orbitals (BMO) and anti-bonding molecular orbital (AMO), illustrated in Figure 1.3, are formed by the respective in phase and out of phase combination of the wavelike AOs.

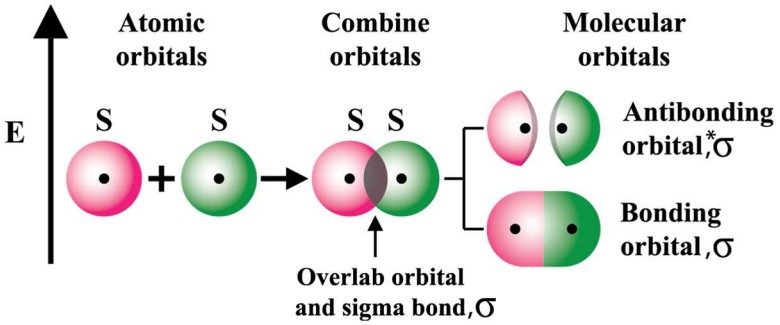

Figure 1.3 The illustration of anti-bonding and bonding orbital which are formed by the in phase and out of phase combination of two s atomic orbitals.[17]

The BMO is at the lower energy than the AMO and for this reason the BMO is filled first. The electrons in a BMO are thus more stable than the electrons in the equivalent AMO providing the electronic energy to form the bond.[14,15]

Increasing numbers of orbital overlaps lead to a periodic spacing between both bonding BMO (at the low energy) and AMO (at the higher energy) 2 electron wave functions. When the number of atoms becomes close to Avogadro's number, the spacing of the energy levels between the MOs is almost infinitely small such that the spacing of the energy levels will look like a continuous bar. The continuous bar of energy levels is named as an ***"Energy band"*** (Figure 1.4). The lowest energy level of the energy band is thus completely bonding whereas the highest energy level of the energy band is totally antibonding.

When the energy levels of the bonding molecular orbitals are sufficiently close together, the resultant band is called the ***"valence band"*** or filled band because this band is filled with electrons. Likewise, when the energy levels of the antibonding molecular orbitals are so close together, the band is termed the ***"conduction band"*** and is not filled with electrons.

The conduction band possesses a higher energy than the valence band and between both bands, there is an energetic separation of the energy levels that is called the ***"band gap"***. Movement of electrons from the filled valence band to the empty conduction band across the band gap, leads to the conduction of electricity in solid materials.

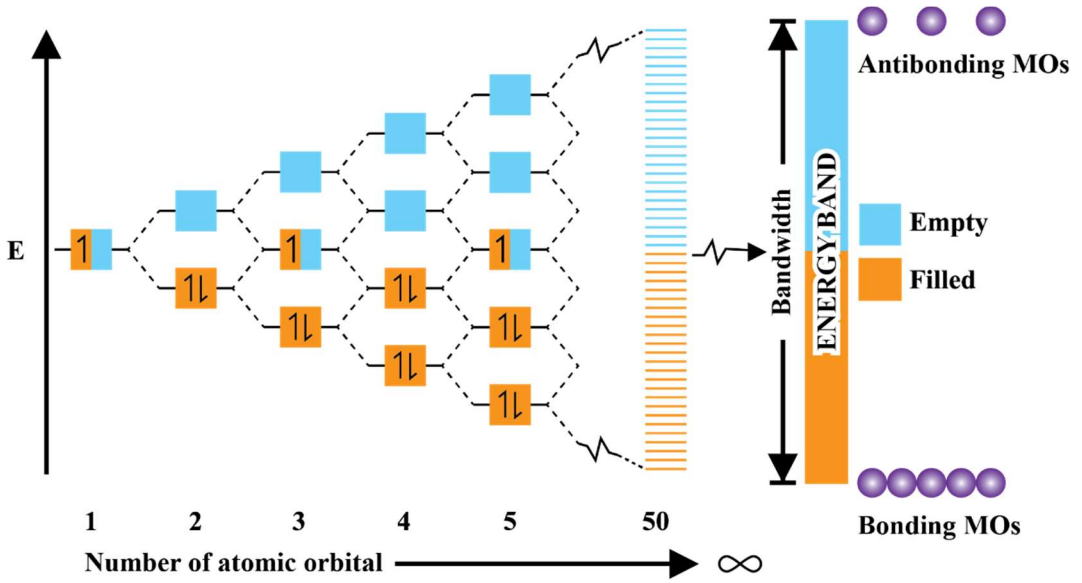

Figure 1.4 The diagram of molecular orbital energy level from the arrangement of numerous atoms.[18]

From Figure 1.5, different types of solid materials can be classified as an insulator, semiconductor and metal or even superconductor by the size of the energy band gap and the position of the Femi energy level (E_F.).

A metal either has a very small band gap or its valence band is overlapped with the conduction band so that the electrons can be easily moved through between valence and conduction band. Consequently, a metal possesses good electrical conductivity, (conductivity,$\sigma > 10^3$ $[\Omega.cm]^{-1}$).

In contrast, an insulator contains a large band gap, hence, the electrons from the valence band are difficult to excite from the valence band to the conduction band. In such cases, the electrical conductivity is poor. ($\sigma < 10^{-7}[\Omega.cm]^{-1}$).

A semiconductor displays a smaller energy band gap than an insulator but wider than a metal. The electrons which reside in the filled band may be excited by receiving sufficient external energy to flow across the band gap including electrical conduction. The conductivity of a semiconductor is, thus, in a range of 10^{-7} to 10^{-3} $[\Omega.cm]^{-1}$, while

external energy may be in the form of increased temperature, an electric field or a magnetic field, etc.

Because of their tunable properties between an insulator and a conductor, semiconductors are vitally important to electronic device technology. Furthermore, a semiconductor may be classified into 3 types that are intrinsic, *n*-type and *p*-type by consideration of the nature of the band gap, (Figure 1.5).

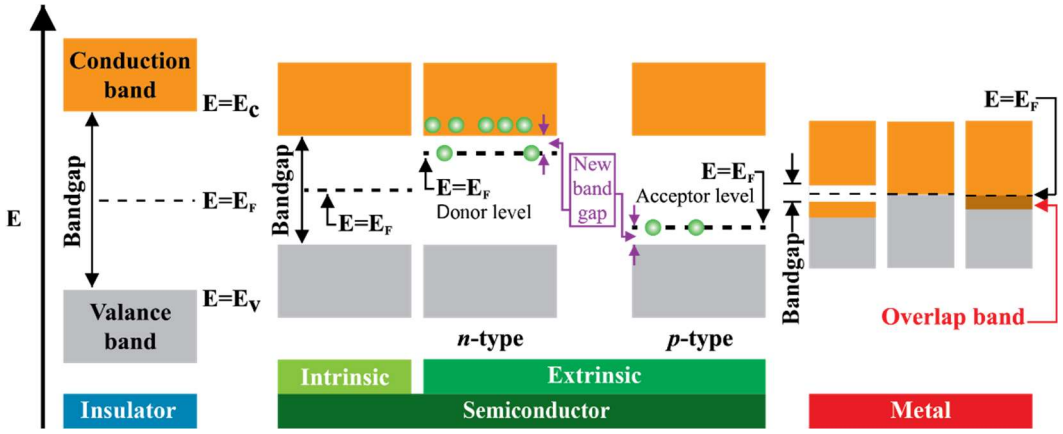

Figure 1.5 Schematic illustration of the band structure of a solid. EF is the Fermi level which is the highest electronically occupied energy level, EC is the lowest energy level of the conduction band and EV is the highest energy level of the valence band.[15]

The electrical and thermal properties of a solid state material are characterized by the ***"Fermi energy level, (E_F)"*** (Figure 1.5). The concept of the E_F derives from the ***"Fermi-Dirac distribution function"***, and is the highest energy level that electrons can achieve at 0 K or the lowest energy that an electron must have in order to be able to change its state from the valence band to the conduction band.

For a metal, E_F lies within the band, whilst for an insulator or a semiconductor, E_F lies between the valence and conduction band. The E_F is potentially useful to characterize the type of semiconductor material. An intrinsic semiconductor is a pure semiconductor which comprises a single atomic structure and possesses the interesting property of electrical conductivity when it receives enough energy from the external sources. In contrast, *n*-type and *p*-type semiconductors are artificially created to improve the performance of electrical conductivity in the semiconductor materials.

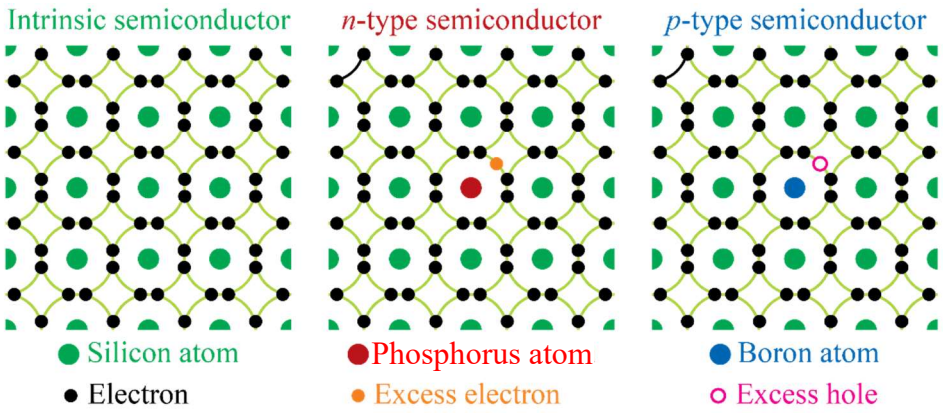

Figure 1.6 Illustration of an intrinsic, n-type and p-type semiconductor.

n-type and *p*-type semiconductors are extrinsic materials which are doped with small amounts of impurities to tune the electrical properties, as illustrated in Figure 1.6.

An *n*-type material is produced by doping the pure semiconductor with impurities which contain an excess of valence electrons in comparison to the pure semiconductor, such that the excess electrons can move freely around the crystal structure lattice. The resultant energy which the excess electrons occupy is called the ***"donor level"*** which lies in the band gap but closer to the conduction band. Consequently, those electrons are more easily excited to the conduction band, Figure 1.5. In an example of an *n*-type semiconductor, impurities such as arsenic (As) or phosphorus (P) are doped into a pure silicon (Si) or germanium (Ge) crystal.

A *p*-type semiconductor is also created by doping elements into the pure semiconductor. In this instance the elements, however, contain a lower number of valence electrons than the pure semiconductor creating holes in the valence band. The electrons from the adjacent atoms can migrate to the holes continuously such that it seems that the holes move around the crystal lattice, resulting in electronic conductivity. The energy level of these electrons is called the ***"acceptor level"***, which lies between the valence band and the conduction band but closer to the valence band, (Figure 1.5). In an example of a *p*-type semiconductor, indium (In) or boron (B) is doped into Si or Ge.

The research of binary transition metal oxide which is presented in this thesis will examine the deposition and characterization of '***copper oxide'*** and '***nickel oxide'*** thin film materials. These oxides are promising *p*-type semiconductor materials for electronic devices and in many fields.

Rare Earth oxides (REOs)

Rare earth elements, also known as the lanthanides comprise a series of seventeen chemical elements in the periodic table which commonly exist as cations with a +3 charge. The oxides of these elements are named as ***'rare earth oxides, REOs'***. REOs typically display a large band gap (E_g), high dielectric constants (κ = 7-30), high resistivity, high thermal and chemical stability, high breakdown electric field, high conduction offset, as well as magnetic and luminescent properties.[19–21] Due to these interesting properties, REOs are crucial for the development of many fields of modern technology such that both the Japanese and the US Department of Energy has described them ***"the seeds of technology"*** and ***"technology metals"***, respectively.[22] Development of REOs in thin film form, therefore, will also help and support the creation and design of new electronic devices and enable a reduction of weight, miniaturization and lower energy consumption.[19,23]

Crystal structure of REOs

All of the rare earth metals from stable oxides and the metals themselves react readily with the oxygen in ambient air.[24–29] Generally, rare earth ions possess a trivalent state in their oxide structures and provide stable phases with the sesquioxide stoichiometry, R_2O_3, (R = rare earth, O = oxygen).[27,29,30]

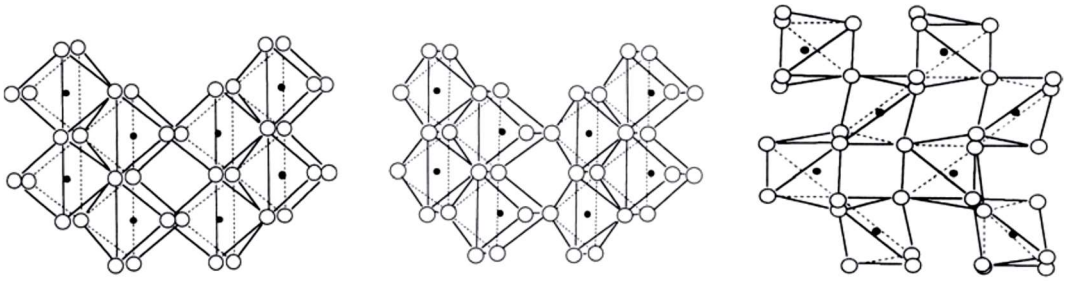

A-type **B-type** **C-type**

Figure 1.7 Polymorphic crystal structures of the sesquioxides R_2O_3: (hexagonal) A-type, (monoclinic) B-type, (Cubic) C-type. The solid dots indicate the metal atoms.[31]

The sesquioxides adopt one of three possible polymorph crystalline structures, which are described as A-type (hexagonal), B-type (monoclinic) and C-type (cubic) structures (Figure 1.7).[27] The adoption of the crystalline structure depends on the ionic radius of the specific rare earth ion in the oxide structure.

The crystalline structures of the sesquioxides can be transformed by the increasing temperature. Figure 1.8 shows the phase transformation of the rare earth oxide when the temperature is changed.

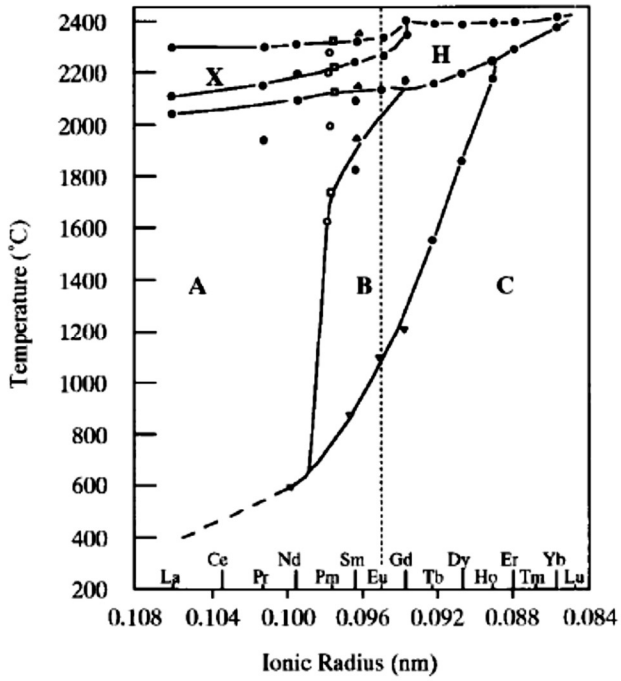

Figure 1.8 Polymorphic transformation for the rare earth sesquioxides.[29,32]

Most remarkably, rare earth sesquioxides which have an ionic radius in the middle range of the series can be found in five polymorphic phases. For instance, Sm_2O_3, at temperatures below 900 °C displays the C-type crystal structure, whereas above 900 °C the C-type structure can be transformed to the B-type structure. Moreover, when the temperature is increased to over 1900 °C, Sm_2O_3 transform to the A-type oxide structure. At even higher temperatures, above 2100 °C, the A-type structure of Sm_2O_3 can be converted to a further H-type structure, while a final phase of Sm_2O_3, the X-type form, is observed at temperatures around 2220 °C before the boiling point at 2335 °C.

In addition, a limited number of rare earths which can achieve the +4 oxidation state possess another oxide structure named as a ***"fluorite-typed dioxide"***, (Figure 1.9). The fluorite-type dioxide structure displays a chemical formula of RO_x, ($1.5 < x < 2$) and some examples of rare earth oxides which display this structure are CeO_2, Pr_6O_{11} and Tb_4O_7. [27,29,30]

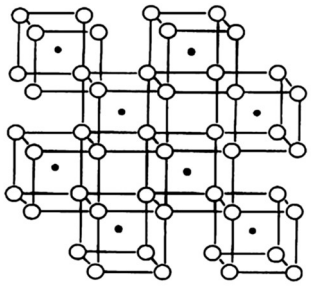

Figure 1.9 Representative fluorite-typed dioxide, RO_2. The solid dots indicate the metal atoms.[31]

The fluorite type structure has a relationship with the C-type oxide structure, in which cubic coordination polyhedra form the three-dimensional network of the oxide structure by edge sharing with the rare earth atoms in the structure in eight-coordinate environments. If one-quarter of the oxygen atoms in the structure are removed, the rare earth atoms change from eight coordination to six coordination and the C-type oxide structure is formed, (Figure 1.10).

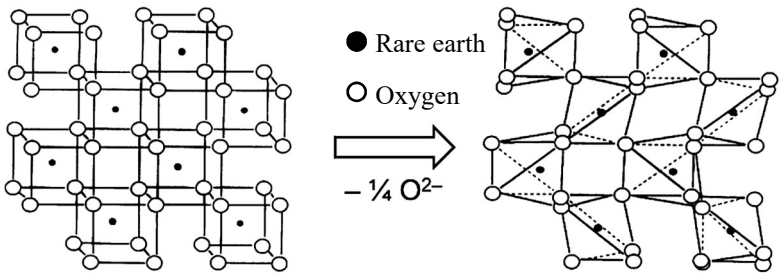

Fluorite-type oxide, RO_2 C-type sesquioxides, R_2O_3

Figure 1.10 The relationship between the cubic fluorite-type dioxide (RO_2) and the cubic C-type sesquioxides (R_2O_3).[31,33–35]

Some rare earths such as Eu^{2+}, Yb^{2+} and Sm^{2+} can also form stable oxide structures with the stoichiometry RO. These compounds commonly adopt NaCl-type cubic structures with EuO being the most stable. [27,29]

The preparation of REOs as thin films is very challenging as the desired properties are provided by the appropriate structure. For example, the A-type structure of the lighter REOs (La_2O_3 to Pr_2O_3) provide κ values which are higher than the B or C type structures.[27]

This thesis will be broadly focused on the deposition of lanthanum oxide and praseodymium oxide thin films and their characterization.

1.2.2 Ternary Metal Oxides (TMOs)

Ternary metal oxides (TMOs) are materials which comprise an oxygen atom with two other dissimilar metal atoms. The chemical formula of such oxides may be generalized as $A_xB_yO_z$, where A and B indicate the metal elements which have low and high oxidation states, respectively. Ternary metal oxides can be categorized into four major groups with the stoichiometries shown in Figure 1.11.

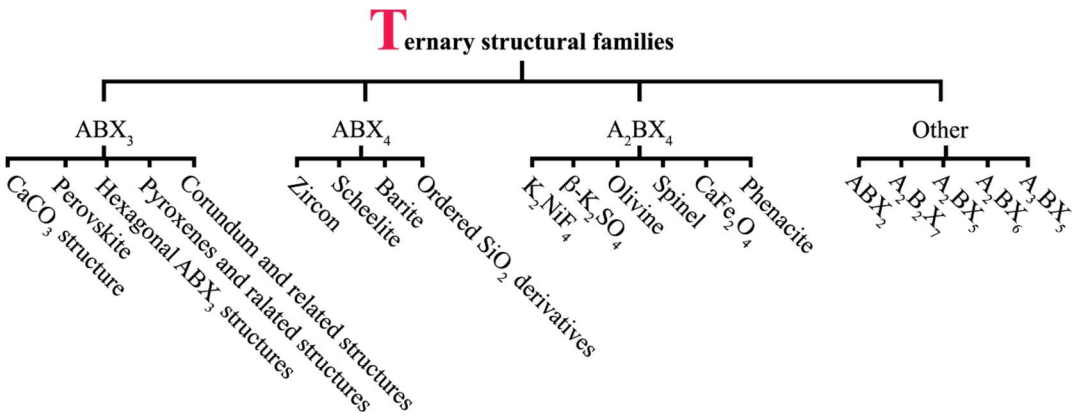

Figure 1.11 The major ternary structure families.[37]

The incorrporation of two metals with different oxidation states into each of these crystalline structures allows the gereration of numerous oxide materials with different characters and unique properties. Examples of ternary metal oxide materials of each stoichmetry and their advantages are presented below.

ABO_3 structure

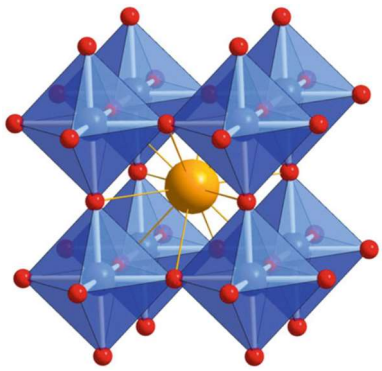

Figure 1.12 Crystal structure of a cubic ABO_3 perovskite. Orange spheres represent the A cation, blue spheres are B cations, and red spheres O anions.[38]

Figure 1.11 shows family of the ABX_3 ternary crystal structures where X is an oxygen atom of the oxide materials. Figure 1.12 represents an exemplary ABO_3 material that is called a ***'Perovskite crystal structure'***.

The ABO_3 structure family includes many materials including $CaCO_3$-[calcite], $CaTiO_3$ (perovskite), pyroxenes and corundum. ABO_3 materials provide numerous interesting properties and some examples are shown in Table 1.4. Because of their advantageous properties, this oxide class may be applied in numerous applications including ceramic capacitors, ferroelectrics, piezoelectric transducers, sensors, catalysis and for solar cell applications.

Table 1.4 The examples materials of ABO_3 structure oxide.[16]

Materials	Attractive properties	Materials	Attractive properties
$LaNiO_3$	Metallic, Pauli paramagnetic	$SrCrO_3$	Pauli paramagnetic
$LaCoO_3$	Paramagnetic	$SrRuO_3$	Metallic ferromagnet
$LaCuO_3$	Metal	$GdTiO_3$	Semiconductor
$LaCrO_3$	Antiferromagnetic	$CaRuO_3$	Antiferromagnetic
$KNbO_3$	Ferroelectric-ferroelastic	$BaTiO_3$	Insulating, Ferroelectric

ABO_4 structure

ABO_4 structures may be found when 'A' is a metal with an oxidation state of +2 or +3 whereas B displays an oxidation state of +6 or +5, respectively. Figure 1.13 illustrates an example of an ABO_4 scheelite-type structure.

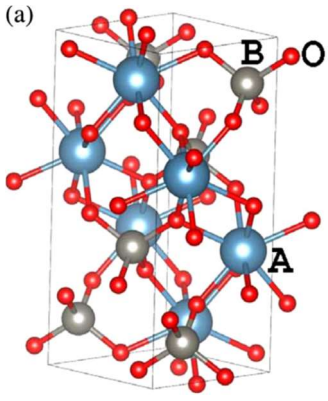

Figure 1.13 Crystal structure of the ABO_4 scheelite-type structure. Example, 'A' atoms (blue sphere) can be Ca, Pb; 'B' atom (grey sphere) can be W, Mo and red spheres are oxygen atoms.[39]

For instance, the 'A' atom can be an alkaline earth metal or Pb, Zn, Cd, Fe, Mn, Co, or Ni in the +2 oxidation state whereas 'B' can be W, Mo, Cr, I, Se or S.[40] A number of commonly occurring minerals exist with the ABO_4 structure, for example, $BaSO_4$ (Barite), $CaWO_4$ (Scheelite), $LnPO_4$ (Monazite), $PbCrO_4$ (Crocoite) and $Fe_{0.5}Mn_{0.5}WO_4$ (Wolframite). Indeed, this oxide structure is well-known to display a phase transformation under pressure without any changes of cation coordination numbers. For instance, $LnAsO_4$ (Ln=Sm-Lu, Sc) displays a zircon structure at ambient pressures, whereas under high pressure it presents as a scheelite structure.[41] The ABO_4 structure oxides provide properties with potential for various applications such as photoluminescence, microwave applications, optical fibres, scintillator materials, humidity sensors, magnetic devices and catalysis.[40] Table 1.5 shows examples of ABO_4 oxides with their applications.

Table 1.5 Example of ABO_4 crystal structure oxides with their applications.

Materials	Applications
$BaWO_4$[40]	• Blue luminescence for the electro-optical industry. • Specific spectral region of a emission for solid-state lasers.
$BaCrO_4$[40]	• Oxidizing agent. • Catalyst for enhancing vapour-phase oxidation reactions. • Highly efficient photocatalyst with response to visible light irradiation.
$NiMoO_4$[42]	• High capacitance, low toxicity, cost-effective for hybrid capacitor devices.
$PbWO_4$[43]	• A promising scintillator for CMS electromagnetic calorimeter, nuclear medicine, CT scanners.
$MnWO_4$	• High sensitivity to humidity changes; this is useful for humidity sensor application.

A_2BO_4 structure

The A_2BO_4 (spinel) oxide materials display a variety of structural types in their family and can provide a number of useful properties such as a coexistence of transparency and conductivity, superconductivity, ferroelectricity, ferro and antiferromagnetism.[44] Figure 1.14 represents a crystal structure of an A_2BO_4 oxide structure which is also named as a spinel. Prominent within the spinel structural family are the ***Ferrite*** phases,

which are compounds containing an iron atom as a constituent B atom and which possesses ferromagnetic properties. The ferrite composition, MFe_2O_4, can be achieved where M can be represented by divalent ions such as Zn, Mn, Ni, Mg etc.[45] The ferrite family of materials have possible applications in computer technology and in advanced electronic instrumentation, e.g. television receivers, transformers, microwave components, telephone communication equipment, etc.[45] Table 1.6 presents some further examples of A_2BO_4 oxide materials and their properties.

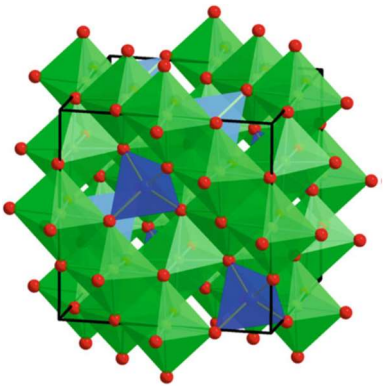

Figure 1.14 Crystal structure of an AB_2O_4 spinel. ***Blue spheres*** represent A cations, ***green spheres*** B cations, and ***red sphere*** represent O anions.[46]

Table 1.6 Example materials of the AB_2O_4 structural family.[16,47]

Materials	Properties
La_2NiO_4	• Antiferromagnetic at 200 K, the semiconductor-metal transition at 600 K.
$La_2NiO_{4+\delta}$	• Superconducting at low-temperature.
La_2CoO_4	• Antiferromagnetic.
La_2CuO_4	• Low-resistivity but non-metallic.
$NiCo_2O_4$	• Electrical conductivity, high electrochemical activity.
Sr_2RuO_4	• Superconductivity.
MFe_2O_4 (M=Mn, Co or Ni)	• Impressive magnetic, electrical and optical properties. Exhibiting different redox states and electrochemical stability that make them suitable for electrode materials in supercapacitors.

Other ternary oxide structures

Although the most important and common ternary oxide phases are represented by the as ABO_3, ABO_4 and A_2BO_4 structures, it is impossible to cover all of the structures of ternary oxides. Hence, alternative ternary oxide phases can also be achieved with other stoichiometries such as ABO_2, $A_2B_2O_7$, A_2BO_5, A_2BO_6 and A_3BO_5.[45]

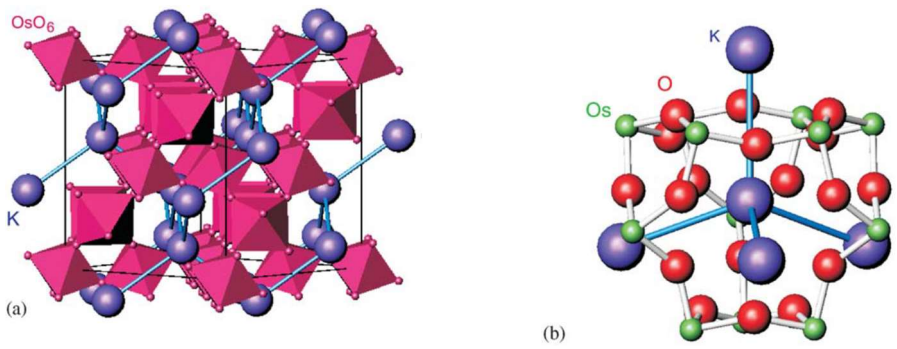

(a) **(b)**

Figure 1.15 Crystal structure of the β-pyrochlore oxide KOs_2O_6. Corner-shared OsO_6 octahedra form a three-dimensional network, and the K atoms at the 8 site are located in the centre of the $Os_{12}O_{18}$ cage as shown in (b). The K atoms hypothetically form a diamond sublattice with a long K-K distance through the four channels of the $Os_{12}O_{18}$ cage along the (111) direction.[48]

For example, the properties of $A_2B_2O_7$ or pyrochlore-type oxide materials (Figure 1.15), are again dependent on the identity of the A and B cations. Generally, in this structure type large cations such as lanthanides (Ln^{3+}) will occupy the "A" position, whilst "B" will be provided a smaller cation from the first or second-row transition elements. The pyrochlore-type oxides possess structures propagated by corner-sharing tetrahedra, and can display a variety of properties such as superconductivity, magnetic frustration, colossal magnetoresistance, metal-insulator transition and ferroelectric behaviour.[48,49] Table 1.7 shows some materials of other ternary oxide structures and their properties.

Table 1.7 Some examples of other ternary oxide materials and their properties.

Materials	Properties
$Tl_2Mn_2O_7$[50]	• Exhibits giant magnetoresistance
$Cd_2Re_2O_7$[48]	• Superconductor with *Tc* = 1.0K

Materials	Properties
$Bi_2Sn_2O_7$[51]	• Semiconducting materials with a wide band gap
AOs_2O_6 (A=Cs, Rb and K)[51]	• Superconductors with *Tc*= 3.3, 6.3 and 9.6 K, respectively
$Ln_2Ti_2O_7$ (Ln=La, Ce, Pr and Nd)[52]	• Ferroelectric with high Curie temperature
$R_2Ru_2O_7$ (R=Tb, Er and Yb)[49]	• Magnetic transitions at 3.4, 5.4 and 6.3 K, respectively

It is clear that the ternary metal oxides are fascinating materials which may be applied to an extensive range of high technology applications e.g. transistors and computing devices, optical, and catalytic process, etc. These materials have thus attracted the interest of a wide variety of industrial and academic researchers. Particularly pressing is the development of these materials in thin film form for application in next generation technologies. This thesis will, thus, focus on the fabrication of ternary oxide thin films specifically lanthanum nickel oxide, which will be reported in chapter 3 of this thesis.

1.3 Metal sulphide materials

Metal sulphides are materials in which metal atoms are bonded with sulfide anions (S^{2-}) in their solid-state structures which present the chemical formula M_xS_y.[53]

Transition metal sulfides (TMS) are well-known materials that can provide useful properties for many applications. The natures of the transition metal atoms in the sulphide structure system dictate their properties, their crystal structures and their overall stoichiometry. Many TMS materials can be found in nature such as the ***Fe-S systems*** e.g. troilite (FeS), pyrite (FeS_2), ***Cu-S systems*** e.g. covellite (CuS), chalcocite (Cu_2S), ***Ni-S systems*** e.g. millerite (NiS), heazlewoodite (Ni_3S_2) and ***Zn-S systems*** e.g. sphalerite (ZnS), wurzite (ZnS).[54]

TMS adopt many crystal structures which are dependent on their stoichiometry, for example, the most stable polymorph of MnS displays a cubic rock salt structure. On the other hand, some other TMS display more unusual structures, for instance, transition metal disulphides (MS_2) e.g. FeS_2, the transition metal trisulphides (MS_3)

e.g. TiS_3, ZrS_3, HfS_3 and the transition metal polysulphides e.g. VS_4, Re_2S_7. Table 1.8 shows some of the typical unit cells of the most common transition metal sulphide materials.[54]

Table 1.8 Some of the typical unit cells of the most common sulphides of the transition metal.[54]

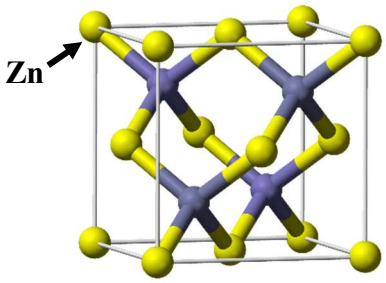	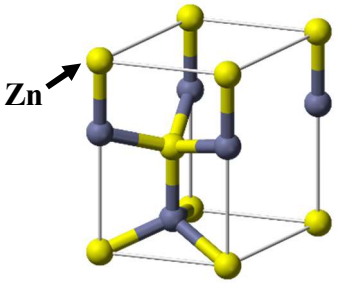
ZnS: Sphalerite or zinc blende[55]	**ZnS: Wurtzite**[56]
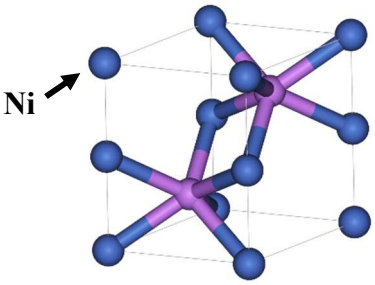	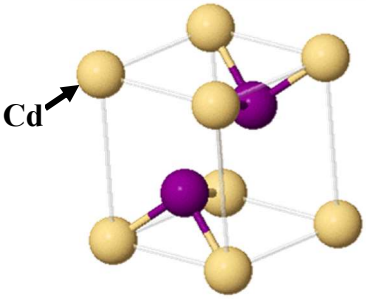
NiAs structure type[57]	**CdI_2-type layer structure**[58]
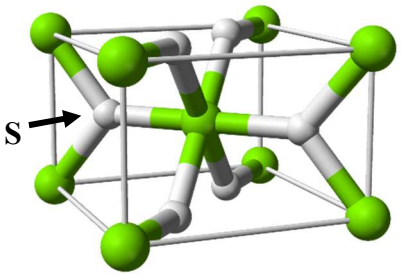	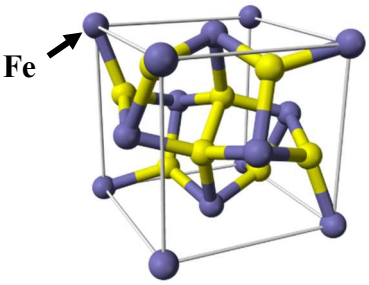
Marcasite (FeS_2),[59] (S-S = 2.21 A°)	**Pyrite(FeS_2),**[60] (S-S = 2.21 A°)
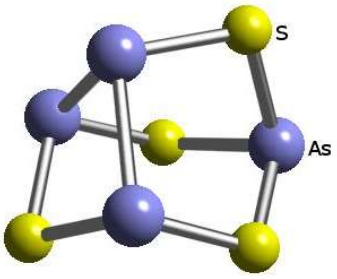	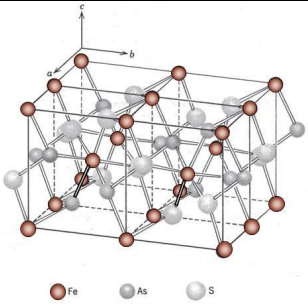
Tetraarsenic tetrasulphide (As_4S_4)[61]	**Arsenopyrite (FeAsS)**[62]

It is difficult to compare sulphide and oxide material as they display such varied properties and chemical reactivity. Sulfur possesses a larger ionic radius as sulphide, (S^{2-} around 1.84 Å) than the oxide ion (around 1.35-1.42Å).[53] The Pauling electronegativity of sulfur is also significantly lower than that of oxygen (sulfur, 2.5; oxygen, 3.5), hence, sulfur bonding to transition metals is typically much more covalent than oxygen bonding with the same metals.[53] Consequently, the structures and chemical properties of the M_xS_y compounds are also influenced by their higher covalent character.

Some properties of transition metal sulphides materials and their applications are illustrated in Table 1.9.

The research described in this thesis will focus on the deposition of zinc sulphide thin films by the AACVD technique and their characterization.

Table 1.9 Examples of transition metal sulphide materials and their properties and applications.

Materials	Properties	Applications
ZnS	• Energy band gap: zinc blend structure 3.6 eV and wurtzite structure 3.5 eV.[63] • High exciton binding energy ~ 40 meV.[64] • Excellent properties of luminescence and photochemistry.[65,66] • High transmittance in the visible range.[67] • Nontoxic[68]	• Light-emitting diodes.[69] • Flat-panel displays and injection lasers.[65,66] • Optoelectronic devices.[64] • Optical bioimaging applications[53] • Electroluminescent devices.[70] • Sensors.[71] • Field emission displays.[72]
Cu_2S	• Energy band gap 1.2 eV, p-type semiconducting materials.[73] • High absorption coefficient, 10^4 cm-^{1}.[74]	• Lithium-ion battery applications.[64,73] • Solar cell layer devices.[73] • Nanoscale switches[64,73]
CuS	• Energy band gap 1.4-2.2 eV.[53]	• Transparent conductive films[75]

Materials	Properties	Applications
	• Metal-like electrical conductivity.[75] • *p*-type semiconductor.[76]	• Catalyst.[77] • Solar cells applications and optoelectronic devices.[77] • Biomedical; DNA detection, drug delivery, immunosensor, etc.[76]
Ni_3S_2[64,78–82]	• Metallic material at room temperature. • Resistivity ~1.8×10^{-5} Ω cm. • Magnetic susceptibility. • Strong electron-electron correlation. • Insulating ground state. • Magnetic instability.	• Semiconductor devices • Photogalvanic cell applications • Hydrogen storage devices • Cathode materials for lithium-ion batteries • Solid oxide fuel cells devices.

1.4 Combustion processing and metal nitrate salts

Although many methods for the preparation of oxide thin film materials have been developed, a majority of these techniques require the use of expensive equipment, high temperatures, complicated operations, are difficult to control and present huge costs for maintenance. For this reason, many researchers have tried to develop new ways to improve the quality of thin films whilst also reducing the cost of thin film production.

In 2011, Tobin J. Marks and co-workers reported the achievement of thin film oxide processing at temperatures as low as 200 °C.[83] This was accomplished through the use of a novel combustion chemical route to grow transparent conducing oxide (TCO) thin films such as indium oxide (In_2O_3), indium-zinc-oxide (IZO), zinc-tin-oxide (ZTO) and indium-tin-oxide (ITO). The process provides simplicity and low cost in the precursor preparation, whilst also providing high quality films. To compare the advantages of the combustion method and the conventional method, Marks and his team reported that thin films when deposited by the combustion route were of a similar

quality when prepared at low temperatures ($T_{completion}$ < 200-300 °C) to those deposited by conventional high temperature synthesis ($T_{completion}$ > 500-600 °C)(Figure 1.16 (a)).

The combustion system requires three basic components; heat, fuel and an oxygen supply to initiate the exothermic chemical reaction (Figure 1.16 b.). The success of the combustion process is dependent on the self-generated heat of the synthesis which provides a localized source of energy that enables a reduction of the processing temperature to lower than that required by conventional processing.

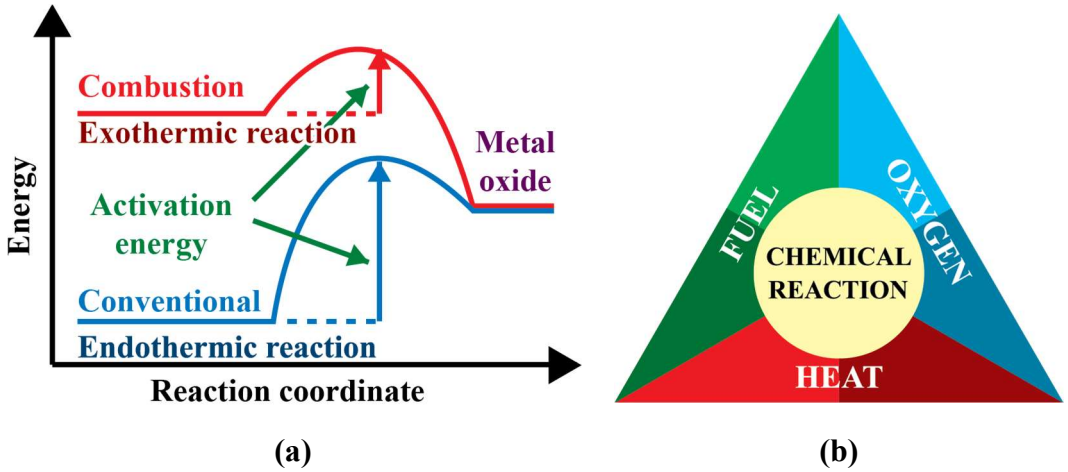

Figure 1.16 a.) The diagram shows the comparison of the energetics between combustion and conventional processes b.) The three main components of the combustion system.[83]

The deposition of TCO thin films employed simple metal nitrates as both the source of the metal and as an oxidizer which provides the oxygen source. Acetylacetone ($C_5H_8O_2$) or urea (CH_4N_2O) were used as a source of fuel in a multi-component spin-coated solution, while the heating of the substrate provided the heat required to initiate the combustion system. Generally, the decomposition of metal nitrates to the oxide, can be generalised in the equation as below:

$$M(NO_3)_{2(s)} \rightarrow MO_{(s)} + 2NO_{2(g)} + \frac{1}{2}O_{2(g)}$$

Scheme 1.1 Decomposition of a metal nitrate.[84]

For example, Scheme 1.2 shows a balanced equation for exothermic ZnO thin film preparation by the combustion process. Zinc nitrate hexahydrate ($Zn(NO_3)_2{\cdot}6H_2O$) and urea were used as the starter chemicals to create the combustion precursor in this process. The heat of the combustion from the reaction is around -2320.4 kJ (ΔH_{298K})

and the adiabatic flame temperature is around 700 °C (T_{ad}). Although the substrate must be heated to a sufficiently high temperature to ignite the precursor, the high self-generated energy sustains the reaction so that the precursor is decomposed to form the desired metal oxide thin film at a low temperature.

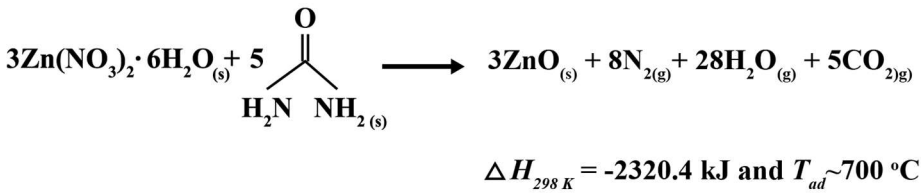

Scheme 1.2 ZnO thin film preparation by the combustion synthesis.[83]

The advantages of thin film fabrication by the combustion chemical route are derived from the low-cost of the precursor preparation and the simplicity of the required equipment. In addition, metal nitrate salts dissolve readily in many solvents including water and also provide a source of oxidant to the system from the presence of the nitrate ion (NO_3^-). The solvents which are used in the combustion process were primarily alcohols solvents such as methanol and ethanol,which also act as a source of the fuel with enthalpies of combustion ($\Delta_c H$) of around -715.0 kJ/mol and 1370.7 kJ/mol, respectively. Examples of the use of metal nitrate salts as precursors for thin film oxide deposition are shown in Table 1.10.

The research described in this thesis will thus, seek to combine the advantages of nitrate combustion with the AACVD technique for thin film deposition.

Table 1.10 Summary of the metal nitrate salts that have been used for thin film deposition.

Metal nitrate salts	Thin film material	Method	Temperature (ºC)	Substrates	Solvents
$La(NO_3)_3 \cdot 6H_2O$	La_2O_3	Spray pyrolysis[85]	300 - 450	Glass	Double distilled water
$In(NO_3)_3 \cdot 2.85H_2O$ + $Zn(NO_3)_2 \cdot 6H_2O$	IZO	Spin-coated[83]	150 - 400	*n*++Si wafer	2-methoxyethanol and acetylacetone
$Ni(NO)_2 \cdot 6H_2O$	NiO	Spray pyrolysis[86]	330 - 350	Bare glasses	Bi-distilled water
$Pr(NO_3)_3 \cdot 6H_2O$	Pr_6O_{11}	Cathodic electrodeposition[87]	500	ITO	Hydrogen peroxide
$Co(NO_3)_2 \cdot 6H_2O$	Co_3O_4	Aerosol generated by ultrasonic excitations[88]	500 - 600	Commercial grey glass	Deionized water
$In(NO_3)_3 \cdot xH_2O$	In_2O_3	Spin-coated[89]	150 - 250	*p*-type Si wafer	Water
$Zr(NO_3)_4$ $Hf(NO_3)_4$	ZrO_2 HfO_2	MOCVD[90]	350 - 650	Al/MO_2/p-Si	Toluene
$In(NO_3)_3 \cdot xH_2O$, $Zn(NO_3)_2 \cdot xH_2O$, $Ga(NO_3)_3 \cdot xH_2O$	IGZO (Indium gallium zinc oxide)	Inkjet printing[91]	300	SiO_2	Deionized water
$La(NO_3)_3 \cdot 6H_2O$, $Sr(CH_3COO)_2$, $Co(CH_3COO)_2 \cdot 4H_2O$	$La_{1-x}Sr_xCoO_3$	Spin coating[92]	400-900	Si(100) wafer	Deionized water and glacial acetic acid

1.5 Thin film deposition techniques

A wide variety of deposition technologies have been developed to fabricate thin films of an appropriate thickness and quality. The technologies may be broadly subdivided as either chemical or physical. Moreover, there are numerous variations of the techniques, which may be considered to combine both physical and chemical reactions.[93] Thin film deposition techniques may, thus, be classified into four main categories: 1. Physical vapour deposition (PVD) 2. Chemical vapour deposition (CVD) 3. Chemical solution deposition (CSD) 4. Electrochemical deposition (ECD). Generally, these techniques rely on the three major steps that are: 1) the creation of atomic, molecular or ionic species 2) the transportation of that species through a medium and 3) the condensation of the species on a substrate. The following sections will introduce each technique and discuss their advantages and disadvantages.

1.5.1 Physical vapour deposition (PVD)

The vaporization and condensation of a preferred target material is the main feature of PVD. This can be achieved as either a thermal or athermal process. In a thermal process the target material is evaporated or sublimed by a source of external thermal energy whilst, in an athermal process, the target material is hit by ionized gas molecules to induce evaporation under vacuum conditions. PVD techniques may be classified by both processes as shows in the Figure 1.17.

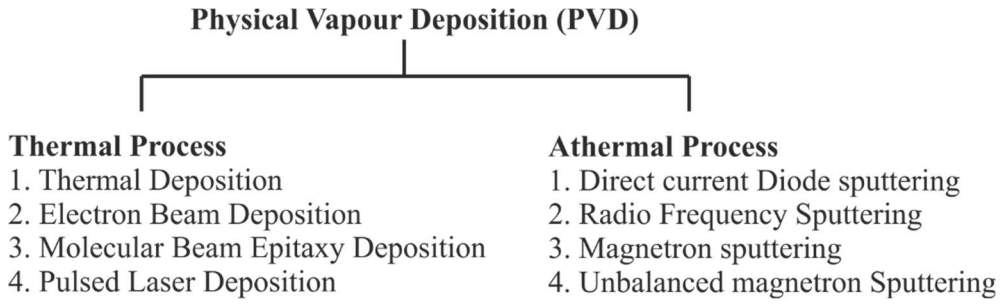

Figure 1.17 Classifications of physical vapour deposition techniques.[94]

The first stage of thin film formation by any PVD technique requires the target material to be evaporated then transferred to a formation chamber which contains a desired substrate. The vaporised target materials adhere to the substrate surface and the reactions between them and/or gas in the chamber ensue to produce the desired

film.[94] The basic steps involved in the PVD process are shown in Figure 1.18 and the advantages and disadvantages of PVD are presented in Table 1.11.

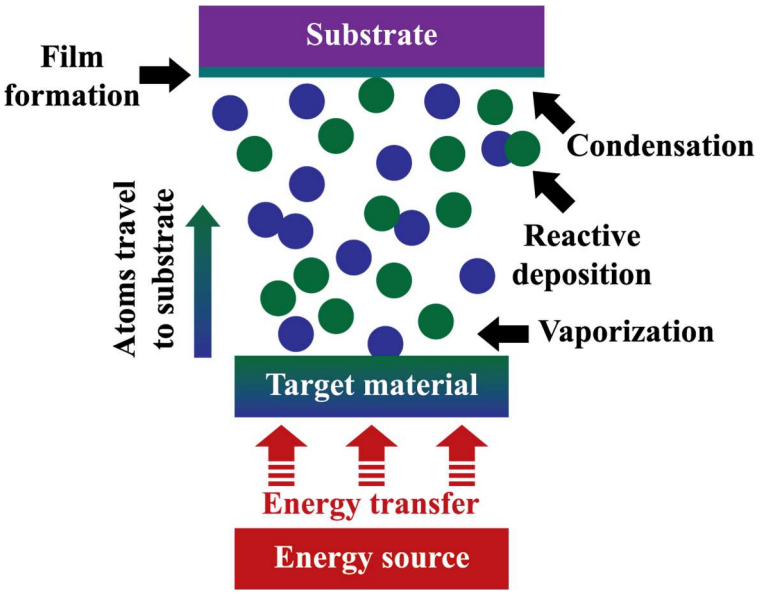

Figure 1.18 Basic steps involved in a PVD process.[94]

Table 1.11 The advantages and disadvantages of the PVD technique.[94]

Advantages	Disadvantages
• Thin film composition can be controlled by the target material. • Alloy film may be deposited by PVD techniques. • PVD technique is suitable to prepare hybrid thin film from inorganic materials and organic materials. • Most PVD techniques require a high vacuum system, hence, to exist the low contamination. • Deposition rate, morphology, texture, porosity, etc. can be controlled and adjusted.	• The basic instruments, equipment or components for PVD are complicated and also expensive and carry a high cost of maintenance resulting in high production costs. • Difficult to control the instrument in the process. • Generally, most PVD techniques require a solid target material; a limitation as the various source materials need to be available in perform.

1.5.2 Chemical vapour deposition (CVD)

CVD requires the reaction of a combination of vapours or gas phase chemical precursors over the substrate surface to form the desired thin film, which can have a chemically simple or complex composition and morphology. The CVD technique typically involves four main stages which enable thin film formation (Figure 1.19). These are;[94,95]

a) The gas phase precursor is transported into the reaction chamber or reaction zone by a carrier gas.
b) Chemical reactions between the gas phase precursors originate near or at the substrate surface to produce reactive intermediates and gaseous by-products. Thermal energy is provided from an energy source such as a heating plate, furnace, radio frequency, light or x-rays, etc. to activate the reactions before adsorption of the reactant gases takes place on the surface.
c) Surface diffusion and surface reaction of those gas phase intermediates ensue over the substrate surface, during which nucleation and growth of the solid phase material takes place and the decomposition by-products are released.
d) Unreacted gas phase precursors and by-products formed on the surface are diffused away and carried out from the surface by a carrier gas through the exhaust.

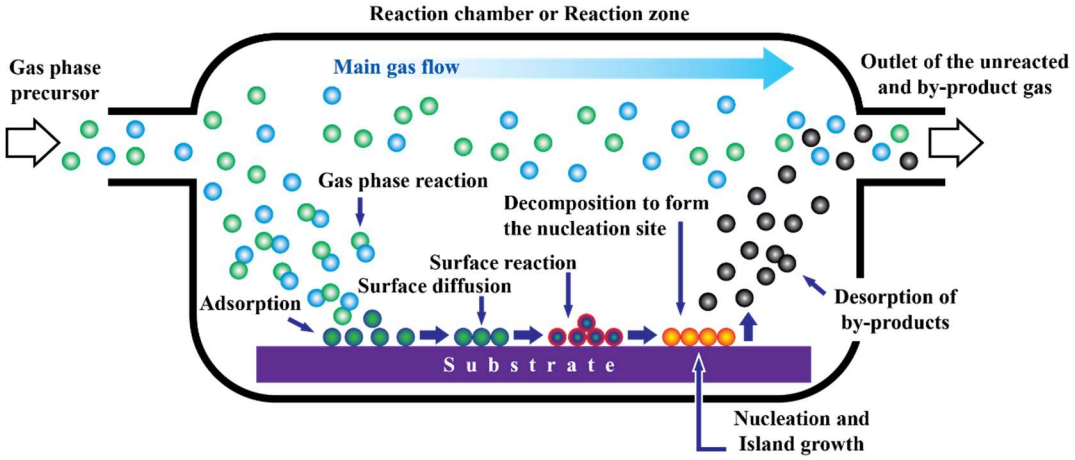

Figure 1.19 Schematic representation of the basic steps in the CVD process during thin film formation.[94,95]

The CVD process can be controlled by adjustment of a number of parameters such as the flow rate of the reactant gases, the chamber and/or substrate temperature, physical and chemical properties of the substrate and deposition time. Table 1.12 highlights the advantages and disadvantages of the CVD technique below.

Table 1.12 The advantages and disadvantages of the CVD technique.[94–96]

Advantages	Disadvantages
• The thin film can be fabricated from various precursors, either inorganic or organic. • Thin films can be grown in a high purity and density. • Easy to upscale to large area thin film production. • Can be achieved using inexpensive scientific and technical apparatus that leads to a low- production costs. • The process is simple and reproducible. • Single source precursors can be used with appropriate compositions • The process can be operated at low temperatures. • The thin film can be prepared at atmospheric pressure.	• The waste by-products can be a toxic and contaminate the environment. • Some thin films need to be prepared with air sensitive precursors which complicates the film growth process and its control. • Some thin films are fabricated from pyrophoric precursors or require potentially explosive chemicals such as alcohol solvents, and ammonium nitrate. • Some precursors incorporate dangerous chemical elements such as cadmium. • These features require intensive consideration for safety. • Need a thermally stable substrate at high-temperature deposition above 600 ºC.

In addition, to the general advantages arising from the CVD technique there are a number of variants have been devised, the use of which is dependent on the thin films which are required. Table 1.13 shows the types of CVD technique which that have been developed.

Table 1.13 Summary of the types of CVD technique.[94–97]

Type of the CVD techniques	Features
Atmospheric pressure CVD (APCVD)	Thin film fabrication operates under an atmospheric pressure. This technique is uncomplicated as a process and it provides a high growth rate of the thin film formation.
Low-pressure CVD (LPCVD)	A reduced pressure is used during thin film processing. The thin films formed with this process are typically very uniform, however growth rates are usually low and the equipment is more expensive and complicated than with APCVD.
Ultra-high vacuum CVD (UHCVD)	This process can be enabled to operate for low-temperature deposition and enables the deposition of high quality thin films. However, the apparatus required for this process is expensive and requires an ultra-high vacuum atmosphere.
Direct liquid injection (CVD) (DLICVD)	The thin film is formed from a liquid precursor which is injected into the vaporization zone. The attraction of this process is the use of a wide range precursors of low vapour pressure, high vapour concentration of the precursor and the high growth rate of the thin film formation.
Microwave plasma-assisted CVD (MPACVD)	Plasma is used to enhance the chemical reaction rate of the precursor. By this method, the thin film can be possibly created at room temperature and with good adhesion between the thin film and the substrate. However, a vacuum system is required.
Atomic layer CVD (ALCVD or ALD)	This method requires complex and specialized equipment but provides accurate control over film thickness. It also allows large area uniformity of the film. Nevertheless, a limitation is that highly volatile and reactive precursors are required.

Type of the CVD techniques	Features
Metal-organic chemical vapour deposition (MOCVD)	Metal-organic chemicals are used as precursors to deposit the thin film. This method provides high quality, uniformity and even epitaxial thin-film deposition but it requires precursors of high thermal stability.
Aerosol-assisted CVD (AACVD)	Does not require a volatile precursor and an environment-friendly solvent such as water can be used. Potentially adapted to large scale production and inexpensive. Requires precursor design to control a film composition. Can be able to use in the deposition of various materials.

1.5.3 Chemical solution deposition (CSD)

Chemical solution deposition (CSD) was initially developed during the 1980s for the deposition of complex electronic oxide thin films. This technique is particularly useful for a wide variety of perovskite materials that are very important to solar-cell and electronic device technology.[98]

Typically, CSD has three main stages which are shown in Figure 1.20.[98]

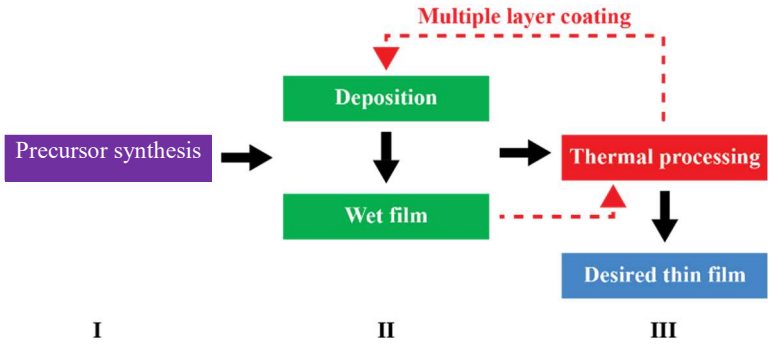

Figure 1.20 Flow chart of typical chemical solution deposition routes.[98]

The precursor synthesis:

Precursor synthesis is the starting point of the CSD technique. The precursor can be prepared from various common chemicals such as metal-organic compounds, salts and carboxylates, etc. Also, an additive such as chemical stabilizer can be added at this

stage to adjust or improve the properties of the final film products. Many kinds of literature processes and industries have applied the sol-gel techniques at this stage to prepare the requisite precursors which contain an appropriate viscosity for the thin film fabrication in the next stage.

The thin film deposition (Wet film):

A number of methods have been used for thin film deposition that rel on CSD. These include spin-coating, dip coating, spray pyrolysis, screen printing, doctor blade coating and ink-jet printing. Each method provides specific advantages and limitations, usually associated with the precursor synthesis stage. Table 1.14 shows some examples of the deposition methods that are based on the CSD technique. However, the deposited films from this stage are still the wet precursor mixtures and require an annealing step to form the dry inorganic film with the desired morphology and properties.

Table 1.14 Examples of deposition methods based on the CSD technique.

Deposition methods	Advantages / Limitations
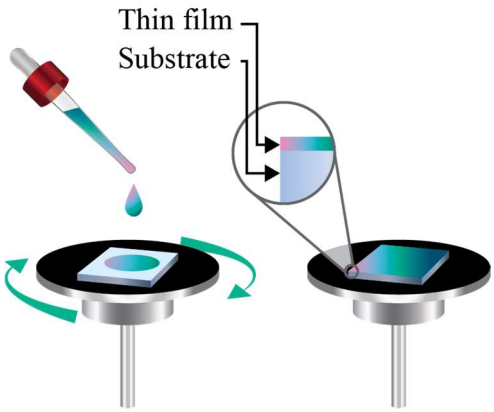 **Spin coating:**[98,99]	**Advantages:** • Simple process. • Needs no clean room. • Low-cost equipment. • Suitable for a low volume production. **Limitations:** • The thickness of the coating layer may vary from the centre to the edge of a product surface. • Not suitable for complex geometry products. • Difficult to apply for large-area coating.

Deposition methods	Advantages / Limitations
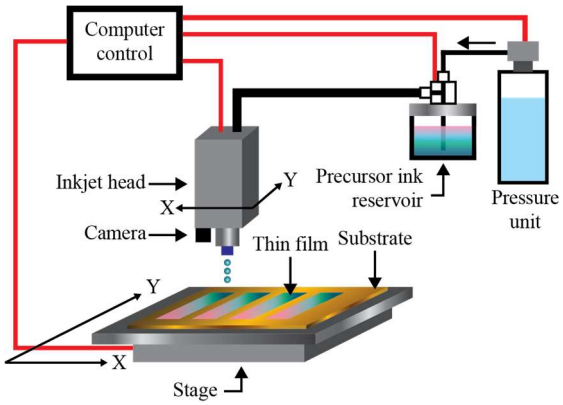 **Ink-jet printing:**[100–103]	**Advantages:** • Good for a structured or conformal coatings. • Reduced materials or precursor consumption. • Gives high precision and high-resolution films and allows patterning of the films. • Flexible materials can use as the substrate. • Does not require a high-temperature or vacuum deposition environment. • Large-area deposition. • Rapid manufacturing and low volume production can do. • Low material waste. **Limitations:** • Speed and yield of the product depends on the printer speed. • The nozzle can be clogged or shorted circuits by the odd droplet jetting. • Need to control the surface tension, viscosity and density of ink or precursor.
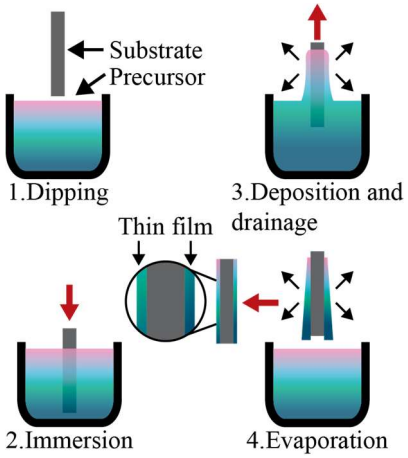 **Dipping coating:**[104–106]	**Advantages:** • Very suitable to coat and provide the complete coverage of the two side or complex geometry products. • Minimal waste systems. • Easy to control the process. **Limitations** • Not suitable too light products, they may float upon immersion or during the dip process. • As the result of the wedge effect, the thickness of film coating layer can vary from top to bottom. • Clean room required.

Deposition methods	Advantages / Limitations
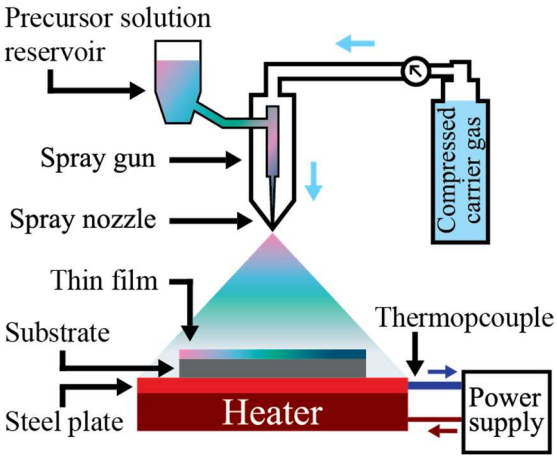 **Spray pyrolysis:**[107,108]	**Advantages:** • A rapid method for the thin film deposition. • Low cost, simple and convenient. • Excellent for the large area thin film deposition. • No needs high-quality substrates or chemicals. • Easy to prepare the multi-layered films. **Limitations:** • Contain lots of small grains as results from the rapid evaporation of the droplets. • This method is very sensitive to variation of the surface temperature of substrates that affects the physical and electronic properties.
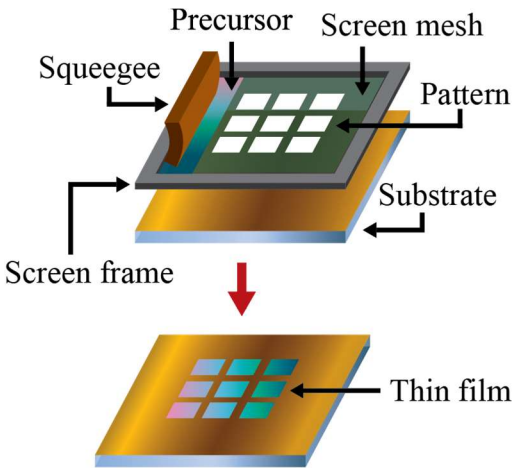 **Screen printing:**[109–111]	**Advantages:** • Simple and cheap method. • A wider range of viscosities and surface tension of ink or precursor. • Large-area substrate deposition and various types of substrate. • Potential for patterned deposition. • Low-temperature processing. • Suitable for mass production. **Limitations:** • More wasted material. • Difficult to control a film thickness and also the thickness of film present in thick films. • Slow drying process.

Thermal processing and crystallization (Dried film):

This stage involves the thermal processing of the wet film to decompose the precursor and to remove any organics in the film and also initiate some reactions and induce crystal formation or phase transformation in the final desired film.[98]

From the Figure 1.21, multiple layer coating of the thin film can be performed after thermal processing of the amorphous or crystallized film to increase the film thickness. When the film obtains the desired thickness, a higher temperature may be utilized for

the final thermal treatment to improve the quality of the film such as its microstructure, density, pore size and volume, crystallinity, surface area, residual hydroxyl content, residual carbon content and in some cases also to improve the opacity of the film.[98] In general the atmosphere (oxidizing, inert or reducing), time and pressure of the thermal treatment process impacts on the decomposition behaviour of the deposited film. In the particular case of metal oxide films, thermal processing may also influence the oxidation state of the elements in the film, as well as the material's crystal structure and physical and chemical properties.

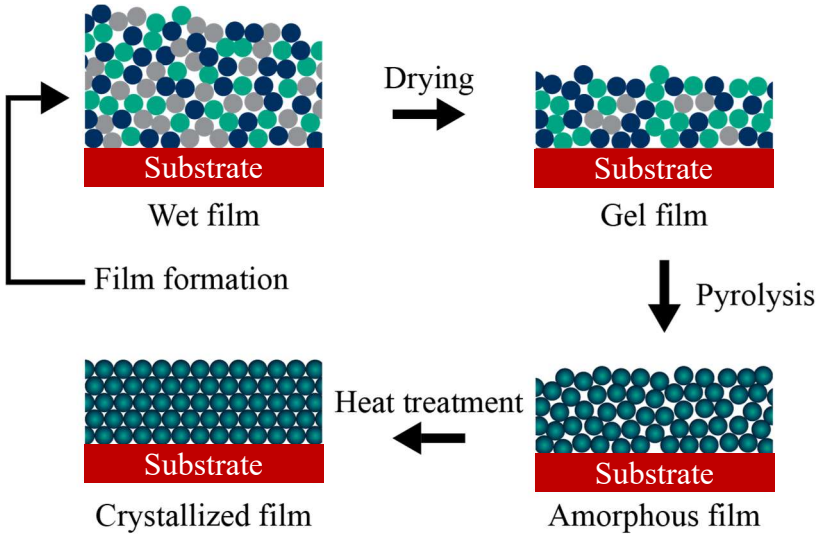

Figure 1.21 Illustration of the thermal treatment and crystallization process.[98]

1.5.4 Electrochemical deposition (ECD)

Electrochemical deposition or ECD is a well-known technique to produce thin metallic films, which can be carried out in conjunction with other techniques to provide a low-cost, efficient, simple and environmentally-friendly method of large area production.

This deposition technique involves the redox reaction (reduction-oxidation) where an oxidation reaction occurs at the anode and a reduction occurs at the cathode. The reduction reaction is used to perform the thin film deposition and is, thus, called an ***"electrochemical deposition"***. The electrochemical reaction associates the transfer of the electrons between an electron conductor as the electrode material and an ionic conductor in an electrolyte solution. The electrolyte solution contains a dissolving compound or an element. The solid thin film which is produced from the reduction reaction is formed on the surface of an electrically conducting electrode. The

electrochemical cell comprises the three electrodes that are termed counter, working and reference electrodes as shown in Figure 1.22.

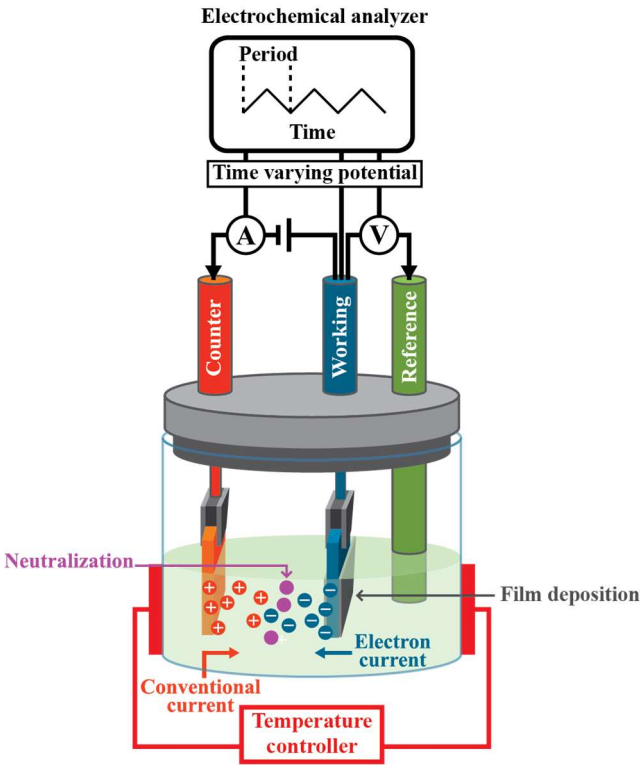

Figure 1.22 Schematic diagram of the electrochemical deposition technique.[112,113]

The counter electrode is used to control the electric current flow in the ECD system and it is connected to the electrochemical analyzer and the working electrode. Usually, the counter electrode requires a larger surface area than the working electrode to maintain and provide the stability of the current flow to diffuse to the working electrode.

The working electrode supplies electrons to the electrolyte solution whereupon the thin film can be deposited on the electrode cell by the reduction reaction. This electrode is connected to the electrochemical analyzer and the reference cell which are used to control and adjust both the desired potential and the cycle time of the potential during the reduction reaction. Electron transfer and the oxidation reaction activity is mediated by the electrolyte at this site and also allows control over the thickness and morphology of the deposited film.

The reference electrode is used to determine and measure the potential of the working electrode cell and responds to the electrochemical analyzer to adjust the potential of the working electrode.

Variation in the current density, potential, deposition time and electrolyte solution composition may be used to control the morphology, quality, composition and properties of the deposited films. In particular, the electrolyte solution is very important due to its effects on electron transfer and electrical conductivity and to induce the reactions in the synthetic system. Normally, the properties of the electrolyte solution depend on the dispersed ionic species, specifically their concentration and uniformity through the solution.

1.5.5 The consideration of thin film deposition technique selection

The properties and characteristics of any thin film are a consequence of preparation process. Each process can offer different features to a film of a particular material. Hence, the technique or process considerations for the thin film deposition are of vital importance for manufacturers or researchers. Table 1.15 shows examples of some of the considerations that a manufacturer or researchers need to take into account during thin film fabrication and Figure 1.23 presents some examples of the varying morphologies of nickel oxide thin film prepared by four different deposition techniques (PVD, CVD, CSD and EDS). It can be seen that their appearance is very different while retaining the interesting properties of the material itself.

Table 1.15 Considerations for thin film fabrication.

Considerations	Example details
Process	Machine and equipment cost, maintenance and management cost, complicated to control, safety, environmentally friendly, knowledge and skill of the operator, law.
Parameters in the process	Temperature: substrate, chamber, deposition. Atmosphere: high or low vacuum, with or without oxygen, inert gas, clean to prevent the contamination. Time, deposition rate, deposition area, substrate materials, condition of the substrate surface.
Features of the output thin film	Morphology, composition, amorphous or crystalline, crystal structure and orientation, crystallite size, chemical formula,

Considerations	Example details
	thickness, roughness, microstructure, chemical and physical properties,

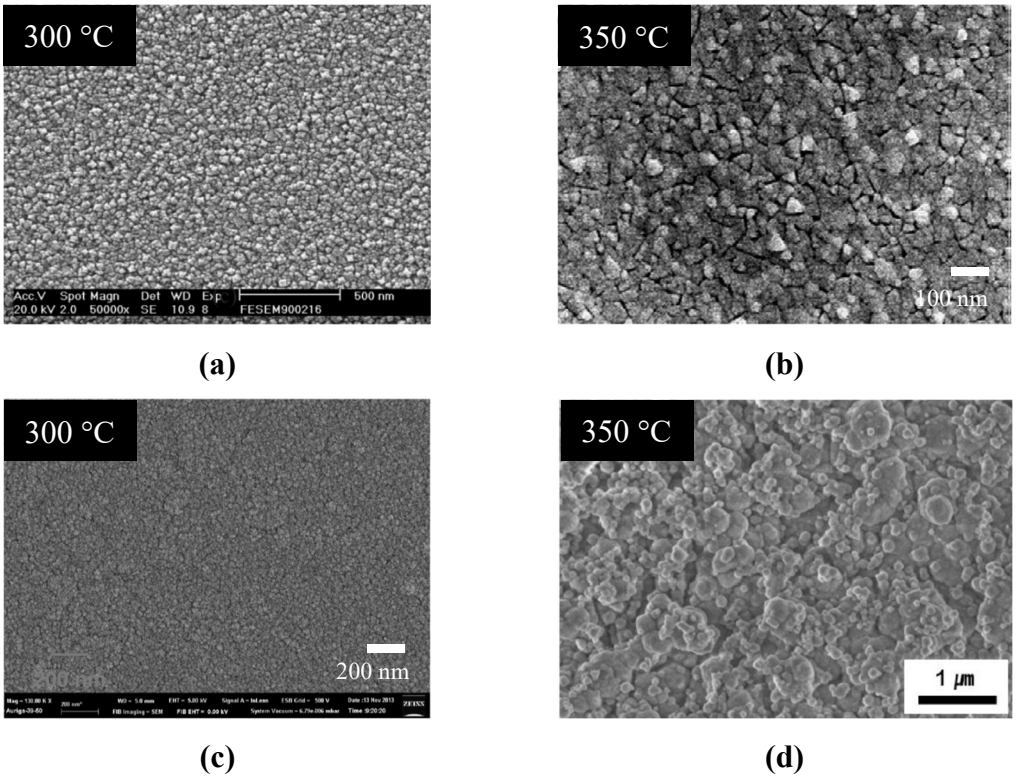

Figure 1.23 SEM micrographs of nickel oxide thin films which are prepared by different techniques but at similar temperatures a.) PVD: RF reactive magnetron sputtering[114] b.) CVD: MOCVD[115] c.) CSD: Spin-coating[116] d.) ECD.[117]

The research described in this thesis applies a simple and inexpensive technique, aerosol assisted chemical vapour deposition or AACVD, which does not require specialized precursor characteristics and is adaptable to large-scale production to provide high quality films.

AACVD offers many of the advantages shown in Table 1.13 and will, thus, be applied to the deposition of binary and ternary oxide and metal sulfide thin films in this thesis.

1.6 Aerosol-assisted chemical vapour deposition (AACVD)

As described above, many variants of the CVD process have been developed to deposit thin films for a wide range of applications. This technique can provide high-quality thin films and it is easy to control the thin film structure at an atomic or nanoscale. The majority of chemical processes in a CVD process are homogeneous and heterogeneous reactions which happen between gaseous reactants during the deposition process. Although a wide range of materials may be deposited, most conventional CVD techniques require the use of readily volatile precursors. This is a particular issue for the deposition of multicomponent thin films, where the stoichiometry of the material will be difficult to control without a series of precursors with complementary volatility, reactivity and physical properties. The precursor requirements of conventional CVD, thus, present a major barrier which may be avoided by adoption of aerosol-assisted CVD. The AACVD technique does not require the use of a volatile precursor. Rather, the only limitation is easy solubility in an appropriate solvent. Without the restriction of volatility, however, an AACVD precursor must still display the features common to all CVD precursor. The AACVD technique can be compared with conventional CVD method but provides the advantages listed below:[118,119]

a) AACVD precursor can be selected from a wider pool of available chemical compounds; this includes both commercially available compounds and bespoke single source precursors for more specialized materials.

b) The precursor solution is generated in aerosol form, providing a means to enable easy delivery and vaporization of the precursor to grow thin films.

c) The easy transportation of the precursor in the system helps to provide control of deposition rates and has the potential to be developed for large-scale production.

d) The stoichiometry of multicomponent films may be controlled by simple variation of the solution composition.

e) Provides flexibility for the control of film texture and morphology.

1.6.1 Principles and Characteristics of the AACVD process

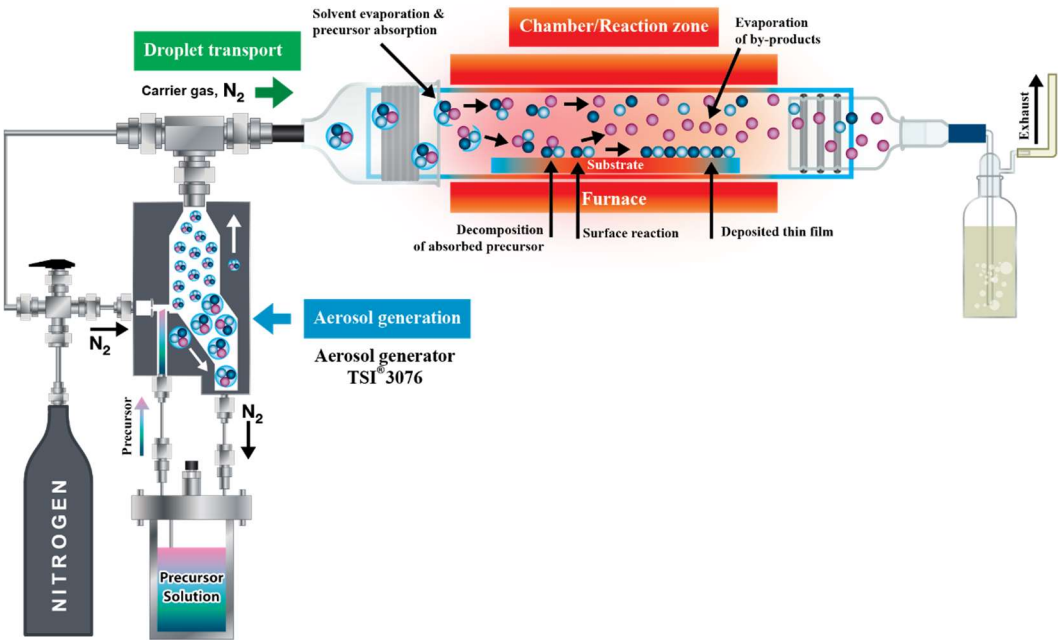

Figure 1.24 Schematic diagram of the hot wall AACVD process used throughout this thesis and showing its major components.

A main attribute of AACVD takes advantage of features of both conventional CVD and spray pyrolysis processes. Figure 1.24 shows a schematic diagram of the hot wall AACVD equipment which is used in this thesis. Generally, this process comprises three main sections that are:

Aerosol generation:

The precursor solution is nebulized into a submicron size aerosol by using an aerosol generator. Aerosol generation may be achieved in a number of ways, of which the major three methods utilize a pneumatic aerosol jet, electrostatic atomization or ultrasonic aerosol generation. These systems are used to break down the surface tension of the liquid precursor allowing the solvent to be entrained in the gas phase as a fine mist.

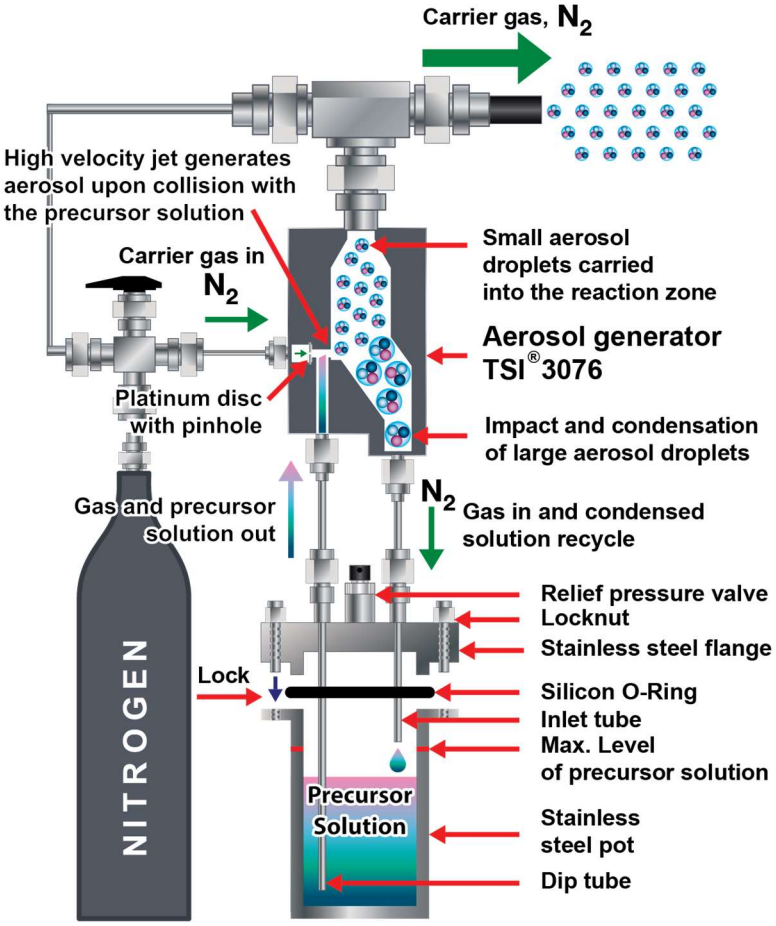

Figure 1.25 Illustration of the precursor aerosol generation by the TSI aerosol generator 3076, pneumatic atomization system.

Figure 1.25 shows a diagram of the aerosol generator which is based on a pneumatic TSI aerosol generator 3076. An inert gas such as nitrogen or argon is generally used to assist the aerosol creation in this system, although for metal oxide deposition compressed air may be employed as an additional source of oxygen. The TSI generator can generate a fine aerosol of the precursor solution, which is transported by the carrier gas into the chamber or the reaction zone to form the desired thin film. This TSI generator is designed to recycle unnebulized solution to reduce and control the precursor consumption.

Transportation:

Fine precursor droplets are transported to the chamber or reaction zone by the carrier gas, at which point further reactive gases such H_2 may also be introduced if required by the final target materials.

Deposition:

Thin film deposition takes place in the reaction zone or in the chamber. The substrate is put in this zone for the film deposition. The chamber attains a higher temperature than the prior section of the reactor system and is heated by a furnace or other energy sources. The energy source provides the temperature or energy for the chemical reaction to take place and form the thin film. Generally, reactor system can be designed with two main configurations, cold-wall and hot-wall. Indeed, the primary difference between many types of reactor is simply the position of their heating source.

Reactor apparatus

In a cold-wall reactor the heating source is most commonly positioned underneath the stage on which the substrate in placed such that the heat source is only provided in this area (Figure 1.26(a)). Because of the heating position only a single substrate deposition is usually accommodated, which presents a limitation for large area production. Nevertheless, this reactor configuration allows control over the deposition parameters and can prevent pre-evaporation of the aerosol droplets and help prevent the formation of powders or particulate films.

For a hot-wall reactor, the position of the heating source is near to or surrounds the reaction zone. Hence, the heating source is applied around the entire chamber entirety and not just at the substrate (Figure 1.26 (b)). This reactor configuration requires appropriate temperature control to prevent pre-evaporation of the precursor droplets, which typically leads to powder and particulate generation. Moreover, a major inconvenience of this reactor configuration is that the deposition can also occur around the reactor walls and not only on the target substrate. With respect to precursor consumption, a hot-wall reactor typically consumes more precursor than a cold-wall reactor. However, a hot-wall reactor is more suitable for large area deposition and can be provide uniform thin films over a larger area.

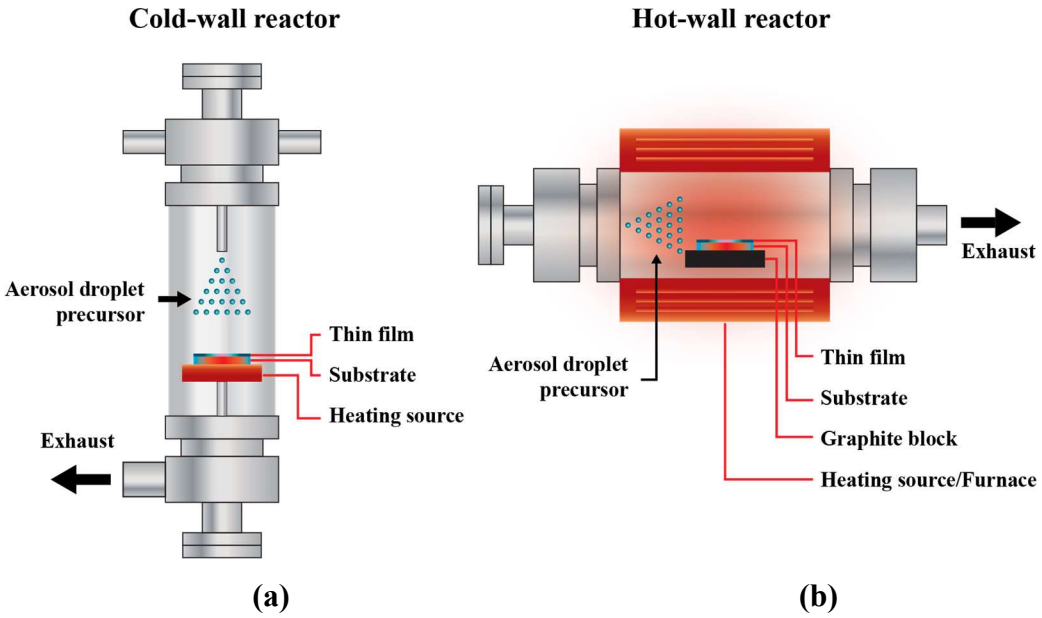

Figure 1.26 Schematic diagram of the basic AACVD reactor. (a) Cold-wall reactor (b) Hot-wall reactor.

1.6.3 Thin film growth

In the reaction or heated zone, the solvent is evaporated and the precursor is vaporised or decomposed rapidly from the aerosol droplets by the increase in temperature. The chemical reactions between the gaseous precusors then allow the desired thin film growth to occur.

The characteristics of the precursors and the reaction temperature are very important and profoundly influence the thin film formation. Figure 1.27 illustrates different routes to thin film formation that depend on the enthalpy of the precursor decomposition; two general routes may be discriminate of 'low' enthalpy and 'high' enthalpy.

At 'low enthalpy', a '***heterogeneous reaction***' will occur leading to the formation of compacted thin films (Figure 1.28 (a)). When the aerosol precursor droplets are introduced into the heated reaction zone vaporisation occurs at or near to the substrate surface. The vaporised precursor can be adsorbed onto the heated substrate surface prior to precursor decomposition or chemical reaction. After this event, the nucleation-growth process will happen allowing thin film formation.[120–122]

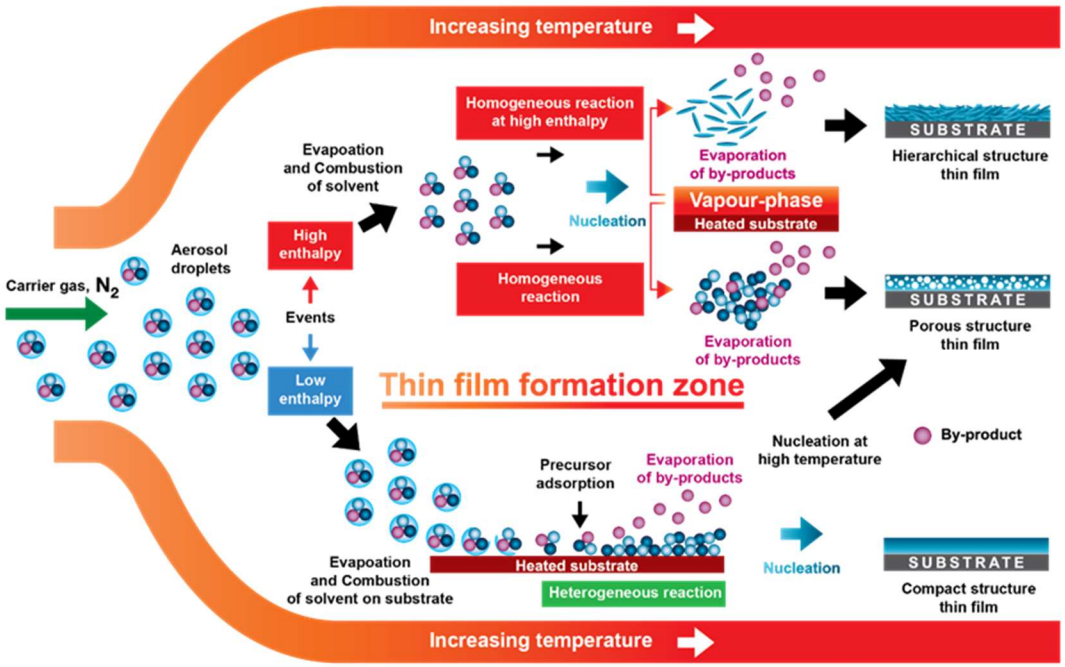

Figure 1.27 Schematic representation of the thin film formation in the reaction chamber or reaction zone.[120–122]

(a) **(b)** **(c)**

Figure 1.28 The structure of thin film characteristics which are affected by (a) low enthalpy (b) high enthalpy (c) low or high enthalpy.

In some cases, the vaporised precursor may be decomposed in the gaseous phase and the gaseous intermediate species are generated before diffusing to the surface. This 'low enthalpy' process can provide compacted thin films with good adhesive strength between the depostited film and the substrate (Figure 1.28 (a)).

At 'high enthalpy', when the aerosol droplets are transported into the reaction chamber and if the temperature in the chamber is too high, the droplets will evaporate immediately to form the vapour phase. This process results in the majority of the decomposition and chemical reaction taking place in the vapour phase prior to its arrival at the substrate surface. Under this regime, significant homogeneous nucleation will happen to typically create numerous fine particles formed in a '***homogeneous reaction***'.[120–122]

The thin film which is formed by the high enthalpy reaction will typically deposit as a hierarchical or porous structure as shown in Figure 1.28 (b) and (c).

The AACVD technique can also use a single source precursor such that the precursor can be combined with combustion chemicals to enable low-temperature deposition on to more delicate substrates, for example, plastics or polymers which possess low melting point tempratures. Moreover, the developent of low-temperature deposition methods can also decrease energy consumption resulting in lower cost thin film production.

1.6.4 The influence of the deposition conditions

During an AACVD process, variation of parameters or conditions such as precursor identity, temperature, substrate, solvent, flow rate of a precursor and deposition time etc. will impact upon the structures and properties of the final films. The following section assesses some of the parameters or conditions that can influence the ultimate thin films.

Precursor

Any precursor for an AACVD system should fulfill the flowing criteria:

- The precursor does not need to be volatile; rather, it must display the necessary solubility in an appropriate solution.
- The precursor should be easy to synthesize, non-toxic, non-explosive or non-flammable and should be available in large quantities and with low-cost production.
- The precursor should be thermally and the chemically stable and should possess clean decomposition steps so as to not leave any residual by-products or impurities which will contaminate the final film.
- The viscosity of the precursor solution should be appropriate for the aerosol generation step; in some types of aerosol generator such as a pneumatic aerosol jet system, a high viscosity precursor solution is not suitable or difficult to generate the aerosol droplets.

Different precursors can provide differing morphologies and properties to the final thin films. For example, Figure 1.29 displays SEMs of the surfaces of two TiO_2 thin films, both of which were deposited on a plain glass substrate but with a different precursor; Figure 1.29 (a) was deposited using ($Ti(O'Pr)_4$) in toluene and (b) using $Ti[OCH(CH_3)_2]_4$ in ethanol. Both material display an anatase structure, however, it can be seen their morphologies are different. Additionally, the band gap energies are slightly different at 3.1 eV and 2.85 eV, respectively.

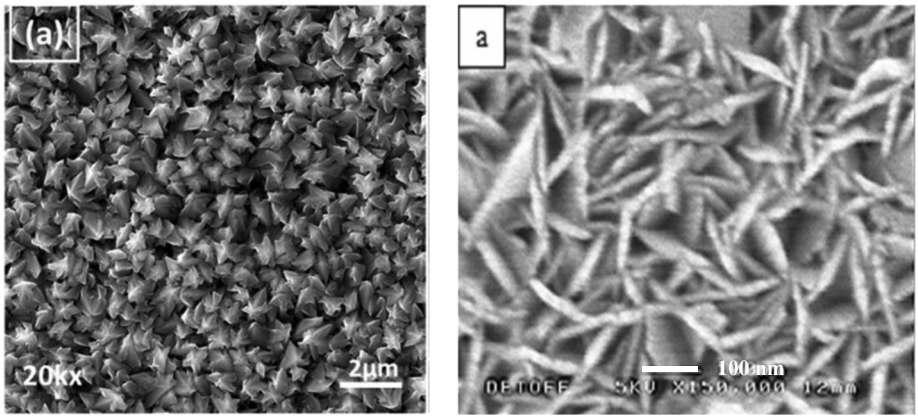

(a) **(b)**

Figure 1.29 SEM images of AACVD-produced TiO_2 thin film on a glass substrate which were prepared by different precursors (a) titanium(IV) isopropoxide ($Ti(O'Pr)_4$)[123] (b) $Ti[OCH(CH_3)_2]_4$.[124]

Solvent

Solvent selection can also impact on the morphology and composition of the thin films. The solvent is used to dissolve the precursor chemicals in the precursor preparation step and it is important to not only consider their physical properties such as viscosity, boiling point, surface tension, but also their elemental composition. For example, during metal sulfide thin film fabrication, the thin film do not require oxygen in the final film composition. Hence, a more appropriate solvent without oxygen such as a toluene (C_7H_8), is required.

Edusi *et al*.,[125] found that the solvent has an influence on the phase formation of TiO_2 thin films when they used different solvents in the deposition process (Figure 1.30). Use of methanol as a solvent for deposition onto a steel substrate provided rutile TiO_2 whereas ethanol resulted in an anatase phase.

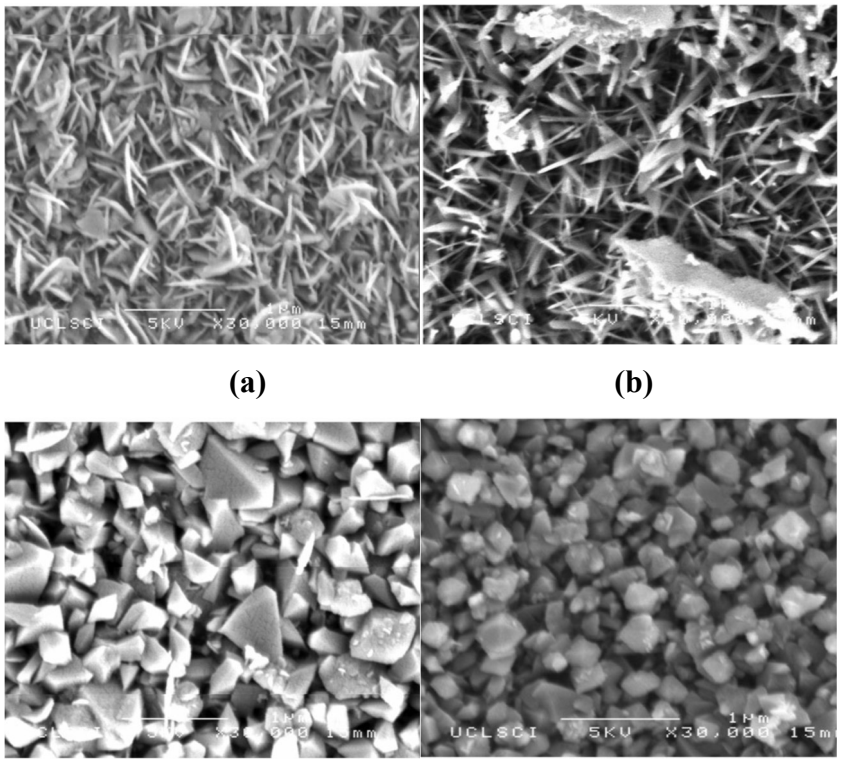

Figure 1.30 SEM of TiO_2 as-deposited on steel by AACVD using various mixtures of carrier solvents, (a) ethanol 100%, (b) methanol 100%, (c) 10% methanol and 90% ethanol and (d) 25% methanol and 75% ethanol.[125]

Furthermore, when a mixed solvent system of methanol and ethanol was used, the thin films displayed only the rutile phase from which it could be determined that choice of alcohol affects the phase formation of the TiO_2 thin film.

Similarly, Tahir and co-workers,[126] found that the morphology of $ZnFe_2O_4$ thin films was affected by the choice of solvent (Figure 1.31). The films which were prepared from an ethanolic precursor solution also presented the highest photocurrent density under illumination.

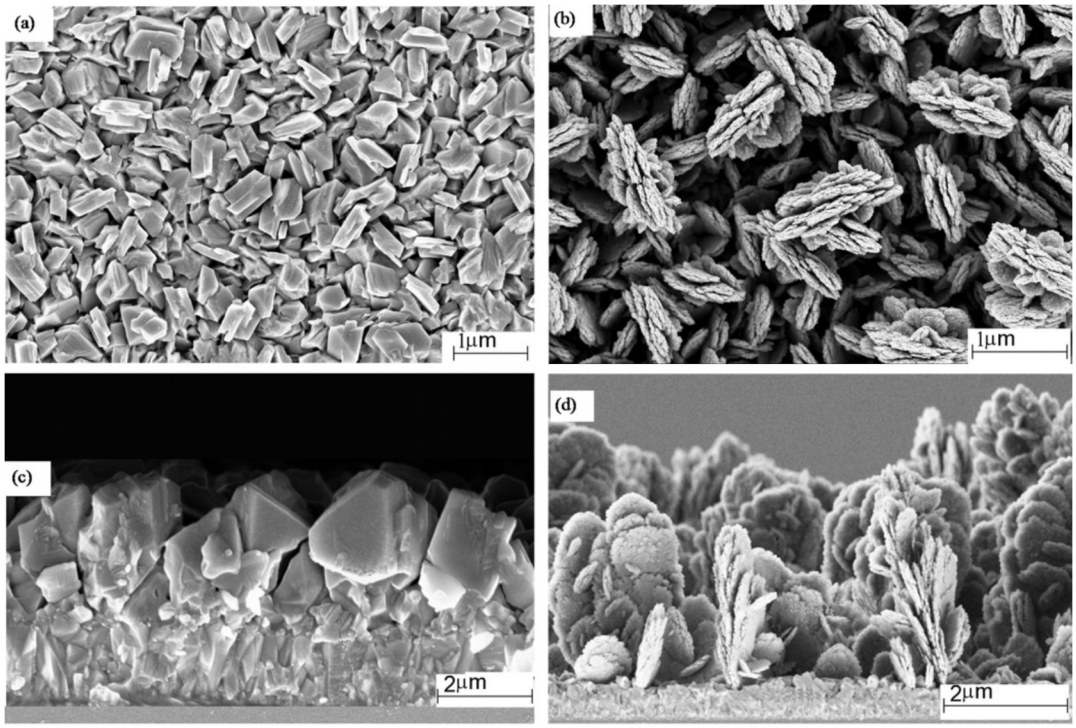

Figure 1.31 SEM images of $ZnFe_2O_4$ thin films deposited on FTO substrates using optimum conditions of a deposition temperature of 450 °C and a deposition time of 35 min. (a) and (c) show surface the morphology and cross-section for the film deposited from a 0.1 M solution of (1) in methanol, whereas (b) and (d) show the same detail for a film deposited from 0.1 M solution of (1) in ethanol.[126]

Substrate

Different substrates can also provide different morphologies and materials properties. For example, Figure 1.32 presents the morphology of CdS thin films which were prepared using identical precursor solutions and deposition temperatures but deposited on two different substrates, FTO and soda lime glass.

Some substrates are difficult to deposit onto because of their surface characteristics such as surface roughness. This problem can be alleviated by a substrate treatment process, for example, plasma cleaning. This technique can simply clean the substrate surface or can modify, adjust or control the behaviour of the surface to be more suitable for thin film deposition.

In addition, some thin film processes require a high deposition temperature. In such cases, the use of substrates which possess a low-melting point such as polymeric materials are inappropriate.

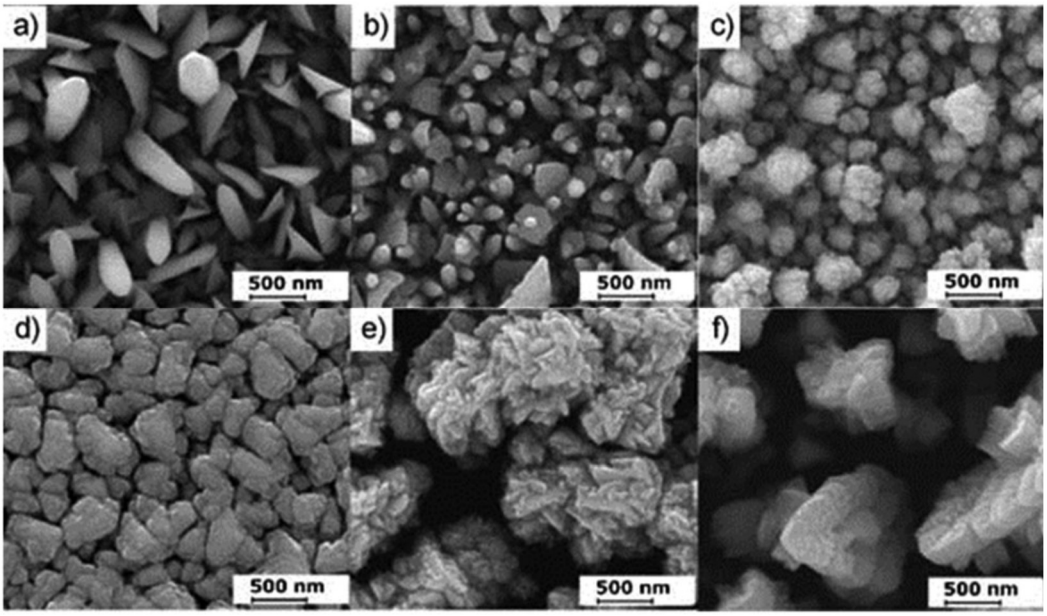

Figure 1.32 SEM images of CdS thin films deposited from $[Cd(S_2CNCy_2)_2 \cdot py]$ on FTO (a–c) and soda glass (d–f) at 350, 400, and 450 1C from THF solution.[127]

Temperature

Generally, the temperature of the thin film deposition via AACVD can also affect the microstructure and properties of the deposited films.

For example, Murtaza *et al*.,[128] have deposited antimony sulphide (Sb_2S_3, stibnite) thin films for use in solar cell applications by AACVD. Films prepared at deposition temperatures of 300, 350 and 400 °C deposited with an orthorhombic stibnite crystal structure. Figure 1.33 shows SEM images of a films which were prepared at 300 - 400 °C. The lower temperature film displays a morphology as crystallite sheets with a size range of 1.5-3 μm, whereas the film deposited at 350 °C displays a longer but thinner shape with size 3-4 μm. In contrast, the thin film which was deposited at 400 °C presents a different morphology that appears as short thick rods rather than thin plates. The transformation of the thin film morphology is due to the deposition temperature.[129]

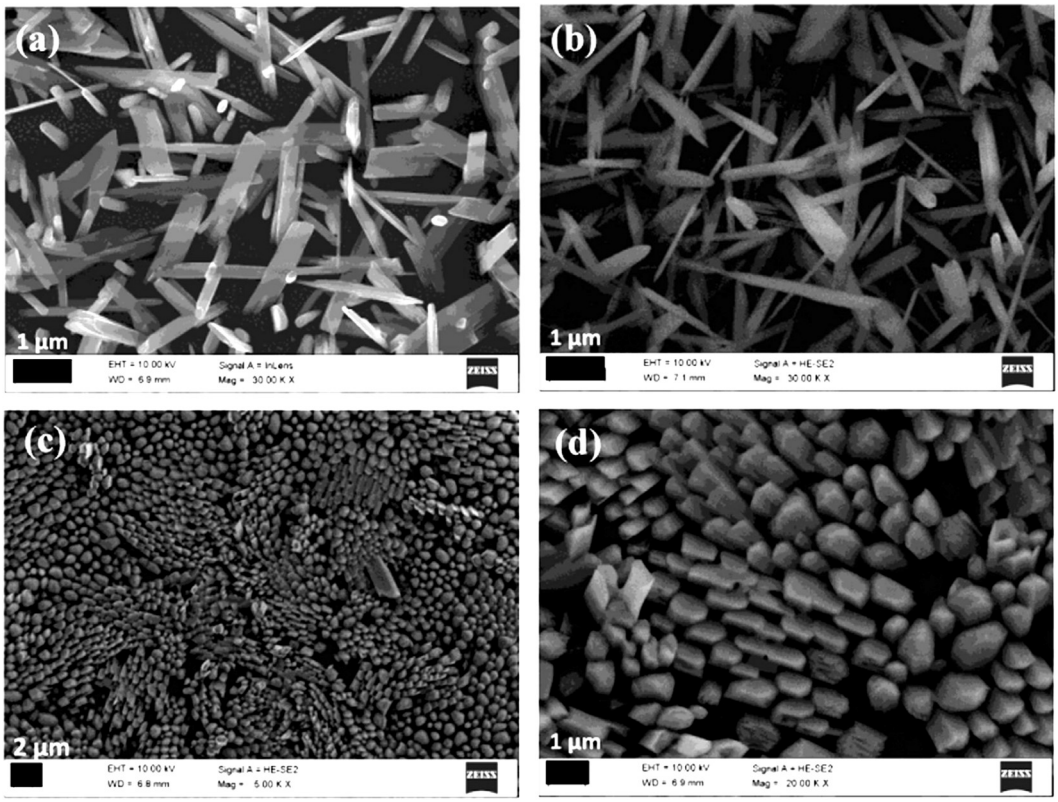

Figure 1.33 SEM images of Sb_2S_3 thin films deposited onto glass substrates at (a) 300 (b) 350 (c) and (d) 400 °C by AACVD from *tris*(thiobenzoato)antimony(III).[128]

1.7 Thesis outline

This thesis will focus on the fabrication of thin film oxide and sulfide materials by using the AACVD technique.

The precursors selected will be as readily available and inexpensive as possible, whilst fulfilling the major AACVD requirement of precursor solubility. Consequently, metal nitrate will be employed to deposit binary and ternary metal oxide thin films.

The initial experimental chapters will describe the deposition of nickel, copper, lanthanum and praseodymium oxide with a view to controlling the film phase formation and morphology. Subsequent work will target the ternary oxide material lanthanum nickel oxide, with the ultimate goal of achieving thin film growth by using a single source precursor prepared from simple metal nitrates.

The second major objective of this thesis will be addressed toward metal sulphide thin film deposition, specifically the growth of zinc sulphide using the AACVD technique. For this objective, the zinc sulphide thin film will be prepared from a variety of different precursor and the composition and morphology of the resultant materials will be assessed.

Finally, all of thin film from both objectives will be investigated for their properties and morphology with respect to the parameters or conditions which may be varied during the AACVD process.

References

1 G. E. Moore, *Proc. IEEE*, 1998, **86**, 82–85.

2 W. Aspray, *IEEE Ann. Hist. Comput.*, 1997, **19**, 4–15.

3 L. Geppert, *IEEE Spectr.*, 2000, **September**, 46–51.

4 L. L. Vadasz, A. S. Grove, T. A. Rowe and G. E. Moore, *IEEE Spectr.*, 1969, **October**, 28–35.

5 Intel® Core™ i9-8950HK Processor, https://www.intel.com/content/www/us/en/products/processors/core/i9-processors/i9-8950hk.html, (accessed 9 May 2018).

6 Sunpartner Technologies Has Increased Wysips® Crystal Power by 50% and Will Unveil a New Prototype Solar Smartphone Created with Kyocera at MWC 2016, http://sunpartnertechnologies.com/new-prototype-solar-smartphone-kyocera-at-mwc-2016/, (accessed 7 May 2018).

7 D. Takahashi, Thin Film Electronics demonstrates a way to make disposable interactive smart labels that replace bar codes | VentureBeat, https://venturebeat.com/2012/12/19/thin-film-electronics-demonstrates-a-way-to-make-disposable-interactive-smart-labels-that-replace-bar-codes/, (accessed 9 May 2018).

8 B. Burton, New nanomaterial offers promise in bendable, wearable electronic devices, https://today.uic.edu/new-nanomaterial-offers-promise-in-bendable-wearable-electronic-devices, (accessed 9 May 2018).

9 S. Sees, Solar sees 8% growth in 2q 2017, www.ewweb.com, (accessed 9 May 2018).

10 US 2015/030139 A1, 2015.

11 A. Jilani, M. S. Abdel-wahab and A. H. Hammad, *Advance Deposition Techniques for Thin Film and Coating*, INTECH, 2017.

12 Susumu International U.S.A.-Thin film Specialist and Innovator, 2.Manufacturing methods and characteristics of thin film resistors | Susumu

International U.S.A. -Specialist in Thin Film Technology-, https://www.susumu.co.jp/usa/tech/know_how_02.php, (accessed 13 May 2018).

13 M. Sterrer and H.-J. Freund, *Surface and Interface Science: Properties of Composite Surface: Alloys, Compounds Semiconductors.*, WILEY-VCH Verlag, First., 2014.

14 P. A. Cox, *Transition Metal Oxides: An introduction to their electronic structure and properties*, Oxford University Press Inc., New York, 1995.

15 C. N. R. Rao and B. Raveau, *Transition Metal Oxides: Structure, Properties, and Synthesis of Ceramic oxides*, John Wiley&Sons,Inc., Second edi., 1998.

16 C. N. R. Rao, *Annu. Rev. Phys. Chern.*, 1989, **40**, 291–326.

17 P. and team Flowers, 8.4 Molecular Orbital Theory – Chemistry, https://opentextbc.ca/chemistry/chapter/8-4-molecular-orbital-theory/, (accessed 22 March 2018).

18 The LibreTexts libraries, 12.1: Classes of Materials - Chemistry LibreTexts, https://chem.libretexts.org/Textbook_Maps/General_Chemistry_Textbook_Maps/Map%3A_Chemistry%3A_The_Central_Science_(Brown_et_al.)/12%3A_Solids_and_Modern_Materials/12.1%3A_Classes_of_Materials, (accessed 22 March 2018).

19 Rare earth technology alliance, What Are Rare Earths?, http://www.rareearthtechalliance.com/What-are-Rare-Earths, (accessed 4 March 2018).

20 L. Wei, Z. Yang, X. Chao and H. Jiao, *Ceram. Int.*, 2014, **40**, 5447–5453.

21 K. H. Goh, A. S. M. A. Haseeb and Y. H. Wong, *Mater. Sci. Semicond. Process.*, 2017, **68**, 302–315.

22 Rare Element Resources Ltd., Rare Earth Elements, http://www.rareelementresources.com/rare-earth-elements#.WpwQcajFLIV, (accessed 4 March 2018).

23 R. E. R. Ltd., Rare Earth Elements,

http://www.rareelementresources.com/rare-earth-elements#.Wp3-0ejFLIU, (accessed 6 March 2018).

24 X. Wang, H. Liu, L. Zhao, C. Fei, X. Feng, S. Chen and Y. Wang, *Nanoscale Res. Lett.*, 2017, **12**, 1–7.

25 S. B. Brachetti-Sibaja, S. E. Rodil, M. A. Domínguez-Crespo, A. M. Torres-Huerta, E. Rodríguez and A. B. López-Oyama, *Thin Solid Films*, 2017, **636**, 615–621.

26 A. Abrutis, M. Lukosius, Z. Saltyte, R. Galvelis and P. K. Baumann, *Thin Solid Films*, 2008, **516**, 4758–4764.

27 J. G.Adachi(Juri Institute fro Environmental Science and Chemistry, Osaka, J. N. Imanaka(Osaka University, Osaka and C. Z.C. Kang(Internatioanl Center for Quantum Structures and State Key Laboratory for Surface Sciences, Beijing, *Binary Rare Earth Oxides*, Kluwer academic publishers, New york, Boston, Dordrecht, London, Moscow, 2005.

28 M. Nieminen, M. Putkonen and L. Niinisto, *Appl. Surf. Sci.*, 2001, **174**, 155–165.

29 G. Adachi and N. Imanaka, *Chem. Rev.*, 1998, **98**, 1479–1514.

30 T. D. Golden, Y. Shang, Q. Wang and T. Zhou, *Advanced Ceramic Processing*, INTECH, 2015.

31 L. Eyring, *Handbook on the Physics and Chemistry of Rare Earths*, Elsevier B.V., Amsterdam, vol. 3., 1979.

32 H. S. Kim, M. D. Kumar, W. H. Park, M. Patel and J. Kim, *Sensors Actuators, A Phys.*, 2017, **253**, 35–40.

33 N. Imanaka and T. Masui, *Chem. Rec.*, 2009, **9**, 40–50.

34 N. Imanaka and T. Masui, *Appl. Catal. A Gen.*, 2012, **431**–**432**, 1–8.

35 M. Haneda and H. Hamada, *Comptes Rendus Chim.*, 2016, **19**, 1254–1265.

36 Politechnika Wrocławska., *Opt. Appl.*, 2014, **14**, 189–193.

37 Z. Wang, P. K. Nayak, J. A. Caraveo-Frescas and H. N. Alshareef, *Adv.*

Mater., 2016, **28**, 3831–3892.

38 M. W. Lufaso and P. M. Woodward, *Bond Valences*, Springer Berlin Heidelberg, 2013.

39 C. Tablero, *Chem. Phys. Lett.*, 2015, **635**, 190–195.

40 Y. Mao, T.-J. Park and S. S. Wong, *Chem. Commun.*, 2005, 5721–5735.

41 O. Fukunaga and S. Yamaoka, *Phys. Chem. Miner.*, 1979, **5**, 167–177.

42 M. Minakshi, T. Watcharatharapong, S. Chakraborty and R. Ahuja, *Cit. APL Mater.*, 2018, **6**, 047701-1–9.

43 P. Kozma, R. Bajgar and P. Kozma, *Radiat. Phys. Chem.*, 2002, **65**, 127–130.

44 V. Stevanovi, M. D 'avezac and A. Zunger, *J. Am. Chem. Soc*, 2011, **133**, 11649–11654.

45 O. Muller and R. Roy, *The Major Ternary Structural Families*, Springer-Verlag, New York, 1974.

46 I. D. Brown, ed. K. R. Poeppelmeier, Springer, 2013.

47 B. Bhujun, M. T. T. Tan and A. S. Shanmugam, *Results Phys.*, 2017, **7**, 345–353.

48 J.-I. Yamaura, S. Yonezawa, Y. Muraoka and Z. Hiroi, *J. Solid State Chem.*, 2006, **179**, 336–340.

49 N. Taira, M. Wakeshima, Y. Hinatsu, A. Tobo and K. Ohoyama, *J. Solid State Chem.*, 2003, **176**, 165–169.

50 B. J. Kennedy, *Phys. B*, 1998, **241**, 303–310.

51 H.-M. Huang, Z.-Y. Jiang, S.-J. Luo-, = Li, K. Na, A. Photocatalyst, W.-L. Zhou, Z.-Y. Zhao-, C.-H. Hu, X.-H. Yin, D.-H. Wang, Y. Zhong, H.-Y. Zhou and G.-H. Rao, *Chin. Phys. B*, 2016, **25**, 067801-1–5.

52 E. Saitzek, Z. Shao, A. Bayart, A. Ferri, M. Hu, P. Roussel and R. Desfeux, *J. Mater. Chem. C*, 2014, **2**, 4037–4043.

53 S. Gross, A. Vittadini and N. Dengo, *Crystals*, 2017, **7**, 1–40.

54 F. T. Firdu and P. Taskinen, *Sulfide Mineralogy -Literature Review*, Aalto University School of Science and Technology Department of Materials Science and Engineering, Aalto, 2010.

55 Wikimedia Commons, Sphalerite-unit-cell-3D-balls, https://commons.wikimedia.org/wiki/File:Sphalerite-unit-cell-3D-balls.png, (accessed 9 May 2018).

56 Wurtzite crystal structure, http://www.wikiwand.com/en/Wurtzite_crystal_structure, (accessed 8 May 2018).

57 Wikipedia, Nickeline, https://en.wikipedia.org/wiki/Nickeline, (accessed 10 May 2018).

58 S. Garge, Cadmium iodide, https://alchetron.com/Cadmium-iodide, (accessed 11 May 2018).

59 Wikipedia, Magnesium hydride, https://en.wikipedia.org/wiki/Magnesium_hydride, (accessed 8 May 2018).

60 Wikimedia Commons, Pyrite, https://commons.wikimedia.org/wiki/File:Pyrite-unit-cell-3D-balls.png, (accessed 8 May 2018).

61 Tetraarsenic tetrasulphide, https://www.webelements.com/compounds/arsenic/tetraarsenic_tetrasulphide.html, (accessed 8 May 2018).

62 Arsenopyrite, http://images.slideplayer.com/23/6867435/slides/slide_36.jpg, (accessed 9 May 2018).

63 R. A. Soref and H. W. Moos, *J. Appl. Phys.*, 1964, **35**, 2152–2158.

64 C.-H. Lai, M.-Y. Lu and L.-J. Chen, *J. Mater. Chem.*, 2012, **22**, 19–30.

65 D. Moore and Z. L. Wang, *J. Mater. Chem.*, 2006, **16**, 3898–3905.

66 X. Fang, Y. Bando, G. Shen, C. Ye, U. K. Gautam, P. M. F. J. Costa, C. Zhi, C. Tang and D. Golberg, *Adv. Mater.*, 2007, **19**, 2593–2596.

67 S.-B. Lei, L.-J. Wan, C. Wang and C.-L. Bai, *Adv. Mater.*, 2004, **16**, 828–831.

68 O. K. Echendu, A. R. Weerasinghe, D. G. Diso, F. Fauzi and I. M. Dharmadasa, *J. Electron. Mater.*, 2013, **42**, 692–700.

69 Y.-G. Yoon and I.-H. Choi, *J. Korean Phys. Soc.*, 2013, **63**, 1609–1614.

70 T. Toyama, T. Hama, D. Adachi, Y. Nakashizu and H. Okamoto, *Nanotechnology*, 2009, **20**, 1–5.

71 Y. He, H. F. Wang and X. P. Yan, *Chem. - A Eur. J.*, 2009, **15**, 5436–5440.

72 S. H. Shin, J. H. Kang, D. Y. Jeon and D. S. Zang, *J. Solid State Chem.*, 2005, **178**, 2205–2210.

73 C.-H. Lai, K.-W. Huang, J.-H. Cheng, C.-Y. Lee, B.-J. Hwang and L.-J. Chen, *J. Mater. Chem.*, 2010, **20**, 6638–6645.

74 V. Klimov, P. Haring Bolivar, H. Kurz, V. Karavanskii, V. Krasovskii and Y. Korkishko, *Appl. Phys. Lett.*, 1995, **67**, 653–655.

75 H. Grijalva, M. Inoue, S. Boggavarapub and P. Calved, *J. Mater. Chem.*, 1996, **6**, 1157–1160.

76 S. Goel, F. Chen and W. Cai, *Small*, 2014, **10**, 631–345.

77 J. Kundu and D. Pradhan, *ACS Appl. Mater. Interfaces*, 2014, **6**, 1823–1834.

78 F. Cao, R. Liu, L. Zhou, S. Song, Y. Lei, W. Shi, F. Zhao and H. Zhang, *J. Mater. Chem.*, 2010, **20**, 1078–1085.

79 W. Zhang, Y. Wang, Z. Wang, Z. Zhong and R. Xu, *Chem. Commun.*, 2010, **46**, 7631–7633.

80 P. A. Metcalf, B. C. Crooker, M. Mcelfresh, Z. Kykol and J. M. Honig, *Phys. Rev. B Condens. matter*, 1994, **50**, 2055–2060.

81 X. Zhu, Z. Wen, Z. Gu and S. Huang, *J. Electrochem. Soc.*, 2006, **153**, A504–A507.

82 C.-H. Lai, K.-W. Huang, J.-H. Cheng, C.-Y. Lee, W.-F. Lee, C.-T. Huang, B.-J. Hwang and L.-J. Chen, *J. Mater. Chem.*, 2009, **19**, 7277–7283.

83 M. G. Kim, M. G. Kanatzidis, A. Facchetti and T. J. Marks, *Nat. Mater.*, 2011, **10**, 382–388.

84 K. H. Stern and K. H. Stern, *J. Phys. Chem. Ref. Data*, 1972, **1**, 747–772.

85 A. A. Yadav, A. C. Lokhande, P. A. Shinde, J. H. Kim and C. D. Lokhande, *J. Mater. Sci. Mater. Electron.*, 2017, **28**, 13112–13119.

86 L. Cattin, B. A. Reguig, A. Khelil, M. Morsli, K. Benchouk and J. C. Bern??de, *Appl. Surf. Sci.*, 2008, **254**, 5814–5821.

87 S. Shrestha, F. Marken, J. Elliott, C. M. Y. Yeung, C. E. Mills and S. C. Tsang, *J. Electrochem. Soc.*, 2006, **157**, 517–520.

88 M. Jergel, M. García, A. Conde-Gallardo, C. Falcony, M. A. Canseco and G. Plesch, *Thin Solid Films*, 1997, **305**, 157–163.

89 Y. S. Rim, H. Chen, T.-B. Song, S.-H. Bae and Y. Yang, *Chem. Mater.*, 2015, **27**, 5808–5812.

90 A. C. Jones, H. C. Aspinall, P. R. Chalker, R. J. Potter, K. Kukli, A. Rahtu, M. Ritala and M. Leskelä, *J. Mater. Chem.*, 2004, **14**, 3101–3112.

91 S. Wu, Q. Zhang, Z. Chen, L. Mo, S. Shao and Z. Cui, *J. Mater. Chem. C*, 2017, **5**, 7495–7503.

92 J.-S. Park and Y.-B. Kim, *Thin Solid Films*, 2016, **599**, 174–178.

93 W. Kern and K. K. Schuegraf, 2001, **i**, 11–43.

94 P. Arunkumar, S. K. Kuanr and K. S. Babu, in *Thin Film Structures in Energy Applications*, Springer International Publishing, Cham, 2015, pp. 1–49.

95 A. C. Jones and M. L. Hitchman, *Chemical Vapour Deposition: Precursors, Processes and Applications*, The Royal Society of Chemistry, 2009.

96 H. O. Pierson, *Handb. Chem. Vap. Depos.*, 1992, 1–16.

97 H. O. Pierson, *Handb. Chem. Vap. Depos.*, 1999, 68–83.

98 T. Schneller and R. Waser, *Chemical Solution Deposition of Functional Oxide Thin Films*, Springer, 2013.

99 S. Thambidurai, N. Suresh, S. Aiswarya and S. Manimegala, *Bull. Pure Appl. Sci. Phys.*, 2017, **36 D**, 10–14.

100 D. Gwinner, *NREL Natl. Renew. energy Lab.*, 2010.

101 E. Sowade, E. Ramon, K. Y. Mitra, C. Martínez-Domingo, M. Pedró, J. Pallarès, F. Loffredo, F. Villani, H. L. Gomes, L. Terés and R. R. Baumann, *All-inkjet-printed thin-film transistors: Manufacturing process reliability by root cause analysis*, 2016.

102 D. Kim, Y. Kwak and J. Park, *Appl. Sci.*, 2018, **8**, 1–9.

103 R. D. Bacelis-Martínez, G. Oskam, G. Rodriguez Gattorno and M. A. Ruiz-Gómez, *Adv. Mater. Sci. Eng.*, 2017, **2017**, 1–9.

104 M. Faustini, B. Louis, P. A. Albouy, M. Kuemmel and D. Grosso, *J. Phys. Chem. C*, 2010, **114**, 7637–7645.

105 C. J. Brinker, *Chemical Solution Deposition of Functional Oxide Thin films*, Springer-Verlag, USA, 2013.

106 S. H. Chaki, K. S. Mahato, T. J. Malek and M. P. Deshpande, *J. Sci. Adv. Mater. Devices*, 2017, **2**, 215–224.

107 J. B. Mooney and S. B. Radding, *Annu. Rev. Mater. Sci.*, 1982, **12**, 81–101.

108 D. Perednis and L. J. Gauckler, *J. Electroceramics*, 2005, **14**, 103–111.

109 M. Burgelman, in *The workshop microtechnology and thermal problems in electronics.*, 1998, pp. 129–135.

110 X. Cao, H. Chen, X. Gu, B. Liu, W. Wang, Y. Cao, F. Wu and C. Zhou, *ACS Nano*, 2014, **8**, 12769–12776.

111 K. Fukada, Y. Maeda, X. Y. Liu, A. Matoba, S. Takagi, S. Inoue and T. Shimoda, *SID Symp. Dig. Tech. Pap.*, 2015, **33.5**, 490–493.

112 S. T. Navale, V. V. Mali, S. A. Pawar, R. S. Mane, M. Naushad, F. J. Stadler and V. B. Patil, *RSC Adv.*, 2015, **5**, 51961.

113 P. Lobaccaro, A. Raygani, A. Oriani, N. Miani, A. Piotto, R. Kapadia, M. Zheng, Z. Yu, L. Magagnin, D. C. Chrzan, R. Maboudian and A. Javey, *J. Electrochem. Soc.*, 2014, **161**, 794–800.

114 Y. M. Lu, W. S. Hwang, J. S. Yang and H. C. Chuang, *Thin Solid Films*,

2002, **420**, 54–61.

115 K.-C. Min, M. Kim, Y.-H. You, S. S. Lee, Y. K. Lee, T.-M. Chung, C. G. Kim, J.-H. Hwang, K.-S. An, N.-S. Lee and Y. Kim, 2007, **201**, 9252–9255.

116 K. C. Wang, J. Y. Jeng, P. S. Shen, Y. C. Chang, E. W. G. Diau, C. H. Tsai, T. Y. Chao, H. C. Hsu, P. Y. Lin, P. Chen, T. F. Guo and T. C. Wen, *Sci. Rep.*, 2014, **4**, 1–8.

117 G.-P. Kim, I. Nam, S. Park, J. Park and J. Yi, *Nanotechnology*, 2013, **24**, 1–8.

118 S. N. Ariffin, H. N. Lim, Z. A. Talib, A. Pandikumar and N. M. Huang, *Int. J. Hydrogen Energy*, 2015, **40**, 2115–2131.

119 X. Hou, J. Williams and K. L. Choy, *Thin Solid Films*, 2006, **495**, 262–265.

120 S. N. Ariffin, H. N. Lim, Z. A. Talib, A. Pandikumar and N. M. Huang, *Int. J. Hydrogen Energy*, 2015, **40**, 2115–2131.

121 W.-J. An, E. Thimsen and P. Biswas, *J. Phys. Chem. Lett.*, 2010, **1**, 249–253.

122 X. Hou and K.-L. Choy, *Chem. Vap. Depos.*, 2006, **12**, 583–596.

123 R. Naeem, M. A. Ehsan, A. Rehman, Z. H. Yamani, A. S. Hakeem and M. Mazhar, *New J. Chem.*, 2018, **42**, 5256–5266.

124 V. Diesen, C. W. Dunnill, J. C. Bear, S. Firth, M. Jonsson and I. P. Parkin, *Chem. Vap. Depos.*, 2014, **20**, 91–97.

125 B. C. Edusi, G. Sankar and I. P. Parkin, *Chem. Vap. Depos.*, 2012, **18**, 126–132.

126 A. A. Tahir and K. G. U. Wijayantha, *J. Photochem. Photobiol. A Chem.*, 2010, **216**, 119–125.

127 C. E. Knapp and C. J. Carmalt, *Chem. Soc. Rev.*, 2016, **45**, 1036–1064.

128 G. Murtaza, M. Akhtar, M. Azad Malik, P. O'Brien and N. Revaprasadu, *Mater. Sci. Semicond. Process.*, 2015, **40**, 643–649.

129 M. Y. Versavel and J. A. Haber, *Thin Solid Films*, 2007, **515**, 7171–7176.

Chapter 2:

Deposition of Binary oxide thin films

2.1 Binary oxide thin film depositions: Transition Metal oxides (TMOs)

2.1.1 Copper oxide thin film deposition

Introduction

Copper oxide is a well-known *p*-type oxide material. Generally, it can occupy three stable phases, cupric tenorite (CuO), cuprite (Cu_2O) and paramelaconite (Cu_4O_3).[1] Table 2.1 shows a summary of copper oxide properties.

Table 2.1 A summary of copper oxide material properties and their applications.

Chemical formula[1]	**Named phases**[1]	**Crystal structure.**[2–7]	**Energy band gap (eV)** [1–3,5–7]	**Colour of thin films.**[2,8]
CuO	Tenorite or cupric oxide	Monoclinic	~2.0-2.5	Black
Cu_2O	Cuprite	Cubic	~1.2-1.9	Brownish-red
Cu_4O_3	Paramelaconite	Tetragonal	~1.75	Light brown
Properties.[3,9]		**Applications**		
• Non-toxic nature • Abundant • Low thermal emittance • High optical absorption coefficient at lower wave lengths and in the visible regions		• Low-cost mass production for solar-cell applications.[2,4] • Photodetector devices.[2,1] • Photo-voltaic energy conservation.[7,5] • Sensor applications.[10,11] • Transparent displays.[12] • Transparent conductive oxides (TCOs).[1] • Transparent integrated circuits.[13] • Photocatalysts.[14,15]		

Copper oxide thin films have been prepared by many different techniques, which provide different properties to the films. Examples of copper oxide thin films which have been prepared by different techniques are presented in Table 2.2.

In 2017 Hong-Sik Kima et al.[1] observed that copper oxide underwent a phase transformation when the temperature was increased. They reported that Cu_2O thin films prepared at room temperature transformed into CuO upon increasing temperature to above 450 °C. Furthermore, when the oxygen concentration was increased during the film deposition process, the Cu_4O_3 phase predominated in the film. Similarly Dolai et al.[3] in 2017 were able to control the deposited copper oxide phase by adjusting the oxygen contents during reactive DC sputtering.

In 2014 Funda Aksoy Akgul et al.[2] found that the crystallinity of CuO thin films prepared by spin coating and annealed under air was dependent on the annealing temperature. The crystalline intensity increased, whereas the optical bandgaps decreased slightly from 2.08 to 1.93 eV with increasing temperature.

Medina-Valtierra et al.[8], in 2009, prepared copper oxide thin films by CVD and found the deposition and sublimation temperature were very important to control the phases and thickness of the oxide films. At deposition temperatures below 330 °C and under an oxygen atmosphere, the deposited film exhibited the CuO phase, while the combined phases of Cu_4O_3 and CuO presented at 330-340 °C. At deposition temperatures above this range the copper oxide deposited solely as the Cu_4O_3 phase.

The research in this chapter of the thesis will be concentrated on the control and an understanding of the factors affecting the oxidation state of copper oxide thin films deposited by AACVD and spin coating techniques.

Table 2.2 Examples of copper oxide thin films which were deposited by different techniques and some of their properties.

Deposition techniques	Substrates	Chemical structure	Band gap (eV)	Notes	Properties	Applications
Spin-coating[2]	Soda-lime silicate glass	CuO	1.93-2.08	Crystalline intensity was increased by increases in the annealing temperatures.	• High absorption coefficient[3] • Abundant ability[3] • Non-toxic nature[3] • Low thermal emittance[9] • Low-cost production[3] • P-type material[1–4] • CuO has monoclinic structure with band gap~1.2-1.9 eV, low thermal emittance and black colour.[2,3,5–7] • Cu_2O has a cubic structure with band	• Solar-cell applications[2,4] • Photodetector devices[2,1] • Photo-voltaic energy conversion[7,5] • Sensor applications[10,11] • High temperature superconductor[10] • Transparent display[12] • Sensor arrays[16]
Chemical vapour deposition[8]	Fibreglass substrate	Cu_4O_3	0.75	Sublimation and deposition temperature are important to control oxide phases and thickness of the film		
Sol-gel-like dip technique[17]	Glass	CuO Cu_2O	1.90 2.10	Over 400-500 °C of baking temperature, Cu_2O phases of the film can be converted to CuO phases		
Pulsed laser deposition (PLD)[5]	Glass	CuO Cu_2O	1.74 2.20	Increasing annealing temperature influence to increases the particle size of the films		
DC and RF magnetron sputtering[1]	Glass	Cu_4O_3	1.75	Cu_2O transforms to CuO by increase temperature over 450 °C and Cu_4O_3 by increasing		

Deposition techniques	Substrates	Chemical structure	Band gap (eV)	Notes	Properties	Applications
				oxygen contents during deposition	gap ~2.0-2.5 eV and brownish-red colour.[3,5–7] • Cu_4O_3 has band gap around 1.75 eV[1] with tetragonal structure and light brown colour.[4,8]	• Transparent integrated circuits[13] Photocatalysts[14,15]
Reactive DC sputtering technique[3]	Glass	Cu_2O	~2.48	Oxygen content in plasma phase is a factor to control copper oxide phases during the deposited process.		
RF magnetron sputtering[18]	Glass	Cu_2O+ CuO	2.05, 1.83	Thicknesses were increased by increasing the power of the sputtering system, while optical band gaps were decreased		

Film characterisation: Copper oxide thin film

Thermogravimetric analysis of Copper (II) nitrate trihydrate

Copper (II) nitrate trihydrate ($Cu(NO_3)_2{\cdot}3H_2O$) is one of the most widely used chemical precursors to copper-containing materials for various application such as high-temperature superconductors and catalysis.[19,20] Furthermore, $Cu(NO_3)_2{\cdot}3H_2O$ is easily dissolved in various solvents, which meets the primary requirement of an AACVD precursor. In this thesis, therefore, copper nitrate will be employed as the primary thin film precursor to copper oxide thin film preparation.

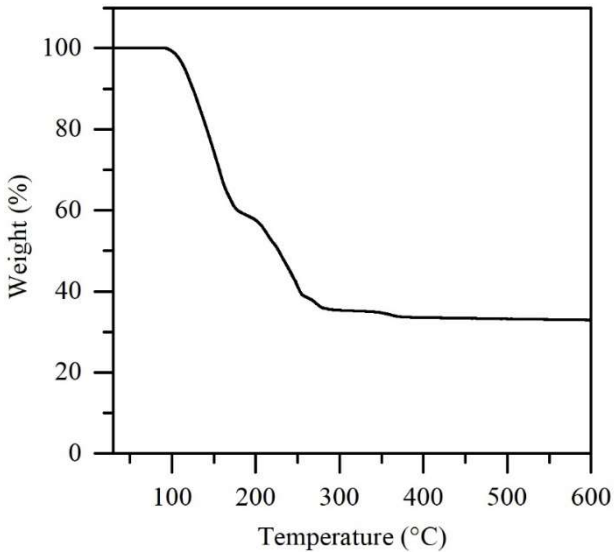

Figure 2.1 TGA curve of $Cu(NO_3)_2{\cdot}3H_2O$.

The decomposition behavior of the precursor was analysed by thermogravimetric analysis (TGA). Figure 2.1 presents the TGA curve of the degradation of $Cu(NO_3)_2{\cdot}3H_2O$ and it present two main steps of thermal decomposition. First step occurs around between 110 and 170 °C that due to the decomposition of water and the weight loss of this step is around 40%. Second step starts around 210 °C which can be attributed to the decomposition of complex then is complete around 375 °C with a stable residual of that expected for CuO of around 32%.

The TGA curve of $Cu(NO_3)_2{\cdot}3H_2O$ was used to identify the temperatures to be used in the thin film formation by spin coating and AACVD. Furthermore, these data allow on assessment of potential annealing temperatures to enable control over the phases of the deposited films.

Spin coating of the Cu(NO3)2·3H2O

Preliminary studies involved the spin coating of $Cu(NO_3)_2{\cdot}3H_2O$ and the application of an annealing process. Ethanol, methanol and water were used as the solvents in the process to allow a comparative study of the influence of the solvent. The thin film deposition was carried out using the conditions in Table 2.3.

The as deposited films presented an opaque gray-brown colouration which transformed to a slightly more transparent but dark brown material after the annealing process in air.

Table 2.3 Deposition conditions for spin coating of $Cu(NO_3)_2{\cdot}3H_2O$.

Variable	Detail
Substrate	Pilkington SiCO glass, 2.5×2.5 cm^2
Precursor concentration	0.05 M
Solvent	Ethanol, Methanol, Water
Deposition layer	5 layers
Annealing atmosphere	Air, Argon
Annealing time	1 hour
Annealing temperature	300–600 °C

Crystallinity

X-ray diffraction was used to investigate the crystallinity and to determine the phase of the films. The deposited thin films prepared from ethanol and methanol as solvent were found to be amorphous (Figure 2.2), while the use of water did not allow the deposition of a thin film on the substrate surface.

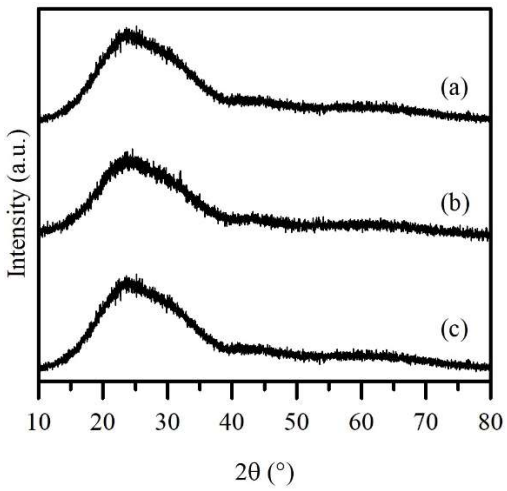

Figure 2.2 XRD patterns of deposited films of $Cu(NO_3)_2 \cdot 3H_2O$ prior to annealing using (a) ethanol or (b) methanol solvents. (c) is a XRD pattern of Pilkington SiCO glass.

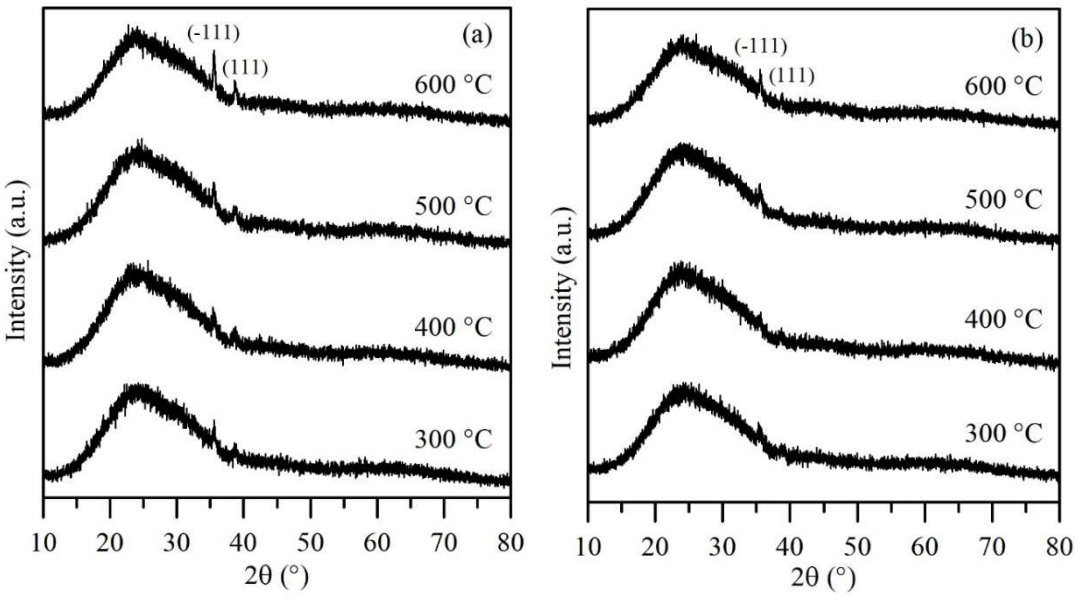

Figure 2.3 XRD patterns of deposited films after annealing under air with the temperature range 300 – 600 °C and using (a) ethanol or (b) methanol as solvent. These peaks corresponding to monoclinic CuO, JCPDS No: 00-002-1040.

The TGA data of Figure 2.1 were used to identify the range of annealing temperatures to be applied between 300 and 600 °C. After the annealing process under an air atmosphere for 1 hour, all the deposited films were identified as crystalline Tenorite copper oxide (CuO, JCPDS No: 00-002-1040) (Figure 2.3) as a result of the decomposition and the oxidation reaction between the deposited material and oxygen in the air. The CuO crystalline phase was observed at temperatures above 300 °C,

while the XRD data indicated that film crystallinity improved with increasing annealing temperatures. In contrast, all the deposited films that were annealed using an argon atmoshere were found to be amorphous.

The crystallite size of the deposited films can be calculated using the Scherrer equation:

$$D = \frac{K\lambda}{B\cos\theta} \quad \textbf{(4)}$$

Where:

D is the crystallite size

K is the shape factor, 0.9 for a unknown shape

λ is the x-ray wavelength

θ is the Bragg diffraction angle

B is the full-width at halt-maximum (FWHM) of the peak corresponding to the crystal structure plane

After the annealing process, the films deposited from both solvents presented similar 2θ positions and crystallite sizes that increased with increasing annealing temperature. In addition, the fims which were deposited using ethanol provided larger crystallites than those using methanol. The comparison of the crystallite size calculated by using the Scherrer equation are shown in Table 2.4.

Table 2.4 Crystallite size of the deposited films prepared using ethanol and methanol as solvent after annealing at various temperatures.

Annealing temperature (°C)	Ethanol Estimated crystallite size (nm) *(hkl)*		Methanol Estimated crystallite size (nm) *(hkl)*	
	(-111)	(111)	(-111)	(111)
300	11	11	11	11
400	21	16	11	10
500	21	26	16	22
600	32	32	21	26

AACVD of $Cu(NO_3)_2{\cdot}3H_2O$

The AACVD technique was also used to deposit copper oxide thin films by using $Cu(NO_3)_2{\cdot}3H_2O$ as a single source precursor. The solvents used to prepare the precursor solutions were the same as those used in the spin coating process, ethanol, methanol and water. The conditions employed for the thin film deposition are shown in Table 2.5.

Table 2.5 Deposition conditions for AACVD of $Cu(NO_3)_2{\cdot}3H_2O$.

Variable	Detail
Substrate	Pilkington SiCO glass, 2.5×15 cm^2
Precursor concentration	0.05 M
Solvent	Ethanol, Methanol, Water
Deposition time	1 hour
Deposition temperature	300 - 600 °C
Deposition atmosphere	Nitrogen
Reactor type	Hot-wall

Crystallinity and morphology

The films deposited between 300 and 600 °C using both ethanol and methanol as the solvent provided similar results and the deposition of shiny, metallic and conductive

copper films. In contrast, the use of aqueous solutions failed to provide any deposited films on the substrate surface. The appearance of the films deposited from both alcohols are displayed in Table 2.6.

Table 2.6 The appearance of the deposited films by AACVD.

Solvent	Deposition temperature (°C)			
	300	**400**	**500**	**600**
Ethanol	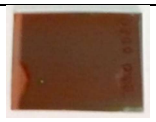			
Methanol		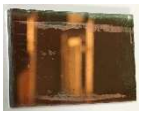		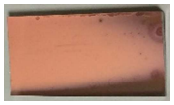

The deposited films were analysed by XRD to identify their crystallographic orientations and the results are shown in Figure 2.4. All of the XRD patterns could be indexed to cubic copper metal (JCPDS No: 01-085-1326) with no impurity phases detected in any samples. The XRD peaks of the films were clearly apparent at temperatures above 300 °C with three 2θ maxima around 43.39°, 50.53° and 74.28° which are associated with the (111), (200) and (220) planes, respectively. The intensity of the peaks also tended to increase when the deposition temperatures were increased.

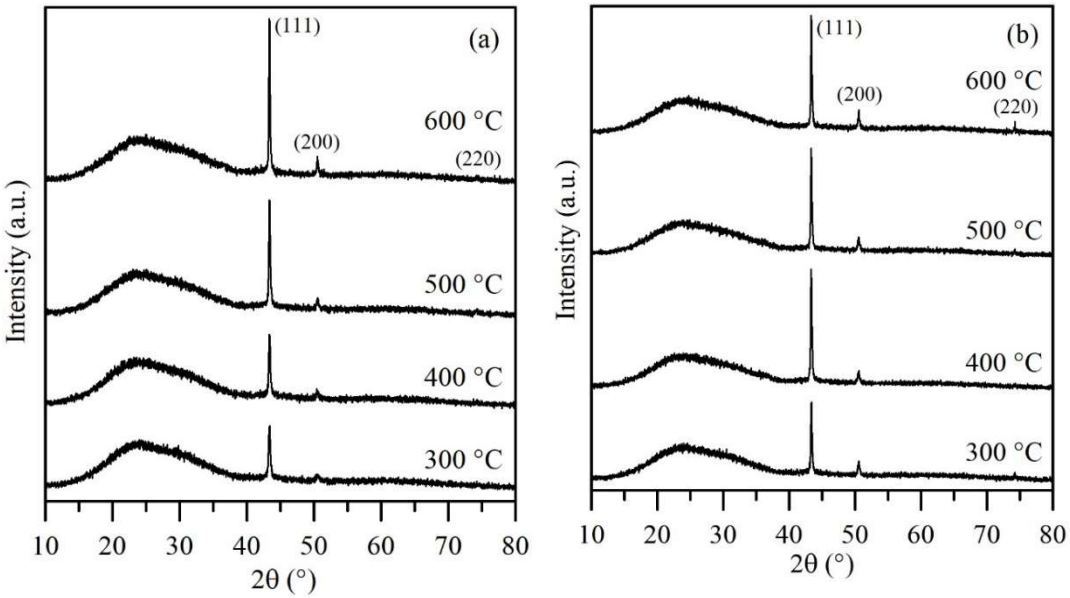

Figure 2.4 XRD patterns of AACVD deposited films from $Cu(NO_3)_2{\cdot}3H_2O$ by using (a) ethanol and (b) methanol as solvent at various deposition temperatures. These peaks corresponding to cubic Cu, JCPDS No: 01-085-1326.

In 2011 Crick et al.[21] described the formation of metallic copper films from copper nitrate and using either methanol or ethanol via AACVD. This report suggested that the copper metal occurred due to the reducing atmosphere from hydrogen generation during the film deposition process. The reducing hydrogen atmosphere can be generated via the decomposition of either methanol or ethanol over the growing copper film.[22] An example of the decomposition of methanol is shown in Scheme 2.1.

$$CH_3OH \leftrightarrow C + H_2 + H_2O \; \Delta H^0_{298} = -42 \; kJ \; mol^{-1}$$

$$CH_3OH \leftrightarrow CO + H_2 \; \Delta H^0_{298} = 49 \; kJ \; mol^{-1}$$

Scheme 2.1 Decomposition of methanol.[22]

The XRD peaks (Figure 2.4) of the films deposited using methanol present a higher intensity than the films from ethanol solution. It is suggested that methanol provides more efficient generation of the reducing hydrogen as its breakdown has been shown to be more efficient than that of ethanol.[23] In addition, the increasing deposition temperature can provide more activation energy to the deposition system, resulting in the generation of a more reducing atmosphere during the film deposition and providing a greater resultant intensity of the XRD peaks.

The Scherrer equation was used to further analyse the crystallinity of the deposited films and demonstrated that the crystallite sizes tended to increase with increasing deposition temperature. At deposition temperatures below 600 °C, the films fabricated from methanol typically provided larger crystallites than films prepared using ethanol. At 600 °C, however, the crystallites were similar, irrespective of solvent (Table 2.7).

Table 2.7 Crystallite sizes of the AACVD deposited films fabricated by using ethanol and methanol as solvent.

Deposition temperature (°C)	**Ethanol** Estimated crystallite size (nm) *(hkl)*			**Methanol** Estimated crystallite size (nm) *(hkl)*		
	(111)	(200)	(220)	(111)	(200)	(220)
300	26	16	-	46	30	12
400	31	23	14	45	29	21
500	40	27	12	51	34	17
600	57	34	16	59	34	21

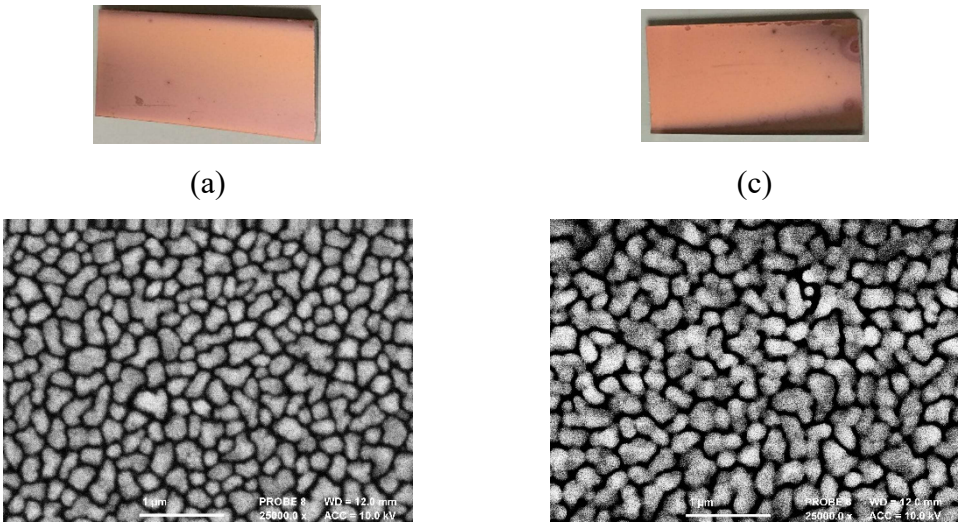

(a) (c)

(b) (d)

Figure 2.5 The appearance of the deposited films with the deposition temperature at 600 °C and their SEM micrographs at 25,000x magnification using ethanol (a/b) and methanol (c/d), respectively.

The morphologies of the deposited films were analysed by Field Emission Scanning Electron Microscope (FESEM). Figure 2.5 shows the visual appearance and the SEM micrographs of the films fabricated at a deposition temperature of 600 °C using ethanol and methanol as solvent. As Figures 2.5 (b) and (d) show the particle sizes on the surface of both films correlate well with the calculated crystallite sizes in Table 2.7.

The XRD results demonstrated that copper oxide thin films cannot be produced using $Cu(NO_3)_2$ as a single source precursor by AACVD. The deposited films were, thus, annealed in air to induce oxidation of the metallic films.

Films prepared from methanol solution at a deposition temperature of 300 °C were selected for annealing because these conditions required the lowest temperature while still providing films of a similar quality and substrate coverage to those deposited at higher deposition temperatures. The annealing process employed and the conditions are summarised in Table 2.8.

Table 2.8 Annealing process conditions to study oxidation of the copper films.

Variable	**Detail**
Annealing temperature	100 - 600 °C
Annealing atmosphere	Air
Annealing time	1 hour

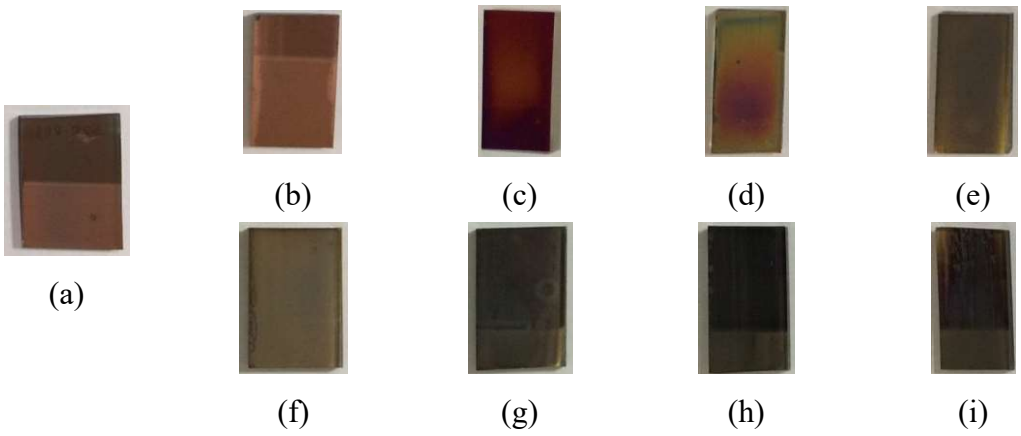

Figure 2.6 The appearance of the films (a) as deposited at 300 °C and after annealing at different temperatures (b) 100°C (c) 150°C (d) 200°C (e) 250°C (f) 300°C (g) 400°C (h) 500°C (i) 600°C.

The appearances of the annealed films are shown in Figure 2.6. The as deposited film possessed a shiny metallic copper colour, whereas the colour was observed to change to a brownish-red after annealing under air at temperatures below 400 °C for 1 hour. In contrast, annealing temperatures above 400 °C induced a colour change to black. In agreement with the literature,[2,8] Cu_2O is brownish-red and CuO is black. Moreover, the presentation of these phases of copper oxide were confirmed by XRD analysis.

These results are shown in Figure 2.7. The annealed films started to display the characteristic peaks of Cu_2O (JCPDS No: 00-005-0667) at annealing temperatures greater that 200 °C. Above 400 °C the predominant peaks indexed to CuO (JCPDS No: 00-041-0254) with no observable evidence of Cu and Cu_2O impurities. Figure 2.8 displays a summary diagram of the transformation of copper described in this section.

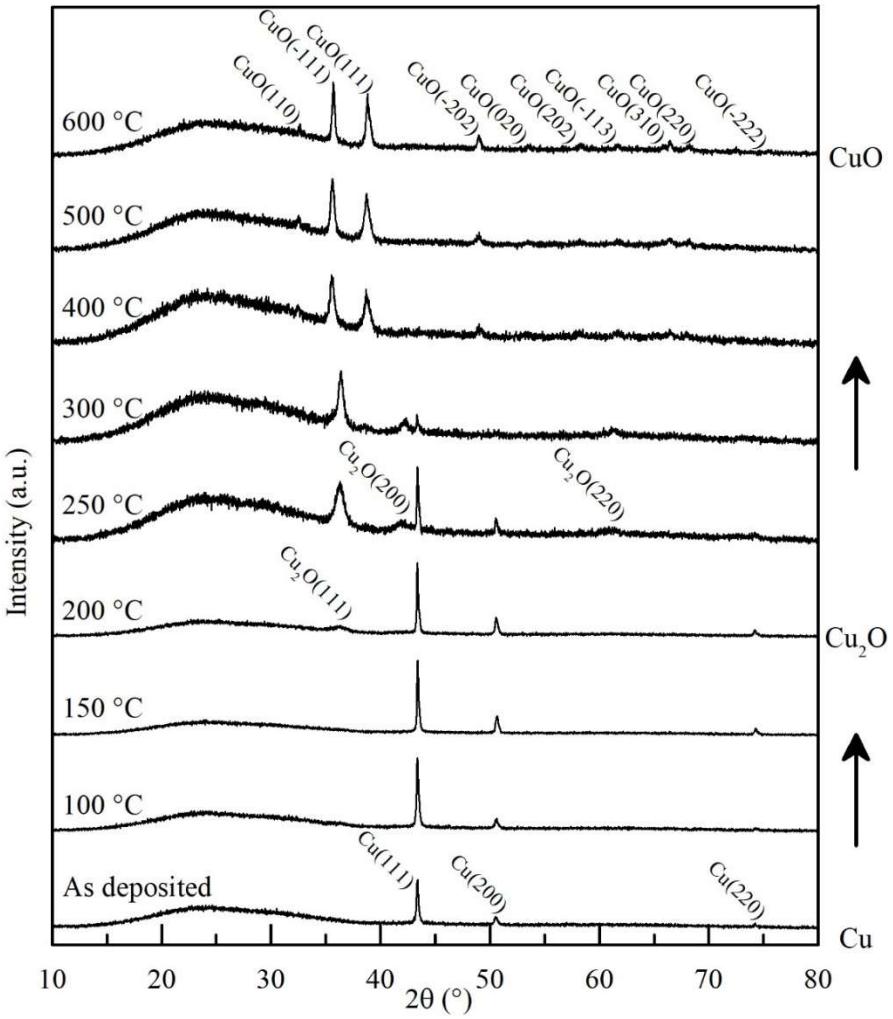

Figure 2.7 XRD patterns of the annealed films at different temperatures under an air atmosphere. Cu_2O (JCPDS No: 00-005-0667), CuO (JCPDS No: 00-041-0254).

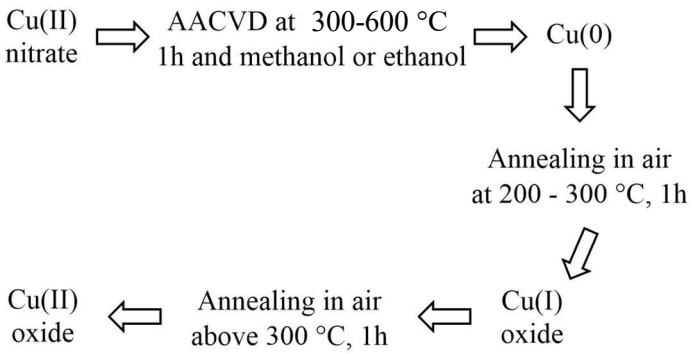

Figure 2.8 Summary of copper/copper oxide transformations described in this section.

Table 2.9 Comparison of the CuO crystallite size of the annealed films at 600 °C, deposited by either spin coating or AACVD.

Deposition technique	**Estimated crystallite size (nm)**	
	(hkl)	
	(-111)	**(111)**
Spin coating	21	26
AACVD	43	43

A comparison of the crystallite size of the CuO films, prepared by both spin-coating and AACVD, is shown in Table 2.9. The AACVD-prepared films typically provided crystallite sizes larger than those deposited by spin coating.

Conclusion

The fabrication of the copper oxide thin films was achieved by using copper(II) nitrate trihydrate ($Cu(NO_3)_2 \cdot 3H_2O$) via AACVD or spin coating and subsequent thermal annealing. The spin coating technique provided amorphous films which transformed to crystalline material after annealing under an air atmosphere. The XRD patterns revealed that the CuO phase started to appear at an annealing temperature of 300°C.

AACVD provided shiny metallic copper films which were transformed to copper oxide by annealing under an air atmosphere. Furthermore, the annealing temperature could be used to control the oxidation state of the deposited films. At annealing temperatures below 300 °C Cu_2O films were deposited, whilst above 300 °C CuO was

produced. The combination of the AACVD technique and annealing provided CuO crystallite sizes larger than the use of the spin coating technique and annealing

2.1.2 Nickel oxide thin film deposition

Introduction

Two nickel oxides are known, the poorly characterised black nickel(III) oxide (Ni_2O_3) and the much more common green nickel(II) oxide (NiO).

Due to nickel vacancies in its lattice structure, NiO typically displays the properties of a *p*-type oxide.[24] In addition, NiO is a transparent semiconductor material which possesses a wide band gap of around 3.6 - 4.0 eV.[25–28] Furthermore, NiO is known to display a variety of other interesting properties such as antiferromagneism,[29] switching phenomena,[30–32] chemical stability,[33] high electrochromic efficiency,[34] high chemical resistance and stability,[35,33] excellent durability,[33] large natural abundance[36] and resultant low cost in production.[36]

These attractive features of NiO hold the potential to impact significantly on a number of technological developments such as for TCO materials and use as a transparent layer in solar cell applications,[37–39] light emitting diodes,[40] ultraviolet detectors,[41] electrochromic devices,[42,43] photodetectors and transparent display,[44] resistive switching random access memory (RRAM),[45] smart windows[34,46–48] and biosensors.[49] For these reasons, nickel oxide is a worthwhile candidate material for further to study and development, particularly with regard to the production and development of thin films.

Nickel oxide thin films have been fabricated by various deposition methods. For example, thermal evaporation has been used to create NiO thin films for large area production.[37] Many techniques have also targeted improvements in the thin film quality by trying to increase the crystallinity of the films, for example, by using increased oxygen partial pressures during pulsed laser deposition,[24] and increases in annealing times during spray pyrolysis.[50] Table 2.10 presents some examples of NiO thin films which have been prepared by various methods, along with a selection of properties and their applications.

Jlassi et al.[51] in 2014 found that when the thickness of the deposited films was increased by increasing deposition time, the resistivity of film also increased while the optical band gaps were decreased. Moreover, limited reports of NiO films prepared by

the aerosol-assisted chemical vapour deposition (AACVD) have been described in which the E_g of the films decreased as the particle size of the films was increased with the increasing deposition temperature.[33] Jlassi et al.,[52] have also deposited nickel oxide films by using sol-gel spin coating. In this case, the as deposited films were amorphous but could be transformed to polycrystalline material post annealing at temperatures above 300 °C under air.

Table 2.10 Examples of nickel oxide thin films (NiO) deposited by various techniques and some of their properties.

Deposition techniques	Substrates	Band gap (eV)	Notes	Properties	Applications
Thermal evaporation[37]	Glass OHP acetate plastic Sapphire	3.5 3.5 4.2	• Large area deposition • Low cost • Simple process	• *p*-type material[34] • Bandgap 3.6-4.0 eV[25–28] • Transparent[44] • Antiferromagnetic[29] • Chemical stability[33] • Switching phenomena[30–32] • High electrochromic efficiency[34] • High chemical resistance[35] • Environment-friendly[36] • Low cost[36] • Large natural abundance[36] • Excellent durability[33]	• *p*-type transparent conducting layer[25] • Electrochromic devices[43] • Gas sensors[53] • Metal-oxide-semiconductor (MOS) devices[54] • Alkaline batteries[55] • Photocatalysts[56] • Smart windows[34,46–48] • Biosensor[49] • Solar cells[38,39] • Resistive switching random access memory (RRAM),[45]
Pulsed laser deposited[24]	Al_2O_3 (0001)	~3.6	Increasing O_2 partial pressure leads to improve crystalline quality.		
Spray deposition[51]	Glass	3.7-3.55	Increasing thickness affect to increase resistivity but to decrease Eg		
AACVD with ultrasonic humidifier[33]	FTO	3.65	Particle size increased with increased deposition temperature.		
Spray pyrolysis[50]	Glass	3.35, 3.43, 3.48, 3.51	Transparency, smoothness and crystallinity increased at increase annealing times.		
Sol-gel spin coating[52]	Glass	3.52, 3.49	The transmittance of film decreased with increasing thickness.		
Atomic layer deposition[28]	Si(100)	3.8	Reflective index of film decrease as annealing temperature increase.		
Solution growth[46]	Glass	3.6	Absorption coefficient increases with annealing temperature.		

Film characterisation: Nickel oxide thin films

Thermogravimetric analysis of Nickel(II) nitrate hexahydrate

Nickel nitrate, $Ni(NO_3)_2 \cdot 6H_2O$, was used to prepare the simple precursor solutions for nickel oxide thin film fabrication in this section. The thermal behavior of $Ni(NO_3)_2 \cdot 6H_2O$ was investigated by TGA and the results are shown in Figure 2.9.

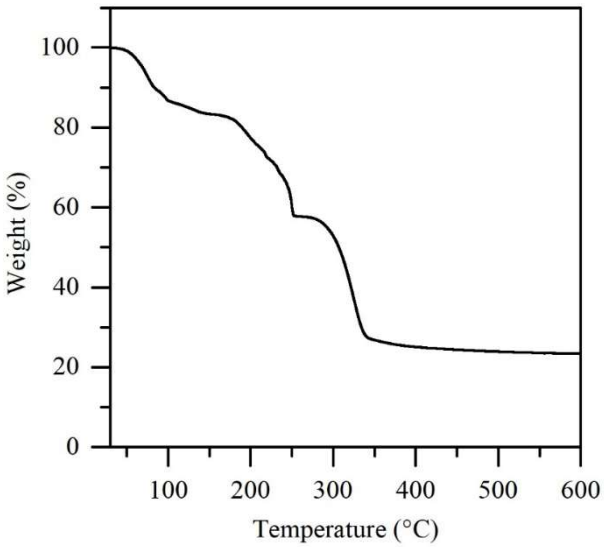

Figure 2.9 TGA curve of $Ni(NO_3)_2 \cdot 6H_2O$.

Thermal decomposition of $Ni(NO_3)_2 \cdot 6H_2O$ comprises two main steps. Initial loss of water and partial decomposition of the nitrate occurs in the temperature range 40 - 252 °C. This process accounts for a weight loss of around 42 %. The results at this stage are consistent with the formation of a complex, which further decomposes to form Ni_2O_3 through release of HNO_3. In a final step, Ni_2O_3 is decomposed to NiO at temperature above 375 °C.

Spin coating of the $Ni(NO_3)_2 \cdot 6H_2O$

Nickel oxide thin films were fabricated by using a spin coating technique and a subsequent annealing process. The precursors were prepared with $Ni(NO_3)_2 \cdot 6H_2O$ and the solvents employed were ethanol, methanol and water. The deposition conditions are summarised in Table 2.11.

Table 2.11 Deposition conditions for spin coating of $Ni(NO_3)_2 \cdot 6H_2O$.

Variable	Detail
Substrate	Pilkington SiCO glass, 2.5×2.5 cm^2
Precursor concentration	0.05 M
Solvent	Ethanol, Methanol, Water
Deposition layer	5 layers
Annealing atmosphere	Air, Argon
Annealing time	1 hour
Annealing temperature	300 - 600 °C

Crystallinity

Thin films were successfully deposited using ethanol and methanol, which provided good coverage of the substrate surface, whereas no films could be deposited from aqueous solution. This phenomenon can be assumed to be a result of the differing the surface tension properties of the solvents. The surface tension of water is around 3.2 times higher than the surface tension of both ethanol and methanol (Table 2.12), with the result that it is more difficult to spread over the substrate surface.

Table 2.12 Surface tension of the solvent.[57]

Solvent	Surface tension ($mN \cdot m^{-1}$) at 25 °C
Methanol	22.51
Ethanol	22.82
Water	72.01

Although all of the as-deposited films were amorphous, after annealing under air they were found to be crystalline nickel oxide (Figure 2.10). The films deposited using ethanol as solvent, provided XRD patterns, which could be indexed to cubic nickel oxide (NiO, JCPDS No: 00-004-0835) and which started to appear at an annealing temperature of 400 °C. In contrast, the films which were prepared using methanol only presented a crystalline nickel oxide phase at the higher temperature of 600°C. All the films that were annealed under an argon atmosphere were amorphous. Table 2.13 shows the crystallite size of the films after annealing at a temperature 600 °C. The

films which were prepared using ethanol as solvent possessed a typical crystallite size which was twice that of films which were prepared using methanol.

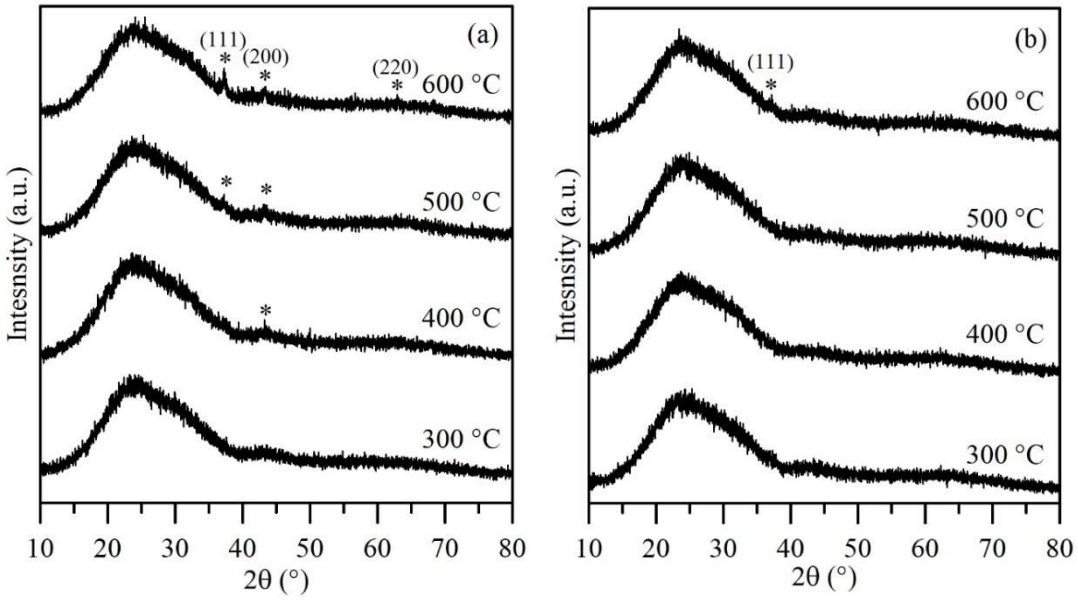

Figure 2.10 X-ray diffraction patterns for the annealed films prepared using (a) ethanol (b) methanol. These corresponding to cubic nickel oxide (NiO, JCPDS No: 00-004-0835).

Table 2.13 Crystallite size of the deposited films prepared using ethanol and methanol as solvent after annealing.

Annealing temperature (°C)	**Ethanol** Estimated crystallite size (nm) *(hkl)*			**Methanol** Estimated crystallite size (nm) *(hkl)*		
	(111)	(200)	(220)	(111)	(200)	(220)
300	-	-	-	-	-	-
400	-	7	-	-	-	-
500	19	8	-	-	-	-
600	24	20	7	11	-	-

AACVD of $Ni(NO_3)_2 \cdot 6H_2O$

Deposition of $Ni(NO_3)_2 \cdot 6H_2O$

The deposition of nickel(II) nitrate was investigated using the AACVD technique following the deposition conditions shown in Table 2.14. The deposited films were analysed by XRD to determine their crystallographic orientation (Figure 2.11)

Table 2.14 Deposition condition for AACVD of $Ni(NO_3)_2 \cdot 6H_2O$.

Variable	Detail
Substrate	Pilkington SiCO glass, 2.5×15 cm^2
Precursor concentration	0.05 M
Solvent	Ethanol, Methanol, Water
Deposition time	1 hour
Deposition temperature	300 - 600 °C
Deposition atmosphere	Nitrogen
Reactor type	Hot-wall

Crystallinity and appearance of as deposited films

The XRD patterns in 2.10 (a) and (b) index to hexagonal nickel metal with the strongest diffraction maximum at 2θ around 44.5° arising from the (011) orientation plane (JCPDS No: 00-045-1027). The films deposited using ethanol generally provided evidence of crystallinity at a lower deposition temperature than those using methanol as solvent. The XRD patterns of none of the deposited films, however, displayed peaks which could be indexed to nickel oxide.

The origin of the phenomenon of metallic nickel formation is suggested to be similar to that described for the formation of copper metal in the copper oxide thin film deposition section; i.e. the hydrogen atmosphere produced by pyrolysis of the alcohol solvent during the deposition process is sufficiently reducing to effect the reduction of Ni(II) provided by the nitrate precursor to nickel metal.

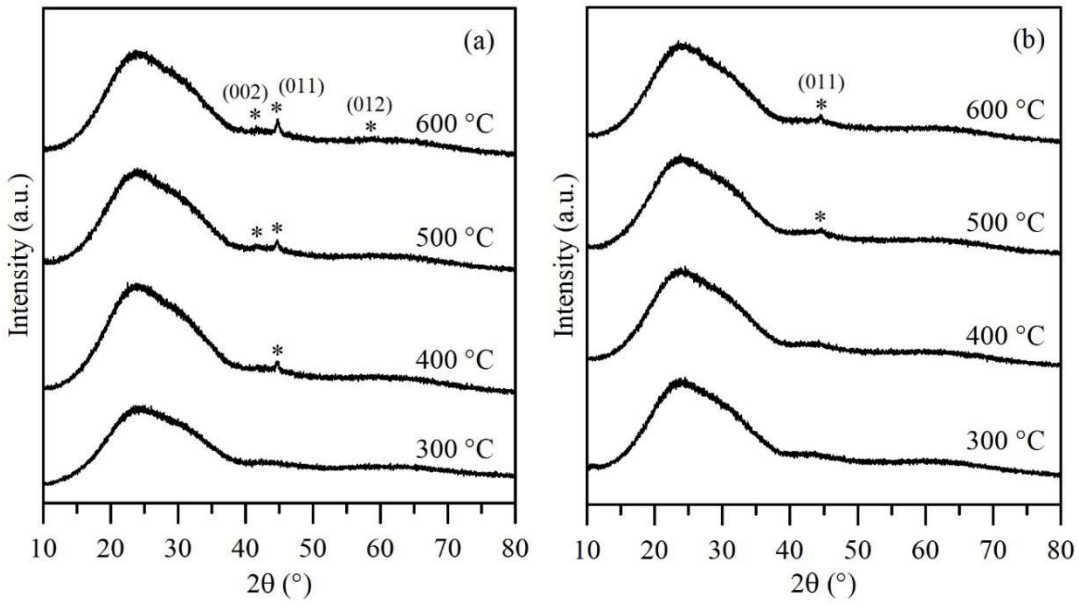

Figure 2.11 XRD patterns of films deposited from $Ni(NO_3)_2 \cdot 6H_2O$ using (a) ethanol and (b) methanol as solvent at various deposition temperatures. These peaks corresponding to hexagonal nickel metal (JCPDS No: 00-045-1027).

Figure 2.12 presents the appearance of the metallic nickel films that were deposited at 600 °C using (a) ethanol and (b) methanol as solvent. Both films were similarly shiny and metallic and conductive.

(a) (b)

Figure 2.12 The appearance of the films which were deposited at 600 °C by using (a) ethanol (b) methanol as solvent.

At this point the use of increased precursor concentrations were considered along with an assessment of Marks' combustion processing technique as a means to allow the direct AACVD of nickel oxide and with the further objective of reducing the deposition temperature. Ammonium nitrate (NH_4NO_3) and urea (CH_4N_2O) were, thus, selected for study in order to provide the combustion energy for the deposition system. Furthermore, the cold-wall reactor was considered more compatible with this process to prevent the early evaporation of the aerosol droplets containing the precursor chemicals prior to its interaction with the substrate surface.

AACVD of nickel oxide film via combustion processing

The deposition conditions are summarised in Table 2.15, while the TGA curve shown in Figure 2.13 highlights the effects on the thermal decomposition of precursor systems in which either ammonium nitrate (NH_4NO_3) or urea (CH_4N_2O) are combined with $Ni(NO_3)_2(H_2O)_6$.

Table 2.15 Deposition conditions for nickel oxide thin film fabrication.

Variable	Detail		
Substrate	Pilkington SiCO glass, 2.5×15 cm^2		
Solvent	Ethanol		
Deposition time	1 hour		
Deposition temperature	225 - 400 °C		
Deposition atmosphere	Nitrogen		
Reactor type	Cold-wall		
Precursor solutions			
Precursor system	$Ni(NO_3)_2{\cdot}6H_2O$	Urea	Ammonium nitrate
N1	0.1 M	-	-
N2	0.1 M	0.1 M	-
N3	0.1 M	-	0.1 M

Thermal decomposition analysis of the precursors

On the basis of the TGA results, N2 and N3 appeared to be the most promising precursor recipes for the low-temperature nickel oxide film deposition, N2 was prepared from the mixed of nickel nitrate and urea, N3 was prepared from the mixed of nickel nitrate and ammonium nitrate and N1 was prepared from only nickel nitrate. The expected and calculated residual weight for NiO from the N1, N2 and N3 precursor systems are shown in Table 2.16. In both the TGA curves of N2 and N3, two weight losses were detected. The first event between 30 °C and 280 °C corresponds to ~ 51-54% weight loss. This initial mass loss is proposed to arise by virtue of water loss and the release of HNO_3. The second mass losses, between 280 °C and 325 °C (~78.75% weight loss) for N2 and approximately 340 °C (~80% weight

loss) for N3, respectively, are attributed to the decomposition of the residual nitrate into NiO. Inspection of these TGA curves confirms that the mixing of an additional combustion chemical can indeed provide nickel oxide at a lower temperature than the nickel nitrate precursor alone.

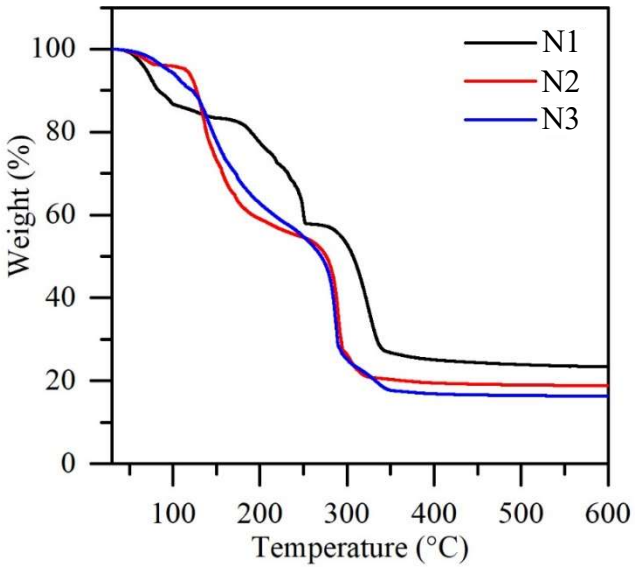

Figure 2.13 TGA curve of N1 N2 and N3.

Table 2.16 The residual weight (%) from TGA curves and calculated weight for NiO from the N1, N2 and N3 precursor systems.

Precursor system	*T* (°C)	Residual weight (%) expected to NiO	
		Experiment	Calculation
N1	~ 375	25.71	25.69
N2	~ 325	20.90	21.29
N3	~ 340	18.18	20.14

All the deposited films in this section were fabricated by following the deposition conditions in Table 2.15 and the characterisation of all films is presented in the next section.

Crystallinity and morphological analysis

The X-ray diffraction results in Figure 2.14 demonstrate the crystalline composition of the thin films deposited by all three precursor solutions. According to the XRD patterns, three precursors provided nickel oxide films by AACVD in one step without

any need for further annealing. The appearances of the deposited films from all precursor mixtures are shown in Table 2.18.

The N3 precursor system allows the deposition of phase-pure nickel oxide at deposition temperatures of 250-325 °C, lower than those provided by the other precursors. The N2 system provided higher deposition temperatures of 300-350 °C to form pure oxide film whilst N1 can be used to deposit a nickel oxide thin film at only 325 °C. It is suggested that the N3 precursor system, with a higher proportion of nitrate, has the potential to provide significantly greater combustion energy to the deposition system and to provide additional oxidizing species to form the oxide at lower temperatures.

When the deposition temperature was increased, however, the nickel metal phase was also observed for all three precursor recipes. Use of the N1 and N3 precursor systems provided a nickel metal phase at the same deposition temperature of 350 °C, whereas the N2 system yielded a nickel phase at the higher deposition temperature of 375 °C.

At a deposition temperature of 325 °C, all three precursor systems deposited films which analysed as nickel oxide as the only crystalline phase. Table 2.17 shows a comparison of their crystallite sizes. The film deposited from the N3 precursor system gave crystallites of approximately 61.11 nm (111), which were larger than both the N1 and N2 systems, 26.32 nm and 27.17nm, respectively.

Table 2.17 Comparison of NiO crystallite size of films fabricated at 325 °C from the N1, N2 and N3 precursor systems.

Precursor system	**Estimated crystallite size (nm) *(hkl)***	
	(111)	**(200)**
N1	26	11
N2	27	17
N3	61	45

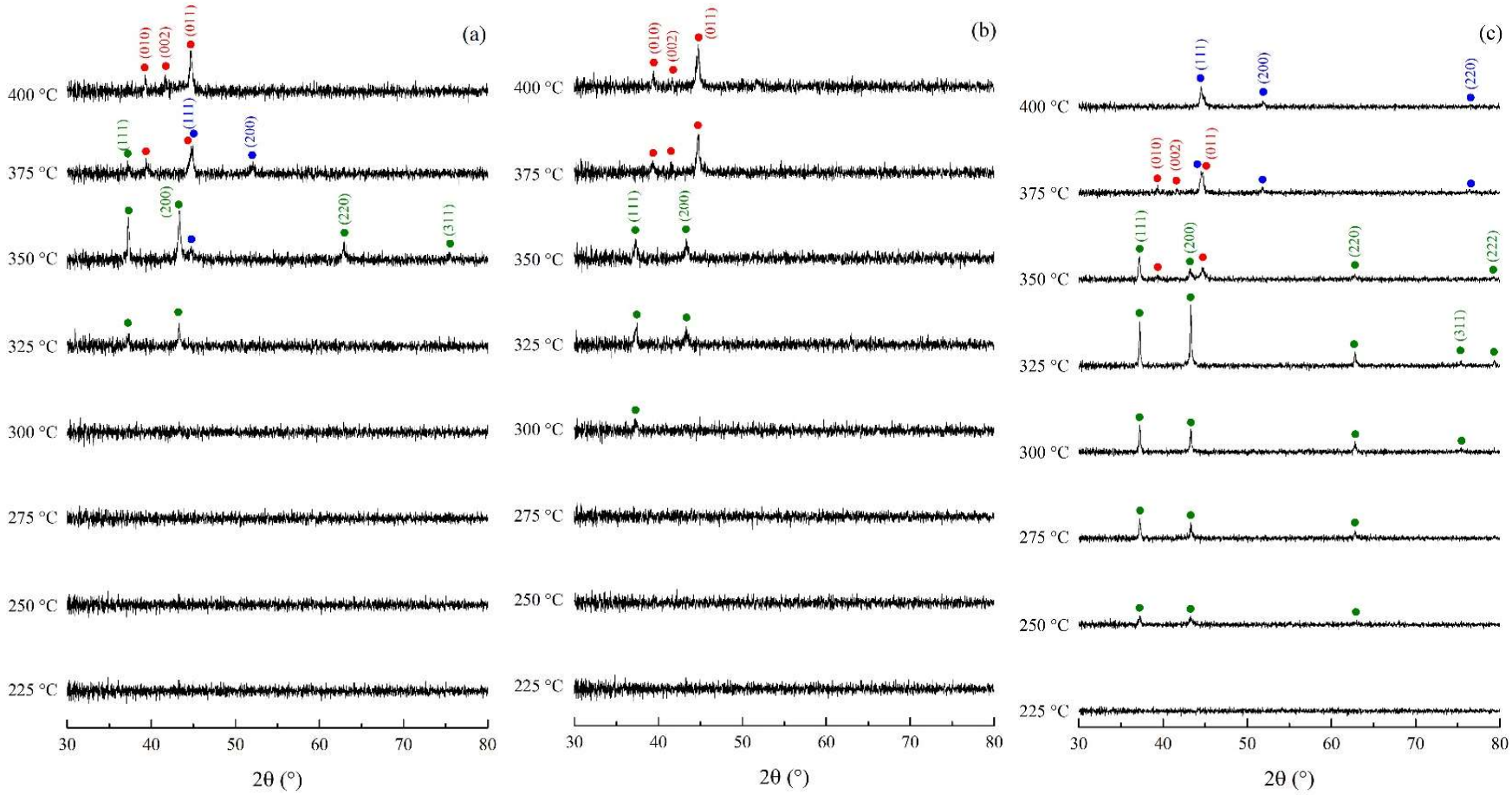

Figure 2.14 XRD patterns of AACVD deposited films from the precursor systems (a) N1 (b) N2 and (c) N3 at various deposition temperatures. Red circles refer to hexagonal nickel (JCPDS No: 00-045-1027), blue circles refer to cubic nickel (JCPDS No: 01-070-1849) and green circles refer to cubic nickel oxide (JCPDS No: 01-078-0423).

Table 2.18 The appearance of the films deposited from the N1, N2 and N3 precursor systems at deposition temperatures between 225 and 400 °C.

Precursor system	Deposition temperature (°C)							
	225	**250**	**275**	**300**	**325**	**350**	**375**	**400**
N1	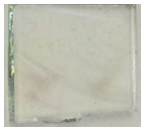							
	Amorphous	Amorphous	Amorphous	Amorphous	NiO	NiO+Ni	NiO+Ni	Ni
N2							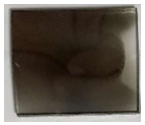	
	Amorphous	Amorphous	Amorphous	NiO	NiO	NiO	Ni	Ni
N3					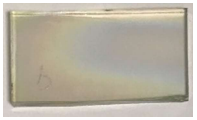	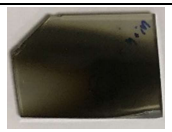		
	Amorphous	NiO	NiO	NiO	NiO	NiO+Ni	Ni	Ni

Atomic force microscopy (AFM) was performed to determine the surface appearance and roughness of the films. The surface morphologies of the nickel oxide films deposited from all three precursor systems at the same deposition temperature at 325 °C are presented in Figure 2.15. The N1 and N2 systems provided a similar surface morphology for the nickel oxide films and crystallite sizes that agreed with those calculated in Table 2.17, whilst the film from the N3 system comprised more densely packed smaller particles.

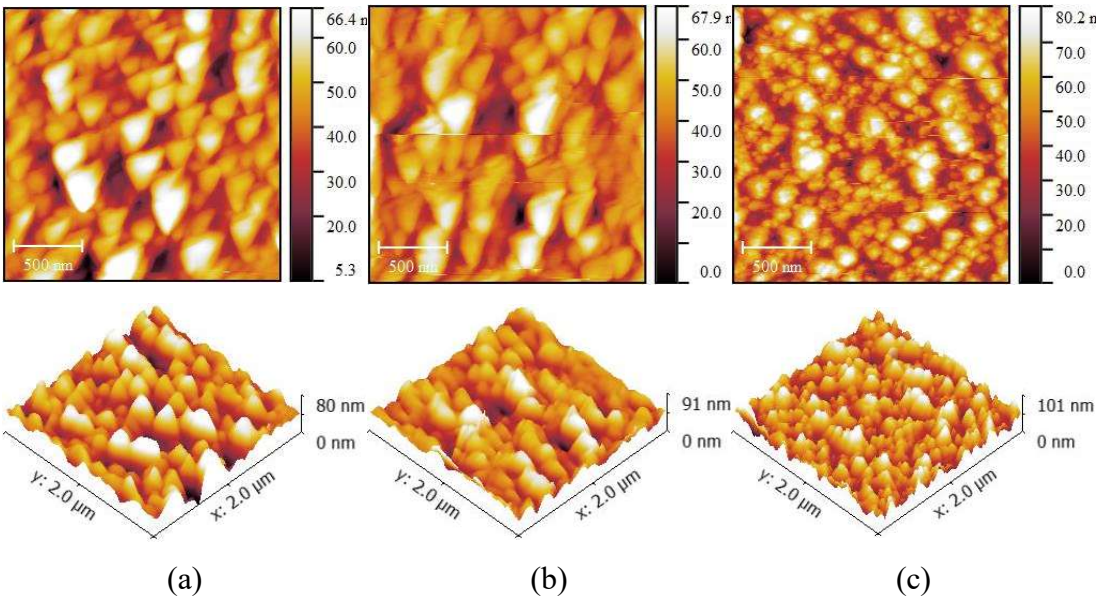

(a) (b) (c)

Figure 2.15 Surface morphologies of the nickel oxide films at a deposition temperature at 325 °C from the (a) NT (b) N2 and (c) N3 precursor systems and analysed by AFM.

The surface roughness of the deposited films was measured over an area of 100 μm^2. The roughness values are shown in Figure 2.16. The N2 precursor provided the lowest RMS roughness value, whereas the N1 precursor gave the highest value. Interestingly, all of the deposited films gave roughness values that increased with the rising deposition temperature. This could be due to the increase in crystallite size, as a result of rising thermal energy as the temperature increases. The roughness values, however, were seen to decline at deposition temperatures over 375 °C when the metallic nickel phase was also observed to emerge.

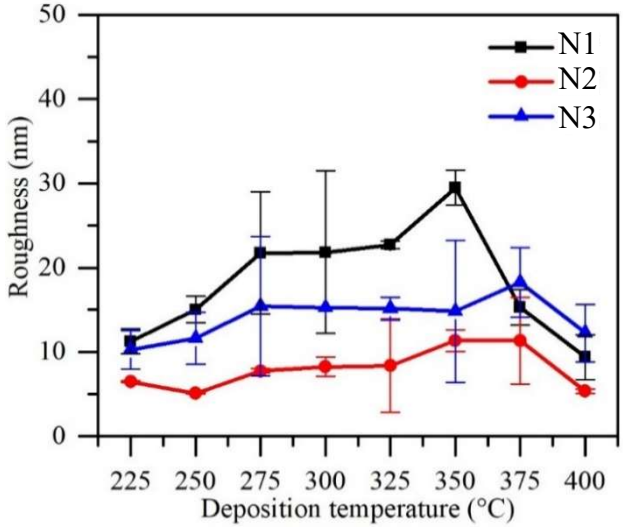

Figure 2.16 AFM surface roughness of the deposited films from the N1, N2 and N3 precursor systems. Area measurement size 100 μm^2.

Optical properties

The optical properties of the deposited films from the N1, N2 and N3 precursors were analysed by UV/Vis spectroscopy and the results of the % transmittance are shown in Figure 2.17. All three precursor systems provided deposited films which presented similar trends across the % transmittance, such that increasing deposition temperatures provided decreasing % transmittance. Moreover, upon the appearance of the nickel metal phase (Figure 2.14), the % transmittance dropped significant to below 60% for the NT precursor and below 20% for both the N2 and N1 precursor systems. The % transmittance for the nickel oxide films deposited at 325 °C from all three precursors are shown in Figure 2.17 (d) and reveal that the films display the transmittance over 60 % with the greatest transparency displayed by films deposited from the N1 precursor system.

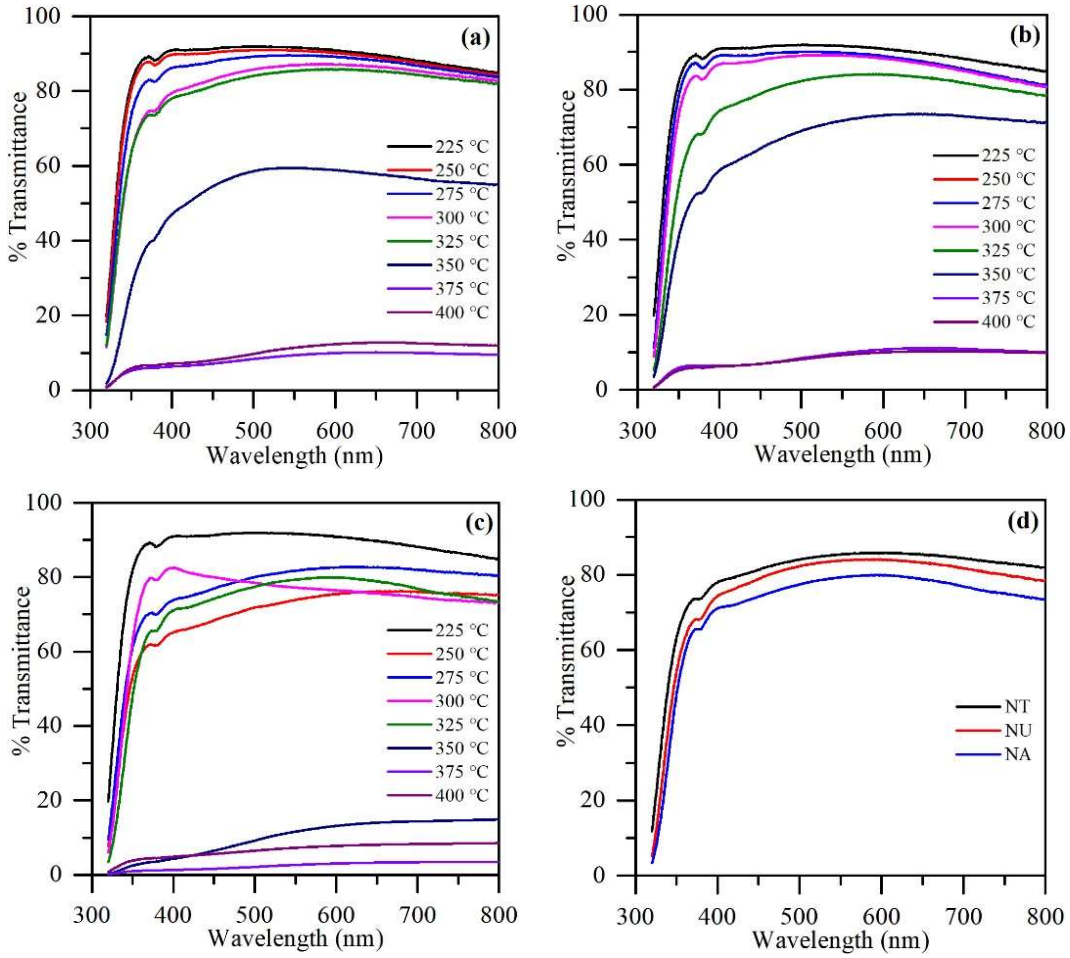

Figure 2.17 Transmittance spectra of the deposited films from the (a) N1 (b) N2 and (c) N3 precursor systems with deposition temperatures between 225 and 400 °C. (d) The deposited films at 325 °C from the N1, N2 and N3 precursor systems.

Deposition of the N3 precursor system

As it provided the lowest deposition temperatures to grow nickel oxide films, the N3 precursor route was investigated in more detail. Moreover, this precursor was also investigated for nickel oxide film deposition on fluorine-doped tin oxide (FTO) substrates employing the deposition conditions summarised in Table 2.19.

Table 2.19 Deposition conditions for nickel oxide thin film fabrication from the N3 precursor system on FTO glass.

Variable	Detail	
Substrate	FTO glass, 2.5×15 cm^2	
Solvent	Ethanol	
Deposition time	1 hour	
Deposition temperature	275 - 400 °C	
Deposition atmosphere	Nitrogen	
Reactor type	Cold-wall	
Precursor solutions in 100 ml		
Precursor code name	$Ni(NO_3)_2{\cdot}6H_2O$	Ammonium nitrate
N3	0.1 M	0.1 M

Crystallinity

Figure 2.18 displays the XRD patterns of the films deposited from the N3 precursor system on Pilkington SiCO glass (Figure 2.18 (a)) and FTO glass substrates (Figure 2.18 (b)). Deposition on these latter substrates is advantageous for a variety of technologies, including electronic and photovoltaic devices.

Nickel oxide can be deposited on the FTO-coated glass by AACVD with the N3 precursor system and the deposition conditions in Table 2.19. The NiO films on the FTO substrate require higher deposition temperatures (300 - 350 °C) than those on Pilkington SiCO glass substrates, (250 - 350 °C). Interestingly, deposition at a temperature of 400 °C on the FTO glass also provided notable XRD peaks which indexed to Ni_3Sn_2 and NiF_2. It is proposed that this is due to surface reduction at this high temperature by the ethanol of the precursor solution at the FTO surface. Experiments to assess the behaviour of the FTO substrate under ethanol AACVD conditions are presented in Chapter 3.

Table 2.20 shows the calculated crystallite size of the deposited films on the Pilkington glass and FTO glass substrates. The data in Table 2.20 illustrate that the same deposition temperature provides NiO crystallites on the FTO substrate that are larger than on the Pilkington glass, due to the differing substrate surfaces. NiO, however,

may be successfully deposited on the FTO substrates at higher deposition temperatures than on Pilkington glass substrates.

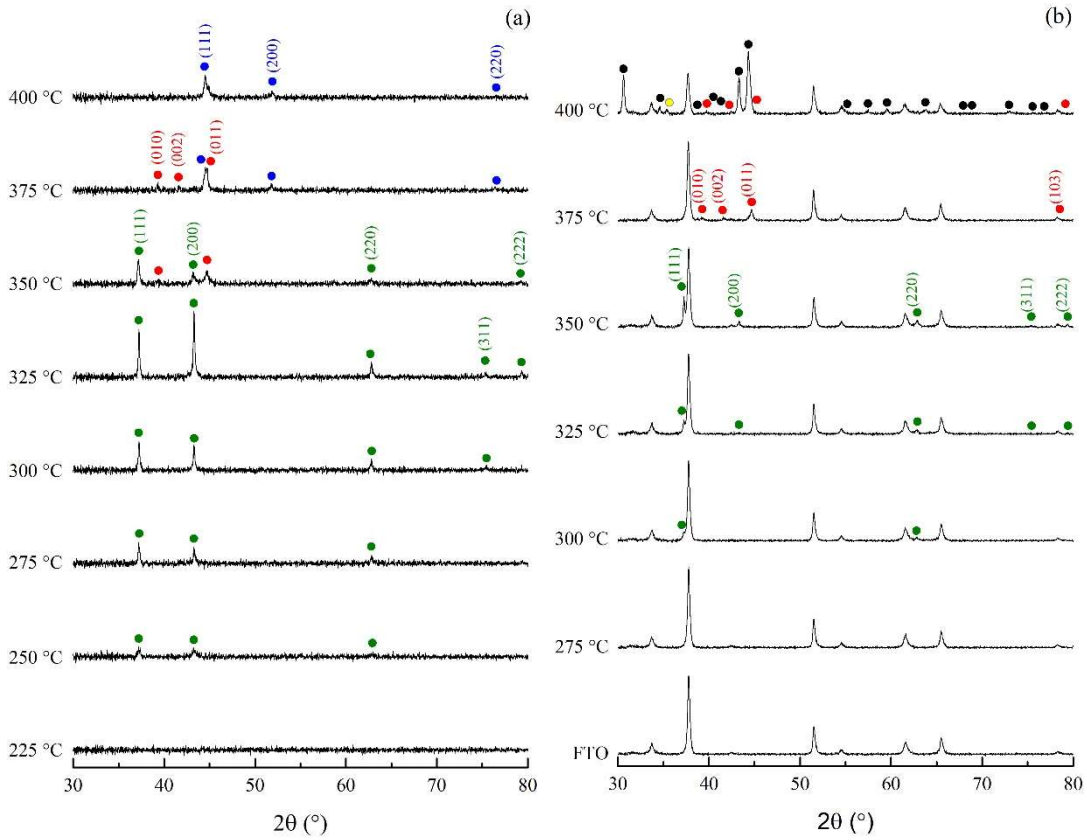

Figure 2.18 XRD patterns of films deposited using the N3 precursor system on (a) Pilkington SiCO glass and (b) FTO glass substrates. Green dots indicate cubic NiO (JCPDS No: 01-078-0423), blue dots indicate cubic Ni (JCPDS No: 01-070-1849), red dots indicate hexagonal nickel (JCPDS No: 00-045-1027), black dots indicate orthorombic Ni_3Sn_2 (JCPDS No: 00-006-0414) and yellow dots indicate orthorhombic NiF_2 (JCPDS No: 00-022-0749).

Table 2.20 Crystallite size of the deposited films on the Pilkington glass and FTO glass substrate.

Deposition temperature (°C)	Pilkington SiCO glass					FTO glass				
	Phase	**Crystal system**	***(hkl)***	**2θ (°)**	**Estimated crystallite size (nm)**	**Phase**	**Crystal system**	***(hkl)***	**2θ (°)**	**Estimated crystallite size (nm)**
225	Amorphous	-	-	-	-	-	-	-	-	-
250	NiO	Cubic	(111) (200) (220)	37.29 43.28 62.66	22 16 6	-	-	-	-	-
275	NiO	Cubic	(111) (200) (220)	37.26 43.37 62.81	33 22 10	Amorphous	-	-	-	-
300	NiO	Cubic	(111) (200) (220) (311)	37.21 43.28 62.84 75.31	54 39 37 5	NiO	Cubic	(111) (220)	37.20 62.83	66 73
325	NiO	Cubic	(111) (200) (220) (311) (222)	37.22 43.27 62.79 75.35 79.35	61 45 50 6 53	NiO	Cubic	(111) (200) (220) (311) (222)	37.24 43.43 62.82 75.23 79.30	66 27 49 26 33
350	NiO	Cubic	(111) (200) (220) (222)	37.15 43.21 62.71 79.24	38 21 37 12	NiO	Cubic	(111) (200) (220) (311)	37.25 43.31 62.88 75.31	66 54 40 65

Deposition temperature (°C)	Pilkington SiCO glass					FTO glass				
	Phase	**Crystal system**	***(hkl)***	**2θ (°)**	**Estimated crystallite size (nm)**	**Phase**	**Crystal system**	***(hkl)***	**2θ (°)**	**Estimated crystallite size (nm)**
	Ni	Hexagonal	(010)	39.19	11			(222)	79.38	66
			(011)	44.69	17					
375	Ni	Hexagonal	(010)	39.13	11	Ni	Hexagonal	(010)	39.31	26
			(002)	41.70	11			(002)	41.61	44
			(011)	44.71	70			(011)	44.71	54
		Cubic	(111)	44.60	11			(103)	78.19	40
			(200)	51.84	12					
			(220)	76.34	11					
400	Ni	Cubic	(111)	44.59	17	Ni	Hexagonal	(010)	38.83	66
			(200)	51.82	12			(002)	41.33	33
			(220)	76.29	11			(011)	44.71	54
								(103)	78.23	53

Surface and cross section morphology

Table 2.21 The surface morphology of the deposited films from the N3 precursor system at different deposition temperature using AFM on various substrate surfaces.

Pilkington SiCO glass

Deposition temperature (°C)	2D	3D
225	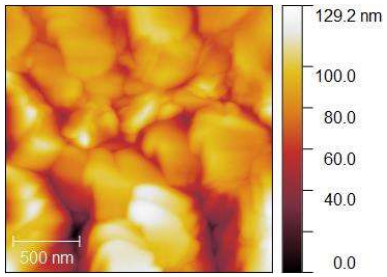	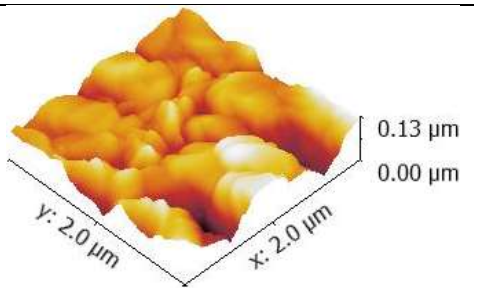
250	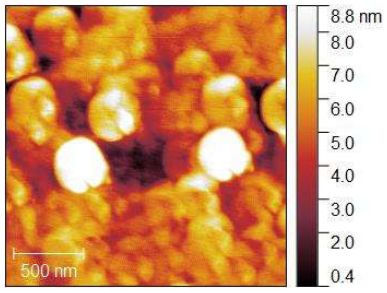	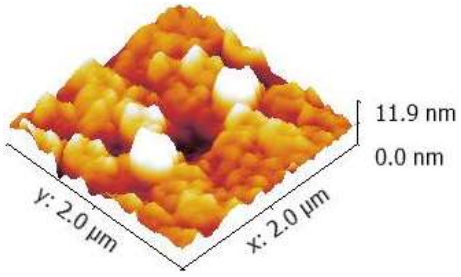
275	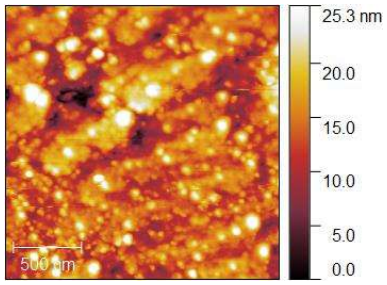	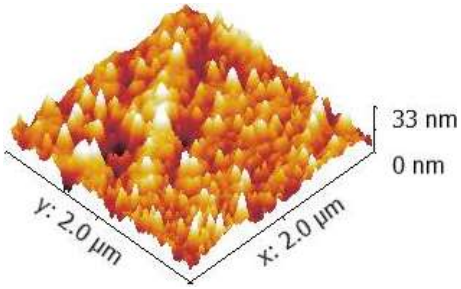
300	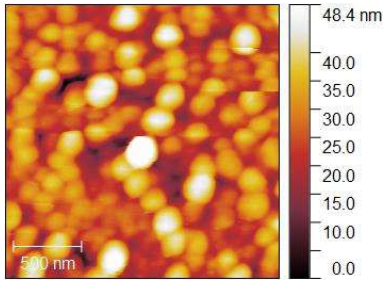	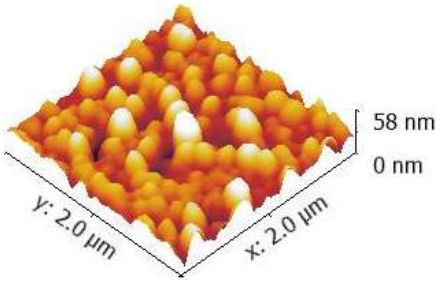

Pilkington SiCO glass

Deposition temperature (°C)	2D	3D
325	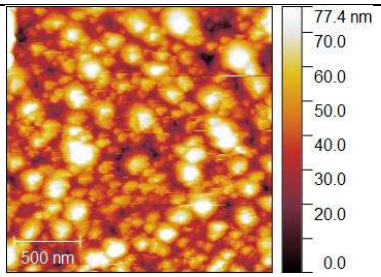	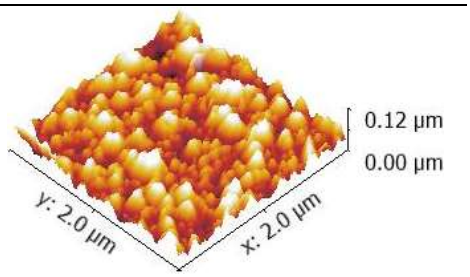
350	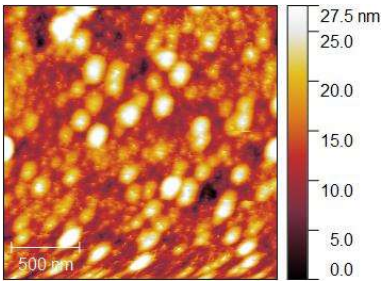	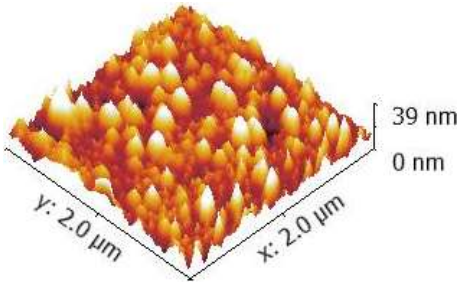
375	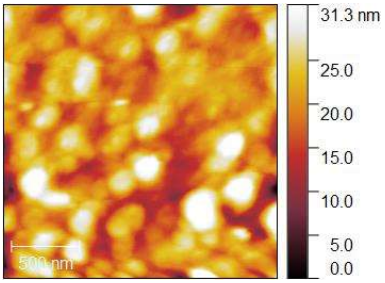	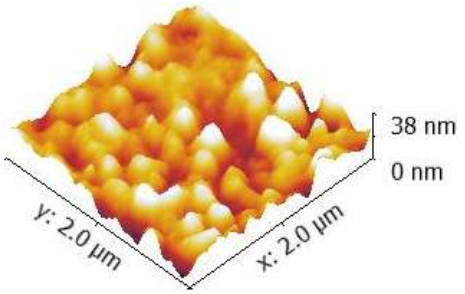
400	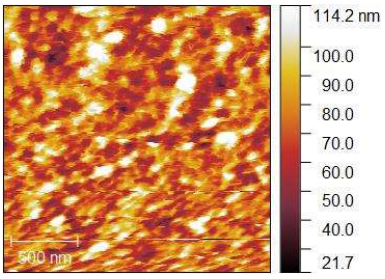	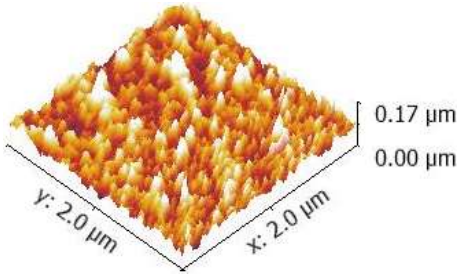

FTO glass

Deposition temperature (°c)	2D	3D
275	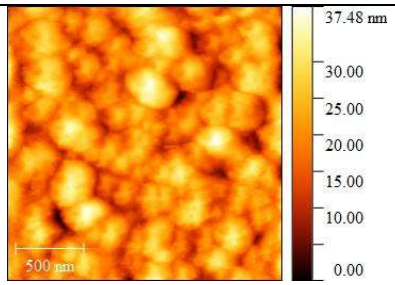	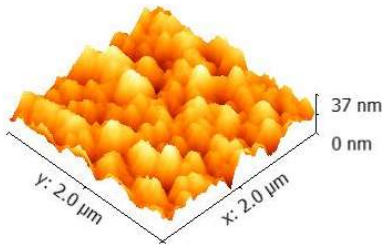
300	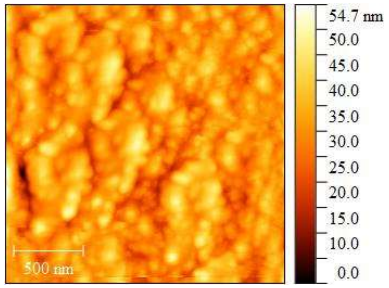	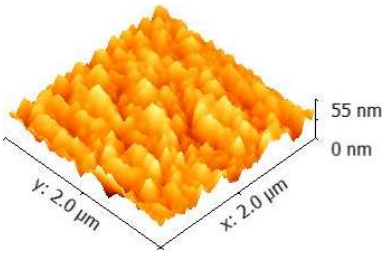
325	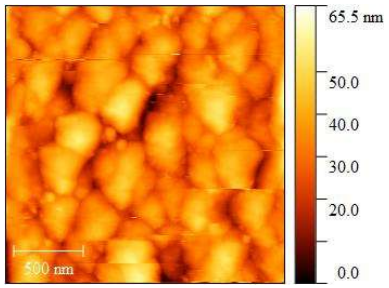	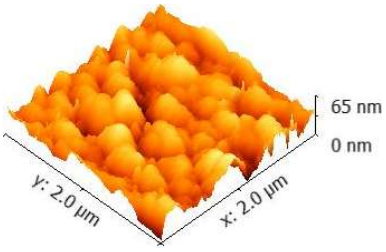
350	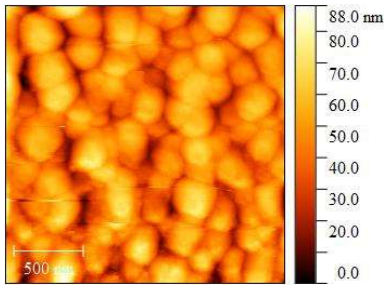	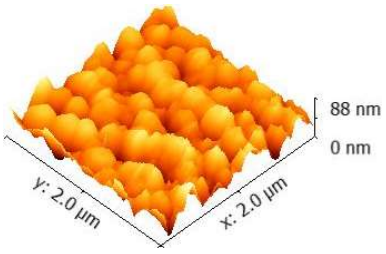
375	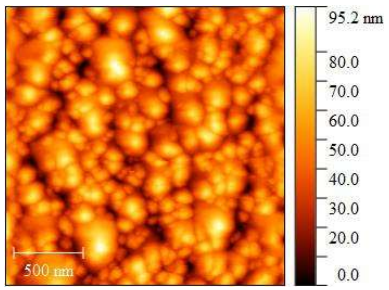	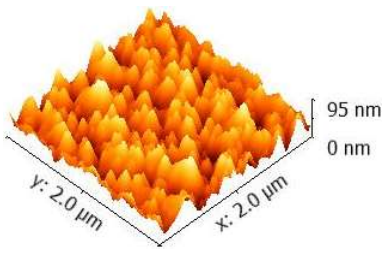

FTO glass

Deposition temperature (°c)	2D	3D
400	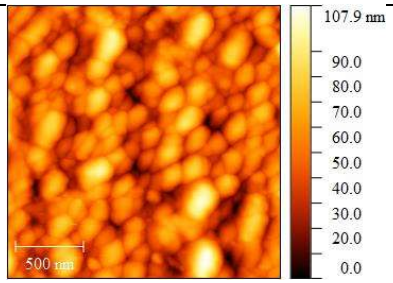	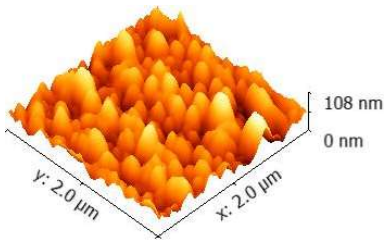

The AFM images in Table 2.21 illustrate the surface morphology of films deposited by using the N3 precursor system at various deposition temperatures on the Pilkington and FTO substrates. As can be seen, crystallites on the substrate surface at lower deposition temperatures are larger than at high deposition temperatures. Increasing deposition temperatures provided decreasing particle size and lead to the formation of agglomerations of rounded small particles (Figure 2.20). As a result, the roughness of the deposited films also increased with increasing deposition temperature.

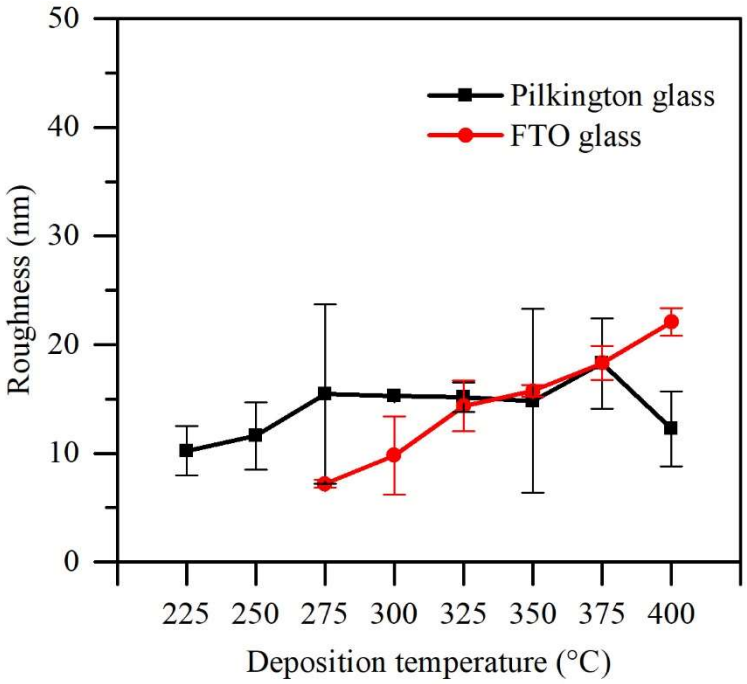

Figure 2.19 AFM surface roughness of the films deposited from the N3 precursor system on Pilkington and FTO glass. Area measurement size 100 μm^2.

Figure 2.19 illustrates a similar trend in roughness on both substrates associated with the increasing deposition temperature. At the deposition temperatures which provided the pure NiO phase (Pilkington glass: 250-325 °C, FTO: 300-350 °C), the oxide films on FTO substrate possessed a lower roughness than on the Pilkington SiCO substrate.

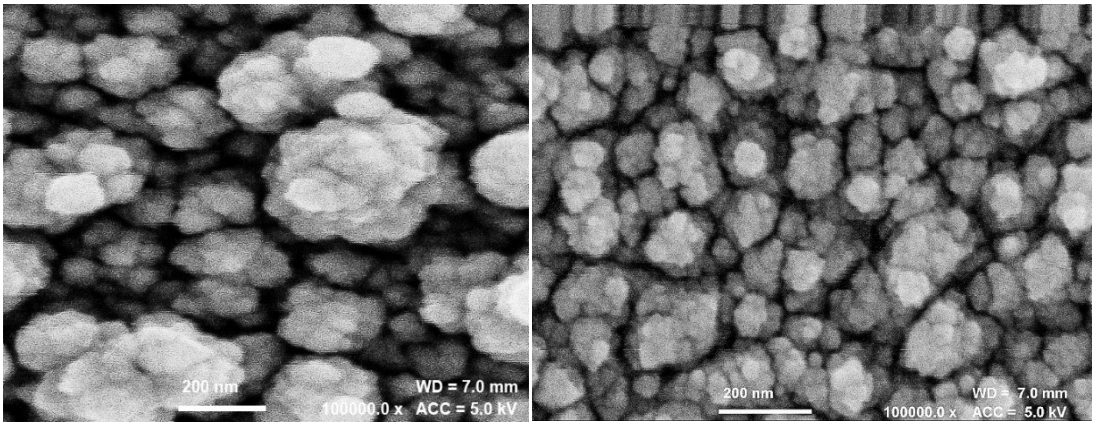

(a) (b)

Figure 2.20 Comparable agglomeration of particles. SEM micrographs at 100,000x magnification of the films deposited at 325 °C (a) on Pilkington SiCO glass (b) FTO-coated glass.

Figures 2.21 and 2.22 show SEM micrographs of films deposited on Pilkington and FTO substrates, respectively. The SEM images show complete coverage over the substrate surface with similar compacted and rounded particles on the substrate surface at deposition temperatures of 300 °C for the Pilkington SiCO substrate and 275 °C for the FTO substrate. The SEM images expose features of the deposited films that are in agreement with the AFM images in Table 2.21.

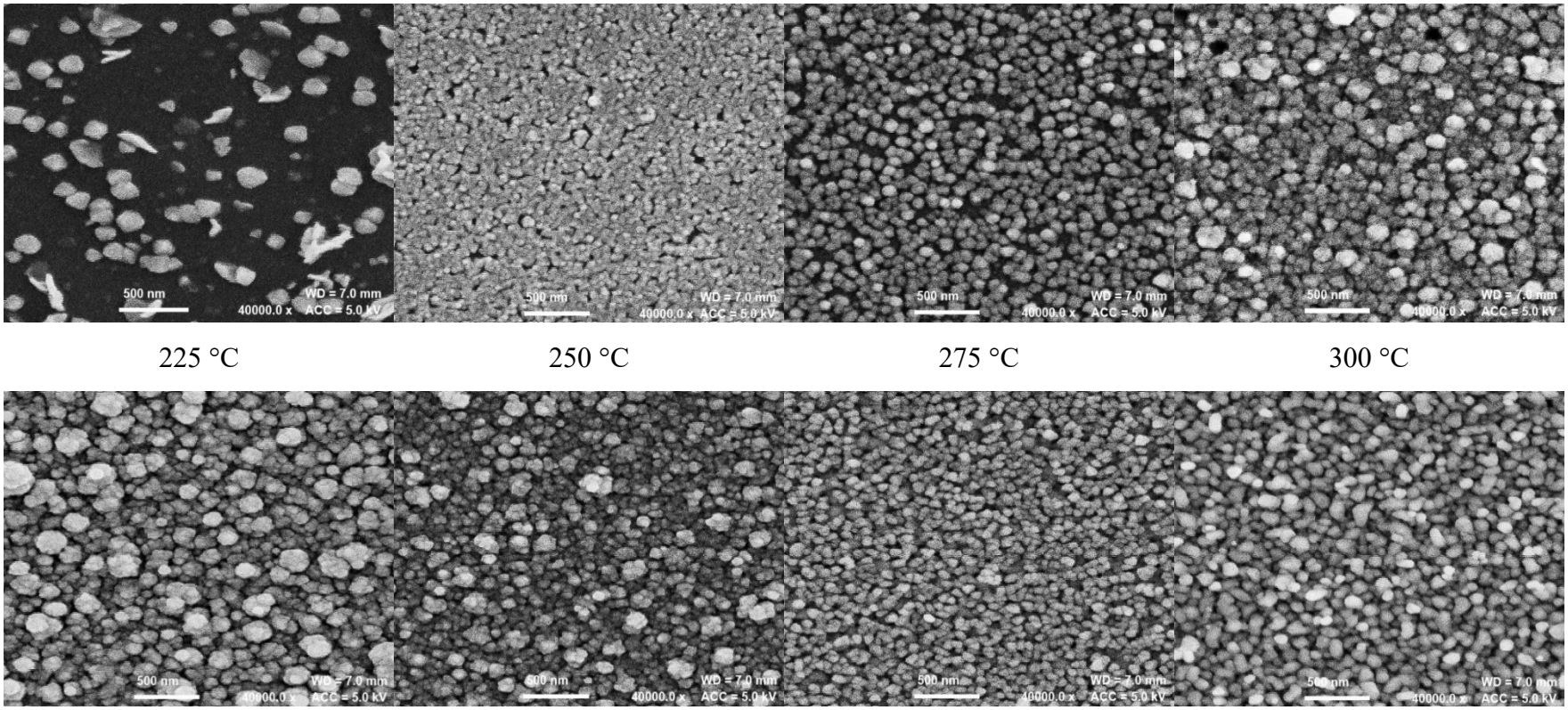

225 °C 250 °C 275 °C 300 °C

325 °C 350 °C 375 °C 400 °C

Figure 2.21 SEM micrographs of the deposited film surface at 40,000x magnification from N3 precursor system at deposition temperature between 225 and 400 °C on Pilkington SiCO glass.

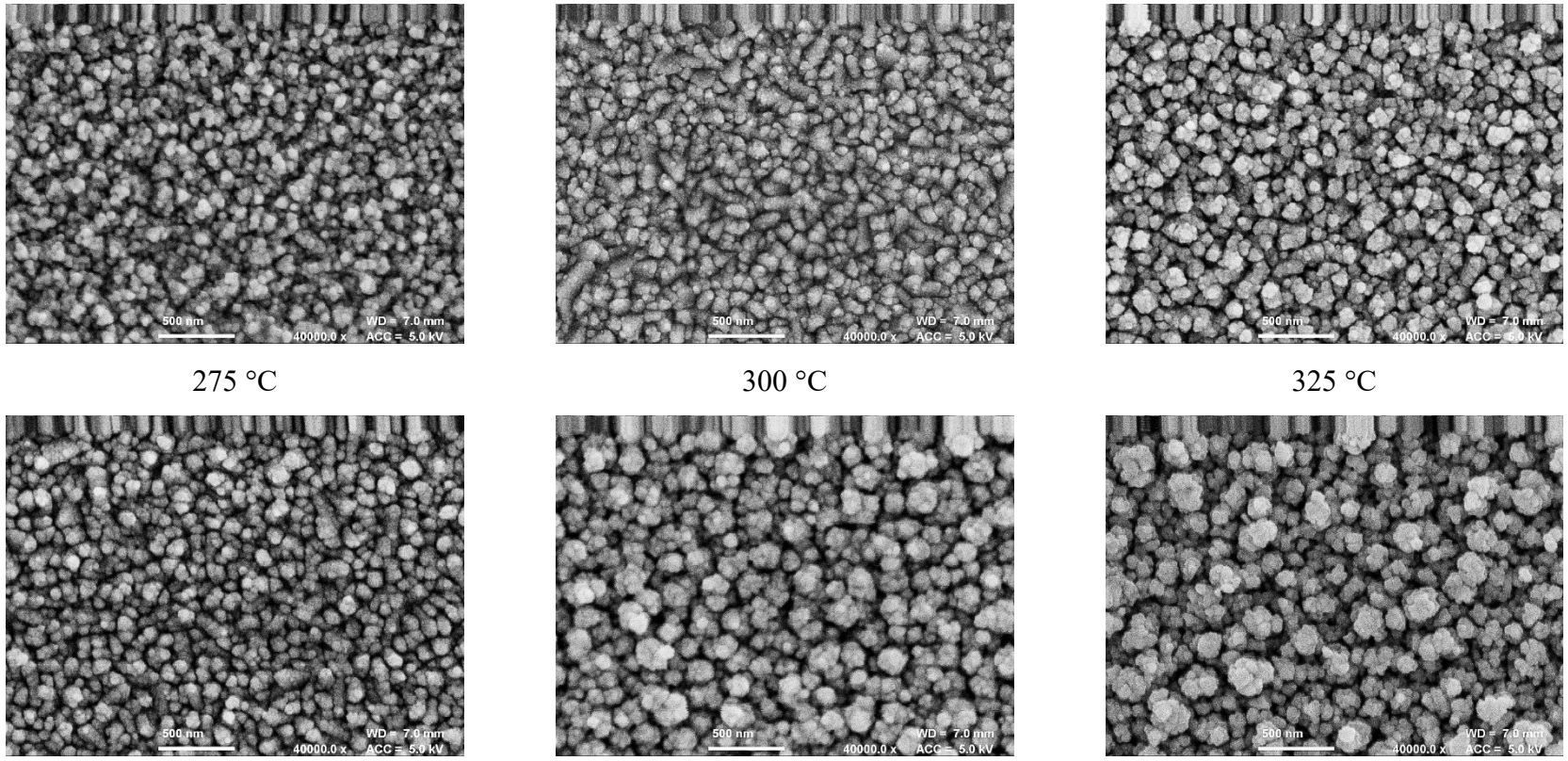

Figure 2.22 SEM micrographs of the deposited film surface at 40,000x magnification from the N3 precursor system at deposition temperatures between 275 and 400 °C on FTO glass.

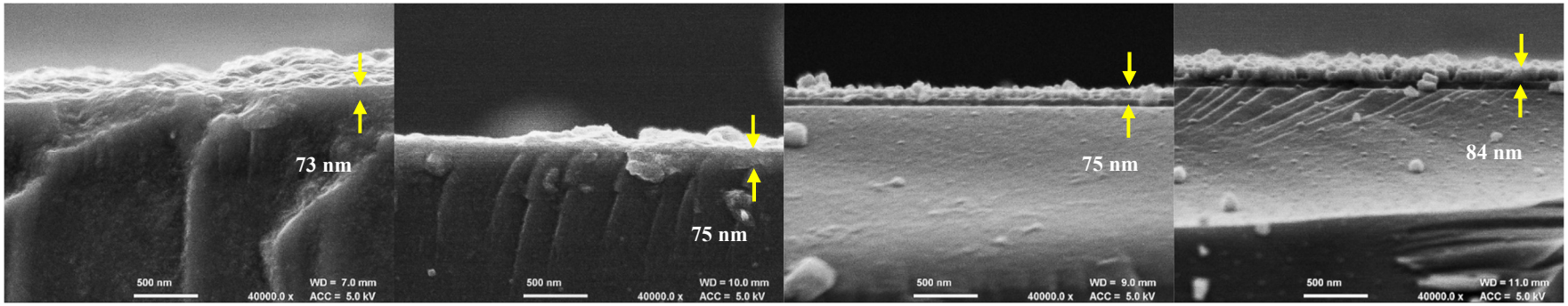

225 °C 250 °C 275 °C 300 °C

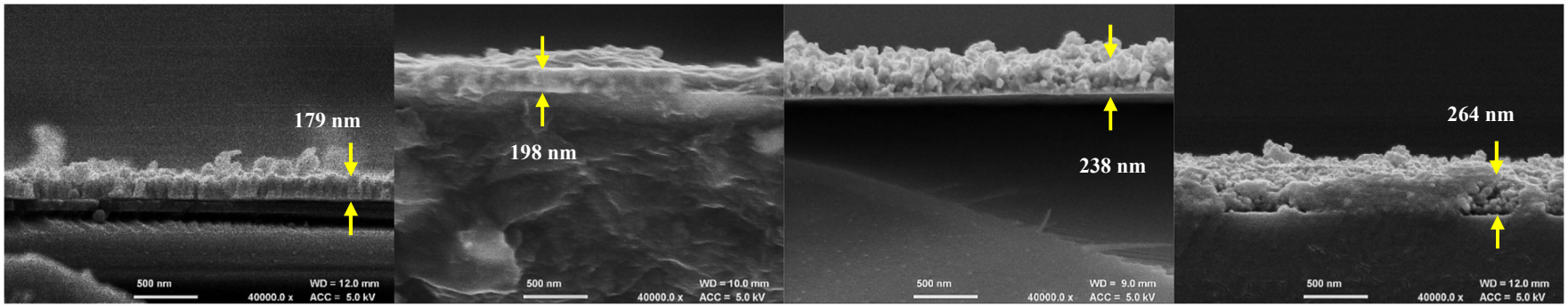

325 °C 350 °C 375 °C 400 °C

Figure 2.23 Cross-section SEM micrographs of the deposited film at 40,000x magnification from the N3 precursor system at deposition temperatures between 225 and 400 °C on Pilkington SiCO glass.

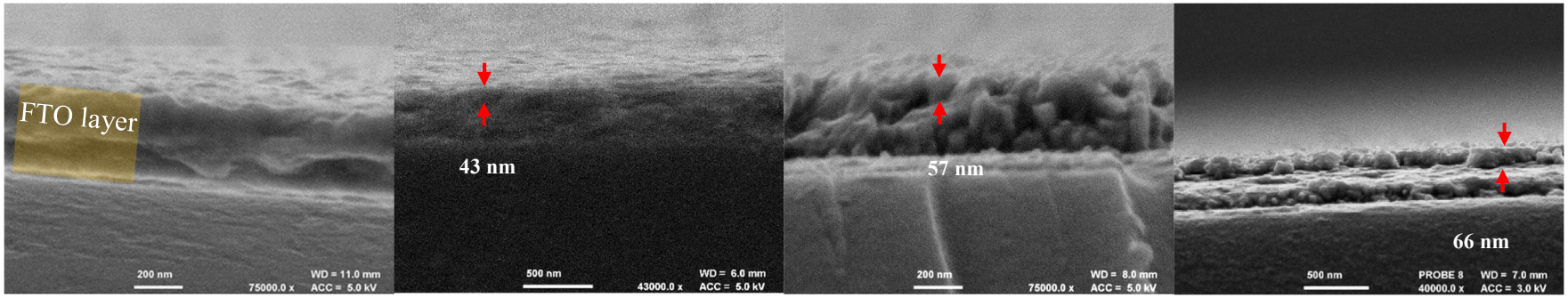

FTO glass substrate before through the deposition process | 275 °C | 300 °C | 325 °C

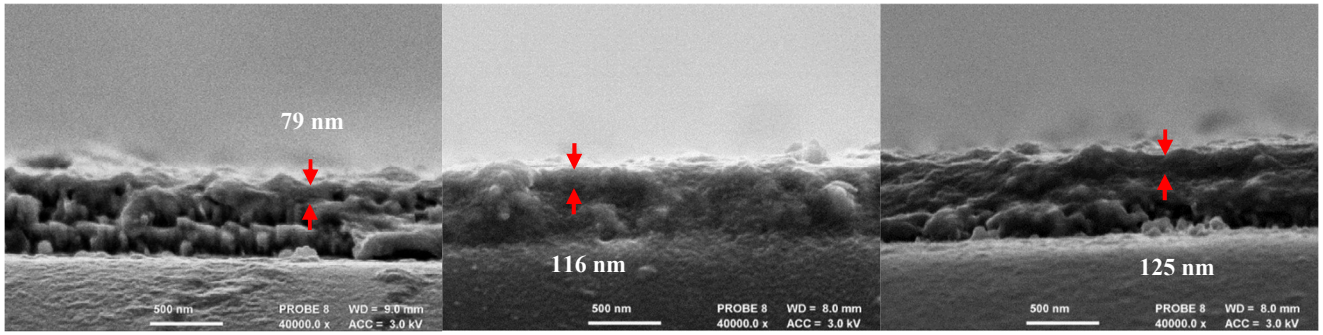

350 °C | 375 °C | 400 °C

Figure 2.24 Cross-section SEM micrographs of the deposited films from the N3 precursor system at deposition temperatures between 275 and 400 °C on FTO glass.

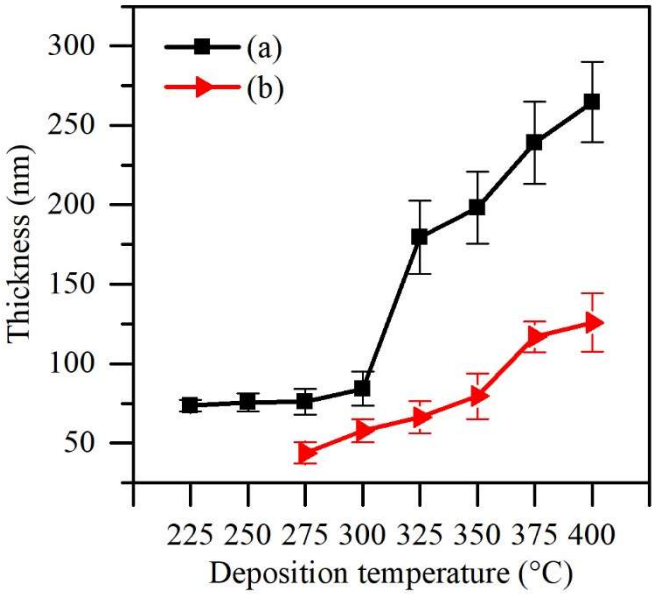

Figure 2.25 The average thickness of films deposited from the N3 precursor system as function of the deposition temperature on (a) Pilkington glass (b) FTO glass.

The thicknesses of the deposited films were determined by using the cross-section of the SEM micrographs. The cross-sectional SEM images in Figure 2.23 and 2.24 demonstrate the compact and continuous nature of the deposited material on the substrate surface.

The deposited pure nickel oxide films on the Pilkington SiCO glass possessed thicknesses between 76 and 180 nm over the temperature range 250 - 325 °C, whilst on the FTO substrate the NiO films displayed thicknesses of 58 - 80 nm over the temperature range 300 - 350 °C.

From the comparison shown in Figure 2.25, it is clear that the thickness of the deposited films increases with increasing deposition temperature. The deposited films on Pilkington glass substrates provided higher thickness and growth rates than the films deposited on the FTO glass substrates over the whole range of deposition temperatures.

Optical properties

The transmission spectra of the films deposited from the N3 precursor system on both Pilkington SiCO glass and FTO glass substrates are shown in Figure 2.26. The deposited films on FTO substrates between 275 °C and 350 °C display transparencies

of 65-85 %, whereas films deposited between 375°C and 400 °C display much lower transparencies of ca.10%. This may be ascribed to the change in composition of the films with changing temperature. Whereas the films prepared at the deposition temperatures between 300 °C and 350 °C contain the transparent NiO phase (Figure 2.18), nickel metal is deposited at deposition temperatures > 375 °C (Figure 2.18) and the % transmittance drops to lower than 10%. A similar observation is made for deposition on Pilkington SiCO glass.

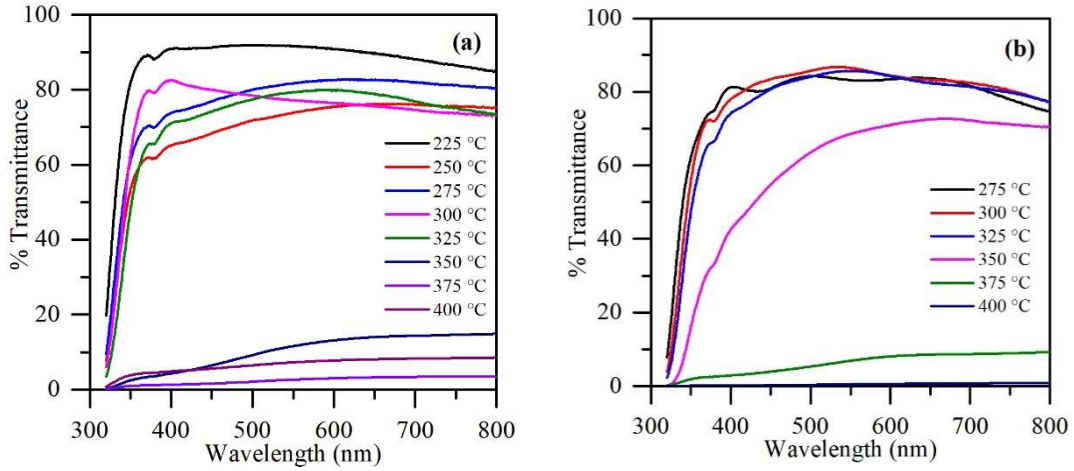

Figure 2.26 Transmittance spectra of the deposited films from the N3 precursor system on (a) Pilkington SiCO glass (b) FTO glass substrate.

Band gap energies (E_g)

Band gap energies of the deposited films were determined from the Tauc plots of the absorption coefficient by using the equation below

$$(\alpha hv)^n = B(hv - E_g) \quad \textbf{(5)}$$

Where:

B is a constant

n is the transition probability, $n = 2$ for direct band gap and

$n = \frac{1}{2}$ for indirect band gap

E_g is the optical band gap

h is the Planck's constant,

The plots of $(\alpha hv)^2$ against hv are shown in Figure 2.27 along with the band gap energies of the deposited films from each deposition temperature on the Pilkington SiCO glass and FTO glass substrates.

The direct band gaps of the deposited films in Figure 2.27 display values between 3.43 - 3.75 eV on the Pilkington substrates and 3.05 - 3.69 eV on the FTO substrates. For the pure NiO phase film, the band gap energy values are 3.69 - 3.73 eV on the Pilkington glass and 3.51 - 3.68 eV on the FTO glass. These values correspond closely to the reported values in the literature for NiO.[25–28]

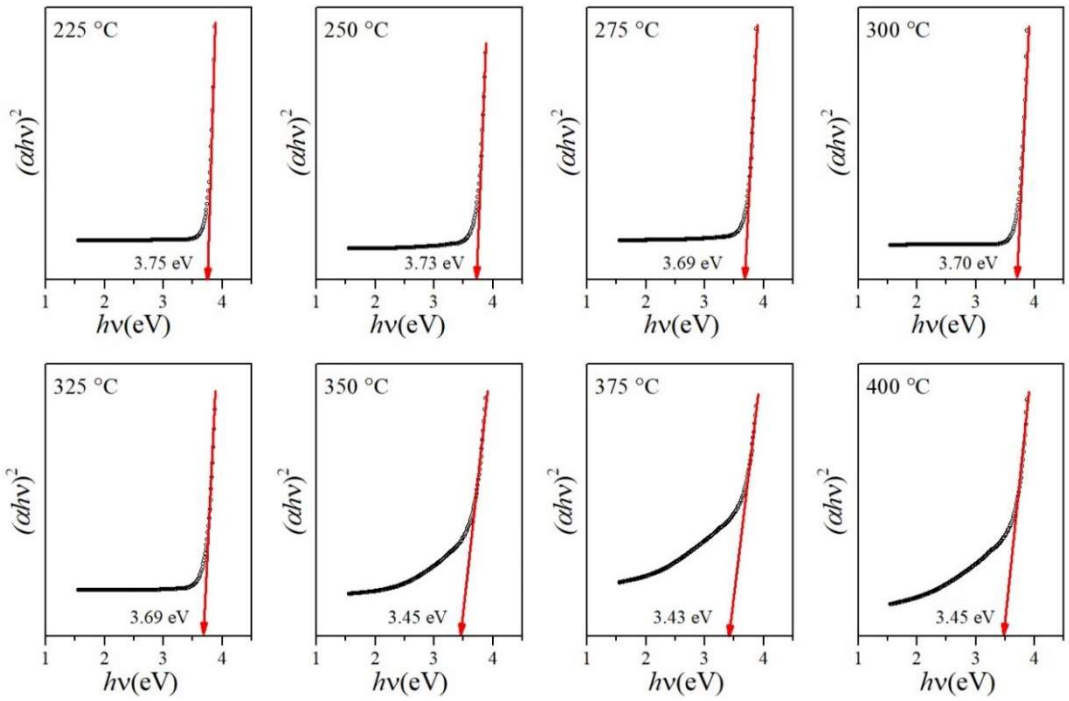

(a)

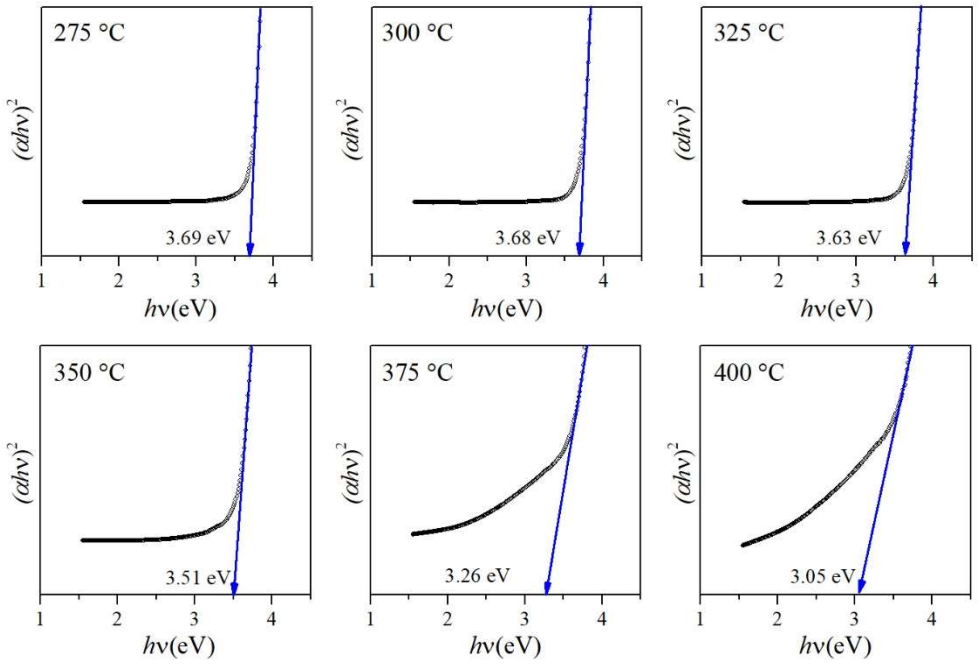

(b)

Figure 2.27 Tauc plots of the films deposited at temperatures 225 - 400 °C on (a) Pilkington SiCO glass and (b) FTO-coated substrates and the direct band gap values.

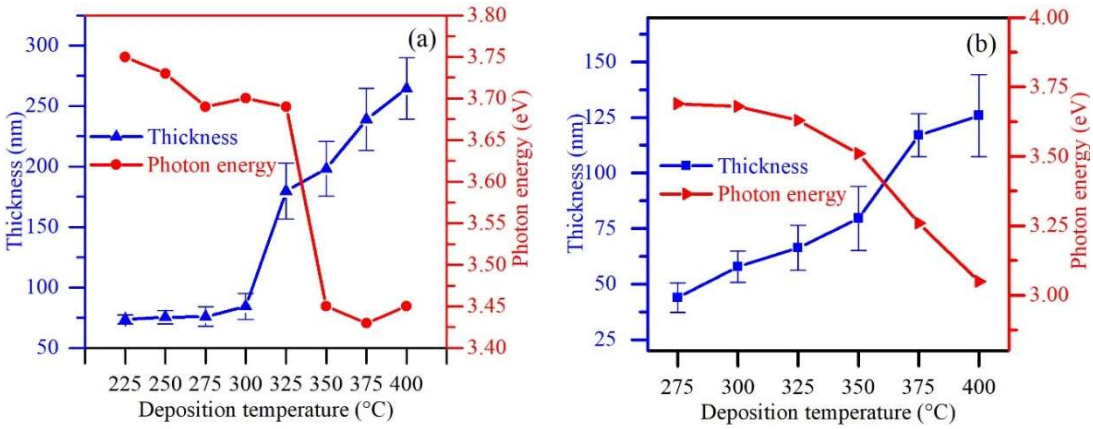

Figure 2.28 The comparison between the film thickness of the deposited films and their band gap energies on (a) Pilkington SiCO glass (b) FTO glass.

The relation between the film thickness and the band gap energy are plotted in Figure 2.28. Both graphs in Figure 2.28 represent the same trend with increasing thickness providing decreased band gap values.

Composition of the deposited films

Energy dispersive X-ray spectroscopy (EDS) was performed on the deposited films to investigate the elemental composition. The results of the analyses are shown in Table 2.22 for the films deposited on Pilkington SiCO substrates and Table 2.23 for the films deposited on FTO substrates.

The EDS data in Table 2.22 indicated that the amorphous film which was deposited at 225 °C possessed Ni and O levels of 4.14% and 52.18%, respectively. This may simply reflect that the film was too thin to analyse. At the deposition temperature of 250 °C, the Ni composition increased significantly to 41.16 % to provide a Ni : O ratio of 1 : 1.06. The XRD patterns in Figure 2.18 also demonstrated that the NiO phase had started to appear at this temperature.

In general the atomic % of Ni was found to increase with increasing deposition temperature, whilst the oxygen level decreased. This again agrees with the XRD results of Figure 2.18, which demonstrated the increasing presence of nickel metal at higher deposition temperatures.

The reduced film thickness provided at lower temperatures was also reflected in the high atomic % of Si detected, arising from the SiCO-coated substrates. Furthermore,

at such low thicknesses, it is not possible to assume that the oxygen detected arises solely from the deposited film because the electron beam from the EDS penetrated the thin film to the substrate which also contains oxygen.

Table 2.22 The EDS analyses of the deposited films from the N3 precursor system on Pilkington SiCO glass substrates. Average atomic % from 3 measured areas.

Deposition temperature (°C)	**Atomic %**					
	Ni	**O**	**C**	**Na**	**Mg**	**Si**
225	4.14 ± 1.51	52.18 ± 0.90	3.18 ± 0.50	1.21 ± 0.04	0.00	39.29 ± 1.61
250	41.16 ± 1.39	43.87 ± 1.12	4.68 ± 1.12	0.28 ± 0.48	0.00	10.01 ± 2.28
275	34.38 ± 5.78	44.11 ± 0.39	7.39 ± 3.25	0.43 ± 0.40	0.39 ± 0.34	13.22 ± 2.46
300	49.72 ± 4.86	35.80 ± 2.67	11.39 ± 1.13	0.47 ± 0.41	0.00	2.61 ± 3.20
325	55.47 ± 1.94	33.92 ± 0.51	9.63 ± 0.66	0.00	0.00	0.98 ± 1.70
350	52.56 ± 0.59	24.36 ± 2.93	21.98 ± 1.83	0.31 ± 0.27	0.00	0.78 ± 1.35
375	70.02 ± 0.79	9.87 ± 0.67	18.50 ± 0.60	0.00	0.00	1.61 ± 1.39
400	74.18 ± 0.81	7.60 ± 0.51	16.80 ± 0.46	0.23 ± 0.40	0.00	1.19 ± 1.03

Table 2.23 shows the EDS analysis results from the films deposited on FTO glass. The table demonstrates a trend of increasing Ni content and decreasing oxygen at % when the deposition temperature is increased. At deposition temperatures above 375 °C, the atomic % of the Sn increases significantly, which is again in agreement with the XRD results in Figure 2.18, which demonstrated the production of the Ni_3Sn_2 phase. Hence, the behaviour of the FTO substrate under AACVD conditions was further investigated and will be reported in Chapter 3.

Table 2.23 The EDS data of the films deposited from the N3 precursor system on FTO glass substrates. Average atomic % from by measuring 3 areas.

Deposition temperature (°C)	Atomic %							
	Ni	**O**	**Sn**	**F**	**C**	**Na**	**Mg**	**Si**
275	5.57± 1.75	60.61± 0.99	31.17± 0.69	1.22± 0.15	0.00	0.06± 0.10	0.03± 0.06	1.34± 0.13
300	19.14± 0.24	53.09± 0.27	22.51± 0.19	2.33± 0.15	2.19± 0.39	0.00	0.00	0.73± 0.03
325	23.15± 0.39	51.43± 0.29	19.91± 0.28	2.43± 0.16	2.43± 0.18	0.00	0.03± 0.05	0.62± 0.04
350	30.27± 2.75	47.38± 1.15	15.14± 1.93	2.56± 0.11	4.22± 0.48	0.00	0.02± 0.04	0.41± 0.06
375	42.77± 0.29	24.30± 0.29	17.97± 0.08	3.38± 0.08	11.09± 0.05	0.00	0.00	0.49± 0 .03
400	48.09± 0.37	7.13± 0.34	39.2± 0.35	4.1± 3.02	0.17± 0.25	0.00	0.00	1.32± 0.08

Conclusion

The readily available nickel(II) nitrate hexahydrate ($Ni(NO_3)_2{\cdot}6H_2O$) used as the starting material for nickel oxide thin film deposition. The deposited films which were prepared by using spin coating presented as amorphous materials prior to annealing under an air atmosphere. Analysis by XRD revealed that annealing of the as-deposited films at temperatures of 400 °C to 600 °C, using either ethanol or methanol as solvent, induced a transformation to crystalline NiO.

According to the TGA analysis of $Ni(NO_3)_2{\cdot}6H_2O$, NiO can be produced at a decomposition temperature of 374 °C. The combustion process was, thus, employed to reduce the temperature of the deposition process by AACVD. Ammonium nitrate and urea were used as the combustion chemical.

Investigations by XRD analysis demonstrated that all precursors provided nickel oxide thin films in one step without the need for subsequent annealing. The precursor system which contained ammonium nitrate (N3) provided NiO thin films at the lowest deposition temperature of 250 °C, whereas the systems comprising urea (N2) or no combustion chemical (N1) provided NiO thin films only at deposition temperatures of 300 °C and 325 °C, respectively. It is proposed that the ammonium nitrate supplies more high energy nitrate species to the precursor solution, which provide increasing activation energy to the deposition system as a whole.

Cross-section analysis by FE-SEM demonstrated that the thickness of the deposited films increased with increasing deposition temperature by AACVD.

The results described in this chapter have also shown that it is possible to deposit nickel oxide on FTO glass substrates with deposition temperatures in the range 300 - 350 °C by using the mixed nickel/ammonium nitrate precursor system. The energy band gap of the nickel oxide on the FTO glass was 3.51 - 3.68 eV, whilst on the Pilkington SiCO glass it was deduced to be 3.69 - 3.73 eV.

2.2 Binary oxide thin film deposition: Rare Earth oxides (REOs)

2.2.1 Lanthanum oxide thin film deposition

Introduction

Lanthanum oxide and other rare earth oxides have been considered to replace SiO_2 as dielectric materials.[58] For comparison, SiO_2 displays a dielectric constant of 3.9, while lanthanum oxide has the highest dielectric constant (~19) and displays a very large band gap around 5.5 eV (Figure 2.29).With regard to its thin film properties, lanthanum oxide is highly transparent over a wide wavelength range between ultraviolet and infrared.[59–61] The structural properties of lanthanum oxide are summarised in Table 2.25. Due to these excellent properties, lanthanum oxide thin films are attractive for electronic device technology and in various areas such as sensors,[59,62] optical devices,[60] complementary metal-oxide-semiconductor (CMOS) technology[63] and metal-oxide-semiconductor field-effect transistors (MOSFETs).[64]

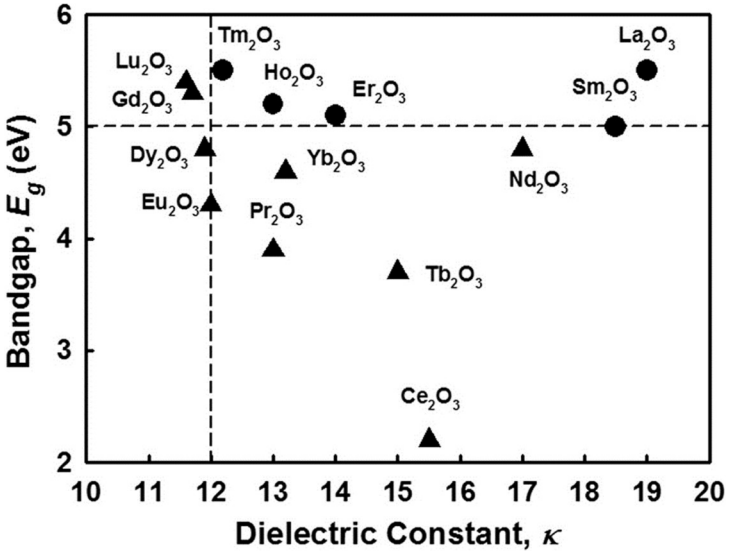

Figure 2.29 The interrelationship between bandgap and dielectric constant of binary rare earth oxides.[65,66]

The fabrication of lanthanum oxide thin film has been reported by a number of different techniques (Table 2.25) such as electron beam deposition,[67–69] spray

pyrolysis,[59,70] metalorganic chemical vapour deposition (MOCVD),[71] atomic layer deposition (ALD)[72,73] and magnetron sputtering.[74] Some techniques, however, require post processing such as an annealing step to control the structure of the thin films and provide the requried properties.

Typically La_2O_3 films deposited at temperatures below 550 °C are amorphous,[69,71,73,75] whereas when the deposition or annealing temperature are increased to higher than 600 °C, polycrystalline structures have been produced.[68,70,71,73] A further aspect of rare earth oxide behaviour should also be borne in mind. La_2O_3 thin films deposited by many techniques have been found to react with CO_2 or moisture in ambient air and be transformed to LaO(OH), $La(OH)_3$ and LaO_2CO_3 phases (Figure 2.30).[73–75]

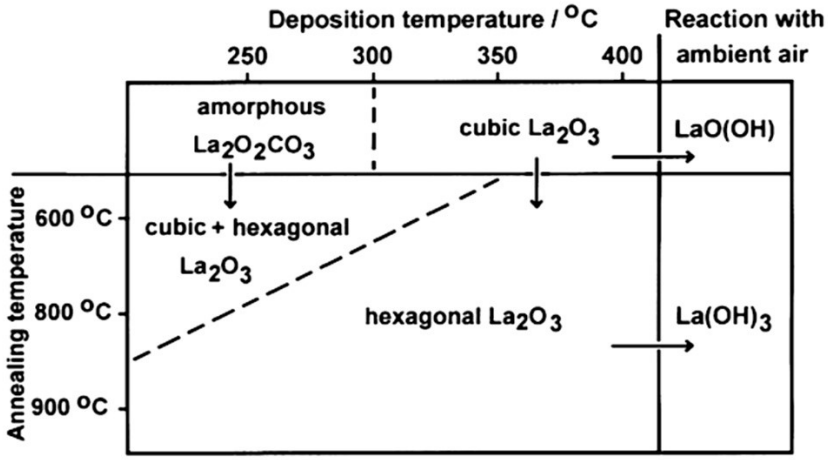

Figure 2.30 A summary of the influence of deposition and annealing temperatures on lanthanum oxide film composition. Also the effect of ambient air on film quality is shown.[75]

Table 2.24 Summary of lanthanum oxide thin films (La_2O_3) deposited by different techniques and some of their properties.

Deposition techniques	Substrates	Processing temperature (°C)		La_2O_3 structures	Notes	Properties	Applications
		Deposition temperature	Annealing temperature				
Ultrahigh vacuum E-beam deposition system[69]	Si(100)	• RT* • 250 • 400	-	Amorphous	Eg = 5.5 eV	• High *k*-dielectric material[76] • Mechanically stable[61,77,78] • Possess high electronic breakdown field strength[60,77,79] • Chemical stable[77] • Dielectric constant[77,79] • Large energy band gap 5.5 eV[80], 6.4 eV[68],5.4-6.0 eV[81] • Lowest lattice energy,-12.687 kJ/mol[69] • Thermodynamic stability[81]	• Protective and corrosion resistive coatings[61,82] • Medicine treatment for acute renal failure[83] • Dielectric layer in electronic devices[77] • Optical coating[60] • CO_2-gas sensor[59,62] • Catalytic materials[84] • High-k gate insulator[76]
Electron beam bombardment[68]	*n*-Si(100)	RT	Air, 600	-	Eg = 6.4 eV		
Pulse ultrasonic spray pyrolysis[70]	Si(100)	~550	-	Monoclinic	Crystalline size increased when pulse/pause ratio was decreased.		
Metalorganic chemical-vapour deposition (MOCVD)[71]	*p*-Si(100)	350	• Air, 600 • Air, 900	Cubic & Hexagonal	After the annealing process, dielectric constant and leakage current		

Deposition techniques	Substrates	Processing temperature (°C)		La_2O_3 structures	Notes	Properties	Applications
		Deposition temperature	Annealing temperature				
					density decreased.	• Transparent from ultraviolet to infrared[59–61] • Low interface trap density • Low leakage current[76]	• Metal-oxide-semiconductor field-effect transistor (MOSFETs)[64] • Ferroelectric ceramic[85] • High-κ gate dielectric for CMOS technology[63]
Atomic layer epitaxy (ALE)[72]	Soda lime glass, Si(100)	• 175 - 275 • 300 - 450	-	• Amorphous • Cubic	La_2O_3 transforms to monoclinic LaO (OH) when it was left in the ambient air.		
Electron-beam evaporation[67]	*n*-Si(100)	RT	• N_2, 300 • N_2, 500	-	Decreasing leakage current and increasing mobility influenced by increasing oxygen atom.		
Spray pyrolysis[59]	Glass	• 300 • 350 • 400 • 450	-	Hexagonal	Eg = • 3.7 • 3.9 • 4.1 • 4.2		

Deposition techniques	Substrates	Processing temperature (°C)		La_2O_3 structures	Notes	Properties	Applications
		Deposition temperature	Annealing temperature				
Atomic layer deposition[73]	*p*-Si(100)	300	Vacuum • 400 • 600 • 800	• Hexagonal • Hexagonal, cubic • Hexagonal, cubic	As deposited Eg=5.45eV After annealed Eg=5.20eV, *h*-La_2O_3 convert to *h*-$La(OH)_3$ after exposure to air 48h		
R.f. magnetron sputtering[74]	Si(100)	200	-	Hexagonal	*h*-La_2O_3 transform to *h*-$La(OH)_3$ or *m*-$La_2O_2CO_3$, in air.		

Film characterisation: Lanthanum oxide thin films

Thermogravimetric analysis of Lanthanum(III) nitrate hexahydrate

The readily available nitrate of lanthanum, ($La(NO_3)_3 \cdot 6H_2O$), was selected for use as the precursor chemical for lanthanum oxide thin film fabrication described in this section. Figure 2.31 presents the thermal behavior of $La(NO_3)_3 \cdot 6H_2O$ and reveals many steps for its decomposition.

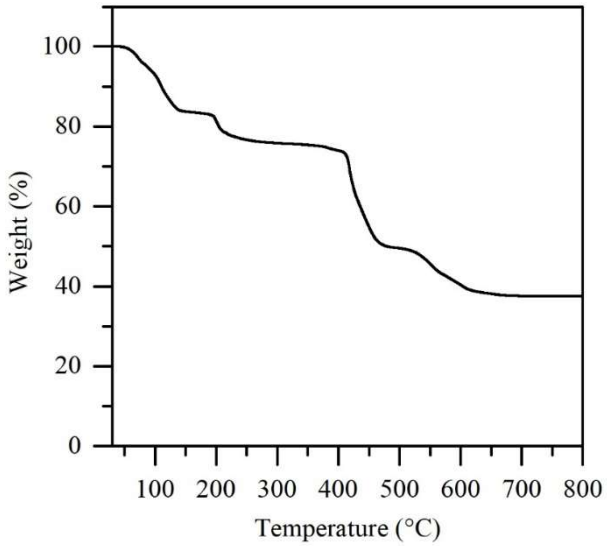

Figure 2.31 TGA curve of $La(NO_3)_3 \cdot 6H_2O$.

The thermal decomposition of $La(NO_3)_3 \cdot 6H_2O$ displayed in the TGA curve shown in Figure 2.31 comprises two major processes, which may be broadly described as dehydration and decomposition. The dehydration process starts with an onset temperature at around 50 °C, which likely corresponds with the melting of the $La(NO_3)_3 \cdot 6H_2O$ or its dissolution in its own water of crystallisation. This process is complete at around 200 °C with a total weight loss around 24 wt%, which can be attributed to the loss of water. The decomposition of the complex nitrate starts at around 400 °C and is complete at around 670 °C with the total weight loss of around 36 wt%. For comparison, the expected residual mass for La_2O_3 is 38 wt%.

Spin coating of the $La(NO_3)_3 \cdot 6H_2O$

The TGA curve in Figure 2.31 revealed that a high decomposition temperature is necessary to produce lanthanum oxide from the pure nitrate. For this reason, urea was selected to act as a combustion co-reagent with the lanthanum nitrate in a 1 to 1 ratio. Spin coating was initially used to investigate the deposition of $La(NO_3)_3 \cdot 6H_2O$ under the deposition conditions presented in Table 2.25.

Table 2.25 Deposition conditions for spin coating of $La(NO_3)_3 \cdot 6H_2O$.

Variable	Detail
Substrate	Pilkington SiCO glass, 2.5×2.5 cm^2
Precursor	$La(NO_3)_3 \cdot 6H_2O$ + urea
	ratio 1:1, concentration 0.05 M
Solvent	Ethanol, Water
Deposition layer	5 layers
Annealing atmosphere	Air, Argon
Annealing time	1 hour
Annealing temperature	300 - 600 °C

Crystallinity

The deposited films prepared using ethanol and water as solvent provided similar XRD results after annealing under an air atmosphere. The X-ray patterns in Figure 2.32 revealed that the films were composed of monoclinic $La_2O_2CO_3$ (JCPDS: 00-048-113) that can be assumed to result from the reaction between carbon dioxide in the air and the lanthanum oxide thin film.

A number of literature reports have previously described that lanthanum oxide films when annealed under an air atmosphere similarly provide $La_2O_2CO_3$.[72–74] Further literature has suggested that a high-temperature treatment can help to prevent the formation of the carbonate phase.[86] This process, however, is limited by the substrate melting point. Annealing under an air atmosphere at a temperature over 650 °C was attempted, however, this resulted in the substrate melting and bending.

When the deposited films were annealed under an argon atmosphere, they remained amorphous (Figure 2.33).

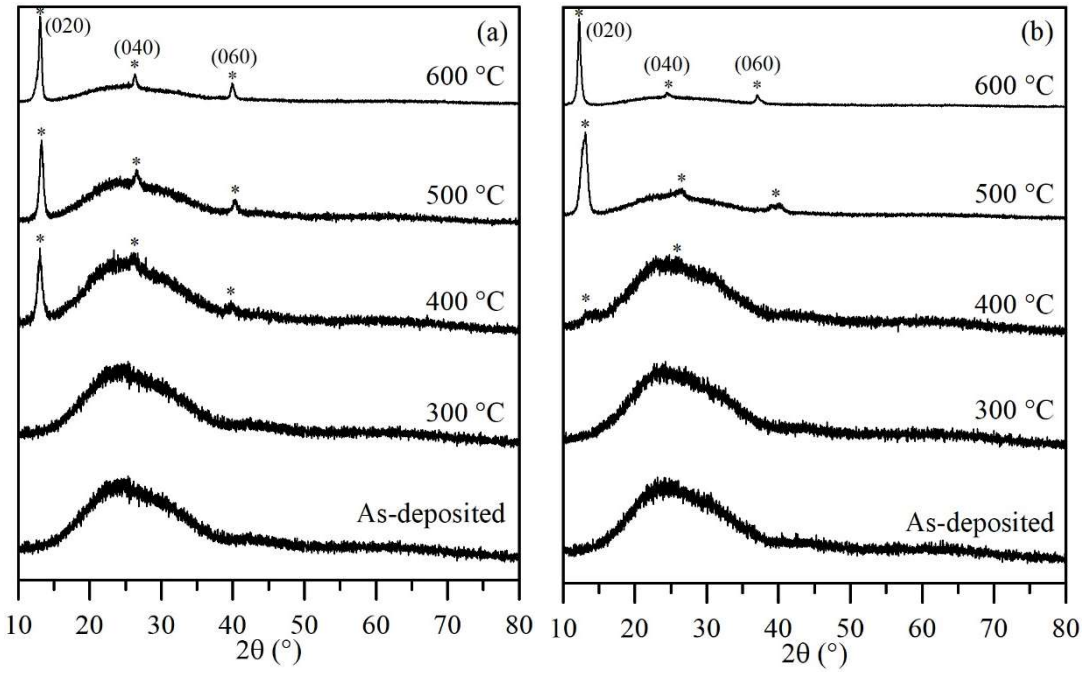

Figure 2.32 XRD patterns of the as-deposited and annealed films by using (a) ethanol and (b) water as solvent. (∗) Features corresponding to monoclinic the $La_2O_2CO_3$ phase. The annealed films were heated under air.

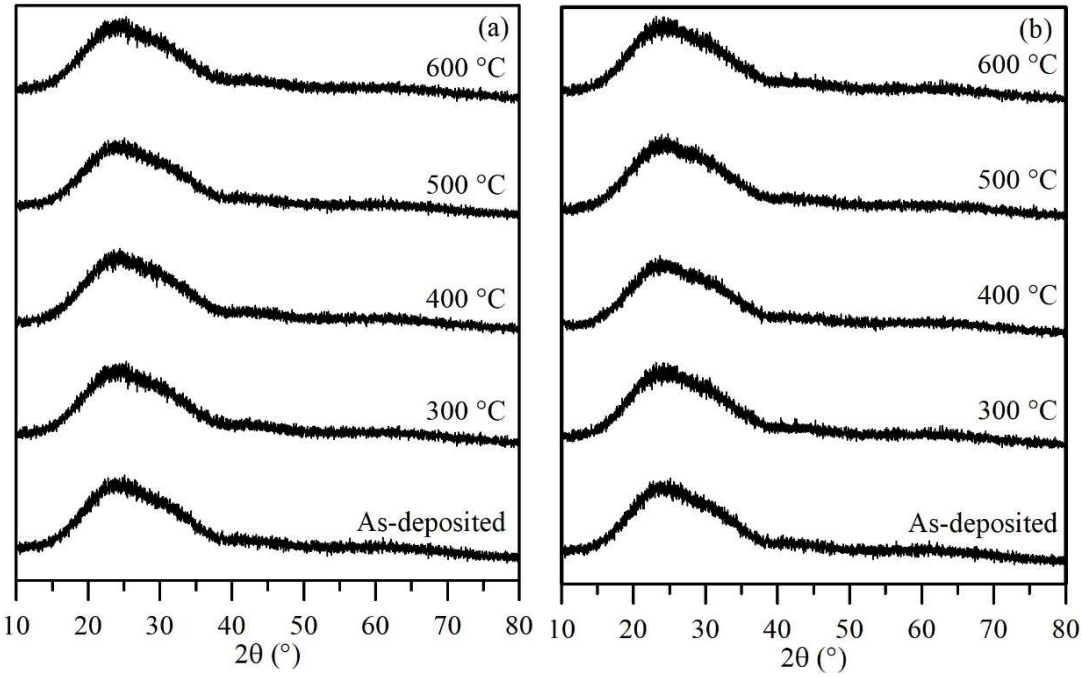

Figure 2.33 XRD patterns of the deposited and annealed films by using (a) ethanol and (b) water as solvent. The annealed films were heated under argon.

AACVD of $La(NO_3)_3 \cdot 6H_2O$

Table 2.26 Deposition conditions for AACVD of $La(NO_3)_3 \cdot 6H_2O$.

Variable	Detail
Substrate	Pilkington SiCO glass, 2.5×15 cm^2
	Microscope slide glass
Precursor concentration	0.05-0.5 M
Solvent	Ethanol, Water
Deposition time	1 hour
Deposition temperature	300 - 600 °C
Deposition atmosphere	Nitrogen
Reactor type	Hot-wall

Crystallinity and morphology

Deposition on Pilkington SiCO substrates

The thin film deposition followed the conditions shown in Table 2.26. Deposition on the Pilkington SiCO glass substrate was problematic and resulted in the formation of white powders on the substrate surface. Figures 2.34 (a) and (b) show the appearance of particles on the Pilkington glass substrate deposited at 300 °C and 600 °C, respectively. It can be clearly seen that the deposited materials cannot be formed as continuous thin films and the particles are separately spread over the substrate surface.

The elemental composition of the particles was analysed by EDS and Figures 2.34 (c) and (d) display the EDS spectra. The area comprising spectrum 2 highlighted on the figure was found to contain a significantly higher atomic % of La (4.19%) than spectrum 1 (0.16%), which was focused on the background area. Hence, it can be assumed that the visible particles comprise the lanthanum oxide-containing material.

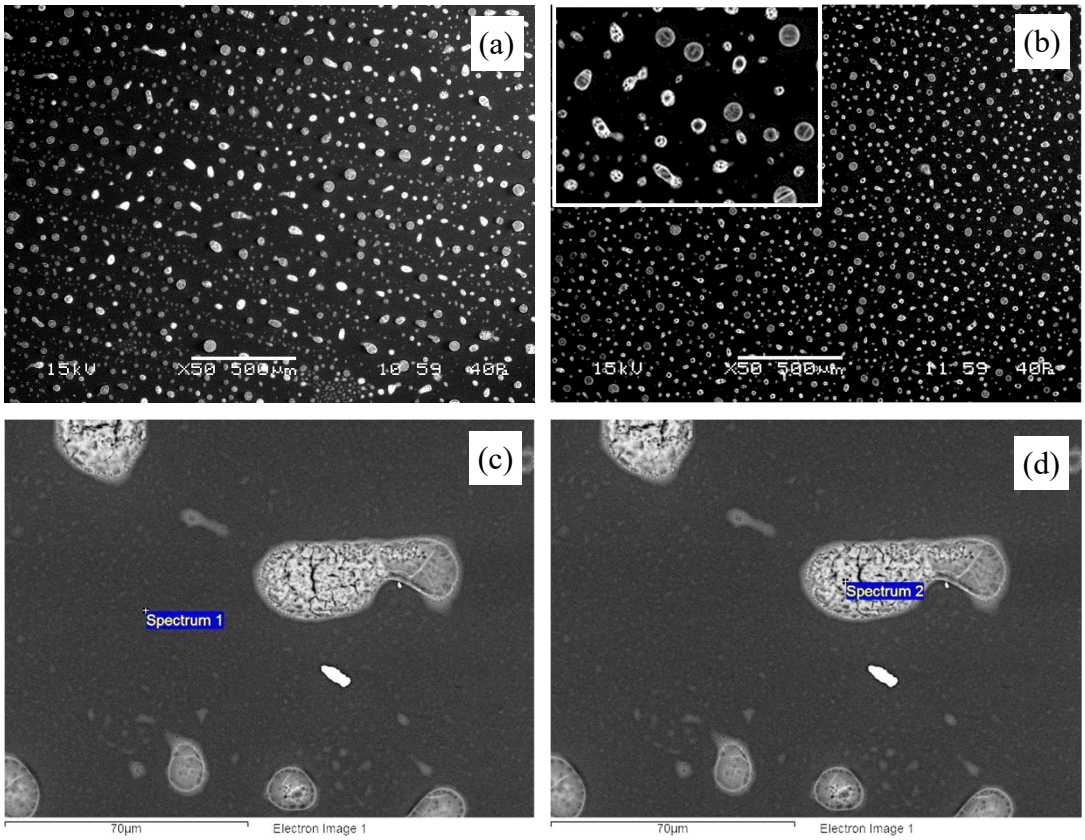

Figure 2.34 SEM micrographs of the material desposited on Pilkington SiCO glass substrates at deposition temperatures of (a) 300 °C and (b) 600 °C. (c) and (d) the positions selected to collect the EDS spectra from the sample deposited at 600 °C.

It is suggested that the formation of the powder results from too rapid evaporation of the precursor solution prior to its diffusion to the substrate surface such that the particles could not coalesce to form a continuous thin film. Increasing the precursor concentration from 0.05 - 0.5 M provided similar results and fine white powder on the surface of the substrate.

The white powders from the increased concentration of the precursor and deposition temperature at 500 °C were collected from the substrate surface and were analysed by XRD. The XRD patterns in Figure 2.35 reveal that the white powder comprises hexagonal La_2O_3 (JCPDS: 01-074-1144) and cubic $La(O)NO_3$ (JCPDS: 00-031-0665) and, as inferred form the TGA curve in Figure 2.31, demonstrate that the precursor and the AACVD technique can provide La_2O_3 but include intermediate oxo-nitrate ($La(O)NO_3$).

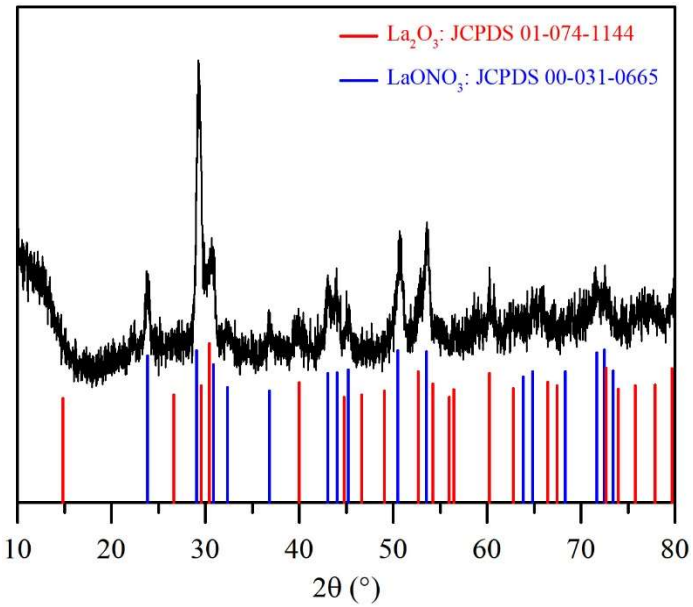

Figure 2.35 XRD patterns of the white powder sample which was collected from the substrate surface with the deposition temperature at 500 °C.

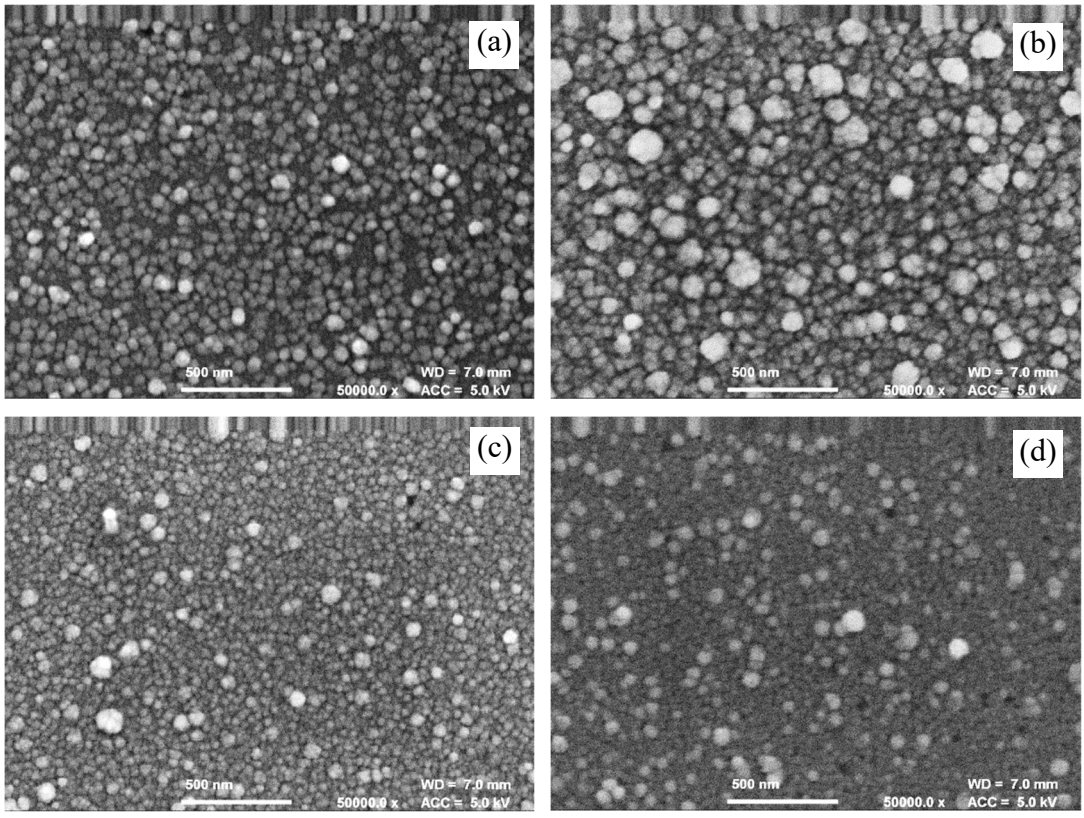

Figure 2.36 SEM micrographs of the particulate powder deposited on the Pilkington SiCO glass substrate at different deposition temperatures (a) 300 °C (b) 400 °C (c) 500 °C and (d) 600 °C.

The morphologies of the particles at different deposition temperatures are shown in Figure 2.36 and indicate that the size of the particles decreased with the increasing deposition temperature.

Deposition at temperatures as low as 150 - 200 °C were attempted to prevent the proposed early aerosol evaporation. The products from this experiment, however, provided amorphous films. Subsequent heating (300-600 °C) in the reaction chamber, however, also produced powder films on the substrate surface without providing any crystallinity. The Scotch tape test was used to assess the adhesion of the powder particles on the substrate. It was found that the particles had not adhered on the surface substrate and were easy to wipe off.

Deposition on microscope slide glass

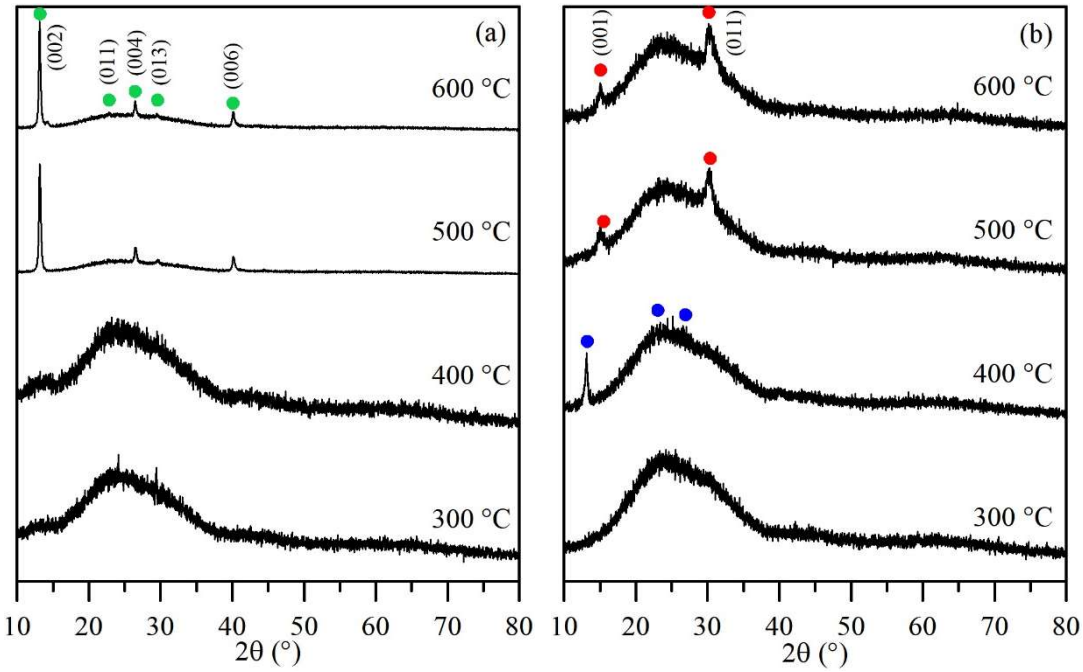

Figure 2.37 XRD patterns of films deposited with different solvents by (a) using ethanol (b) using water as solvent. ● Features corresponding to monoclinic $La_2O_2CO_3$ phases, ● features corresponding to hexagonal La_2O_3 and ● features corresponding to $LaONO_3$.

Microscope slide glass was then considered as substrate. Figure 2.37 presents the XRD pattern of the deposited film in this case. These data indicate that the deposited films prepared from using ethanol as solvent were composed primarily of the monoclinic $La_2O_2CO_3$ phase (JCPDS: 00-023-0435) with the deposition temperature at 500 - 600

°C. In contrast, films fabricated using water as solvent presented the $LaONO_3$ phase (JCPDS: 00-028-0513) at the deposition temperature at 400 °C and, at a deposition temperature at 500-600 °C, the hexagonal La_2O_3 phases (JCPDS: 01-0741144). At this point, it was assumed that the use of ethanol as solvent acts as a source of carbon dioxide to the deposition system with which the lanthanum oxide can easily react to produce $La_2O_2CO_3$.[59,74,86–89] On the other hand, the XRD patterns of the film deposited using water as solvent provided $LaONO_3$ at deposition temperature 400 °C and La_2O_3 at deposition temperatures between 500 and 600 °C. This is again consistent with the decomposition steps of the TGA analysis presented in Figure 2.31.

The improved deposition on the microscope slide glass in comparison to the Pilkington glass substrate may be attributed to the differing morphology, surface energy and chemical character of the bare glass substrate surface. The Scotch tape test, however, indicated that the deposition still provided a powder coating on the substrate rather than adherent continuous films.

Conclusion

The TGA analysis of lanthanum (III) nitrate hexahydrate ($La(NO_3)_3 \cdot 6H_2O$) suggested that the lanthanum oxide will only be found at high temperatures around 670 °C. The mixing of lanthanum nitrate and urea was, thus, used as the precursor and a spin coating technique and annealing process were used to form the films. XRD analysis reported that the annealed films were dominated by the transformation of the monoclinic $La_2O_2CO_3$ phase at annealing temperatures of 400 - 600 °C under an air atmosphere due to reaction with CO_2 in agreement with literature data. In contrast, the films which were annealed under an argon atmosphere presented an amorphous phase irrespective of the temperature applied.

Deposition by AACVD on Pilkington SiCO substrates tended to provide white powdery products on the substrate surface. The powder product from the deposition temperature at 500 °C was collected and analysed by XRD and the results reported that the powder products comprised La_2O_3 and $La(O)NO_3$.

XRD analysis was also performed on samples prepared on microscope slide glass at deposition temperatures at 500 - 600 °C. The results revealed that the hexagonal La_2O_3

phase could be achieved using water as solvent, whereas ethanol provided monoclinic $La_2O_2CO_3$. It can be assumed that ethanol provided the necessary carbon to the deposition system to enable carbonate formation. The Scotch tape test, however, indicated that the deposition still provided non-adherent powder coating on the substrates.

2.2.2. Praseodymium oxide thin films

Introduction

Generally, praseodymium oxide exists in its common sesquioxide, Pr_2O_3 phase, although it can also achieve the higher PrO_2 oxide which displays a fluorite structure. A range of intermediate stoichiometries, Pr_nO_{2n-2m}, are also known.[81,90,91]

The more common Pr_2O_3 displays a number of potentially useful properties such as a high κ dielectric constant (~30),[92] high breakdown strength, wide band gap (~3.9 eV)[93] low leak gate current (10^{-7} A/cm^2)[94] and also thermodynamic stability when in contact with silicon.[95]

Because of these excellent characteristics, praseodymium oxide thin films have been identified as good candidates for the next generation of gate dielectric materials to support future semiconductor technology such CMOS devices.[63,95] Furthermore, Pr_2O_3 thin films have been reported to display a high capacitance density of around 9.1 to 20 F/μm^2.[94] Increased capacitance density is necessary for miniaturization of metal-insulator-metal (MIM) capacitor technology. Owing to their suitable properties, therefore, PrO_x has been considered as a potential replacement for silicon dioxide and silicon nitride, which are the current materials of choice in MIM capacitors.[94,96]

Table 2.27 shows some examples of techniques which have been reported to grow praseodymium oxide thin films. The table also includes a summary of properties and applications. Most of the reported praseodymium oxide films are amorphous when it is deposited below 500 ºC, while crystalline forms are displayed when the oxides are grown or annealed at higher temperatures.[95,97–101] The Pr_2O_3 phase also predominates at higher temperatures than Pr_6O_{11}, whereas at lower temperatures, Pr_6O_{11} is the most stable intermediate phase.[102] In a similar manner to lanthanum oxide, praseodymium oxide films when left in a ambient air may degrade and transform from the hexagonal Pr_2O_3 phase to hexagonal $Pr(OH)_3$. In contrast Pr_6O_{11} is not degraded.[97] In addition, leakage current values of the oxide thin film decrease as the thickness is increased,[100,103] with hexagonal Pr_2O_3 possessing a smaller leakage current and higher thermal stability than cubic Pr_2O_3.[63] Consequently, appropriate methods are needed to control the structure and quality of the praseodymium oxide thin films if its promising properties are to fulfill their potential in future applications.

Table 2.27 Summary of praseodymium oxide thin films which have been deposited by different techniques and some of their properties.

Deposition techniques	Substrates	Processing temperature		Chemical formulas	Notes	Properties	Applications
		Deposition temperature	Annealing temperature				
Metal-organic chemical vapour deposition (MOCVD)[97]	Si(100)	600 ºC	750 ºC under vacuum	As deposited, amorphous, after annealed, Pr_2O_3	After to exposed in air, the oxide films degraded from hexagonal Pr_2O_3 phase transform to hexagonal $Pr(OH)_3$ but Pr_6O_{11} is not degraded.	• High dielectric constant (κ=~26-30)[93,96,104,105] • Large band gap (~3.9 eV)[93] • High thermodynamic stability on silicon[93] • Low leakage current densities[104] • CO_2 adsorption and desorption CO[88]	• Gate dielectric materials[98,106–108] • Complementary metal oxide semiconductor (CMOS) technology.[98,106–108] • Sensor devices[89] • Carbon capture and storage application[88] • Matrix devices and high-speed driving circuit application[101] • Metal-insulator-metal
		650 ºC		As deposited, Pr_6O_{11}, after annealed, Pr_7O_{12}			
Metal-organic chemical vapour deposition (MOCVD)[96]	p-type Si (001)	500 ºC	-	Amorphous	Thin film which obtains a thickness as 15 nm, it gives dielectric constant ~16 and leakage current densities~1×10^{-7} A cm^{-2}, while as 9 nm		
		600 ºC		Pr_2O_3, Hexagonal			
		750 ºC		Pr_2O_3, Hexagonal			

Deposition techniques	Substrates	Processing temperature		Chemical formulas	Notes	Properties	Applications
		Deposition temperature	Annealing temperature				
					thickness film gives ~10 of dielectric constant and ~0.025 A cm^{-2} of leakage current densities.		capacitor (MIM)[58] • DRAM technologies[97] • RF application[94]
Molecular beam epitaxial growth (MBE)[100]	Si(100)	675 ºC	-	Pr_2O_3	Leakage current is reduced with increasing thickness and *k*.		
Layer-by-layer deposition[109]	ITO	Room temperature	500 ºC under Air	Pr_6O_{11}	Electrical conductivity of ITO is improved with praseodymium oxide layer on surface.		
Physical vapor	Si	550 ºC	600 ºC	Pr_2O_3	Nitrogen implantation		

Deposition techniques	Substrates	Processing temperature		Chemical formulas	Notes	Properties	Applications
		Deposition temperature	Annealing temperature				
deposition (PVD)[101]	Poly-Si film				technique can be helped to improve electrical properties of film.		
Electrochemical deposition[110]	ITO	Room temperature	500 ºC under Air	Pr_6O_{11}	Thickness of the ultrathin film can be controlled by cycles of electrodeposition.		
Electron beam evaporation[98]	Si(001)	725 ºC	-	Pr_2O_3, D 5_3[98]	Different planar characters of the substrate can be provided by different crystal structures of the thin film.		
	Si(111)	625 ºC		Pr_2O_3, hexagonal			

Film characterisation: Praseodymium oxide thin films

Thermogravimetric analysis of Praseodymium (III) nitrate hexahydrate

$Pr(NO_3)_3 \cdot 6H_2O$ was used as the precursor chemical for praseodymium oxide thin film fabrication and its thermal decomposition behavior was assessed by TGA analysis (Figure 2.38).

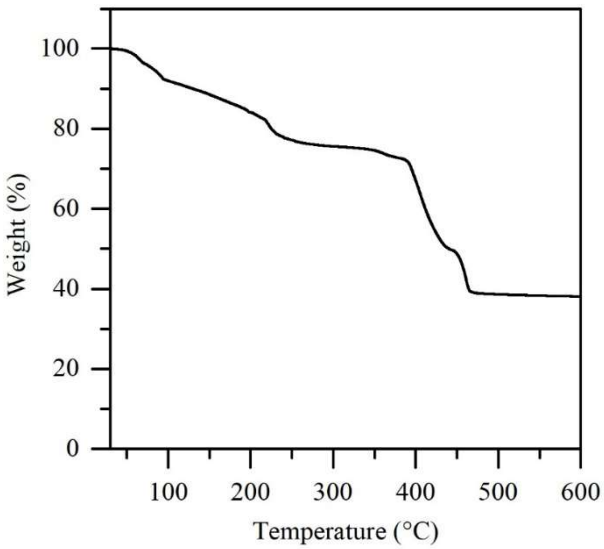

Figure 2.38 TGA curve of $Pr(NO_3)_3 \cdot 6H_2O$.

TGA analyses have been conducted on praseodymium nitrate and the results are shown in Figure 2.38. These data reveal the decomposition comprises 2 main processes. The first process involves the melting or dissolving of the sample in its water of crystallisation at around 50 °C and its subsequent dehydration starts at 74.2 °C. This process is complete at around 210 °C with a weight loss of 18 wt%, which can be attributed to the loss of water. The second process starts at around 370 °C. This can be attributed to the decomposition of the nitrate complex, which is complete around 475 °C with a total weight loss of 34 wt% and which compares well with the expected residual mass of 39 wt% for Pr_6O_{11}.

Spin coating of $Pr(NO_3)_3 \cdot 6H_2O$

The investigation of $Pr(NO_3)_3 \cdot 6H_2O$ deposition by spin coating followed the deposition conditions in Table 2.28.

Table 2.28 Deposition conditions for spin coating of $Pr(NO_3)_3 \cdot 6H_2O$.

Variable	Detail
Substrate	Pilkington SiCO glass, 2.5×2.5 cm^2
Precursor	$Pr(NO_3)_3 \cdot 6H_2O$ + urea ratio 1:1, concentration 0.05 M
Solvent	Ethanol, Water
Deposition layer	5 layers
Annealing atmosphere	Air
Annealing time	1 hour
Annealing temperature	300 - 600 °C

Crystallinity

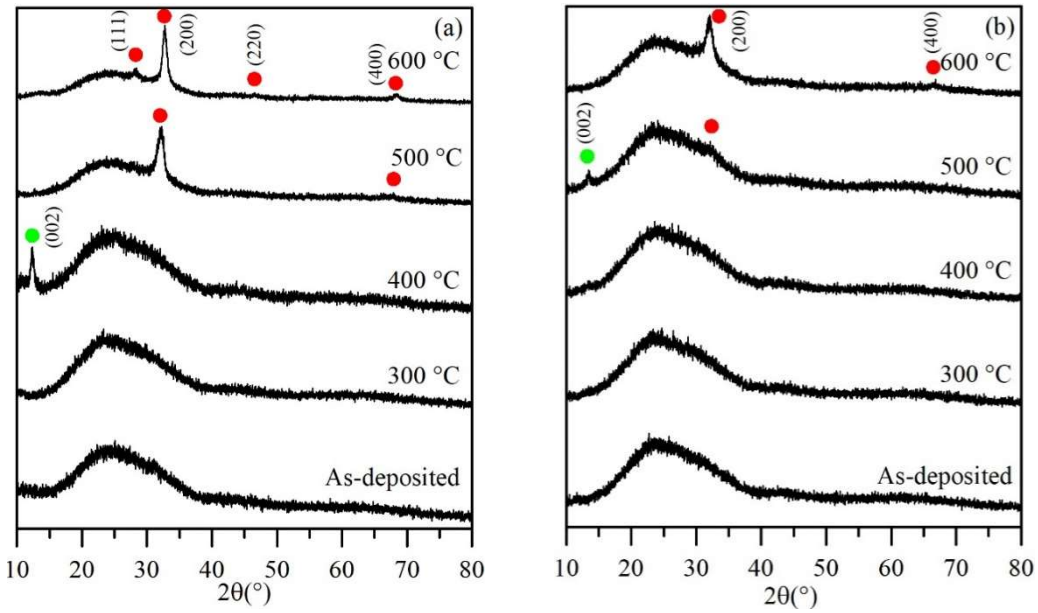

Figure 2.39 XRD patterns of the deposited and annealed films by using (a) ethanol and (b) water as solvent. ● Features corresponding to monoclinic Pr_2CO_5 (JCPDS: 00-025-0696) and ● features corresponding to cubic Pr_6O_{11} (JCPDS: 00-042-1121).

Table 2.29 Crystallite size of the deposited films on the Pilkington SiCO glass using ethanol and water as solvents.

Annealing temperature (°C)	Ethanol					Water				
	Phase	**Crystal system**	***(hkl)***	**2θ (°)**	**Estimated crystallite size (nm)**	**Phase**	**Crystal system**	***(hkl)***	**2θ (°)**	**Estimated crystallite size (nm)**
300	Amorphous	-	-	-	-	Amorphous	-	-	-	-
400	Pr_2CO_5	monoclinic	(002)	12.38	15	Amorphous	-	-	-	-
500	Pr_6O_{11}	cubic	(200)	31.99	9	Pr_2CO_5	monoclinic	(002)	13.42	15
			(400)	66.69	7	Pr_6O_{11}	cubic	(200)	32.33	6
600	Pr_6O_{11}	cubic	(111)	28.21	10	Pr_6O_{11}	cubic	(200)	31.99	8
			(200)	32.73	11					
			(220)	46.66	11		cubic	(400)	66.69	7
			(400)	68.41	10					

The XRD patterns of the deposited and annealed films are shown in Figure 2.39. The results confirmed that the pure monoclinic Pr_6O_{11} structure can be observed after the deposited films were annealed under an air atmosphere at 500 °C and 600 °C using either ethanol or water as the solvent, respectively. The $Pr_2O_2(CO_3)$ phase was found when the deposited films were annealed in air at 400 - 500 °C. At this point, it can be assumed that ambient carbon dioxide reacts with the deposited praseodymium oxide to form the carbonate. This could be eliminated, however, by increasing the annealing temperature after which phase pure praseodymium oxide was obtained.

The calculated crystallite sizes of the Pr_6O_{11} phase of the annealed films are presented in Table 2.29. It was found that, at the same annealing temperature and utilizing the same crystallographic planes, the films which used ethanol as the solvent provided crystallite sizes slightly bigger than the films which were prepared using water.

AACVD with $Pr(NO_3)_3{\cdot}6H_2O$

Table 2.30 Deposition conditions for AACVD of $Pr(NO_3)_3{\cdot}6H_2O$.

Variable	Detail
Substrate	Microscope slide glass
Precursor concentration	0.5 M
Solvent	Methanol
Deposition time	1 hour
Deposition temperature	330 and 600 °C
Deposition atmosphere	Nitrogen
Reactor type	Hot-wall

The XRD patterns in Figure 2.40 (a) reveal that the deposited films are amorphous. When, however, the deposited film at 600 °C was annealed in the deposition chamber maintained at 600 °C under a nitrogen atmosphere for 1 hour, the deposited film was transformed to the crystalline phase of cubic Pr_6O_{11} (Figure 2.40 (b)). A similar amorphous to crystalline transformation induced by annealing has been described previously in the literature.[111–113]

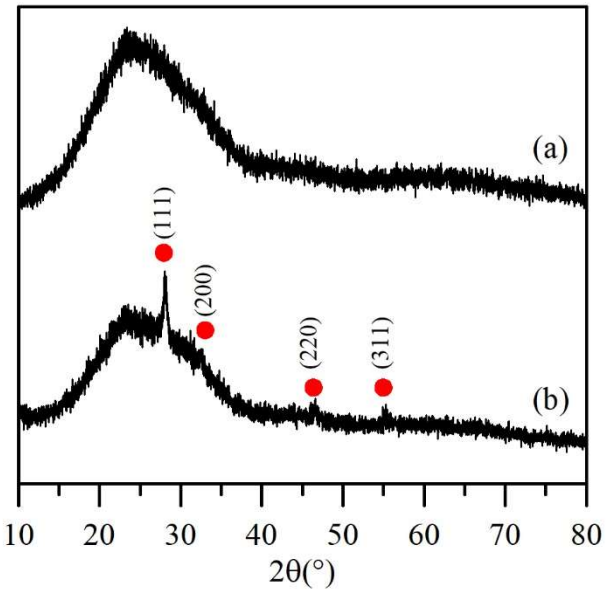

Figure 2.40 XRD pattern of films deposited at a deposition temperature of (a) 600 °C. (b) is the XRD pattern of deposited film at 600 °C annealed under nitrogen 1 hour at 600 °C in the deposition chamber. ● Features corresponding to cubic Pr_6O_{11} (JCPDS: 00-042-1121).

As a result of this observation, subsequent experiments carried out the deposition at lower temperature, while annealing was carried out under a nitrogen atmosphere. The films were deposited at 330 °C and left under a nitrogen atmosphere in the deposition chamber for 1 hour at temperatures between 330 and 600 °C. XRD was used to investigate the phases of the films.

At annealing temperatures below 500 °C, the XRD patterns in Figure 2.41 reveal that the films comprised phases of $Pr(OH)_3$, $Pr(C_2H_3O_2)_3$ and $PrOHCO_3$. The formation of the hydroxyl-carbonate phase can be assumed to have occurred by 2 potential routes. First, it was formed during the gaseous phases between the starting materials and residual carbon which emerged from the decomposition or combustion of the solvent (methanol) in the deposition step.[114] Alternatively, the annealed films were unstable and, when exposed to an air atmosphere for ageing, transformed to the hydroxyl-carbonate phase.[114,115]

The $Pr(C_2H_3O_2)_3$ and $PrOHCO_3$ phases disappeared when the annealing temperature was increased to 500 °C. This coincided with the appearance of a mixture of Pr_2CO_5

and $PrO_{1.833}$ in agreement with previous literature. Furthermore, $Pr(C_2H_3O_2)_3$ and $PrOHCO_3$ can be transformed to Pr_2CO_5 by raising the annealing temperature.[114,115]

The XRD patterns of the annealed film at 600 °C shown in Figure 2.41 indicated the formation of phase pure Pr_6O_{11}. Furthermore, the Pr_6O_{11} is stable at room temperature in the air, in contrast to the other phases.[116]

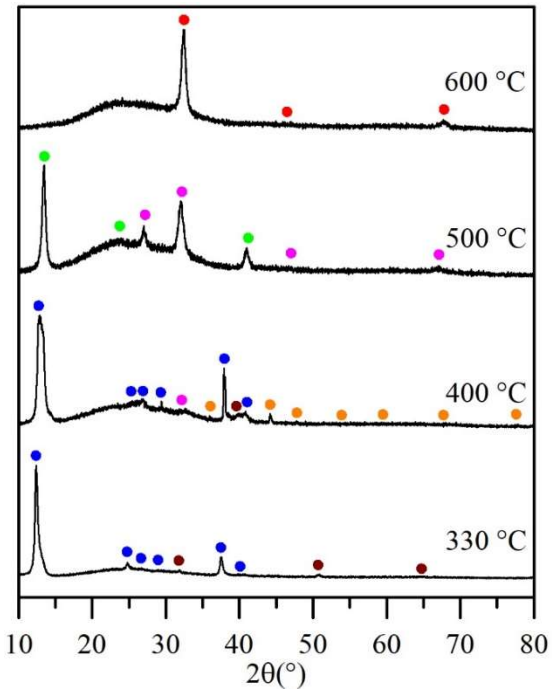

Figure 2.41 XRD patterns of the annealed films with temperature 330 – 600 °C under nitrogen atmosphere for 1 hour. ●Features index to cubic Pr_6O_{11} (JCPDS: 00-042-1121), ●features index to cubic $PrO_{1.833}$ (JCPDS: 00-006-0329), ● features index to monoclinic Pr_2CO_5 (JCPDS: 00-025-0696), ● features index to $Pr(C_2H_3O_2)_3$ (JCPDS: 00-022-0878), ● features index to hexagonal $PrOHCO_3$ (JCPDS: 00-027-1376) and ● features index to hexagonal $Pr(OH)_3$ (JCPDS: 01-083-2304).

Conclusion

XRD analysis revealed that deposition of $Pr(NO_3)_3{\cdot}6H_2O$ using spin coating and subsequent annealing under air provided crystalline cubic Pr_6O_{11} at annealing temperatures between 500 °C and 600 °C. Lower annealing temperatures provided Pr_2CO_5 and amorphous materials. It was also shown that high annealing temperatures can eliminate the carbon from the final film composition.

The combination of the AACVD technique and subsequent annealing under nitrogen atmosphere in the deposition chamber succeeded in transforming the hydroxyl and carbonate phases in the films to phase pure cubic Pr_6O_{11} at a temperature of 600 °C.

This chapter studied and explored the use of simple nitrate chemical precursors for binary transition metal and lanthanide oxide thin film fabrication via AACVD and spin coating. The major advantages of nitrate use is their availability and solubility in various solvents. The experiments in this chapter demonstrate that oxide thin film fabrication is possible by using a simple nitrate salt by either AACVD or spin coating technique in conjunction with a subsequent thermal annealing process.

These results provide the foundation on which to attempt to deposit ternary perovskite thin films ($LaNiO_3$) which will be presented in Chapter 3.

References

1 H. S. Kim, M. D. Kumar, W. H. Park, M. Patel and J. Kim, *Sensors Actuators, A Phys.*, 2017, **253**, 35–40.

2 F. A. Akgul, G. Akgul, N. Yildirim, H. E. Unalan and R. Turan, *Mater. Chem. Phys.*, 2014, **147**, 987–995.

3 S. Dolai, S. Das, S. Hussain, R. Bhar and A. K. Pal, *Vacuum*, 2017, **141**, 296–306.

4 B. K. Meyer, A. Polity, D. Reppin, M. Becker, P. Hering, P. J. Klar, T. Sander, C. Reindl, J. Benz, M. Eickhoff, C. Heiliger, M. Heinemann, J. Bläsing, A. Krost, S. Shokovets, C. Müller and C. Ronning, *Phys. Status Solidi*, 2012, **249**, 1487–1509.

5 V. H. Mistry, B. V. Mistry, B. P. Modi and U. S. Joshi, *Funct. oxides Nanomater.*, 2017, **1837**, 0400701–0400703.

6 M. R. Johan, M. Shahadan, M. Suan, N. L. Hawari and H. A. Ching, *Int. J. Electrochem. Sci. Int. J. Electrochem. Sci*, 2011, **6**, 6094–6104.

7 N. Serin, T. Serin, S. Horzum and Y. Celik, *Semicond. Sci. Technol.*, 2005, **20**, 398–401.

8 J. Medina-Valtierra, C. Frausto-Reyes, G. Camarillo-Martínez and J. A. Ramírez-Ortiz, *Appl. Catal. A Gen.*, 2009, **356**, 36–42.

9 T. Maruyama, *Sol. Energy Mater. Sol. Cells*, 1998, **56**, 85–92.

10 H. Derin and K. Kantarli, *Appl. Phys. A Mater. Sci. Process.*, 2002, **395**, 391–395.

11 K. Hyun, W. Jin and D. Heon, *Thin Solid Films*, 2000, **372**, 250–256.

12 H. A. Al-Jawhari, *Mater. Sci. Semicond. Process.*, 2015, **40**, 241–252.

13 H. Frenzel, A. Lajn and M. Grundmann, *Phys. Status Solidi - Rapid Res. Lett.*, 2013, **7**, 605–615.

14 R. Li, X. Tao, R. Chen, F. Fan and C. Li, *Chem. - A Eur. J.*, 2015, **21**, 14337–

14341.

15 D. Barreca, G. Carraro, V. Gombac, A. Gasparotto, C. Maccato, P. Fornasiero and E. Tondello, *Adv. Funct. Mater.*, 2011, **21**, 2611–2623.

16 V. Balouria, N. S. Ramgir, A. Singh, A. K. Debnath, A. Mahajan, R. K. Bedi, D. K. Aswal and S. K. Gupta, *Sensors Actuators B. Chem.*, 2015, **219**, 125–132.

17 S. C. Ray, *Sol. Energy Mater. Sol. Cells*, 2001, **68**, 307–312.

18 Ş. Korkmaz, B. Geçici, S. D. Korkmaz, R. Mohammadigharehbagh, S. Pat, S. Özen, V. Şenay and H. H. Yudar, *Vacuum*, 2016, **131**, 142–146.

19 R. Kon, Seung, W. K. Lee and S. J. Park, *Carbon Sci.*, 2004, **5**, 180–185.

20 I. V. Morozov, K. O. Znamenkov, Y. M. Korenev and O. A. Shlyakhtin, *Thermochim. Acta*, 2003, **403**, 173–179.

21 C. R. Crick and I. P. Parkin, *J. Mater. Chem.*, 2011, **21**, 14712–14716.

22 S. D. Jackson, D. S. Anderson, G. J. Kelly, T. Lear, D. Lennon and S. R. Watson, *Top. Catal.*, 2003, **22**, 3–4.

23 S. R. Segal, K. A. Carrado, C. L. Marshall and K. B. Anderson, *Appl. Catal. A Gen.*, 2003, **248**, 33–45.

24 S. D. Singh, A. Das, R. S. Ajimsha, M. N. Singh, A. Upadhyay, R. Kamparath, C. Mukherjee, P. Misra, S. K. Rai, A. K. Sinha and T. Ganguli, *Mater. Sci. Semicond. Process.*, 2017, **66**, 186–190.

25 H. Sato, T. Minami, S. Takata and T. Yamada, *Thin Solid Films*, 1993, **236**, 27–31.

26 J.-W. Park, K. N. Choi, S. H. Baek, K. S. Chung and H. Lee, *J. Korean Phys. Soc.*, 2008, **52**, 1868–1876.

27 H. Yang, Q. Tao, X. Zhang, A. Tang and J. Ouyang, *J. Alloys Compd.*, 2008, **459**, 98–102.

28 H. L. Lu, G. Scarel, M. Alia, M. Fanciulli, S. J. Ding and D. W. Zhang, *Appl. Phys. Lett.*, 2008, **92**, 2006–2009.

29 C. Díaz-Guerra, A. Remón, J. A. García and J. Piqueras, *Phys. Status Solidi Appl. Res.*, 1997, **163**, 497–503.

30 J. F. Gibbons and W. E. Beadle, *Solid. State. Electron.*, 1964, **7**, 785–790.

31 Y.-H. You, B.-S. So, J.-H. Hwang, W. Cho, S. S. Lee, T.-M. Chung, C. G. Kim and K.-S. An, *Appl. Phys. Lett.*, 2006, **89**, 222105-1–3.

32 S. Seo, M. J. Lee, D. H. Seo, S. K. Choi, D.-S. Suh, Y. S. Joung, I. K. Yoo, I. S. Byun, I. R. Hwang, S. H. Kim and B. H. Park, *Appl. Phys. Lett.*, 2005, **86**, 093509-1–3.

33 M. A. Mat-Teridi, A. A. Tahir, S. Senthilarasu, K. G. U. Wijayantha, M. Y. Sulaiman, N. Ahmad-Ludin, M. A. Ibrahim and K. Sopian, *Phys. Status Solidi - Rapid Res. Lett.*, 2014, **8**, 982–986.

34 B. Sasi, K. G. Gopchandran, P. K. Manoj, P. Koshy, P. Prabhakara Rao and V. K. Vaidyan, *Vacuum*, 2003, **68**, 149–154.

35 M. Guziewicz, J. Grochowski, M. Borysiewicz, E. Kaminska, J. Z. Domagala, W. Rzodkiewicz, B. S. Witkowski, K. Golaszewska, R. Kruszka, M. Ekielski and A. Piotrowska, *Opt. Appl.*, 2011, **XLI**, 431–440.

36 Y. Zhang, L. Li, H. Su, W. Huang and X. Dong, *J. Mater. Chem. A*, 2015, **3**, 43–59.

37 K. Nama Manjunatha and S. Paul, *Appl. Surf. Sci.*, 2015, **352**, 10–15.

38 M. D. Irwin, D. B. Buchholz, A. W. Hains, R. P. H. Chang and T. J. Marks, *Proc. Natl. Acad. Sci.*, 2008, **105**, 2783–2787.

39 L. Cattin, B. A. Reguig, A. Khelil, M. Morsli, K. Benchouk and J. C. Bern??de, *Appl. Surf. Sci.*, 2008, **254**, 5814–5821.

40 S.-W. Park, J.-M. Choi, E. Kim and S. Im, *Appl. Surf. Sci.*, 2005, **244**, 439–443.

41 S.-Y. Tsai, M.-H. Hon and Y.-M. Lu, *Solid. State. Electron.*, 2011, **63**, 37–41.

42 R. C. Korošec and P. Bukovec, *Acta Chim. Slov.*, 2006, **53**, 136–147.

43 E. L. Miller and R. E. Rocheleau, *J. Electrochem. Soc.*, 1997, **144**, 3072–

3077.

44 P. Zhai, Q. Yi, J. Jian, H. Wang, P. Song, C. Dong, X. Lu, Y. Sun, J. Zhao, X. Dai, Y. Lou, H. Yang and G. Zou, *Chem. Commun.*, 2014, **50**, 1854–1856.

45 H. Wang, C. Zou, L. Zhou, C. Tian and D. Fu, *Microelectron. Eng.*, 2012, **91**, 144–146.

46 B. Pejova, T. Kocareva, M. Najdoski and I. Grozdanov, *Appl. Surf. Sci.*, 2000, **165**, 271–278.

47 G. A. Niklasson and C. G. Granqvist, *J. Mater. Chem.*, 2007, **17**, 127–156.

48 N. Browne, N. C. Duesberg, M. P. Browne, H. Nolan, N. C. Berner, G. S. Duesberg, P. E. Colavita and M. E. G. Lyons, *Int. J. Electrochem. Sci. Int. J. Electrochem. Sci*, 2016, **11**, 6636–6647.

49 S. Mohan, P. Srivastava, S. N. Maheshwari, S. Sundar and R. Prakash, *Analyst*, 2011, **136**, 2845–2851.

50 R. Sharma, A. D. Acharya, S. B. Shrivastava, T. Shripathi and V. Ganesan, *Optik (Stuttg).*, 2014, **125**, 6751–6756.

51 M. Jlassi, I. Sta, M. Hajji and H. Ezzaouia, *Appl. Surf. Sci.*, 2014, **308**, 199–205.

52 M. Jlassi, I. Sta, M. Hajji and H. Ezzaouia, *Mater. Sci. Semicond. Process.*, 2014, **21**, 7–13.

53 G. Mattei, P. Mazzoldi, M. L. Post, D. Buso, M. Guglielmi and A. Martucci, *Adv. Mater.*, 2007, **19**, 561–564.

54 A. Venter and J. R. Botha, *S. Afr. J. Sci.*, 2011, **107**, 1–6.

55 A. J. Varkey and A. F. Fort, *Thin Solid Films*, 1993, **235**, 47–50.

56 X. Song and L. Gao, *J. Phys. Chem. C*, 2008, **112**, 15299–15305.

57 G. Vázquez, E. Alvarez and J. M. Navaza, *J. Chem. Eng. Data*, 1995, **40**, 611–614.

58 A. U. Mane, C. Wenger, G. Lupina, T. Schroeder, G. Lippert, R. Sorge, P. Zaumseil, G. Weidner, J. Dabrowski and H. J. Müssig, *Microelectron. Eng.*,

2005, **82**, 148–153.

59 A. A. Yadav, A. C. Lokhande, P. A. Shinde, J. H. Kim and C. D. Lokhande, *J. Mater. Sci. Mater. Electron.*, 2017, **28**, 13112–13119.

60 K. Dwight, P. Wu, Y. Gao and W. Wold, *J. Solid State Chem.*, 1991, **90**, 228–233.

61 G. Hass, J. B. Ramsey and R. Thun, *J. Opt. Soc. Am.*, 1959, **49**, 116.

62 D. H. Kim, J. Y. Yoon, H. C. Park and K. H. Kim, *Sensors Actuators B Chem.*, 2000, **62**, 61–66.

63 T. Watahiki, B. P. Tinkham, B. Jenichen, W. Braun and K. H. Ploog, *J. Cryst. Growth*, 2007, **301**–**302**, 381–385.

64 G. D. Wilk, R. M. Wallace and J. M. Anthony, *J. Appl. Phys.*, 2001, **89**, 5243–5275.

65 B. Zhou, Z. Li and C. Chen, *Minerals*, 2017, **7**, 1–14.

66 K. H. Goh, A. S. M. A. Haseeb and Y. H. Wong, *Mater. Sci. Semicond. Process.*, 2017, **68**, 302–315.

67 S. Inamoto, J. Yamasaki, E. Okunishi, K. Kakushima, H. Iwai and N. Tanaka, *J. Appl. Phys.*, 2010, **107**, 124510-1–10.

68 H. Nohira, T. Shiraishi, K. Takahashi, T. Hattori, I. Kashiwagi, C. Ohshima, S. Ohmi, H. Iwai, S. Joumori, K. Nakajima, M. Suzuki and K. Kimura, *Appl. Surf. Sci.*, 2004, **234**, 493–496.

69 S. Ohmi, C. Kobayashi, I. Kashiwagi, C. Ohshima, H. Ishiwara and H. Iwai, *J. Electrochem. Soc.*, 2003, **150**, F134–F140.

70 S. Wang, W. Wang and Y. Qian, *Thin Solid Films*, 2000, **372**, 50–53.

71 J. Jun, C. Wang, D. Won and D. Choi, *J. Korean. Phys. Soc.*, 2002, **41**, 998–1002.

72 M. Nieminen, M. Putkonen and L. Niinisto, *Appl. Surf. Sci.*, 2001, **174**, 155–165.

73 X. Wang, H. Liu, L. Zhao, C. Fei, X. Feng, S. Chen and Y. Wang, *Nanoscale*

Res. Lett., 2017, **12**, 1–7.

74 S. B. Brachetti-Sibaja, S. E. Rodil, M. A. Domínguez-Crespo, A. M. Torres-Huerta, E. Rodríguez and A. B. López-Oyama, *Thin Solid Films*, 2017, **636**, 615–621.

75 M. Nieminen, M. Putkonen and L. Niinisto, *Appl. Surf. Sci.*, 2001, **174**, 155–165.

76 A. Chin, Y. H. Wu, S. B. Chen, C. C. Liao and W. J. Chen, *VLSI Technol. 2000. Dig. Tech. Pap. 2000 Symp.*, 2000, 16–17.

77 M. R. and C. P. T.Mahalingam, *Thin Solid Films*, 1981, **78**, 229–233.

78 A. M. Herrero, B. P. Gila, C. R. Abernathy, S. J. Pearton, V. Craciun, K. Siebein, F. Ren, A. M. Herrero, B. P. Gila, C. R. Abernathy and S. J. Pearton, *Mater. Sci. Eng. C*, 2003, **23**, 123–128.

79 A. Singh, *Thin Solid Films*, 1983, **105**, 163–168.

80 A. V. Prokofiev, A. I. Shelykh and B. T. Melekh, *J. Alloys Compd.*, 1996, **242**, 41–44.

81 G. Adachi and N. Imanaka, *Chem. Rev.*, 1998, **98**, 1479–1514.

82 G. BONNET, M. LACHKAR, J. LARPIN and J. COLSON, *Solid State Ionics*, 1994, **72**, 344–348.

83 R. Sarbajna, A. Sivalakshmi Devi, K. Purandhar and M. V. Suryanarayana, *Int. J. ChemTech Res.*, 2013, **5**, 2810–2820.

84 L. Wang, Y. Ma, Y. Wang, S. Liu and Y. Deng, *Catal. Commun.*, 2011, **12**, 1459–1462.

85 L. Wei, Z. Yang, X. Chao and H. Jiao, *Ceram. Int.*, 2014, **40**, 5447–5453.

86 K. Ouzaouit, S. Villain, A. Essoumhi, A. Benlhachemi, H. Benyaich and J.-R. Gavarri, *Moroccan Phys. Condens. Matter Soc.*, 2009, **11**, 60–64.

87 M. I. Din, A. G. Nabi, A. Rani, A. Aihetasham and M. Mukhtar, *Environ. Nanotechnology, Monit. Manag.*, 2018, **9**, 29–36.

88 Z. Huang, K. Teramura, H. Asakura, S. Hosokawa and T. Tanaka, *J. Mater.*

Chem. A, 2017, **5**, 19351–19357.

89 Y. Wang, Z. Wei, P. Li, G. Li, K. Lian, W. Zhang, S. Zhuiykov and J. Hu, *IEEE Sens. J.*, 2018, **18**, 933–940.

90 T. D. Golden, Y. Shang, Q. Wang and T. Zhou, *Advanced Ceramic Processing*, INTECH, 2015.

91 J. G.Adachi(Juri Institute fro Environmental Science and Chemistry, Osaka, J. N. Imanaka(Osaka University, Osaka and C. Z.C. Kang(Internatioanl Center for Quantum Structures and State Key Laboratory for Surface Sciences, Beijing, *Binary Rare Earth Oxides*, Kluwer academic publishers, New york, Boston, Dordrecht, London, Moscow, 2005.

92 R. Kögler, A. Mücklich, F. Eichhorn, N. Schell, W. Skorupa and J. S. Christensen, *Vacuum*, 2007, **81**, 1318–1322.

93 B. H. C. Aspinall, J. Gaskell, P. A. Williams, A. C. Jones, P. R. Chalker, P. A. Marshall, J. F. Bickley, L. M. Smith and G. W. Critchlow, *Chem. Vap. Depos.*, 2003, **9**, 235–238.

94 C. Wenger, J. Dąbrowski, P. Zaumseil, R. Sorge, P. Formanek, G. Lippert and H. J. Müssig, *Mater. Sci. Semicond. Process.*, 2004, **7**, 227–230.

95 R. Lo, R. G. Toro, G. Malandrino, V. Raineri and I. L. Fragal, *Mater. Sci. Eng. B*, 2005, **118**, 192–196.

96 R. Lo, R. G. Toro, G. Malandrino, P. Fiorenza, V. Raineri and I. L. Fragal, *Mater. Sci. Eng. B*, 2005, **118**, 117–121.

97 A. Abrutis, M. Lukosius, Z. Saltyte, R. Galvelis and P. K. Baumann, *Thin Solid Films*, 2008, **516**, 4758–4764.

98 H. J. Osten, J. P. Liu, E. Bugiel and H. J. M, *J. Cryst. Growth*, 2002, **235**, 229–234.

99 D. Wolfframm, M. Ratzke, S. Kouteva-Arguirova and J. Reif, *Mater. Sci. Semicond. Process.*, 2003, **5**, 429–434.

100 H. J. Osten, E. Bugiel and A. Fissel, *Solid. State. Electron.*, 2003, **47**, 2161–2165.

101 C. K. Deng, H. R. Chang and B. S. Chiou, *Jpn. J. Appl. Phys.*, 2008, **47**, 853–856.

102 J. Zhang, R. B. Von Dreele and L. Eyring, *J. Solid State Chem.*, 1996, **122**, 53–58.

103 R. Lo Nigro, R. G. Toro, G. Malandrino, V. Raineri and I. L. Fragalà, *Mater. Sci. Eng. B Solid-State Mater. Adv. Technol.*, 2005, **118**, 192–196.

104 H. J. Osten, J. P. Liu, P. Gaworzewski, E. Bugiel and P. Zaumseil, *Tech. Dig. - Int. Electron Devices Meet.*, 2000, **25**, 653–656.

105 S. J. S. Jeon, K. I. K. Im, H. Y. H. Yang, H. L. H. Lee, H. S. H. Sim, S. C. S. Choi, T. J. T. Jang and H. H. H. Hwang, *Int. Electron Devices Meet. Tech. Dig. (Cat. No.01CH37224)*, 2001, **01**, 471–474.

106 H. J. Osten, J. P. Liu and H. J. Müssig, *Appl. Phys. Lett.*, 2002, **80**, 297–299.

107 J. P. Liu, P. Zaumseil, E. Bugiel and H. J. Osten, *Appl. Phys. Lett.*, 2001, **79**, 671–673.

108 H. J. Osten, J. P. Liu, E. Bugiel, H. J. Mu and P. Zaumseil, *Mater. Sci. Eng. R*, 2001, **87**, 297–302.

109 S. Shrestha, C. M. Y. Yeung, F. Marken, C. E. Mills and S. C. Tsang, *Sensors Actuators B Chem.*, 2007, **123**, 400–406.

110 S. Shrestha, F. Marken, J. Elliott, C. M. Y. Yeung, C. E. Mills and S. C. Tsang, *J. Electrochem. Soc.*, 2006, **157**, 517–520.

111 Y. Yuan, C. Liu, X. Cao, L. Cheng, L. Yuan, X. Zhang, M. Zhu, M. Xia, F. Rao, X. Li, L. Wu, X. Ji, S. Lv, Z. Song, S. Feng, H. Sun, S. Zhang, S. J. Wei, H. F. Zhu, K. Chen, D. Xu, J. Li, F. X. Gan, X. Zhang, Y. J. Xia and G. H. Li, *Opt. Mater. Express*, 2017, **7**, 4147–4155.

112 M. S. Kim, T. H. Kim, D. Y. Kim, D.-Y. Lee, S.-O. Kim and J.-Y. Leem, *Electron. Mater. Lett.*, 2012, **8**, 123–129.

113 V. Zatekin, K. Shcherbachev, Ny. Tabachkova, K. Eidelman, S. Ksenich, A. Batrakov, V. V Privezentsev, V. S. Kulikauskas, V. V Zatekin, K. D. Shcherbachev, N. Yu Tabachkova, K. B. Eidelman, S. V Ksenich and A. A.

Batrakov, *ISSN*, 2017, **11**, 1027–4510.

114 B. M. Abu-Zied and S. A. Soliman, *Thermochim. Acta*, 2008, **470**, 91–97.

115 B. M. Abu-Zied, Y. A. Mohamed and A. M. Asiri, *J. Rare Earths*, 2013, **31**, 701.

116 S. Ferro, *Int. J. Electrochem.*, 2011, **2011**, 1–7.

Chapter 3:

Deposition of Ternary oxide thin films

3.1 Introduction: Ternary oxide thin film deposition Lanthanum nickel oxide

This chapter will be focused on the fabrication of the ternary oxide, lanthanum nickel oxide, in thin film form by using a mixture of basic metal nitrates. Lanthanum nickel oxide ($LaNiO_3$) is an important metallic oxide with a perovskite-type structure[1] and it possesses a number of useful properties such as superconductivity,[2–4] good catalytic properties,[5,6] metallic properties with Pauli paramagnetic behavior over a wide range temperatures (temp. down to 4.2 K),[7–9] high chemical stability and is very stable in air.[10,11]

At room temperature, $LaNiO_3$ exhibits a rhombohedral crystal structure and at higher temperatures can be transformed to a cubic structure.[7,12] In addition, $LaNiO_3$ displays a lattice parameter of 3.84 Å, which is close to the unit cells of the common superconductor ($YBa_2Cu_3O_{7-x}$, YBCO), while its resistivity is 225 μΩ cm at 300 K.[12]

With these interesting properties, $LaNiO_3$ has been attractive for various applications, for example, in solid oxide fuel cells (SOFCs)[13], polymer electrolyte membrane fuel cells (PEMFCs) and molten carbonate fuel cells (MCFCs).[14] Moreover, it is a candidate bottom thin layer of electrode materials for ferroelectric thin film devices.[2,15,16] and ferroelectric memories.[1,17,18] Furthermore, $LaNiO_3$ with the (100) orientation structure can be utilised to control the orientation of perovskite-type ferroelectric thin films during the deposition process.[19]

$LaNiO_3$ thin film fabrication has been investigated by a variety of techniques including atomic layer deposition (ALD),[9] spin coating,[5,11] pulsed laser deposition (PLD),[12,20] conventional air-pressure-based spray,[21] sol-gel methods,[19,22] spray pyrolysis,[23] metal-organic deposition (MOD),[24,25] pulsed liquid-injection MOCVD,[17,26] mist plasma evaporation (MPE),[16] R.F. magnetron sputtering[1] and chemical solution deposition.[27]

Most of these techniques do, however, require high deposition or annealing temperatures (> 600 °C)[10,11,21,23,28,29] to achieve film formation and the composition of the final films also typically contains impurities such as La_2O_3, NiO and $La(OH)_3$.[8,23,30–33] Furthermore, some deposition methods are complicated and expensive,[9,12,20,28] inhibiting scale up for large and/or low-cost production. The study

described in this chapter will again be concentrated on the use of metal nitrate solution precursor systems, which will be used for AACVD or spin coating to fabricate the desired lanthanum nickel oxide thin films.

3.2 Lanthanum nickel oxide thin film deposition by AACVD

Table 3.1 List of precursor solution systems used in this chapter.

Precursor system	Ratio		
	$La(NO_3)_3 \cdot 6H_2O$	$Ni(NO_3)_2 \cdot 6H_2O$	NH_4NO_3
LNR11	1	1	-
LNR12	1	2	-
LNR13	1	3	-
LNR14	1	4	-
LNR15	1	5	-
LNR21	2	1	-
LNR31	3	1	-
LNR41	4	1	-
LN R51	5	1	-
LNAR111	1	1	1
LNAR112	1	1	2
LNAR115	1	1	5
LNAR1110	1	1	10

Table 3.1 shows the precursor recipes employed for lanthanum nickel oxide thin film deposition. Due to its successful implementation to reduce the deposition temperature in the described previous chapter, ammonium nitrate was also included in the mixed metal nitrate systems.

3.2.1 Thermogravimetric analysis of the precursor mixtures

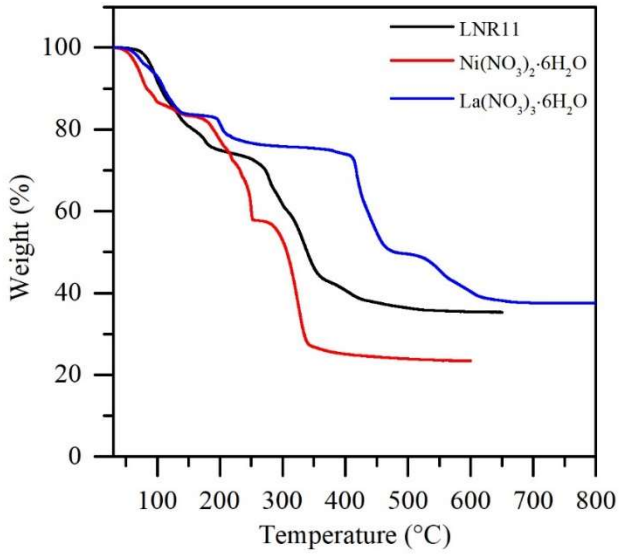

Figure 3.1 TGA curve of LNR11 precursor system and a comparison with $La(NO_3)_3{\cdot}6H_2O$ and $Ni(NO_3)_2{\cdot}6H_2O$.

Figure 3.1 presents the TGA curves of LNR11, $La(NO_3)_3{\cdot}6H_2O$ and $Ni(NO_3)_2{\cdot}6H_2O$ to compare the thermal decomposition of the combined nitrate system. The black TGA curve shows a decomposition of the LNR11 precursor system, which overlaps with the TGA curves of both the lanthanum and nickel nitrates at temperatures below 225 °C.

The TGA curve of the LNR11 precursor can be divided into two parts between 30 °C and 550 °C. The first weight loss of 24.29 % can be attributed to the loss of water of crystallization, which is complete by 188.33 °C. The second weight losses located between 260 and 430 °C can be attributed to the decomposition of the complex. Finally, a weight loss of 2.52% was observed between 432.58 and 550.50 °C to provide a stable residue of around 35.68% of the original mass, close to that expected for $LaNiO_3$ (calculated: 33.93%).

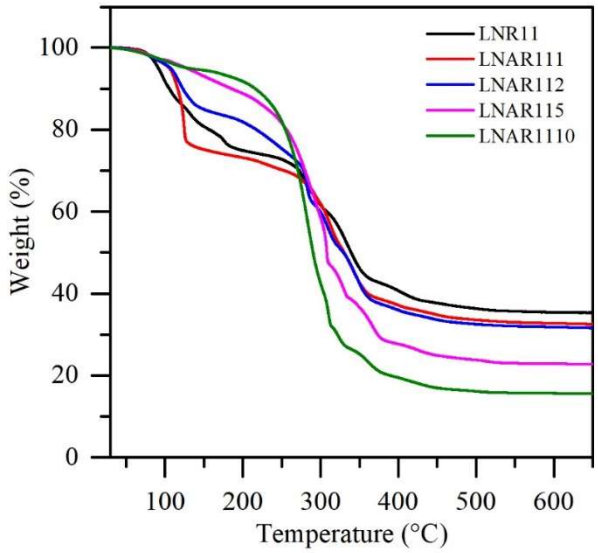

Figure 3.2 TGA curves of the LN R11 and LNA precursor systems.

Ammonium nitrate was also included in the thin film preparation described in this chapter in order to reduce the deposition temperature and to provide more oxidizing species in the deposition system to promote metal oxide formation. The TGA curves in Figure 3.2 present the thermal decompositions of mixtures with increasing ammonium nitrate ratios in the precursor recipes. These data reveal that an increasing ammonium nitrate ratio provides a lower thermal decomposition temperature than the LNR11 precursor system alone. The curves also demonstrate a trend of decreasing decomposition temperature with increasing ammonium nitrate content.

The precursor systems in Table 3.1 were studied by using AACVD under hot-wall conditions with the deposition results summarised in Table 3.2.

Powder formation on the substrate surface was a major problem during lanthanum nickel oxide thin film deposition using the hot-wall reactor. This problem was reminiscent of the deposition process observed for the lanthanum oxide thin films described in Chapter 2. The cold-wall reactor was, therefore, again employed to limit the powder formation problem using the deposition conditions shown in Table 3.3.

Table 3.2 Deposition conditions for of hot-wall AACVD of lanthanum nickel oxide thin films.

Precursor system	Ratio	Conc. (mol L^{-1})	Solvents	Substrate	Deposition		Annealing in Air	
					Temp. (°C)	Time (min)	Temp. (°C)	Time (min)
$La(NO_3)_3 \cdot 6H_2O$ $Ni(NO_3)_2 \cdot 6H_2O$	1:1-1:5 1:1-5:1	0.1-0.5	Ethanol, Methanol and water	Pilkington SiCO glass, FTO, Si wafer	150 -600	20 - 60	300 -600	60
$La(NO_3)_3 \cdot 6H_2O$ $Ni(NO_3)_2 \cdot 6H_2O$ NH_4NO_3	1:1:1-1:1:10	0.2	Ethanol, Methanol and water	Pilkington SiCO glass, FTO, Si wafer	150 -600	20 - 60	300 -600	60

Comments

- Increasing a ratio of lanthanum nitrate (LNR11-LNR51) offered amorphous films and white powder on the substrate surface.
- Increasing a ratio of nickel nitrate (LNR11-LNR15) provided shiny nickel metal films at 400 °C and black opaque films above 400 °C.
- Increasing concentrate of precursor provided shiny nickel metal film.
- Using water as solvent provided no deposition.
- Deposition at 150 °C to prepare the roughness surface and then increasing temperature deposition was performed. At the final results, the powder formation appeared on the substrate surface.
- Deposition at 150 °C and annealing under air provided white powder left on the substrate surface.
- After annealed under air, the deposited black film and/or shiny nickel metal film were transformed to nickel oxide film (transparent film).
- Increasing the ratio of ammonium nitrate (LNAR111-LNAR1110) provided nickel oxide films.
- A low ratio of ammonium nitrate provided amorphous film and powder films.
- Additive chemicals such as PVA, PEG, ethylcellulose and EDTA were used to increase a viscosity of the precursor solution but tended block the TSI generator operation.

Table 3.3 Deposition conditions for AACVD of lanthanum nickel oxide thin film.

Variable	Details
Substrate	FTO glass, 2.5×6 cm^2
Precursor	LNR11, concentration; 0.1 M
Solvent	Ethanol
Deposition time	1 hour
Deposition temperature	250-500 °C
Deposition atmosphere	Nitrogen
Reactor type	Cold-wall

3.2.2 Appearance of deposited films

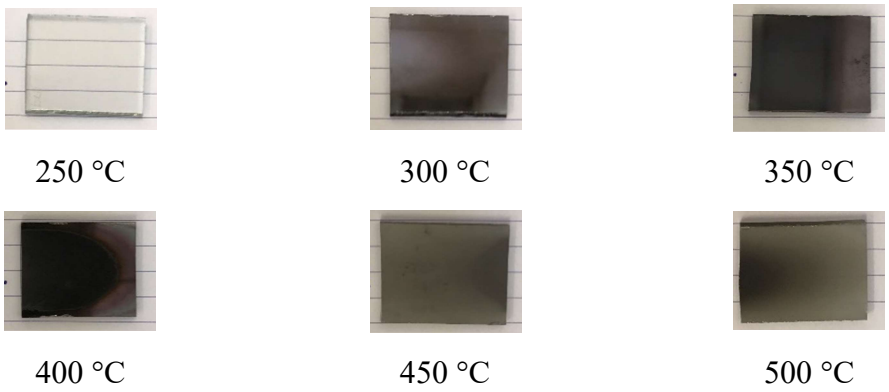

Figure 3.3 Appearance of the deposited films following the deposition conditions in Table 3.3 at various deposition temperatures.

Figure 3.3 displays the appearance of all the deposited films. It can be seen that the deposition temperature of 250 °C provided a transparent film, whilst film growth at 300 °C and 350 °C provided shiny metallic black films with some transparent material. Deposition at 400 °C yielded an opaque matt black film, whereas deposition temperatures of 450 °C and 500 °C offered opaque grey films. Some powdery material, however, was found on all the sample surfaces.

3.2.3 Crystallinity

The XRD patterns of all deposited films on FTO glass (Figure 3.4 (a)) reveal that crystalline films are produced at a deposition temperature of 300 °C. It is clear from

the XRD analysis that deposition of lanthanum nickel oxide ($LaNiO_3$, red dots) can be performed at a deposition temperature at 350°C. At this temperature, however, not only the $LaNiO_3$ phase but also $LaONO_3$, $Ni(NO_3)_2$, NiO and Ni_2O_3 could be identified. The XRD peaks which represent $LaNiO_3$ were observed to increase with raised deposition temperatures.

Interestingly, the XRD patterns of samples prepared at deposition temperatures between 400 °C and 500°C also presented diffraction maxima which could be attributed to other material phases comprising Sn and F elements (Figure 3.4 (b)). The FTO glass substrate is the only source of these elements in the deposition system.

To prove this assumption, an experiment under the conditions detailed in Table 3.4 was undertaken to investigate the behaviour of the FTO glass substrate itself when subjected to the AACVD process but in the absence of the nitrate reagents. XRD analysis was performed on the samples and the resultant appearance and sample names are displayed in Table 3.4.

The samples N400 and N500 which were treated at temperatures of 400 and 500 °C, respectively, but without ethanol, possessed a transparent appearance (Table 3.4) and both presented identical XRD patterns to the FTO glass substrate (Figure 3.4(b)).

In contrast, samples E375, E400 and E500 were treated at temperatures of 375, 400 and 500 °C, respectively, with a pure ethanol aerosol. The resultant appearance of these samples was an opaque grey. The XRD patterns of samples E375, E400 and E500 in Figure 3.4(b) display peaks arising from Sn, SnO, SnO_2 and Sn_2F_6, whereas sample E350, which was treated at the lower testing temperature of 350 °C, displayed maxima arising from the unchanged FTO glass. Thus, it can be shown that ethanol can reduce Sn and incorporate fluoride from the FTO glass at temperatures above 350 °C, even under a nitrogen atmosphere.

Furthermore, XRD patterns of sample E500A600 provided similar 2θ positions to those of FTO glass indicating that the ‘reduced’ FTO glass which was subjected to ethanol at 500 °C can be reconverted to FTO, albeit with some loss of transparency and conductivity (checked with a multi-meter).

Table 3.4 Conditions of the FTO glass performance test and appearance of FTO glass after the process.

Sample	Deposition condition details								
	Substrate	**Precursor**	**Testing temperature (°C)**	**Testing time (hour)**	**Testing atmosphere**	**Ethanol**	**Annealing temperature (°C)**	**Annealing time (hour)**	**Appearance**
FTO glass	FTO glass	-	-	-	-	-	-	-	
N400	FTO glass	-	400	1	N_2	-	-	-	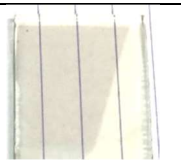
N500	FTO glass	-	500	1	N_2	-	-	-	
E350	FTO glass	-	350	1	N_2	✓	-	-	
E375	FTO glass	-	375	1	N_2	✓	-	-	
E400	FTO glass	-	400	1	N_2	✓	-	-	

Sample	Deposition condition details								
	Substrate	**Precursor**	**Testing temperature (°C)**	**Testing time (hour)**	**Testing atmosphere**	**Ethanol**	**Annealing temperature (°C)**	**Annealing time (hour)**	**Appearance**
E500	FTO glass	-	500	1	N_2	✓	-	-	
E500A600	FTO glass	-	500	1	N_2	✓	600	1	

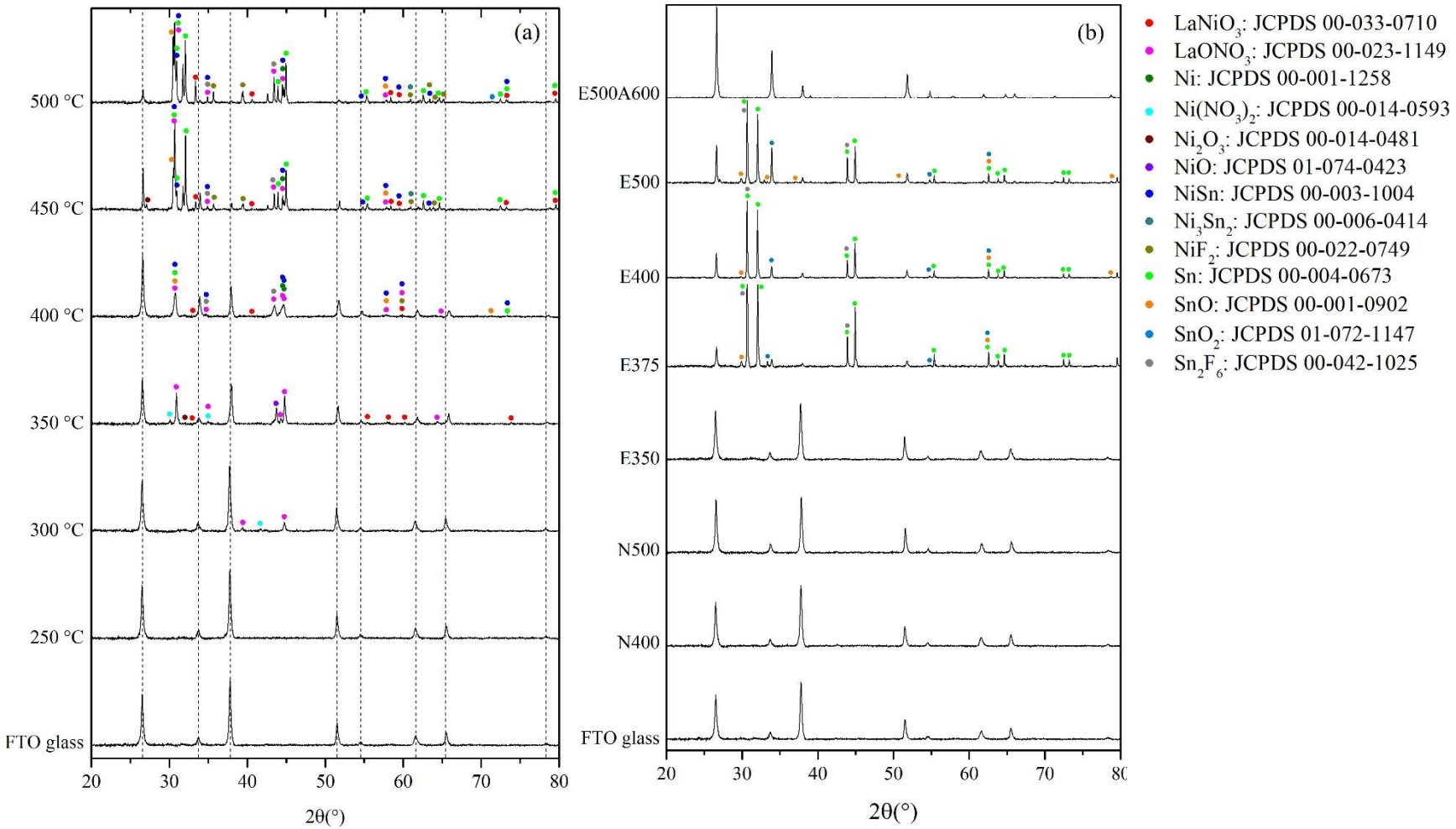

Figure 3.4 XRD patterns of (a) films deposited at different temperatures using the LNR11 precursor system and (b) testing the FTO glass performance.

3.2.4 Compositional analysis

EDS analysis was performed on all the samples fabricated following the deposition conditions of Table 3.3. The results are shown in Table 3.5.

Table 3.5 Atomic % of elements on samples fabricated using the LNR11 precursor system at various deposition temperatures.

Deposition temperature (°C)	Atomic %									
	La	**Ni**	**O**	**Sn**	**F**	**C**	**Si**	**Na**	**Mg**	**Ca**
250	0.18	12.02	54.89	28.43	1.86	1.56	0.94	0.12	0.00	0.00
300	1.18	32.92	20.42	29.84	3.27	0.00	8.72	2.37	0.69	0.59
350	6.44	26.63	24.04	27.27	2.25	1.98	8.45	2.30	0.61	0.00
400	12.70	34.74	26.16	16.70	4.83	3.59	1.00	0.27	0.00	0.00
450	3.81	24.48	19.61	37.17	2.28	3.06	7.52	1.67	0.38	3.95
500	0.15	2.87	43.25	13.41	1.66	0	27.57	5.35	1.54	2.06

Table 3.5 reveals all samples contained significant proportions of La, Ni and O which can all contribute to lanthanum nickel oxide. The EDS results demonstrate an increasing atomic % of La and Ni with increasing deposition temperature until 400 °C when these proportions dropped. The sample prepared at 400 °C exhibited the highest atomic % of La and Ni, whereas samples deposited at 250 and 500 °C possessed atomic %, lower than 1%. Due to noise from the FTO substrate, however, more quantitative measurements were not possible.

EDS mapping analysis was employed to further confirm the elemental distribution of the selected samples and the results are shown in Figures 3.5 and 3.6 for films deposited at 450 and 500 °C, respectively, on FTO glass substrates

Figures 3.5 and 3.6 illustrate areas containing high proportions (atomic %) of La and Ni as represented by the circular white ball-like features. This may reflect the particulate nature of the lanthanum oxide deposited by the AACVD technique.

Deposition temperature of 450 °C

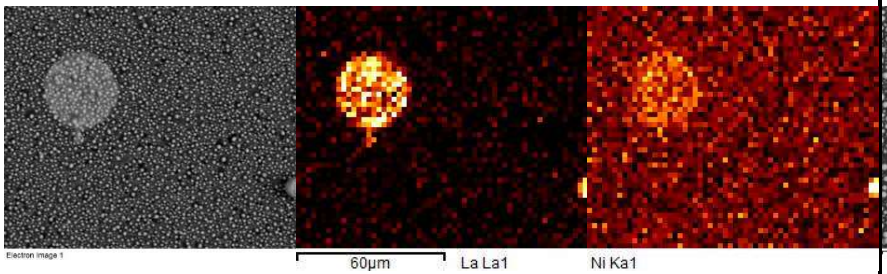

La: 0.28 % **Ni**: 5.38 %

O: 39.43 % **Sn**: 13.88 % **F**: 1.88 %

Figure 3.5 EDS Mapping analysis of the film deposited from LNR11 precursor system at 450 °C on a FTO glass substrate.

Deposition temperature of 500 °C

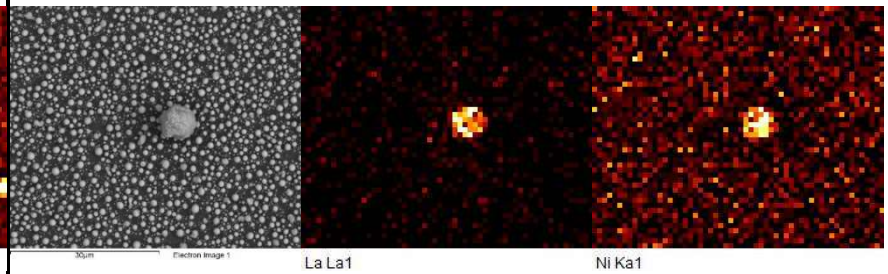

La: 0.15 % **Ni**: 2.87 %

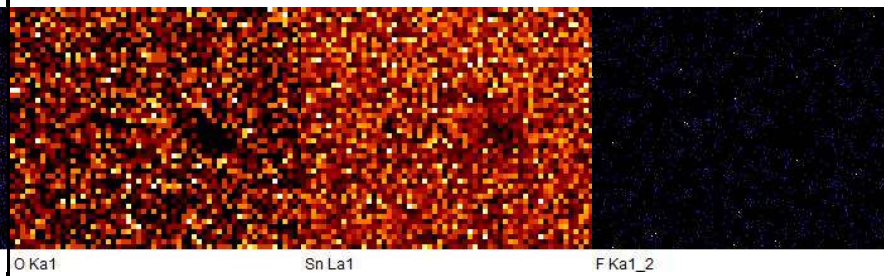

O: 43.25 % **Sn**: 13.41 % **F**: 1.66 %

Figure 3.6 EDS Mapping analysis of the film deposited from LNR11 precursor system at 500 °C on a FTO glass substrate.

3.2.5 Surface and cross-section morphology

SEM analysis was performed on all samples which were prepared by the deposition conditions shown in Table 3.3. SEM micrographs in Figures 3.7 (surface) and 3.7 (cross-section) show a distinct difference in character between the samples prepared with low and high deposition temperatures, 250 - 350 °C and 400 - 500 °C, respectively.

Samples fabricated at the lower deposition temperatures clearly showed complete and uniform coverage of the FTO substrate. Deposition temperatures of 250 and 300 °C provided rounded particles on the sample surface (Figures 3.7 (a) and (b)), whereas 350 °C provided more angular shapes and larger particles (Figure 3.7 (c)).

The film deposited at 400 °C provided a sample comprising agglomerated particles (Figure 3.7 (d)) and a higher thickness (around 703 nm) (Figure 3.8 (d)) than other samples. Interestingly, nanorods with a dimension of around 725 × 96 nm were found only at this deposition temperature, Figure 3.8 (d).

Samples which were deposited at 450 and 500 °C contained a unique feature with numerous large oval particles across the surface (Figures 3.7 (e) - (f) and Figures 3.8 (e) - (f)), which had deposited on to a more continuous thin film underneath. Similar oval particles were found in the analogous deposition on FTO.

Figure 3.9 displays cross-section views of the samples from the experiments on FTO (Table 3.4). It was found that the material deposited at 350 °C, sample E350, appeared to be visually very similar to the FTO glass substrate (Figures 3.9 (b) and (e)). At the higher testing temperature of 500 °C, however, the cross-section SEM micrographs (Figures 3.9 (d) and (f)) evidenced similar large oval particles as observed in Figures 3.8 (e) and (f).

It can be concluded, therefore, that the oval particles result from a reaction between ethanol and the FTO surface at temperatures above 350 °C. Furthermore, the XRD patterns (Figure 3.4 (b)) and the appearance of the samples shown in Table 3.4 can be deduced to be a result of the formation of the large oval particulates.

AFM analysis was also performed on the samples prepared with the deposition conditions summarised in Table 3.3 and the results are shown in Table 3.6. The surface

morphologies of all the samples were consistent with the production of compacted rounded particles, comparable to those observed in the SEM micrographs (Figure 3.7) with a particle size that increased with increasing deposition temperatures. The surface roughness data of all the samples are summarised in Figure 3.10 and are consistent with increasing deposition temperature effecting an increase of the surface roughness of the samples. The surface roughness graph in Figure 3.10 reveals the sharply increasing values between deposition temperatures 350 - 400 °C and 400 - 450 °C alongside the occurrence of the nanorods and large oval particles, respectively (Figures 3.8 (d) and (e)).

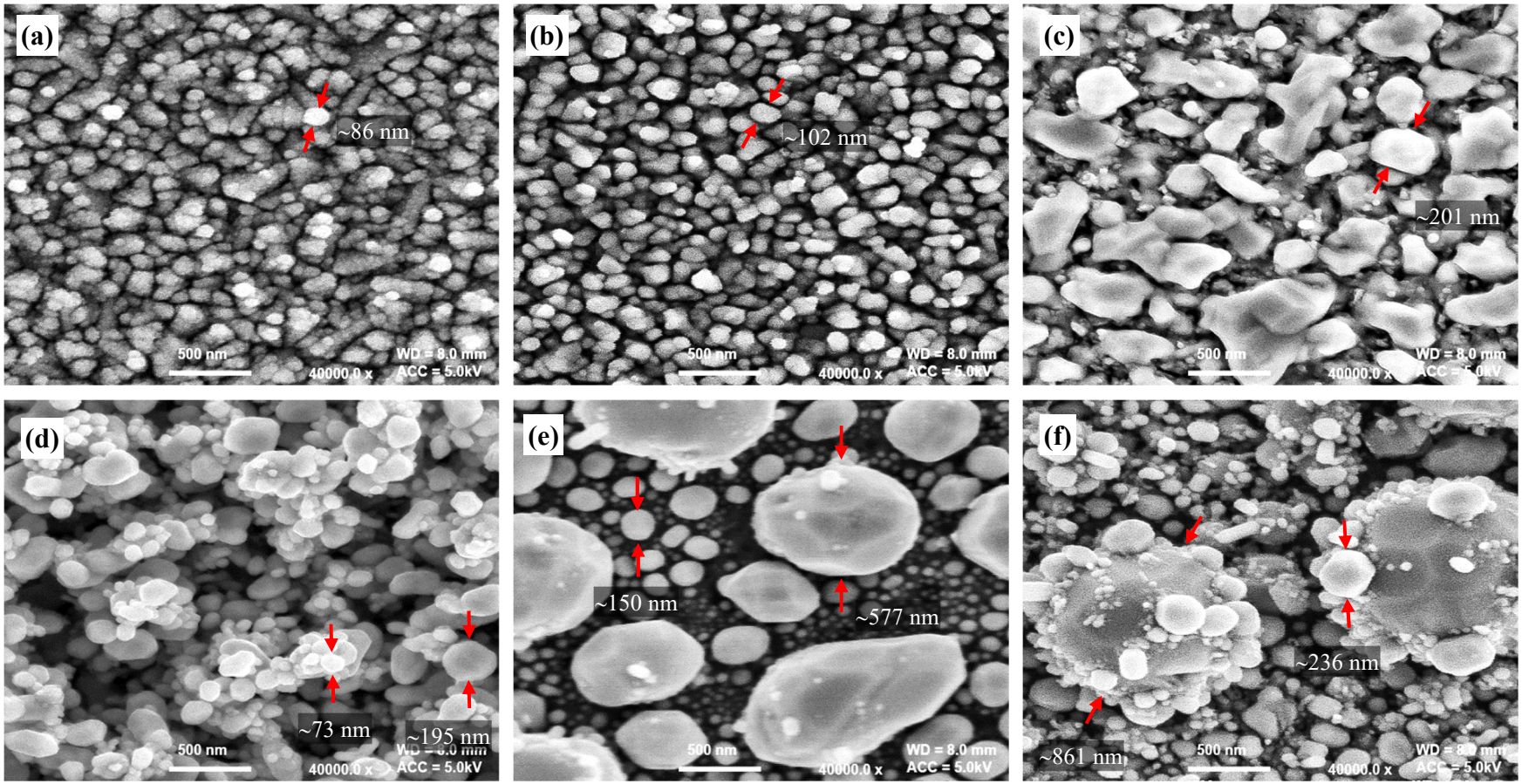

Figure 3.7 SEM micrographs of samples prepared using the LNR11 precursor system on FTO glass with the deposition temperatures at (a) 250 °C, (b) 300 °C, (c) 350 °C, (d) 400 °C, (e) 450 °C and (f) 500 °C.

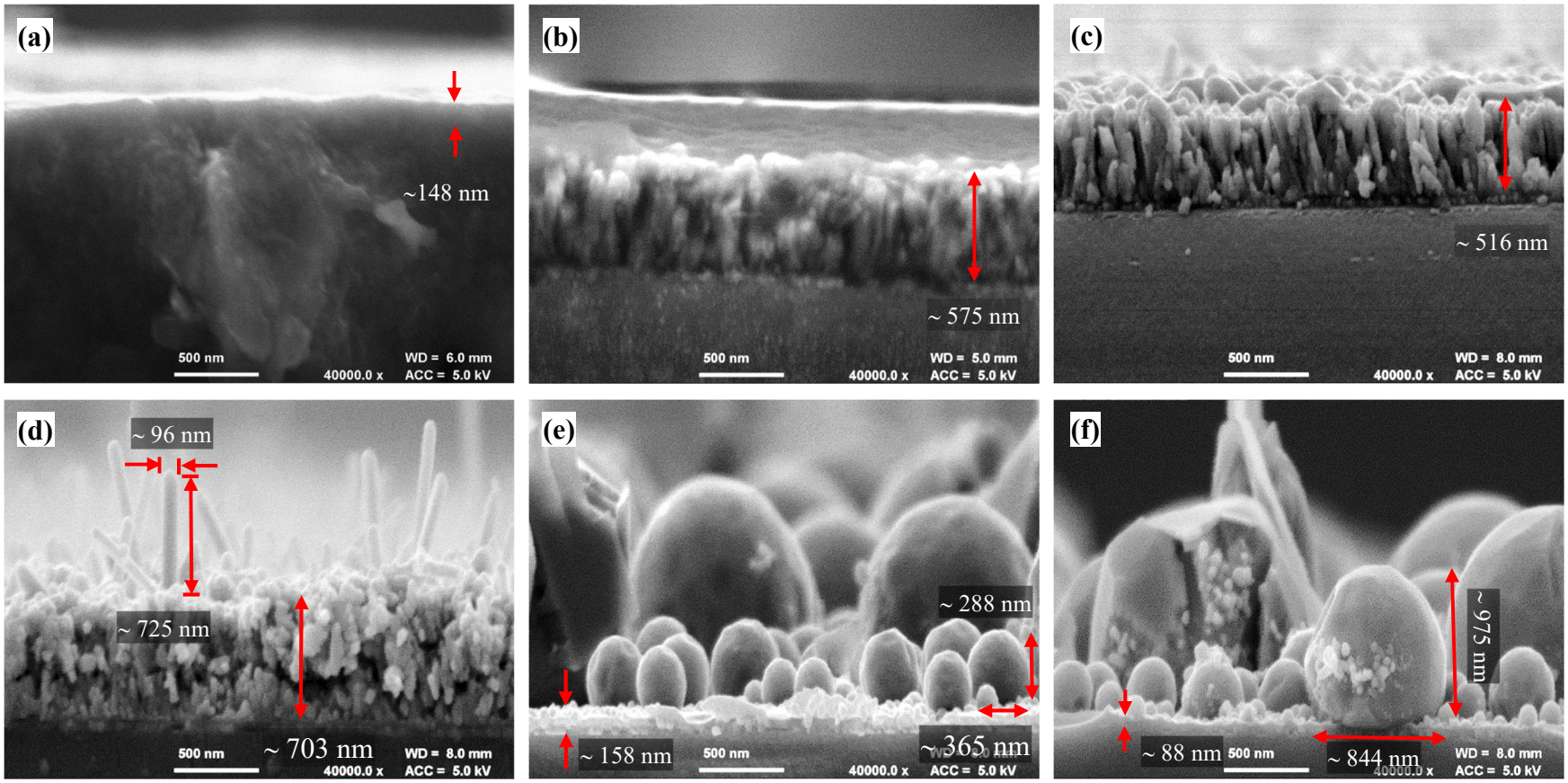

Figure 3.8 Cross-section SEM micrographs of samples prepared using the LNR11 precursor system on FTO glass with the deposition temperatures at (a) 250 °C, (b) 300 °C, (c) 350 °C, (d) 400 °C, (e) 450 °C and (f) 500 °C.

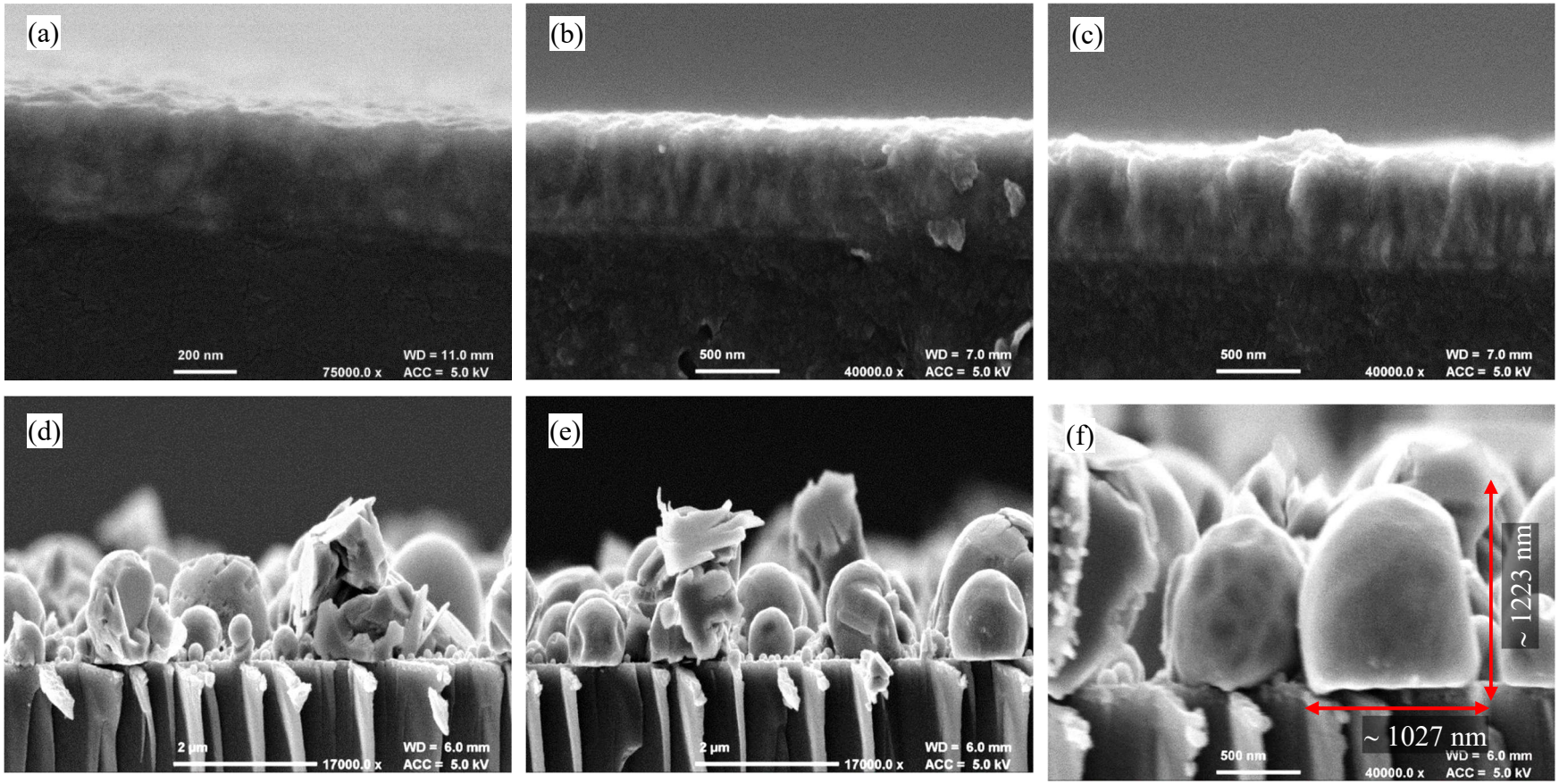

Figure 3.9 Cross-section SEM micrographs of samples (a) FTO glass, (b)-(c) E350 and (d)-(f) E500.

Table 3.6 Surface morphology of samples from the deposition conditions shown in Table 3.3 assessed by AFM on various substrate surfaces.

Deposition temperature (°C)	2D	3D
250	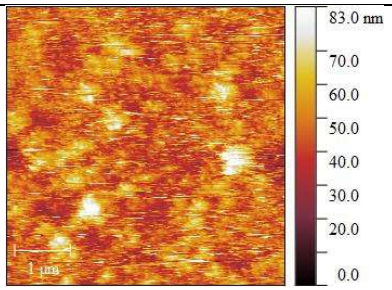	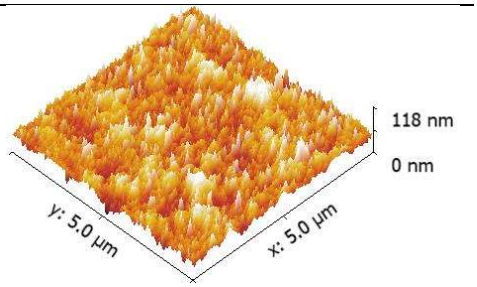
300	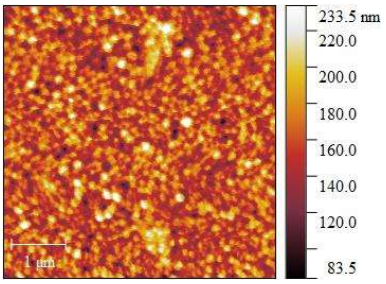	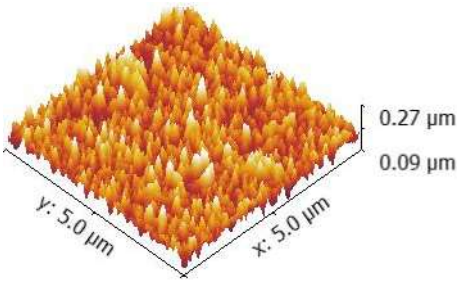
350	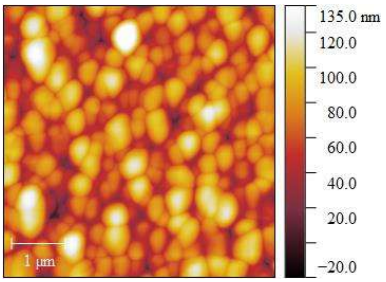	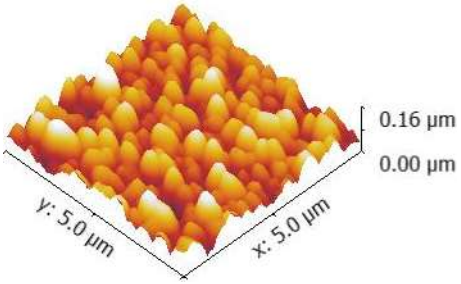
400	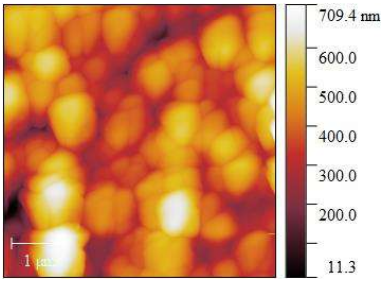	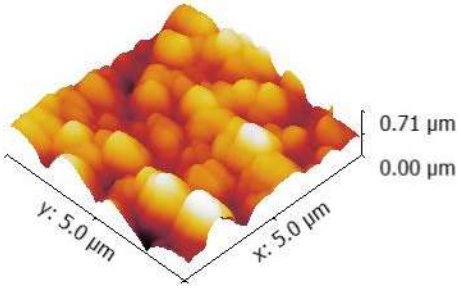
450	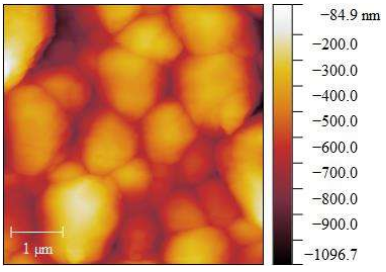	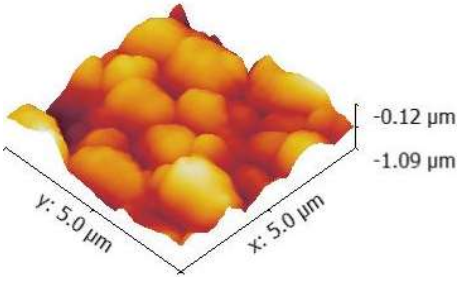

Deposition temperature (°C)	2D	3D
500	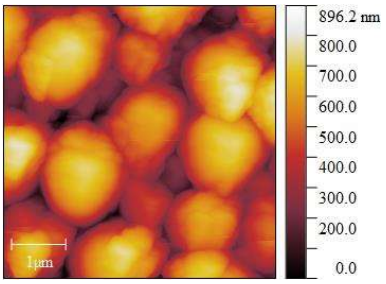	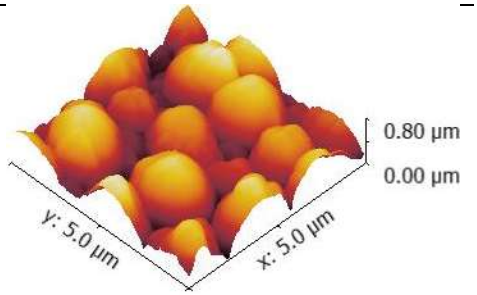

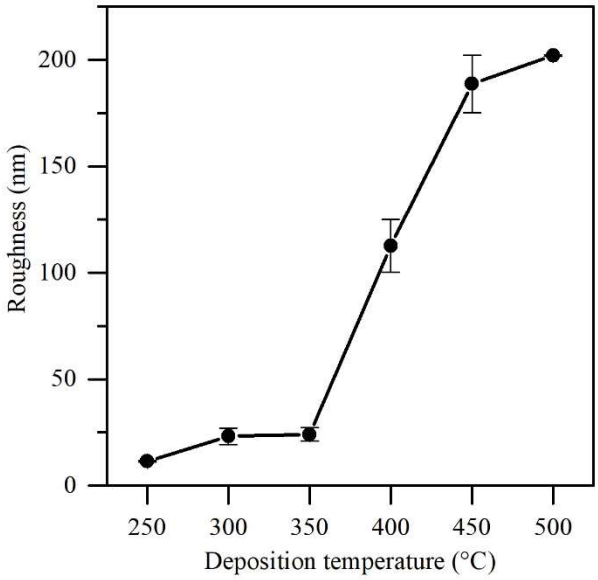

Figure 3.10 AFM surface roughness of samples from the deposition conditions of Table 3.3 on FTO glass. Area measurement: 5 μm^2.

3.3 Lanthanum nickel oxide thin film deposition by spin coating

Due to initial difficulties encountered resulting from poor spreading and adhesion of the precursor solutions across the substrate surface, acetic acid was added the precursor solutions during the thin film spin coating described throughout this section.

The inclusion of acetic acid as a component of the precursor solution for oxide thin film fabrication has been reported in the literature for a variety of spin coated materials such as ZnO, CdO, GIO, TiO_2 and ITO,[34–39] in order to act as a stabilising and chelating agent.[38,40,41] The added acetic acid is also thought to act as a condensation and hydrolysis catalyst as it suppresses the reactivity of metal alkoxides and metal hydroxide species, both of which are considered to be detrimental to the growth of oxide films.[38,41–44]

The inclusion of acetic acid has also been reported to improve the morphology of thin films by providing improved uniformity, fewer pinholes, increased grain size and reduced roughness. Furthermore, the adherence between the thin film and substrate is enhanced,[36,38,43,45,46] alongside increased crystallinity and improved electrical properties of the resultant thin films.[38,43,45] Literature reports of acetic acid use have described the inclusion of quantities ranging from a few droplets to 40 vol. %. [40]

For these reasons, acetic acid was introduced to the lanthanum nickel oxide thin film recipe for the spin-coating reported in this section. The deposition conditions are shown in Table 3.7.

Table 3.7 Deposition conditions for spin coating of lanthanum nickel oxide thin film.

Variable	Detail		
Substrate	Pilkington SiCO glass, 2.5×2.5 cm^2		
Solvent	Ethanol		
Deposition layer	15 layers		
Drying temperature	150 °C, 15 min		
Annealing atmosphere	Air		
Annealing time	1 hour		
Annealing temperature	300–600 °C		
Precursor solutions	**Ratio (Conc. 0.2 M)**		
	$La(NO_3)_3{\cdot}6H_2O$	**$Ni(NO_3)_2{\cdot}6H_2O$**	**CH_3COOH (vol. %)**
LNR11	1	1	-
LNR11-AA5	1	1	5

3.3.1 Thermogravimetric analysis of the precursor components

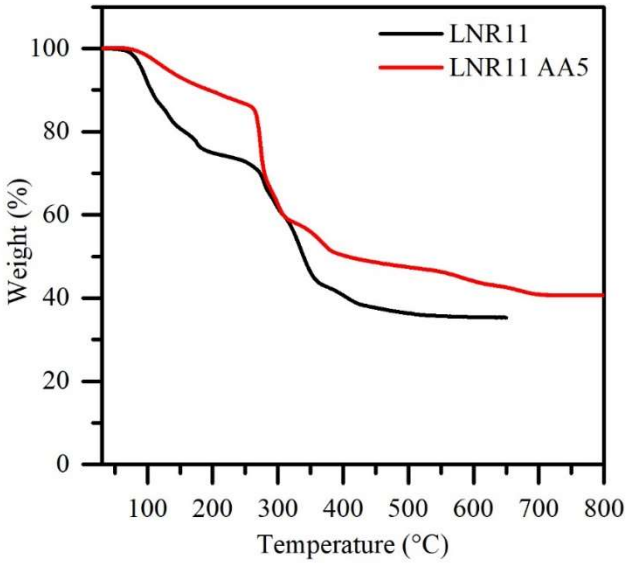

Figure 3.11 Comparison of the TGA curves of LN R11 and LNR11 AA5 precursor systems.

TGA measurement was performed on the LNR11-AA5 precursor system. Figure 3.11 presents a comparison of the TGA curves provided by the LNR11-AA5 and the LNR11 precursor systems. The TGA curve of LNR11-AA5 (red line) revealed three

main stages of weight loss. The first, with around 14 % weight loss occurring between 100 and 260 °C, can be attributed to the loss of water, solvent residues and some acetate groups. Around 36% of weight is lost at decomposition temperatures between 260 and 400 °C, which can be attributed to the decomposition of the nitrate complexes. Finally, a weight loss of around 6% is observed between 535 and 710 °C. The LNR11-AA5 precursor system containing acetic acid left a higher percentage residual mass than LNR11 which contained no an acetic acid.

3.3.2 Appearance of deposited films

Table 3.8 illustrates the appearances of the films deposited from LNR11 and LNR11-AA5. It can be clearly seen that LNR11-AA5, which contained acetic acid in the precursor recipes, had a significant effect on the film appearance, providing better spreading over the substrate surface and improved homogeneity than the LNR11 precursor alone. LNR11-AA5 yielded opaque grey films after drying whereas the LNR11precursor system was more transparent, primarily because LNR11 was more difficult to deposit on the substrate.

Table 3.8 Appearance of the deposited films from the LNR11 and LNR11-AA5 precursor systems.

Precursor system	**As-deposited film**	**Annealing films with various temperature**			
		300 °C	**400 °C**	**500 °C**	**600 °C**
LNR11				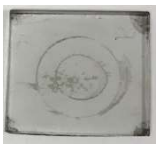	
LNR11-AA5					

After annealing under an air atmosphere with temperatures ranging from 300 to 500 °C, the deposited films presented an opaque grey colour, which was similar to the pre-annealed films. At an annealing temperature of 600 °C, however, the colour of the deposited film was transformed from grey to black. The XRD results in Figure 3.16

indicate that the $LaNiO_3$ phase was produced at this temperature. Conductivity measurments of all the films assessed by using a multi-meter, indicated that only annealing temperature of 600 °C had provided a conductive film, Table 3.9.

Table 3.9 Conductivity of deposited films.

Precursor system	As-deposited	Annealing temperature (°C)			
		300	400	500	600
LNR11	×	×	×	×	×
LNR11-AA5	×	×	×	×	Conductive

3.3.3 Surface and cross-section morphology

The surface morphology of the as-deposited and annealed films using both the LNR11 and LNR11-AA5 precursors was analysed by FESEM and AFM. Figure 3.12 shows the FESEM micrographs of the films prepared from the LNR11 precursor. The as-deposited film was relatively rough, containing some cracks and large particles on the surface. After annealing at 600 °C, the deposited material comprised numerous particles across the substrate surface rather than a continuous films (Figures 3.12 (b) and (c)).

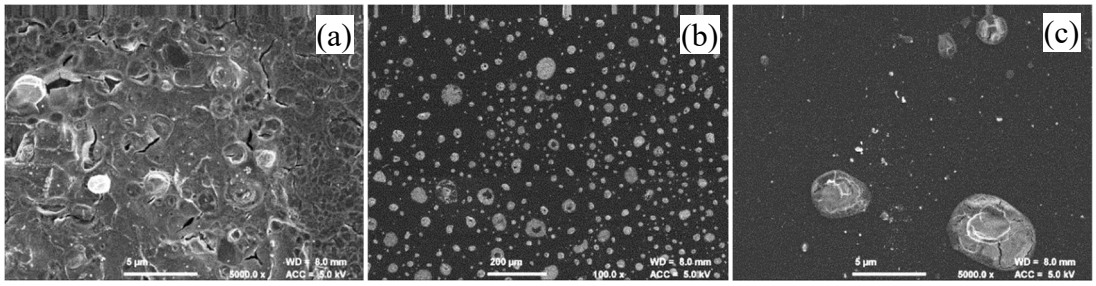

Figure 3.12 SEM micrographs of films from the LNR11 precursor system; (a) as-deposited film (b) annealed film at 600 °C at 100.0x magnification and (c) annealed film at 600 °C at 5000.0x magnification.

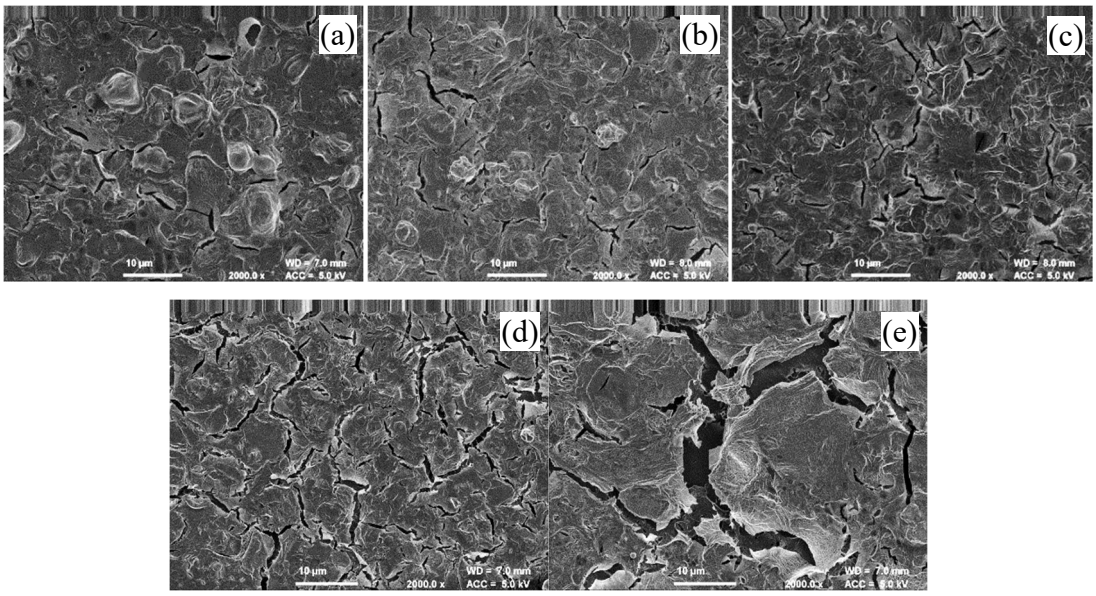

Figure 3.13 SEM micrographs of films from the LNR11-AA5 precursor system (a) as-deposited film and annealed films annealed at different temperatures: (b) 300 °C (c) 400 °C (d) 500 °C and (e) 600 °C.

Figure 3.13 illustrates the FESEM micrographs of the films prepared by using the LNR11-AA5 precursor system. The as-deposited film possessed large particles, some cracks and displayed significant roughness. On annealing, however, the size of the cracks increased and appeared of expand. Although this was particularly pronounced for the film annealed at 600 °C, the films prepared with this precursor recipe displayed significantly improved continuity in comparison to those provided by LNR11. It may be assumed, therefore, that addition of acetic acid increases the adhesiveness and spreading ability of the precursor solution. Indeed, Smith and co-workers have previously suggested that the selective adsorption of acetic acid on specific facets of the substrate surface can increase the adhesive performance of the precursor solution on the desired substrate.[47]

Table 3.10 illustrates the surface morphology of the as-deposited films from the LNR11-AA5 precursor determined by AFM, while Figure 3.14 reveals a relation between the average surface roughness values and the annealing temperatures. After annealing, the average surface roughness of the deposited films is observed to decrease. This is possibly due to improved removal of impurities from the surface with increasing temperature. This is also consistent with the EDS results shown in Table 3.11 that show a decrease in the atomic % of carbon with increasing temperature.

In addition, the film annealed at 600 °C was crystalline. Figure 3.15 shows this film in cross-section and reveals a film thickness of 2.24 µm.

Table 3.10 Surface morphology of the as-deposited and annealed films from the LNR11 and LNR11-AA5 precursor systems at different annealing temperatures using AFM on various substrate surfaces.

LNR11 precursor system		
Annealing temperature (°C)	**2D**	**3D**
As-deposited	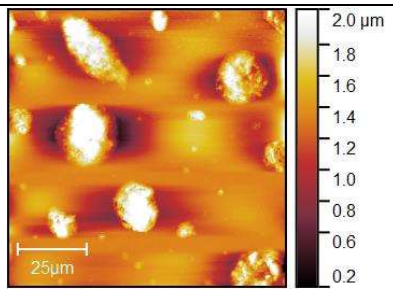	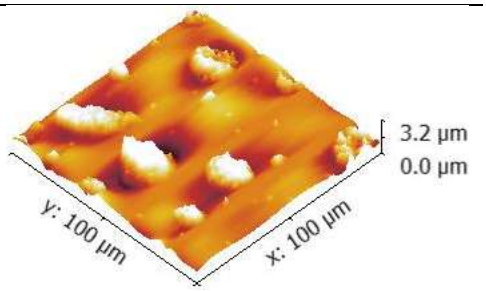
600	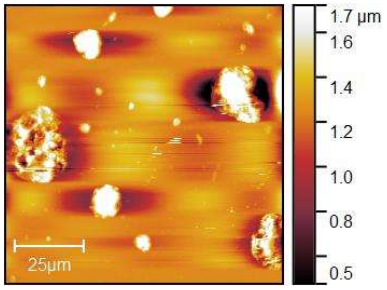	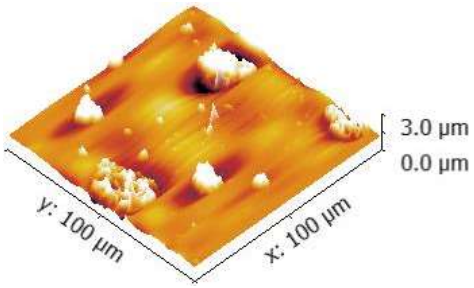

LNR11-AA5 precursor system		
Annealing temperature (°C)	**2D**	**3D**
As-deposited	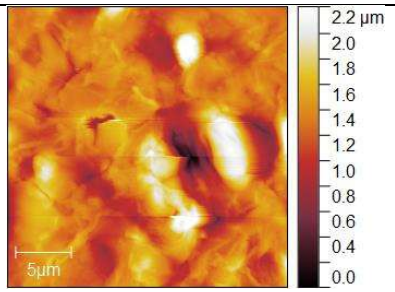	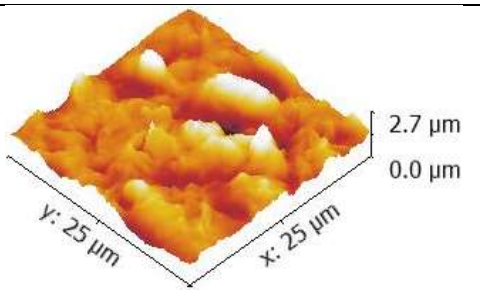
300	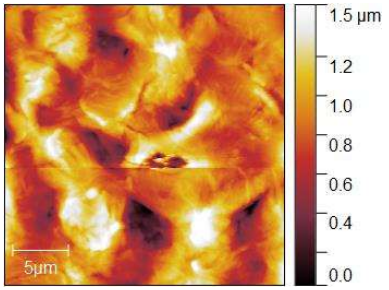	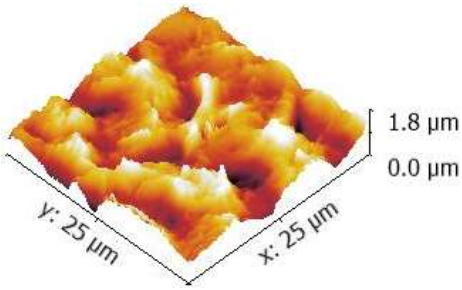
400	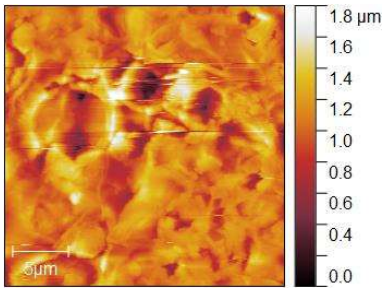	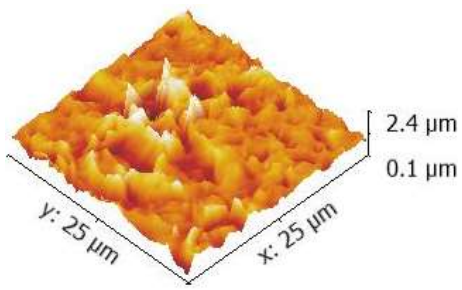
500	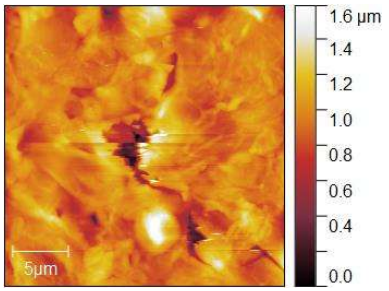	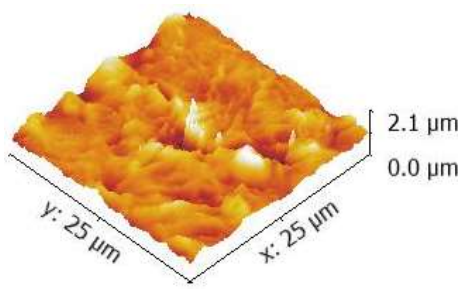
600	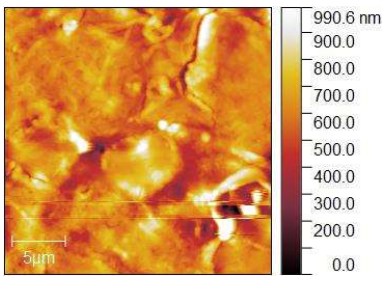	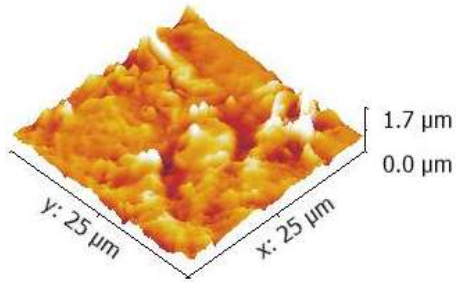

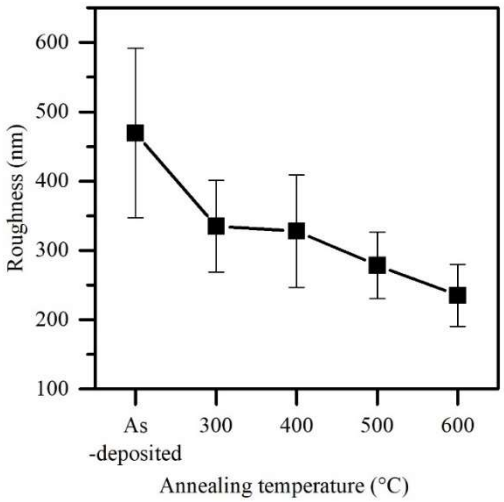

Figure 3.14 Average surface roughness of the films deposited from the LNR11-AA5 precursor system with various annealing temperatures. Area measurement 25μm^2.

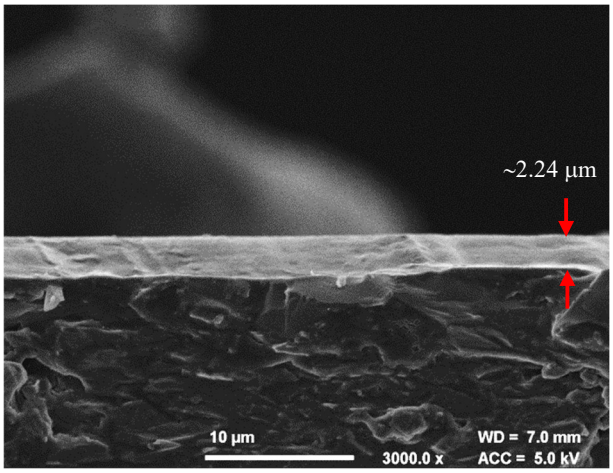

Figure 3.15 Cross-section SEM micrograph of the film annealed at 600 °C from the LNR11-AA5 precursor system.

3.3.4 Crystallinity

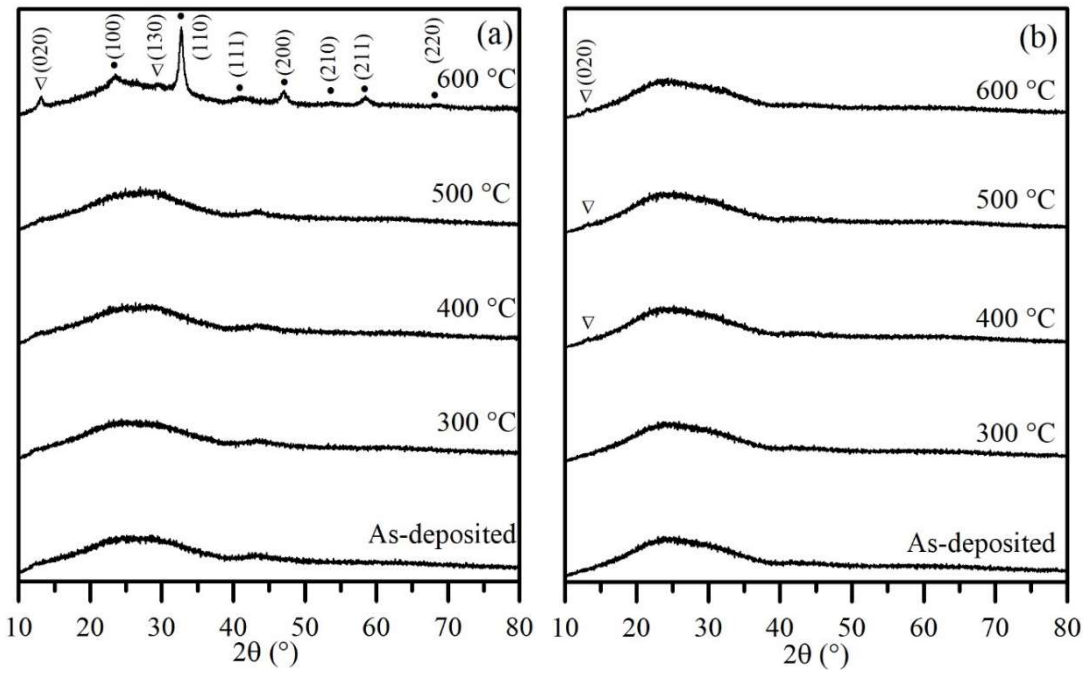

Figure 3.16 XRD patterns of the as-deposited and annealed films using (a) LNR11-AA5 and (b) LNR11 precursor systems. (•) and (∇) Features corresponding to cubic $LaNiO_3$ (JCPDS: 00-033-0710) and monoclinic $La_2O_2CO_3$ (JCPDS: 00-048-1113), respectively.

The XRD patterns shown in Figure 3.16 (a) revealed that the deposited film prepared by use of the LNR11-AA5 precursor was composed of the $LaNiO_3$ and $La_2O_2CO_3$ phases after annealing under an air atmosphere at a temperature of 600 °C. Below this temperature all the other films were amorphous. In contrast, the LNR11 precursor system did not provide any $LaNiO_3$ and the only cystalline phase obtained was $La_2O_2CO_3$ (Figure 3.16 (b)). From the XRD analysis, it can be deduced that addition of acetic acid assists the formation of the crystalline ternary oxide film, $LaNiO_3$.

3.3.5 Compositional analysis

EDS analysis was performed on all deposited films prepared from the LNR11-AA5 precursor; the analysis results are shown in Table 3.11. The EDS data confirmed that pre-and post-annealed films contained constant La and Ni contents, whilst the oxygen and carbon contents displayed a decreasing trend with increasing annealing temperature.

Noticeably, the atomic % of Si, Na, Mg and Ca associated with the substrate increased with increasing annealing temperature, most likely due to reducing film thickness. Furthermore, the quantitative analysis evidences a reducing atomic percentage of oxygen from around 47.39% (as-deposited film) to 39.27% (annealed film at 600 °C), which may be assumed to be due to a loss of oxygen from the deposited film when heated at high temperature.

Table 3.12 shows the atomic ratio between La, Ni and O for all the deposited films. These data indicate that the crystalline film produced at 600 °C, which contained the $LaNiO_3$ and $La_2O_2CO_3$ phases, provided an atomic ratio of 1:0.73:1.60, for La, Ni and O, respectively. In contrast, the amorphous film contained the ratio of 1:0.75-1.01:1.94-2.88, for La:Ni:O.

Table 3.11 Summary of the EDS elemental analysis for films deposited onto Pilkington SiCO glass substrates from the LNR11-A55 precursor system after annealing under an air atmosphere. Average atomic % from 3 measured areas

Annealing temperature (°C)	Atomic %							
	La	Ni	O	C	Si	Na	Mg	Ca
As-deposited	21.41±1.58	16.51±0.83	47.39±0.83	11.39±1.93	2.10±1.09	0.59±0.09	0.03±0.06	0.57±0.22
300	17.89±1.04	16.61±0.23	45.37±0.69	13.69±0.48	4.76±1.01	0.72±0.20	0.11±0.11	0.85±0.16
400	23.03±0.30	17.16±0.08	44.69±0.15	11.19±0.06	2.66±0.39	0.59±0.09	0.00	0.66±0.04
500	18.58±0.21	18.73±0.65	42.40±0.36	8.60±0.20	8.59±0.51	1.41±0.09	0.29±0.11	1.38±0.07
600	24.52±0.26	17.89±0.56	39.27±0.12	8.32±0.56	7.20±0.46	1.31±0.72	0.21±0.04	1.29±0.06

Table 3.12 Summary of the ratio of La, Ni and O contents on the deposited films using EDS analysis.

Annealing temperature (°C)	Atomic ratio		
	La	Ni	O
As-deposited	1	0.77	2.21
300	1	0.93	2.23
400	1	0.75	1.94
500	1	1.01	2.28
600	1	0.73	1.60

3.3.6 Optical properties

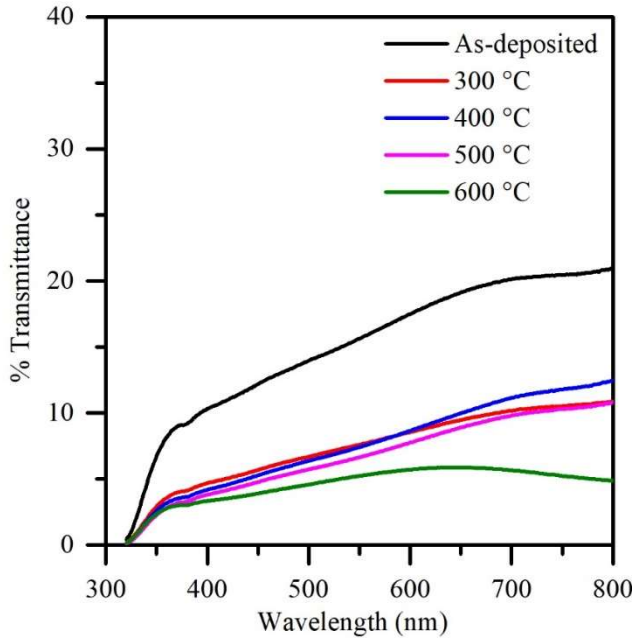

Figure 3.17 Transmittance spectra of the films deposited from the LNR11 AA5 precursor system.

The optical properties of the as-deposited and annealed films from the LNR11-AA5 precursor system were assessed by UV/Vis spectroscopy over the visible region. The % transmittances are shown in Figure 3.17. The as-deposited films displayed higher spectral transmission than the other films. After annealing, the % transmittance of the deposited films decreased with increasing annealing temperature. In particular, the film resulting from annealing at 600 °C possessed the lowest % transmittance of < 5%.

Noticeably, films annealed in the range 300 - 500 °C, which provided amorphous films, displayed similar % transmittance spectra.

3.4 Lanthanum nickel oxide thin film deposition with various vol.% of acetic acid by spin coating

The noted improvement to the quality deposited film using acetic acid described in the previous section prompted further investigation of the effects of acetic acid on film fabrication. A series of precursor systems prepared with varying added volumes of acetic acid in the precursor solution were employed in spin coating using the deposition conditions summarised in Table 3.13.

Table 3.13 Deposition conditions for spin coating of lanthanum nickel oxide thin film.

Variable	Detail
Substrate	Pilkington SiCO glass, 2.5×2.5 cm^2
Solvent	Ethanol
Deposition layer	5 layers
Drying temperature	150 °C, 15 min
Annealing atmosphere	Air
Annealing time	1 hour
Annealing temperature	600 °C

Precursor solutions (Conc. 0.2M)				
Precursor system	**Ratio**		**CH_3COOH**	
	$La(NO_3)_3 \cdot 6H_2O$	**$Ni(NO_3)_2 \cdot 6H_2O$**	**(vol. %)**	**pH**
LNR11*	1	1	0	3.466 ± 0.103
LNR11-AA5	1	1	5	2.146 ± 0.032
LNR11-AA10	1	1	10	1.469 ± 0.005
LNR11-AA15	1	1	15	1.369 ± 0.004
LNR11-AA20	1	1	20	1.033 ± 0.005
LNR11-AA30	1	1	30	0.788 ± 0.002

* Not use to deposit the films in this section

3.4.1 Thermogravimetric analysis of the precursor

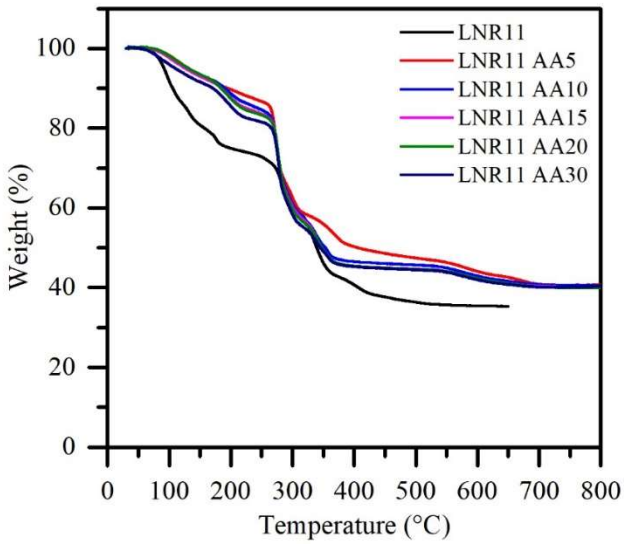

Figure 3.18 TGA curves of LNR11, LNR11-AA5, LNR11-A10, LNR11-AA15, LNR11-AA20 and LNR11-AA30 precursor systems.

The results from the thermal analysis (TGA) studies are presented in Figure 3.18. The series of LNR11-AA5-30 precursor systems display similar TGA curves comprising three main stages. Weight loss between 100 and 260 °C is considered to be due to the volatilization and loss of water, solvent residues and acetate groups. Mass loss between 260 and 375 °C is associated with decomposition of complex and loss of CO_2, prior to the final weight loss between 525 and 705 °C, which leads to the complete decomposition of the residue then expected residual mass for $LaNiO_3$.

Notably, an increased acetic acid loading had little impact on the appearance of the TGA traces with decomposition, most likely, providing ethanol and water. Acetic acid decomposition and resultant H_2O loss occur concurrently between 100 - 260 °C, thus, weight losses in this temperature range presents a decreasing trend with increasing acetic acid loading in the precursor solutions.

3.4.2 Appearance of deposited films by using the LNR11 AA5-30 precursor systems.

The appearances of the as-deposited and annealed films from the LNR11 AA5-30 precursor systems are shown in Table 3.14. The as-deposited films from the LNR11

AA5 and LNR11 AA10 precursor system were a transparent light-brown colour, whereas the LNR11 AA15, LNR11 AA20 and LNR11 AA30 precursor systems were transparent but darker in colour. After annealing at 600 °C, all films were opaque and black in colour. Increasing additional proportions of acetic acid in general provided smoother and more homogeneous films. Multi-meter tests performed on the annealed films revealed that they were all conductive, Table 3.15.

Table 3.14 Appearance of the films from the LNR11 AA5-30 precursor systems.

Condition	Precursor systems				
	LNR11 AA5	**LNR11 AA10**	**LNR11 AA15**	**LNR11 AA20**	**LNR11 AA30**
As-deposited					
Annealed at 600 °C		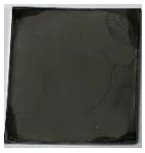	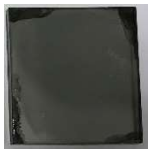		

Table 3.15 Conductivity of deposited films.

Precursor system	As-deposited film	Annealed film
LNR11-AA5	×	Conductive
LNR11-AA10	×	Conductive
LNR11-AA15	×	Conductive
LNR11-AA20	×	Conductive
LNR11-AA30	×	Conductive

3.4.3 Surface and cross-section morphology

The surface and cross-sectional morphologies of the deposited films were analysed by FESEM and AFM. FESEM micrographs of the as-deposited and annealed films from the LNR11-AA5 and LNR11-AA10 precursor systems revealed cracks, pinholes and lumps on their surfaces. The formation of cracks and lumps on the films is most likely a result of differential thermal expansion of, and resultant strain between, the glass substrate and the deposited films. It can be clearly seen, however, that addition of

acetic acid at the 15-30 vol.% level leads to a reduction in the cracks and lumps and produces smaller pinholes.

Figure 3.20 illustrates the decreasing average surface roughness values of the films after annealing, most likely due to the removal of organic impurities. This is also clearly seen in the FESEM micrographs in Figure 3.19 and the AFM images in Table 3.16. Furthermore, higher proportions of acetic acid provided increasingly smooth surfaces of the annealed films, up to a limit of 30 vol.%, at which point the surface roughness appeared to display a moderate increase.

Cross-sections of the deposited films using the LNR11-AA family of precursor systems are illustrated in Figure 3.22. The annealed films possessed dense and well packed layers with lower thickness values (67-103 nm) than the as-deposited precursor films (80-137 nm), due to the elimination of organic side products and the formation of a denser crystalline structure by the annealing process.

Figure 3.21 shows the relationship between the vol.% of added acetic acid and the thickness values of the as-deposited and annealed films. It indicates that increasing addition of acetic acid led to a decrease in the thickness of the deposited films, due to greater mass of organic material lost during the thermal decomposition process. Edinger et al.[40] have also suggested that a higher vol.% of acetic acid can reduce the surface tension of the precursor solution resulting in better spreading and coverage over the substrate surface but inducing a decreasing thickness.

As-deposited films

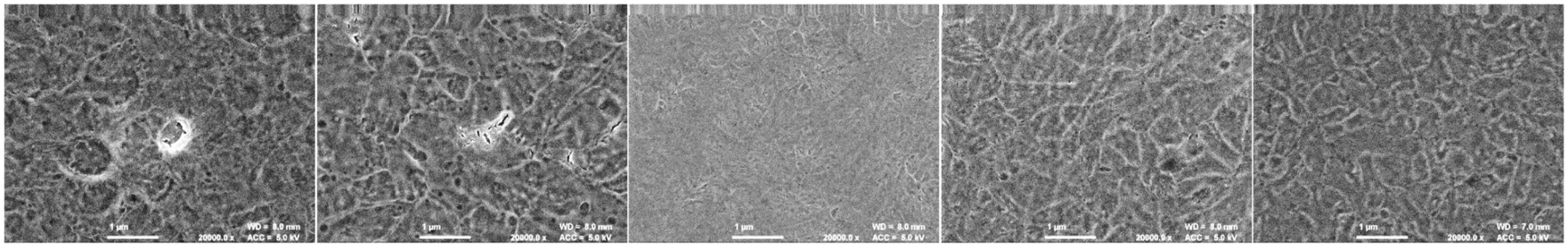

Annealed films at 600 °C

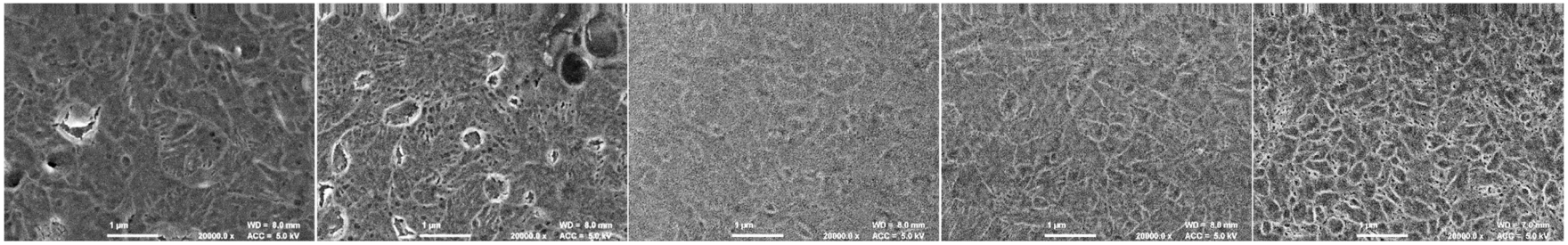

LNR11-AA5 **LNR11-AA10** **LNR11-AA15** **LNR11-AA20** **LNR11-AA30**

Figure 3.19 FESEM micrographs of as-deposited and annealed films from LNR11-AA5, LNR11-AA10, LNR11-AA15, LNR11-AA20 and LNR11-AA30 precursor systems.

Table 3.16 Surface morphology of as-deposited and annealed films from LNR11-AA5, LNR11-AA10, LNR11-AA15, LNR11-AA20 and LNR11-AA30 precursor systems with and annealing temperature of 600 °C using AFM on various substrate surfaces.

	2D	
Precursor system	**As-deposited film**	**Annealed film at 600 °C**
LNR11-AA5	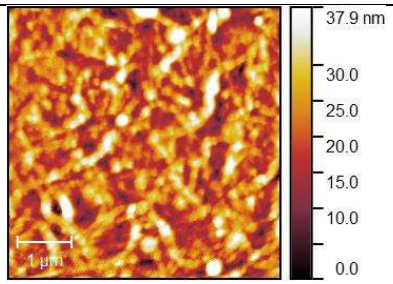	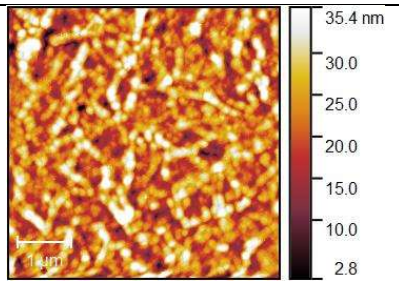
LNR11-AA10	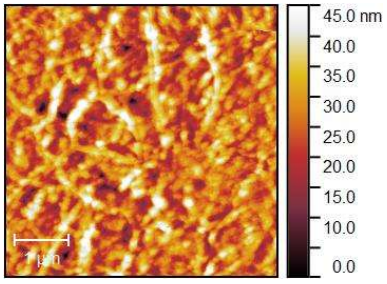	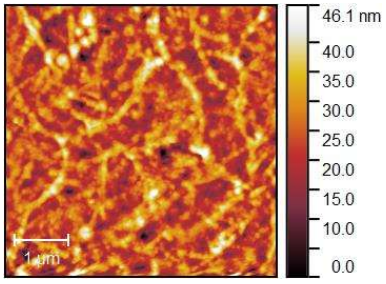
LNR11-AA15	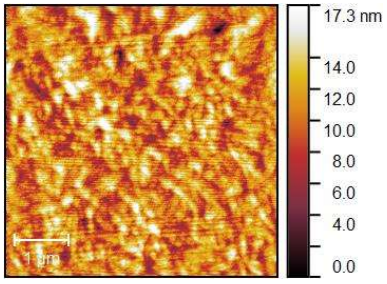	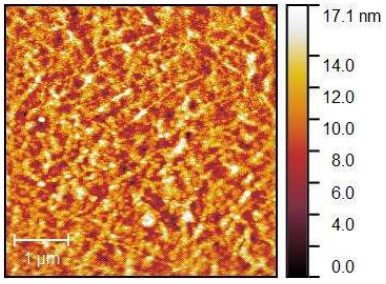
LNR11-AA20	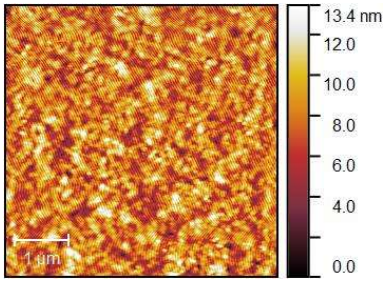	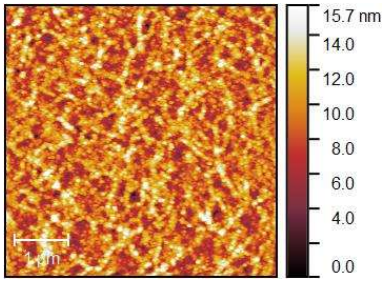
LNR11-AA30	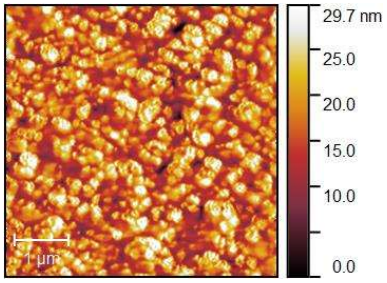	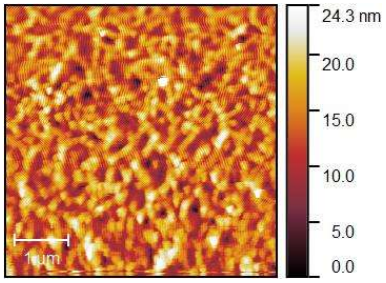

Precursor system	3D	
	As-deposited film	**Annealed film at 600 °C**
LNR11-AA5	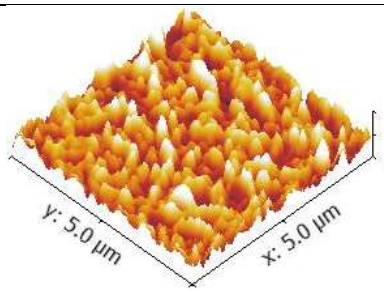	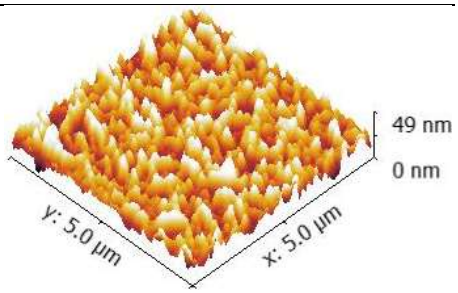
LNR11-AA10	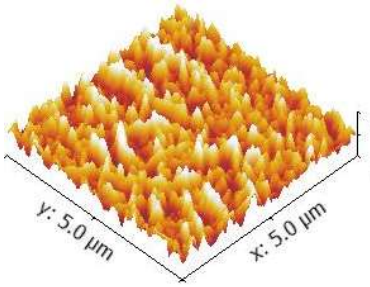	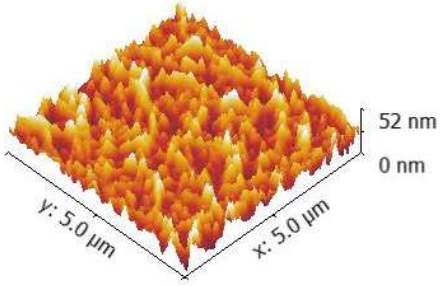
LNR11-AA15	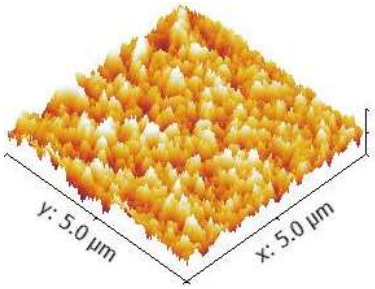	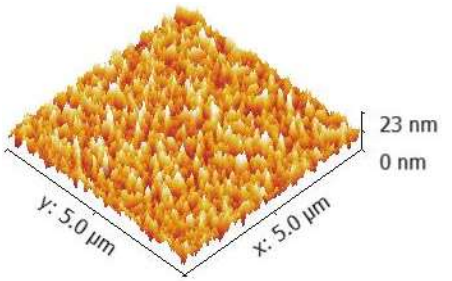
LNR11-AA20	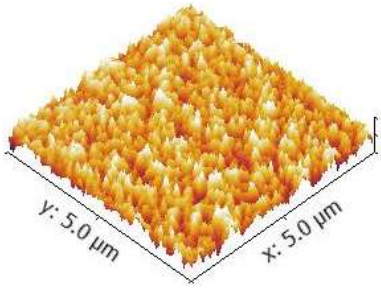	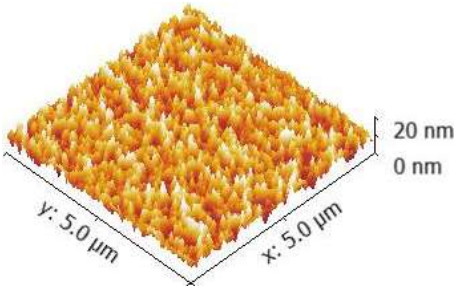
LNR11-AA30	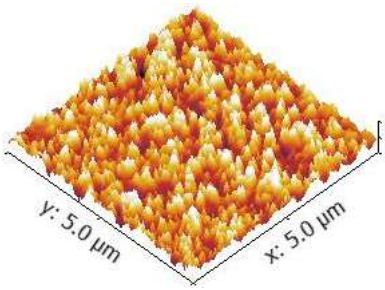	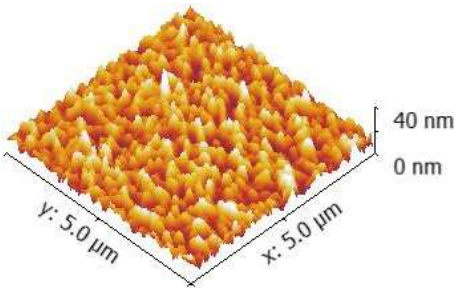

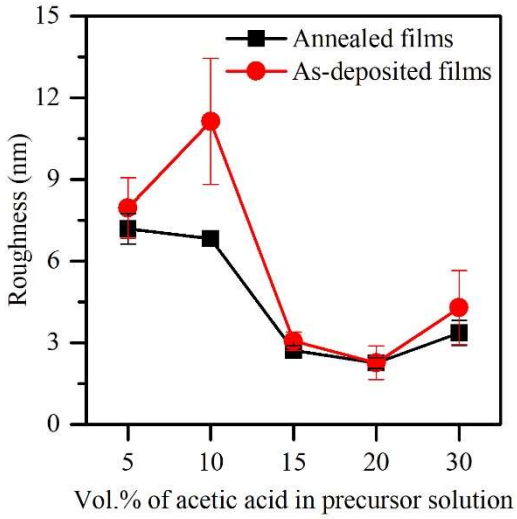

Figure 3.20 Average surface roughness of the as-deposited and annealed films from LNR11-AA5, LNR11-AA10, LNR11-AA15, LNR11-AA20 and LNR11-AA30 precursor systems. Area measurement 25μm^2.

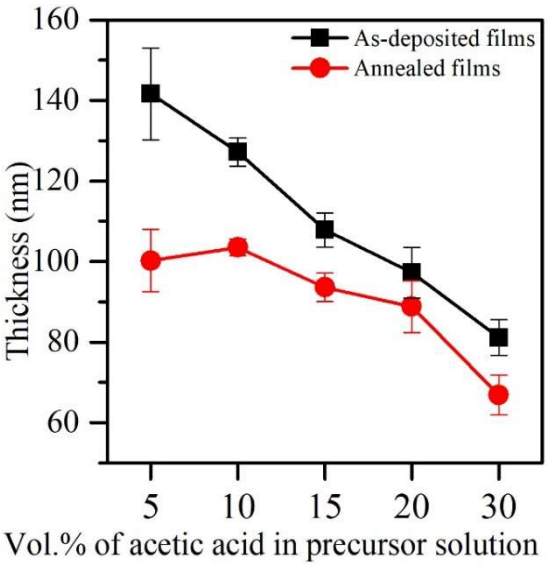

Figure 3.21 Average thickness of the as-deposited and annealed films from LNR11-AA5, LNR11-AA10, LNR11-AA15, LNR11-AA20 and LNR11-AA30 precursor systems.

As-deposited films

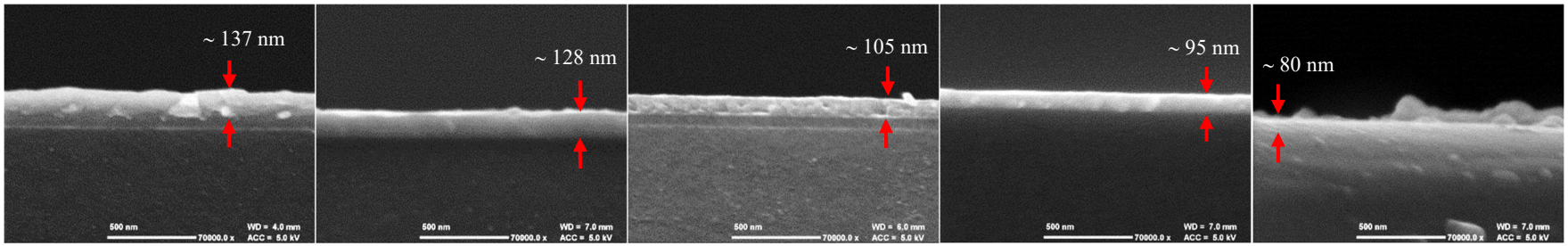

Annealed films at 600 °C

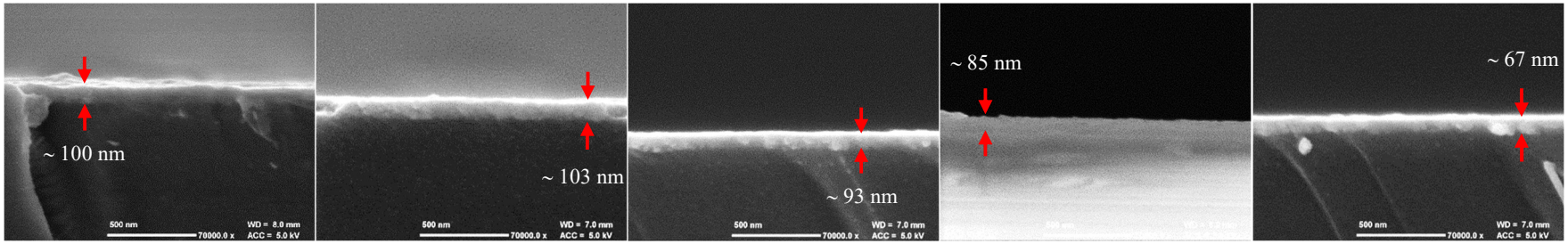

LNR11 AA5 LNR11 AA10 LNR11 AA15 LNR11 AA20 LNR11 AA30

Figure 3.22 FESEM cross-section micrographs of the as-deposited and annealed films from LNR11-AA5, LNR11-AA10, LNR11-AA15, LNR11-AA20 and LNR11-AA30 precursor systems.

3.4.4 Crystallinity

The crystallinity of the as-deposited and annealed films was investigated by XRD analysis and the results are shown in Figure 3.23. It can be seen that all the as-deposited films were amorphous (Figure 3.23 (a)). In contrast, all of the annealed films were polycrystalline and indexed well as cubic $LaNiO_3$ (JCPDS: 00-033-0710) and, notably, without any detected binary oxide phases such as La_2O_3 or NiO. The monoclinic $La_2O_2CO_3$ phase (JCPDS: 00-048-1113), however, was found with the LNR11-AA5 and LNR11-AA10 precursor systems, which contained 5 and 10 vol.% of acetic acid, respectively. Furthermore, Table 3.17 presents the calculated crystallite sizes of the annealed films from all of the precursor systems. These data indicate that the crystallite size slightly decreases with increasing acetic acid content.

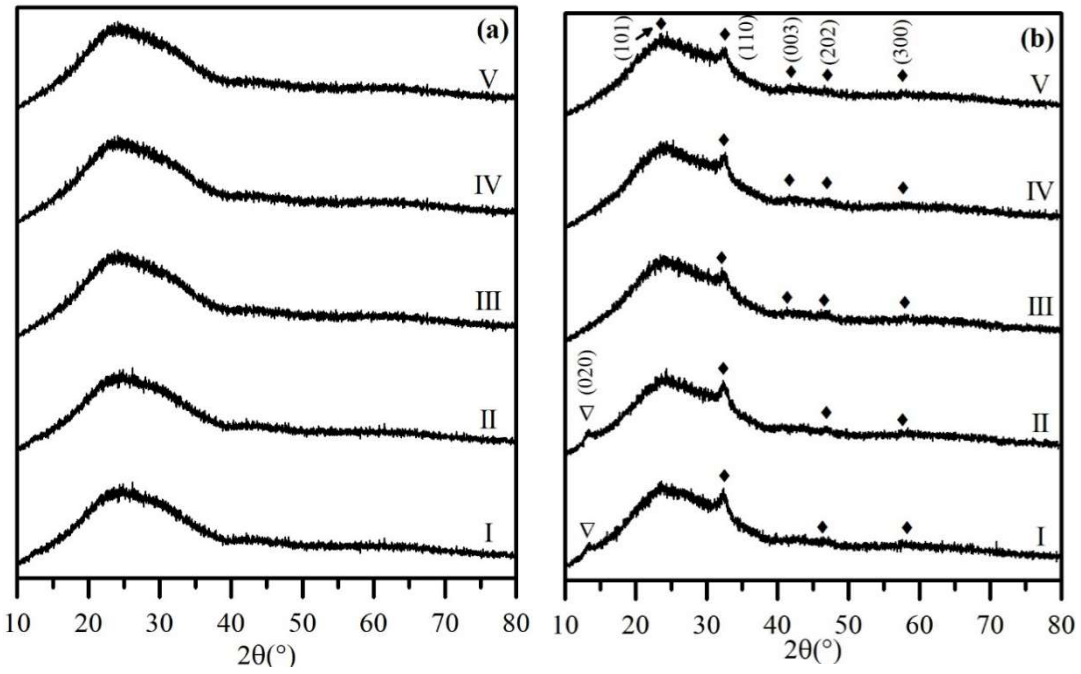

Figure 3.23 XRD patterns of the (a) as-deposited and (b) annealed films with different precursors containing varying vol.% of acetic acid. I=LNR11-AA5, II=LNR11-AA10, III=LNR11-AA15, IV=LNR11-AA20, V=LNR11-AA30. (♦) corresponding to cubic $LaNiO_3$ (JCPDS: 00-033-0710) and (∇) corresponding to monoclinic $La_2O_2CO_3$ phase (JCPDS: 00-048-1113).

Table 3.17 Crystallite size of annealed films.

Precursor system	Crystallite size at (110) (nm)
LNR11-AA5	11.55
LNR11-AA10	11.54
LNR11-AA15	8.66
LNR11-AA20	8.35
LNR11-AA30	8.12

3.4.5 Compositional analysis

Elemental analysis of the films deposited from all precursor systems was performed by EDS. The summary of the analysis results presented in Table 3.18 indicates that all films possessed La, Ni and O in their composition. The films were too thin, however, (<140 nm) with regard to the depth resolution of the technique and X-rays were detected arising from the oxygen content in the SiCO glass substrates. As a result, the results include on overestimate of the atomic % of oxygen.

The EDX analysis did, however, reveal a trend of decreasing atomic% of La and Ni with increasing content of added acetic acid in the precursor solution, albeit this may also be consequence of decreasing film thickness as deduced from the cross-section investigation.

Table 3.19 reveals that all films contained a La:Ni ratio of 1:1 and it can be inferred that this arises from $LaNiO_3$, as supported by the XRD analysis. Interestingly, the increasing vol.% of acetic acid in the precursor mixtures led to a stoichiometric 1:1 ratio of La and Ni in the films' composition. Especially noteworthy was the LNR11-AA30 precursor solution which contained the maximum acetic acid content (30 vol.%) and provided La: Ni ratios of 1:1.02 and 1.:1.07, for the as-deposited and annealed films, respectively.

Table 3.18 Summary of the EDS elemental analysis of as-deposited and annealed films from the LNR11-AA5, LNR11-AA10, LNR11-AA15, LNR11-AA20 and LNR11-AA30 precursor systems. Average atomic % from 3 measured areas.

Atomic % of as-deposited films

Precursor system	La	Ni	O	C	Si	Na	Ca	Mg
LNR11-AA5	6.43±1.82	5.17±0.96	45.59±0.58	4.88±0.41	28.74±1.20	4.99±0.34	2.78±0.32	1.42±0.10
LNR11-AA10	4.95±0.01	4.02±0.26	44.15±3.59	8.87±6.63	28.34±2.41	5.21±0.31	3.05±0.13	1.41±0.03
LNR11-AA15	3.12±0.10	2.88±0.15	48.16±0.57	3.40±0.48	31.48±0.15	5.96±0.16	3.30±0.09	1.70±0.08
LNR11-AA20	3.43±0.12	3.29±0.19	47.01±0.54	4.27±0.13	31.20±0.10	5.90±0.12	3.30±0.05	1.59±0.06
LNR11-AA30	3.13±0.06	3.20±0.10	47.38±0.45	4.02±0.15	31.32±0.36	5.98±0.21	3.38±0.04	1.61±0.02

Atomic % of annealed films

Precursor system	La	Ni	O	C	Si	Na	Ca	Mg
LNR11-AA5	4.77±0.33	4.36±0.25	45.58±0.60	4.18±0.03	30.48±0.17	5.95±0.11	3.27±0.04	1.55±0.02
LNR11-AA10	4.16±0.77	3.71±0.77	43.29±5.98	10.67±15.62	28.28±6.18	5.40±1.27	3.07±0.51	1.41±0.31
LNR11-AA15	2.30±0.04	2.76±0.12	47.18±0.18	3.71±0.40	31.72±0.18	6.45±0.11	3.46±0.02	1.71±0.05
LNR11-AA20	3.91±0.11	3.43±0.12	45.55±1.88	6.40±4.03	29.66±2.00	5.90±0.13	3.59±0.46	1.58±0.14
LNR11-AA30	2.60±0.63	2.79±0.63	43.50±6.53	11.45±15.93	28.94±6.16	5.94±1.40	3.24±0.34	1.55±0.37

Table 3.19 Atomic % ratio between La, Ni and O of the as-deposited and annealed films from all precursor systems.

As-deposited films

Precursor system	Atom% ratio		
	La	Ni	O
LNR11-AA5	1.00	0.80	7.09
LNR11-AA10	1.00	0.81	8.92
LNR11-AA15	1.00	0.92	15.45
LNR11-AA20	1.00	0.96	13.69
LNR11-AA30	1.00	1.02	15.15

Annealed films

Precursor system	Atom% ratio		
	La	Ni	O
LNR11-AA5	1.00	0.91	9.55
LNR11-AA10	1.00	0.89	10.42
LNR11-AA15	1.00	0.92	15.74
LNR11-AA20	1.00	0.88	11.66
LNR11-AA30	1.00	1.07	16.73

3.4.6 Optical properties

The optical properties of all films were assessed by UV-Vis spectroscopy. Figure 3.24 shows the transmission spectra of the as-deposited and annealed films. These data reveal the % transmittance of each film decreases after annealing, concurrent with the transformation of the amorphous to the crystalline $LaNiO_3$ phase deduced from the XRD investigation. Furthermore, the spectra reflect the colour of the films reported in Table 3.13 and the transformation of the light-brown and light-black of the as-deposited films to black and opaque after annealing.

The annealed films comprising the $LaNiO_3$ crystalline phase present an increasing % transparency at increased vol.% of acetic acid in the precursor solution. This increasing % transmittance, however, could be possibly be due to the decreasing thickness and grain size of the films at higher proportions of acetic acid.

In the visible region, the as-deposited films present a % transparency of around 39% to 60%, while the annealed films were between 28% and 40%. In addition, the annealed films prepared using the precursor solutions containing high quantities of acetic acid (20-30%) presented the highest % transmittance around 38- 40% in the visible region.

The reflectance spectra of all films are shown in Figure 3.25. Over the visible region, the as-deposited films provided a % reflectance around 4 - 21%, whereas the % reflectance of the annealed films was slightly increased to around 8 - 25%. The increased % reflectance could be due to the enhanced crystallinity and decreasing roughness of the films after the annealing process.

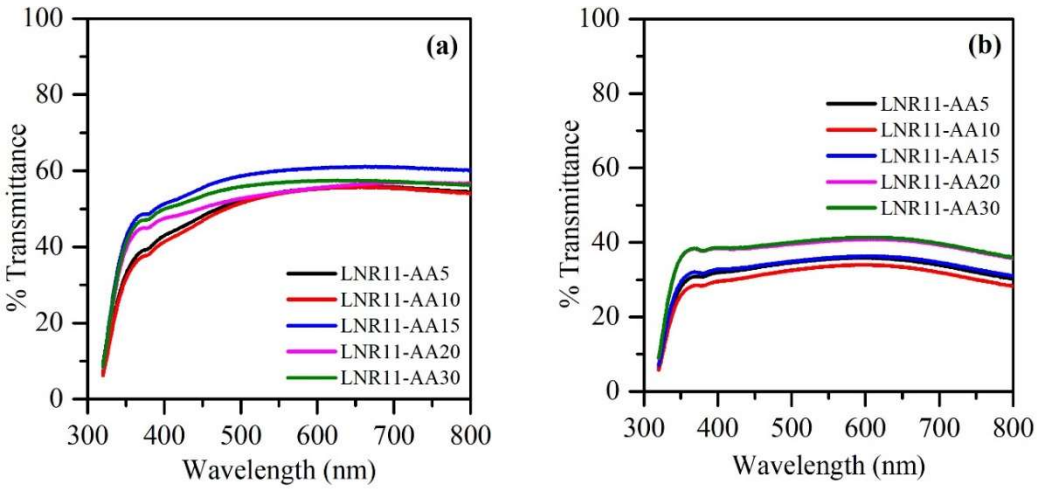

Figure 3.24 Transmittance spectra of (a) as-deposited and (b) annealed films from LNR11-AA5, LNR11-AA10, LNR11-AA15, LNR11-AA20 and LNR11-AA30 precursor systems.

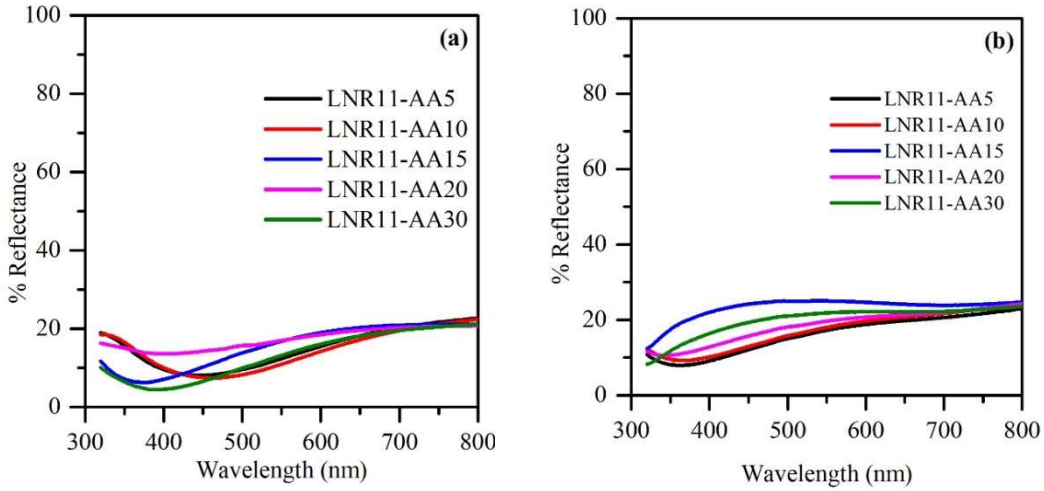

Figure 3.25 Reflectance spectra of (a) as-deposited films and (b) annealed films from LNR11-AA5, LNR11-AA10, LNR11-AA15, LNR11-AA20 and LNR11-AA30 precursor systems.

3.5 Single crystal complex from LNR11 precursor system in an acetic acid

3.5.1 Single crystal analysis

The successful use of the spin coated LN11 precursor system to provide $LiNiO_3$ thin films prompted an assessment of the likely nature and composition of the as deposited films prior to annealing. A precursor solution prepared from a 1:1 mixture of $La(NO_3)_3{\cdot}6H_2O$ and $Ni(NO_3)_2{\cdot}6H_2O$ in acetic acid was allowed to evaporate slowly at room temperature to provide light-green crystals. Single crystal X-ray diffraction was performed on the complex crystal and the result of this analysis is shown in Figure 3.26. Selected bonds and angles are shown in Tables 3.20 and 3.21, respectively.

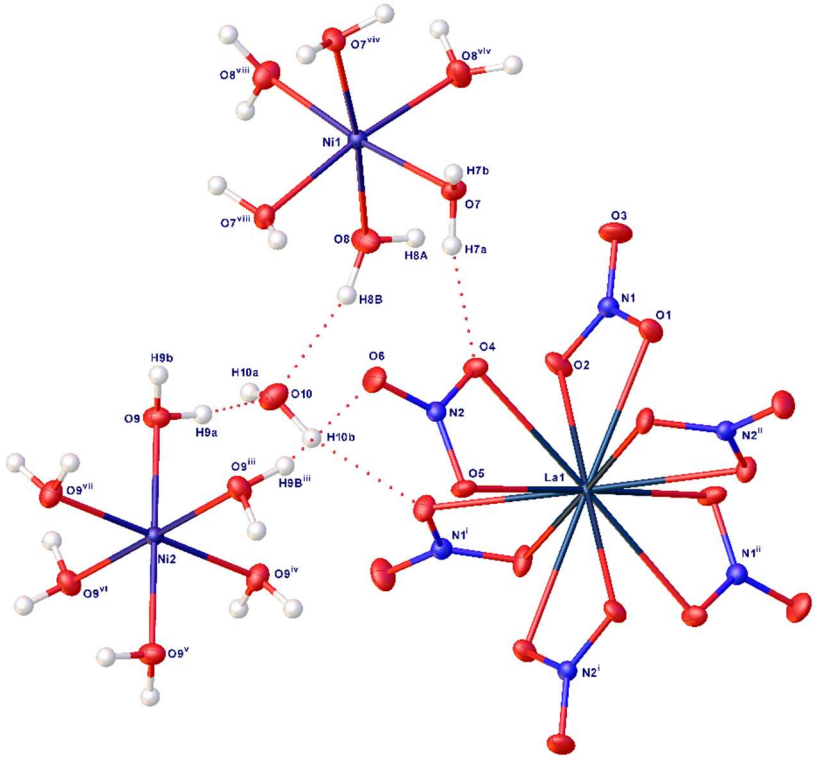

Figure 3.26 Single crystal structure of complex from lanthanum nitrate and nickel nitrate in an acetic acid.

The complex is a co-crystal of the hydrated lanthanum and nickel nitrates. The two unique nickel centres are octahedral hexa-aquo $[Ni(H_2O)_6]^{2+}$ complexes in which any coordinated nitrate groups in the $Ni(NO_3)_2{\cdot}6H_2O$ have been displaced by water molecules, Figure 3.27. Each nickel centre is coordinated by six water (H_2O) molecules through Ni-O bonds with bond lengths of 2.0499(10) - 2.0584(11) Å. In contrast, the lanthanum centre is coordinated by six bidentate nitrate anions. As a large trivalent cation (2.50 Å) lanthanum can exhibit a wide variety of stereochemistries and can adopt coordination numbers from 6 to 12. In this case, the La centres in the $[La(NO_3)_6]^{3-}$ trianions are 12-coordinate and are bound to the nitrates through La-O bonds which are 2.6469(10) - 2.7008(10) Å in length. The crystalline lattice is propagated by a network of hydrogen bonds between the nickel cations and lanthanum-centred anions bridged occluded molecules of free water.

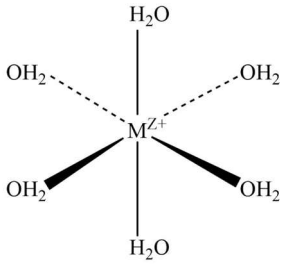

(a)

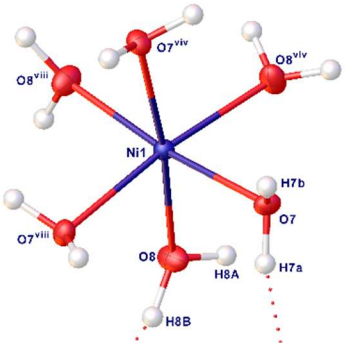

(b)

Figure 3.27 (a) molecular structure of metal aquo complex (b) molecular structure from the experiment in this section.

Table 3.20 Selected bond lengths (Å) for complex from lanthanum nitrate and nickel nitrate in an acetic acid.

Selected Bond	(Å)	Selected Bond	(Å)
Ni1- $O7^{1}$	2.0500(10)	La1- $O5^{8}$	2.7008(10)
Ni1- O7	2.0499(10)	La1- O5	2.7007(10)
Ni1- $O8^{1}$	2.0584(11)	N1- O1	1.2743(15)
Ni2- $O9^{3}$	2.0574(10)	N1- O2	1.2720(16)
Ni2- O9	2.0575(10)	N1- O3	1.2264(16)
La1- $O1^{8}$	2.6275(10)	N2- O4	1.2737(15)
La1- $O2^{8}$	2.6564(11)	N2- O5	1.2680(15)
La1- $O4^{8}$	2.6469(10)	N2- O6	1.2305(16)

Table 3.21 Selected angles (Å) for complex from lanthanum nitrate and nickel nitrate in an acetic acid.

Selected Angle	(°)	Selected Angle	(°)
$O7^{1}$- Ni1- O7	91.23(4)	$O1^{8}$-La1-$O1^{9}$	114.735(17)
O7-Ni1-O8	93.41(4)	O1-La1-$O2^{8}$	72.73(3)
$O7^{2}$-Ni1-O8	84.42(4)	$O1^{8}$-La1-$O2^{8}$	48.40(3)
O7-Ni1 -$O8^{2}$	173.71(4)	O1-La1-$O2^{9}$	116.09(3)
$O7^{1}$-Ni1-$O8^{2}$	84.43(4)	$O1^{9}$-La1-O2	72.73(3)
$O7^{1}$-Ni1-O8	173.71(4)	$O1^{9}$-La1-$O2^{8}$	116.09(3)
$O8^{2}$-Ni1-$O8^{1}$	91.28(4)	O1-La1-O4	67.34(3)
$O9^{3}$-Ni2-$O9^{4}$	91.05(4)	$O1^{9}$-La1-O4	65.28(3)

Selected Angle	(°)	Selected Angle	(°)
$O9^4$-Ni2-$O9^5$	180.0	$O1^8$-La1-O4	177.06(3)
$O1^8$-La1-O5	129.37(3)	$O1^8$-La1-$O4^9$	65.28(3)
$O1^9$-La1-$O5^9$	108.29(3)	O4-La1-$O2^9$	108.46(3)
O1-La1-$O5^8$	66.00(3)	O4-La1-O2	66.82(3)
$O1^9$-La1-$O5^8$	129.37(3)	O4-La1-$O2^8$	134.46(3)
$O2^9$-La1-O2	70.62(4)	$O4^9$-La1-$O4^8$	112.531(19)
$O2^9$-La1-$O5^9$	112.04(3)	$O4^8$-La1-O4	112.530(19)
O2-La1-$O5^8$	110.80(3)	O4-La1-$O5^9$	111.10(3)
$O2^8$-La1-O5	177.22(3)	$O4^9$-La1-$O5^9$	47.74(3)
$O9^7$-Ni2-$O9^4$	88.95(4)	$O4^9$-La1-O5	70.39(3)
$O4^8$-La1-$O5^9$	70.39(3)	O6-N2-O4	121.16(12)
O5-La1-$O5^8$	66.51(4)	O6-N2-O5	122.06(12)
O2-N1-O1	116.58(11)	N1-O1-La1	98.14(8)
O3-N1-O1	121.44(12)	N1-O2-La1	96.81(8)
O3-N1-O2	121.98(12)	N2-O4-La1	98.89(7)
O5-N2-O4	116.78(11)	N2-O5-La1	96.45(8)

Notably, there was no formation of any metal acetate (M-CH_3COO) or metal hydroxyl (M-OH) residues. M. de la L. Olvera et al.,[42] and S. Pavithra et al.,[37] have used acetic acid in oxide thin film fabrications to prevent metal-OH species formation which can lead to a decrease the growth rate of oxide thin films. During the $LaNiO_3$ spin coating described in this chapter, therefore, it can be assumed that the added acetic acid in the precursor solution also helps prevent the formation of metal-OH species and provides better quality thin film growth, Figure 3.16, but without any need for metal acetate formation.

Furthermore, it may be inferred that the structure of this crystalline material also reflects the composition of the as-deposited spin coated films prior to annealing. The observation of nitrate coordination solely to the lanthanum ions and the intimate molecular level combination of the dissimilar metal centres, therefore, may be significant contributing factors in the successful use of spin coating for $LaNiO_3$ fabrication.

3.5.2 Thermogravimetric analysis of single crystal complex

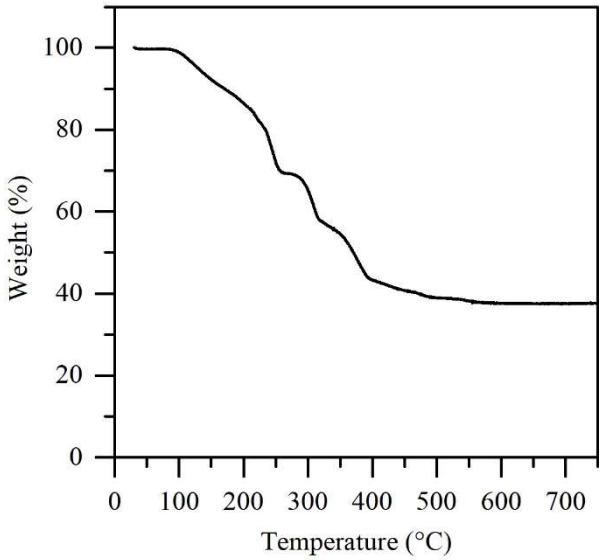

Figure 3.28 TGA curve of single crystal complex from $La(NO_3)_3 \cdot 6H_2O$ and $Ni(NO_3)_2 \cdot 6H_2O$ in an acetic acid.

Figure 3.28 presents a thermal investigation of the single crystal complex from $La(NO_3)_3 \cdot 6H_2O$ and $Ni(NO_3)_2 \cdot 6H_2O$ in acetic acid. The TGA curve illustrates 2 main stages of the decomposition. A first stage occurred around 100 - 215 °C due to the loss of water and further volatilization with a % weight loss of 16%. A second stage displayed around 210 - 400 °C is considered to be due to the decomposition of the complex with % weight loss of 41%, while decomposition is complete at around 555 °C to leave the residue with an expected residual mass corresponding to $LaNiO_3$ (37%).

3.6 Conclusions

The results in this chapter report that the fabrication of the ternary oxide thin film perovskite material, lanthanum nickel oxide, $LaNiO_3$, can be performed using a precursor system prepared from the simple metal nitrates, lanthanum (III) nitrate hexahydrate and nickel (II) nitrate hexahydrate. Also, the effects of ammonium nitrate and acetic acid addition on thin film formation by AACVD and spin coating have been studied.

3.6.1 Lanthanum nickel oxide by AACVD

A series of precursor solutions containing lanthanum nitrate, nickel nitrate and ammonium nitrate were applied to the AACVD experiments. TGA results demonstrated that all the precursor recipes decomposed to leave stable residues corresponding to lanthanum nickel oxide at temperatures around 500 °C. Attempted AACVD onto Pilkington SiCO glass substrates and silicon wafers, however, tended to provide powdery materials similar to that observed during the deposition of lanthanum oxide described in chapter 2.

After deposition onto FTO glass substrates, XRD analysis revealed that the $LaNiO_3$ phase appeared at a deposition temperature of 350 °C as a shiny black thin film material. Interestingly, at temperatures above 350 °C impurities were found in the deposited films corresponding to Sn, SnO, SnO_2 and Sn_2F_6, which were deduced to be a result of reaction between the FTO glass and ethanol under the deposition atmosphere. In addition, FESEM indicated that high aspect ratio nanorods with dimension around 96×725 nm, W×L appeared at the deposition temperature of 400 °C on FTO glass substrates.

3.6.2 Lanthanum nickel oxide by spin coating

$LaNiO_3$ thin film fabrication was successfully achieved using a simple nitrate precursor system of lanthanum and nickel nitrates in conjunction with acetic acid. Precursor systems which contained acetic acid provided good coverage over the substrate surfaces and smooth, homogeneous and well adhered films.

While the as-deposited films from the series of precursor systems were amorphous by PXRD with a transparent light-brown and light-black appearance, all the films were transformed to a crystalline phase of $LaNiO_3$ after annealing at 600 °C under ambient air for 1 hour. These films displayed a black colouration, which was more opaque than the as-deposited material. Furthermore, all of the annealed films were conductive.

FESEM cross-section investigations found that the film thickness decreased with increasing additional volumes of acetic acid in the precursor solution. EDS analysis, however, revealed that a high vol.% of acetic acid provided La/Ni ratios close to 1:1 and materials which indexed to the correct stoichiometric ratio of $LaNiO_3$.

3.6.3 Comparison of solution processing by the AACVD and spin coating techniques

The formation of either powdery material or a nickel metal phase in the AACVD process can be assumed to result from the gas phase nature of the precursors as the aerosol is introduced into the deposition chamber at high temperature. In the deposition zone, the AACVD process is designed such that precursor aerosol droplets are evaporated prior to any wetting of, or solution phase delivery to, the substrate surface. As a result, the lanthanum and nickel precursor species are well separated during the evaporative process and their entrainment in the gas phase. As a consequence, their properties as materials precursors are more likely to reflect those of the individual components providing, as described in Chapter 2, nickel metal and particulate La_2O_3, rather than the desired $LaNiO_3$ phase.

In contrast, the spin coating process requires an initial wetting of the substrate surface by the precursor solution and subsequent solvent evaporation prior to decomposition of the nitrate precursors. The composition of the as-deposited films prior to annealing, therefore, may be assumed to reflect the molecular level combination of metal centres observed in the single crystal X-ray structure described in section 3.5. The spin coating process, however, will always be limited by the spreading ability of the precursor solution over the substrate surface and the batch-type nature of the process (Table 3.8 and Figure 3.12).

Spray pyrolysis is further technique that may be employed to fabricate thin films via the delivery of aerosol droplets of a precursor solution. Although this process displays

some similarity to AACVD, the precursor solution employed directly wets a hot substrate surface with simultaneous solvent evaporation and precursor decomposition to generate the desired material. Spray pyrolysis, therefore, may be considered as a hybrid of the two techniques explored in this thesis.

As a prelude to future work, therefore, a preliminary study has been carried out to investigate the use of the LNR 11 precursor system for the deposition of $LaNiO_3$ via spray pyrolysis. This brief study is outlined below.

3.6.4 Spray pyrolysis of precursor LNR11

The fabrication of $LaNiO_3$ thin films was investigated by spray pyrolysis employing the deposition conditions shown in Table 3.22. The appearances of the resultant film are shown in Table 3.23.

Table 3.22 Deposition conditions for spray pyrolysis of lanthanum nickel oxide thin films from the LNR11 precursor system.

Variable	Detail	
Precursor, LNR11 system	Concentration: 0.1 M	
	Recipe ratio	
	$La(NO_3)_3{\cdot}6H_2O$	$Ni(NO_3)_2{\cdot}6H_2O$
	1	1
Substrate	Pilkington SiCO glass, 2.5×2.5 cm^2	
Solvent	Ethanol	
Deposition layer	5 layers	
Drying temperature	150 °C, 15 min	
Annealing atmosphere	Air, nitrogen	
Annealing time	1 hour	
Annealing temperature	500 and 600 °C	

Appearance of deposited films

The as-deposited films were an opaque brown-grey in colour. After annealing at 500 °C, under either nitrogen or air, the films presented a slightly darker appearance while

annealing at 600 °C provided a back colouration. Notably, the film annealed under air was darker than that annealed under a nitrogen atmosphere, albeit both films annealed at 600 °C were conductive.

Table 3.23 Appearances of the deposited films from the LNR11 precursor system via spray pyrolysis.

As-deposited film	Annealing atmosphere			
	Nitrogen		Air	
	500 °C	600 °C	500 °C	600 °C
				

Crystallinity

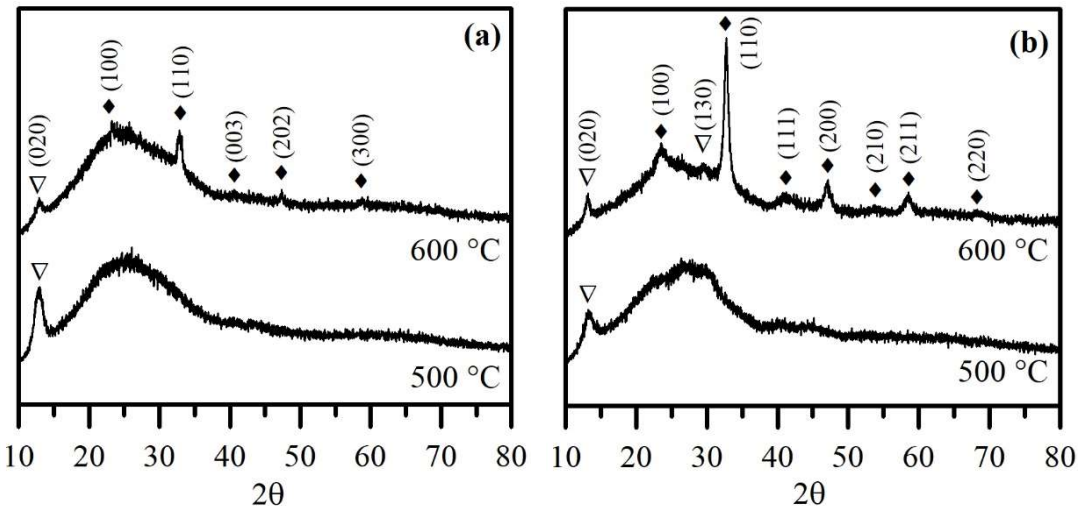

Figure 3.29 XRD patterns of the annealed films under difference atmosphere by (a) nitrogen and (b) air with annealing temperature at 500 and 600 °C. (♦) and (∇) Feature corresponding to cubic $LaNiO_3$ (JCPDS: 00-033-0710) and monoclinic $La_2O_2CO_3$ (JCPDS: 00-048-1113), respectively.

Figure 3.29 illustrates the XRD patterns of the annealed films. It was found that annealing at 600 °C provided cubic $LaNiO_3$ containing some monoclinic $La_2O_2CO_3$. The film annealed at 600 °C under air, however, provided higher intensity diffraction

maxima than the film heated under N_2 and provided crystallite sizes derived from the $LaNiO_3$ (110) reflections of 16.25 nm and 5.42 nm, respectively.

Compositional analysis

The film annealed at 600 °C under air was selected for EDS analysis and the results are shown in Table 3.24. The SEM micrographs show the surface of the annealed film comprises numerous cracks and pinholes. Notably, some large spherical particles present on the surface can also be assumed to occur during the spraying process.

The elemental analysis results indicate that the film contains atomic % of La, Ni and O of 26.39, 17.52 and 43.93 %, respectively. Interestingly, EDS performed on the spherical particles revealed a high % of Ni but indicated a ratio of La:Ni close to 1:1 at 1:0.97.

The results of this preliminary study indicate that the LNR 11 precursor system, previously employed in AACVD, can be used to prepare $LaNiO_3$ thin film materials via spray pyrolysis. The ternary oxide material can, thus, be fabricated from simple nitrates without any further participants in a separate process that displays features of both the AACVD and spin coating techniques.

Table 3.24 Compositional analysis of the annealed film from annealing temperature of 600 °C under air atmosphere.

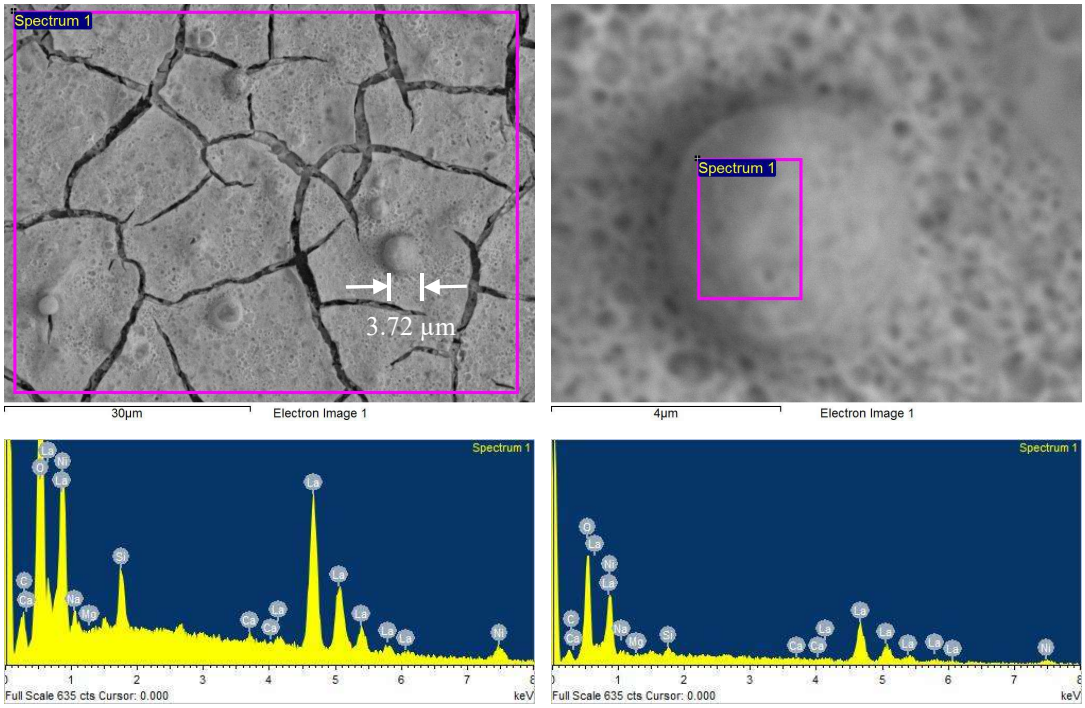

Element	Atomic%	Element	Atomic%
C	6.72	C	6.78
O	43.93	O	45.18
Na	1.20	Na	0.00
Mg	0.00	Mg	0.50
Si	3.62	Si	1.93
Ca	0.62	Ca	0.00
Ni	17.52	Ni	22.51
La	26.39	La	23.10

Atomic % ratio between La, Ni and O			**Atomic % ratio between La, Ni and O**		
La	Ni	O	La	Ni	O
1.00	0.66	1.66	1.00	0.97	1.96

References

1 X. D. Zhang, X. J. Meng, J. L. Sun, T. Lin, J. H. Ma, J. H. Chu, D. Y. Kwon, C. W. Kim and B. G. Kim, *Thin Solid Films*, 2008, **516**, 919–924.

2 S. Ueno, Y. Sakamoto, H. Taguchi, K. Nakashima and S. Wada, *J. Ceram. Soc. Japan*, 2015, **123**, 351–354.

3 N. Hamada, *Phys. Chem Solids*, 1993, **54**, 1157–1160.

4 D. Misra and T. Kumar Kundu, *Eur. Phys. J. B*, 2016, **89**, 1–8.

5 Y. Liu, N. Xu, X. G. Zheng, T. Watanabe, O. Agyeman and M. Akiyama, *J. Mater. Sci.*, 2000, **35**, 937–941.

6 C. O. Soares, • M D Carvalho, • M E Melo, J. • A. Gomes, R. A. Silva, • C M Rangel, • M I Da and S. Pereira, *J. Appl Electrochem*, 2012, **42**, 325–332.

7 L. Guan, B. Liu, L. Jin, J. Guo, Q. Zhao, Y. Wang and G. Fu, *Solid State Commun.*, 2010, **150**, 210–2014.

8 Y. Zhu, H. Wang, P. Liu, W. Yao and L. Cao, *Thin Solid Films*, 2005, **471**, 48–52.

9 H. Seim, H. Mölsä, M. Nieminen, H. Fjellvåg and L. Niinistö, *J. Mater. Chem.*, 1997, **7**, 449–454.

10 M. W. Zhu, Z. J. Wang, Y. N. Chen, H. L. Wang and Z. D. Zhang, *Appl. Phys. A*, 2013, **112**, 1011–1018.

11 M. W. Zhu, H. L. Wang, H. Lei, Y. J. Zhang, N. Jia and Z. J. Wang, *Appl. Phys. A*, 2016, **122**, 36.

12 J. Zhu, L. Zheng, Y. Zhang, X. H. Wei, W. B. Luo and Y. R. Li, *Mater. Chem. Phys.*, 2006, **100**, 451–456.

13 M. Zinkevich and F. Aldinger, 2004, **375**, 147–161.

14 C. Shivakumara, M. S. Hegde, A. S. Prakash, A. M. A. Khadar, G. N. Subbanna and N. P. Lalla, *Solid State Sci.*, 2003, **5**, 351–357.

15 M. Počuča-nešić, G. Branković, S. Bernik, A. Rečnik, D. Vasiljević-radović

and Z. Branković, 2012, 103–107.

16 H. Huang and X. Yao, *Mater. Chem. Phys.*, 2004, **87**, 134–137.

17 O. Gorbenko, A. Kaul, A. Molodyk, V. Fuflyigin, M. Novozhiov, A. Bosak, U. Krause and G. Wahl, *J. Alloys Compd.*, 1997, **251**, 337–341.

18 G. H. Haertling, *J. Appl. Phys.*, 1991, **9**, 414–420.

19 S. Miyake, S. Fujihara and T. Kimura, *J. Eur. Cern. Soc.*, 2001, **21**, 1525–1528.

20 S. Sergeenkov, L. Cichetto, E. Longo and F. M. Araujo-Moreira, *JETP Lett.*, 2015, **102**, 383–386.

21 M. K. Zayed, A. Solieman and M. Ebaid, *Acta Mater.*, 2013, **61**, 5674–5684.

22 M. W. Zhu, Z. J. Wang, Y. N. Chen and Z. D. Zhang, *Surf. Coatings Technol.*, 2013, **216**, 139–144.

23 T. Ryll, P. Reibisch, L. Schlagenhauf, A. Bieberle-huetter, M. Döbeli, J. L. M. Rupp and L. J. Gauckler, *Jounal Eur. Ceram. Soc.*, 2012, **32**, 1701–1709.

24 Y. a O. Wang, G. Zhang, C. Li, G. U. O. Yan and Y. Lu, 2011, **34**, 1379–1383.

25 Z. J. Wang, T. Kumagai and H. Kokawa, *J. Cryst. Growth*, 2006, **290**, 161–165.

26 V. Faucheux, S. Pignard and M. Audier, *J. Solid State Chem.*, 2004, **177**, 4616–4625.

27 H. Miyazaki, T. Goto, Y. Miwa, T. Ohno and H. Suzuki, *J. Eur. Ceram. Soc.*, 2004, **24**, 1005–1008.

28 B. S. Barros, J. Kulesza, D. M. De Arajo Melo and A. Kiennemand, *Mater. Res.*, 2015, **18**, 732–739.

29 M. W. Zhu, Z. J. Wang, Y. N. Chen and Z. D. Zhang, *J. Cryst. Growth*, 2011, **336**, 44–49.

30 M. W. Zhu, Z. J. Wang, Y. N. Chen and Z. D. Zhang, *Surf. Coat. Technol.*, 2013, **216**, 139–144.

31 S. Ueno, Y. Sakamoto, H. Taguchi, K. Nakashima and S. Wada, *J. thre Ceram. Soc. Japan*, 2015, **123**, 351–354.

32 K. Liang, N. Wang, M. Zhou, Z. Cao, T. Gu, Q. Zhang, X. Tang, W. Hu and B. Wei, *J. Mater. Chem. A*, 2013, **1**, 9730–9736.

33 J. Y. Liu, C. C. Lee, C. H. Wang, C. T. Yeh and C. Bin Wang, *Int. J. Hydrogen Energy*, 2010, **35**, 4069–4075.

34 A. S. Enigochitra, P. Perumal, C. Sanjeeviraja, D. Deivamani and M. Boomashri, *Superlattices Microstruct.*, 2016, **90**, 313–320.

35 A. Hadri, C. Nassiri, F. Z. Chafi, M. Loghmarti and A. Mzerd, *Energy Environ. Focus*, 2015, **4**, 12–17.

36 M. Ramamurthy, M. Balaji and P. Thirunavukkarasu, *Optik (Stuttg).*, 2016, **127**, 3809–3819.

37 S. Pavithra, D. Balamurugan, R. Pandeeswari and B. G. Jeyaprakash, *Superlattices Microstruct.*, 2014, **75**, 435–444.

38 M. K. Ahmad and M. Rusop, in *Nanoscience andNanotechnology, International Conference on Nanoscience andNanotechnology*, 2009, vol. 1136, pp. 339–344.

39 T. Olav, L. Sunde, E. Garskaite, B. Otter, H. E. Fossheim, R. Saeterli, R. Holmestad, M.-A. Einarsrud and T. Grande, *J. Mater. Chem.*, 2012, **22**, 15740–15749.

40 S. Edinger, J. Bekacz, M. Richter, R. Hamid, R. A. Wibowo, A. Peić and T. Dimopoulos, *Thin Solid Films*, 2015, **594**, 238–244.

41 J. H. Park, Y. B. Yoo, K. H. Lee, S. W. Han, W. J. Choi and H. K. Baik, *J. Sol-Gel Sci. Technol.*, 2013, **67**, 130–134.

42 M. L. De La Olvera, A. Maldonado, R. Asomoza and M. Meléndez-Lira, *Sol. Energy Mater. Sol. Cells*, 2002, **71**, 61–71.

43 B. C. Jiao, X. D. Zhang, C. C. Wei, J. Sun, Q. Huang and Y. Zhao, *Thin Solid Films*, 2011, **520**, 1323–1329.

44 B. Malič, N. Setter, K. Brooks, M. Kosec and G. Dražič, *J. Sol-Gel Sci.*

Technol., 1998, 13, 833–836.

45 N. Quandt, F. Syrowatka, R. Roth and S. G. Ebbinghaus, *Thin Solid Films*, 2017, **636**, 573–584.

46 J. Rodríguez-Báez, A. Maldonado, L. Castañeda, G. T. Delgado, R. Castanedo-Pérez and M. de la, *Thin Solid Films*, 2007, **515**, 8689–8694.

47 A. Smith and R. Rodriguez-Clemente, *Thin Solid Films*, 1999, **345**, 192–196.

Chapter 4:

Deposition of zinc sulphide thin films

4.1 Introduction

Zinc sulphide (ZnS) is a group II-VI semiconductor material. Generally, ZnS can exist as two simple polymorphs, cubic sphalerite (or zinc blende) and hexagonal wurtzite.[1–3] The structure of zinc blende and wurtzite are very similar and contain tetrahedrally bonded Zn and S centres in their structures, but with differences arising in the stacking sequence of atomic layers.[4,5] Cubic zinc blende is stable at room temperature but can be transformed to the hexagonal wurtzite phase at 1020 °C and melted at 1650 °C.[2–6] Bulk ZnS has a large direct bandgap energy of 3.67 eV and 3.9 eV for cubic zinc blende and hexagonal wurtzite, respectively.[7,8] In the visible region, ZnS possesses a high transmittance and a high index of reflection.[5]

ZnS possesses a number of attractive features such as low-toxicity,[1,9,10] useful optoelectronic behaviour,[9] abnormal luminescence,[11–13] photocatalytic properties,[14] high-energy photon absorption,[9] displays good thermal and environmental stability[15,16] and is a potential environmentally friendly buffer material.[17]

Due to its various notable properties, ZnS has been considered as a promising material in many applications. For example, ZnS is a candidate to replace the CdS window material in single-heterojunction solar cell applications because ZnS is non-toxic and contains a wider and higher bandgap than CdS (2.4 eV). [9,10,18,19] Moreover, ZnS also has a potential other applications such as in electroluminescent devices, luminescent semiconductor quantum dots (QDs), bio-imaging and biosensor ultraviolet-light-emitting diodes, infrared windows, photoconductors, field effect transistors, as an optical coating for transducers, photovoltaic cells and as a promising n-type semiconductor for photocatalytic hydrogen production.[4,5,23–28,6,9,12,13,18,20–22]

The exploitation of these attractive properties requires the fabrication of ZnS in thin film form. Several deposition techniques have, thus, been employed to develop ZnS thin films, including electrochemical methods,[9] chemical bath deposition (CBD),[19,29,30] thermal evaporation,[12,13] RF magnetron sputtering,[7] and metal-organic chemical vapour deposition.[18] However, many of these techniques display significant limitations, are expensive and complicated or provide low-quality films.

The preparation of ZnS thin films in this chapter employ a simple single source precursors in conjunction with the AACVD technique to address these limitations.

Metal xanthate or dithiocarbonate, $[M(S_2COR)_n]$ and metal thioureide complexes $[M(RNCSNMe_2)_2]$ have been used as single source precursors for the ZnS film deposition in this chapter. These complexes decompose at low temperatures and can be easily dissolved in common organic solvents. They are, thus, useful for thin film deposition via AACVD at low temperatures enabling potentially low-cost ZnS thin film production.

4.1.1 Zinc xanthate complex precursors

Metal xanthates $[M(S_2COR)_n$, R=Et, nPr, iPr, n-Bu, n-Hex] are well known and attractive complexes for the formation of metal sulphide materials.[31–35] The remarkable advantages of the metal xanthates are a consequence of the low-temperature Chugaev rearrangement, which may be exploited during the AACVD technique to provide metal sulphide thin films at low deposition temperatures.[36] Furthermore, xanthates can provide an oxide-free route for metal sulphide thin film deposition.[36] Many metal xanthates have been used to prepare metal sulphide thin films and some examples are shown in Table 4.1.

Table 4.1 Examples of metal sulphide thin films from metal xanthate complex single source precursors.

Metal sulphide thin film materials	Metal xanthate complex precursors
(Zn,Cd)S	$M(O\text{-}^{i}PrXan)_2$, (M = Zn,Cd)[37]
ZnS	$Zn(O\text{-}EtXan)_2$[38]
Cu_2S	$Cu(S_2COEt)_2{\cdot}TMEDA$, (TMEDA = *N,N* tetramethylethylenediamine[32]
CdS	$Cd(S_2COEt)_2{\cdot}L_2$ (L = pyridine coligands)[31]
Sb_2S_3	$Sb(S_2COR)_3$[36]
PbS	$Pb(S_2COEt)_2$[39]
NiS	$Ni(S_2COHex)_2$,[35] $Ni(S_2COOct)_2$[35]
Pd_4S	$PdPh(S_2COPr^{i})(PMe_2Ph)$[40]

Generally, the thermal decomposition of the metal xanthate involves the Chugaev elimination reaction. The decomposition comprises two main events. First, the oxygen-bound organic R group is lost as an alkene via a six-membered cyclic concentrated syn-elimination transition state. Carbonyl sulphide and hydrogen sulphide are then lost to form the metal sulphide.[41] The example of nickel sulphide (NiS) formation from a metal xanthate complex via the Chugaev elimination mechanism is illustrated in Scheme 4.1.

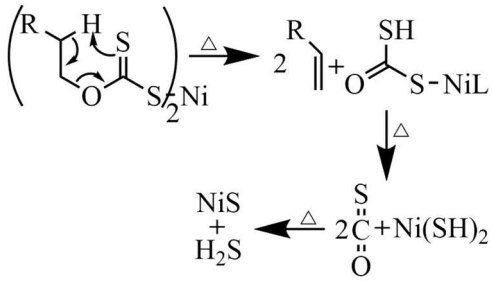

Scheme 4.1 Example of nickel sulphide (NiS) formation from a metal xanthate complex via the Chugaev elimination mechanism.[41]

The synthesis of metal xanthates complexes can be easily achieved from an insertion reaction of CS_2 with a metal alkoxide or the oxidation of a metal carbonyl by a dixanthogen.[42] The typical synthetic routes to metal xanthates are presented in Scheme 4.2.

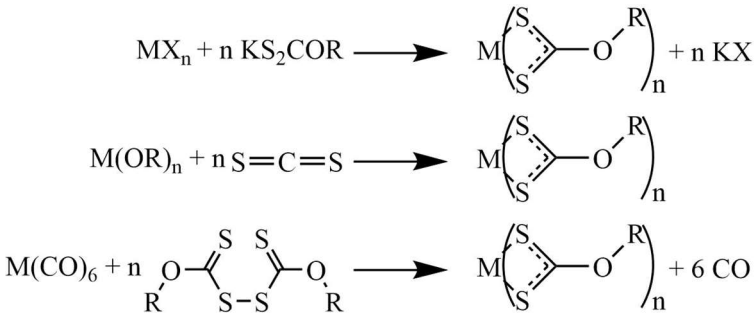

Scheme 4.2 Typical synthetic routes of metal xanthates.[43]

The metal xanthate precursors used to deposit the ZnS thin film described in this chapter were $Zn(S_2COEt)_2$ and 2-MePy·$Zn(S_2COEt)_2$, Figure 4.1.

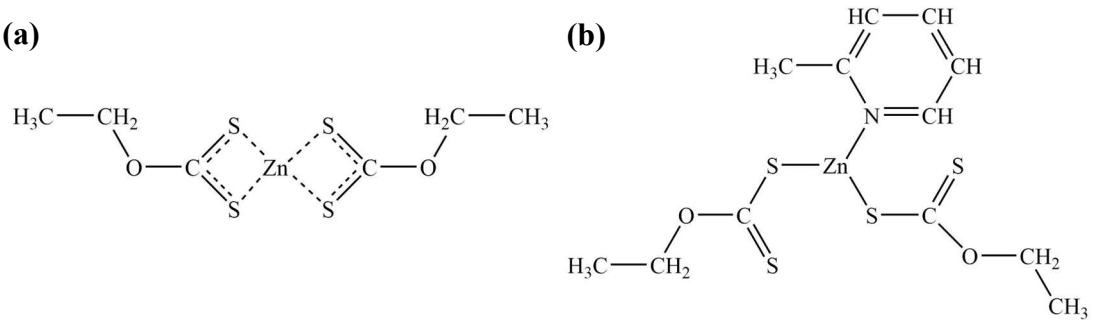

Figure 4.1 Metal xanthate precursors used to deposit the ZnS thin film in this chapter. (a) $Zn(S_2COEt)_2$ (b) 2-MePy·$Zn(S_2COEt)_2$.

4.1.2 Zinc thioureide complex precursors

Metal thioureide complexes are promising, but relatively underexploited, precursors to metal sulphide thin film materials. Generally, the thiourea-derived ligand is employed as a source of sulphur in thin film fabrication to form the desired metal sulphide thin film. Like the xanthates, facile decomposition allows the use of low deposition temperatures for thin film growth. Examples of metal sulphide growth from this class of complex are more limited but include CdS,[44] ZnS,[45] Cu_2ZnSnS_4,[46] CoS_2[47] and Bi_2S_3.[48] Thioureide-based precursors can be synthesised as shown in Scheme 4.3 below. Isothiocyanates react readily with metal amide bonds via an insertion reaction to provide the bidentate thioureide. [43,47,49–51]

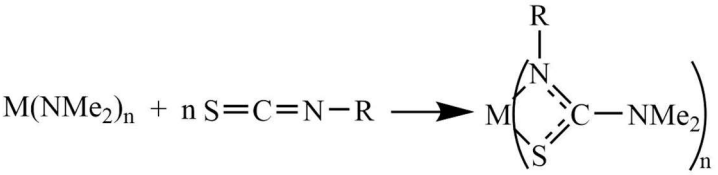

Scheme 4.3 Synthesis of metal thioureide complexes.[43]

The thioureide ligand can adopt three possible different binding modes with the observed mode dependent on the identity of the metal and the ligand substituents (Figure 4.2).

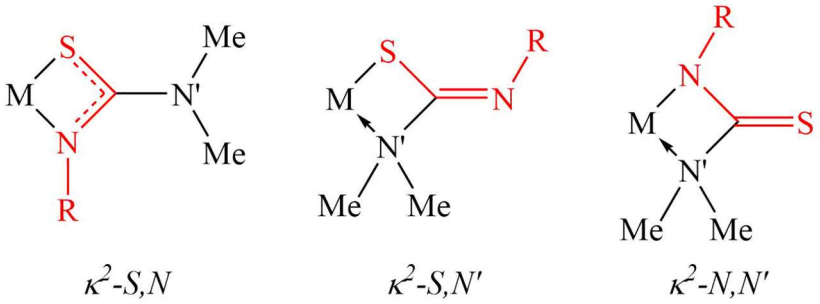

κ^2-*S,N* κ^2-*S,N'* κ^2-*N,N'*

Figure 4.2 The binding modes of thioureide ligands. Inserted isothiocyanate is shown in red and the original metal amide nitrogen is designated as N'.[43,52]

The κ^2-*S,N* mode, in which the metal centre atom is bonded to sulphur and the nitrogen atom arising from the isothiocyanate ligand, is most commonly observed. In the alternative κ^2-*S,N'* mode, the metal centre is bonded to a sulphur atom and the nitrogen atom of the original amide group. Alternatively, the ligand may adopt a κ^2-*N,N'* mode in which the metal centre binds to the ligand via the isothiocyanate N and that of the original amide group. In such cases, a double bond between carbon and sulphur atom is formed.[52]

Thioureide complexes have been used to prepare various metal sulphide thin films. Examples of these complexes and the resultant metal sulphide thin film materials are presented in Table 4.2.

Table 4.2 Examples of metal sulphide thin films from metal thioureide single source precursors.

Metal sulphide thin film materials	Metal thioureide complex precursors
SnS	$Sn((C_6H_5)NCSN(Me_2))(NMe_2)$[49]
CoS_2, Co_3S_4	$CoCl_2(CS(NH_2)_2)_2$[47]
$Co_{1-x}S$	$Co(N(SCNMe_2)_2)_3$[53]
Ni_9S_8	$Ni(C_{14}H_{28}N_3OS)_2$[53]

Zn(isopropyl thioureide),[$Zn(S{=}C(NMe)_2NCH(Me)_2)_2$] was selected to investigate and deposit the ZnS thin filmsdescribed in this chapter. Its chemical structure is presented in Figure 4.3.

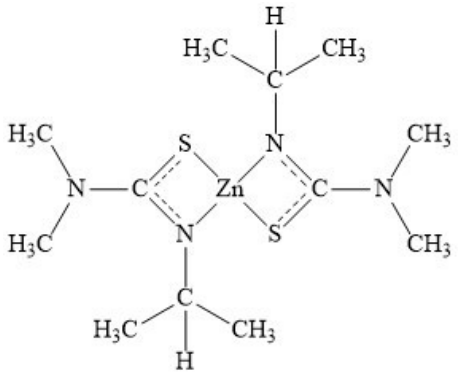

Figure 4.3 Zn(isopropyl thioureide), $Zn(S=C(NMe)_2\ NCH(Me)_2)_2$.

This chapter will describe the ZnS thin films resulting from the zinc xanthate complexes ($Zn(S_2COEt)_2$ and 2-MePy $Zn(S_2COEt)_2$) and the zinc thioureide complex ($Zn\ (S=C(NMe)_2\ NCH(Me)_2)_2$) via the AACVD technique. The characterisation of the deposited films from all three precursors will be performed and also compared.

4.2 Thermal analysis

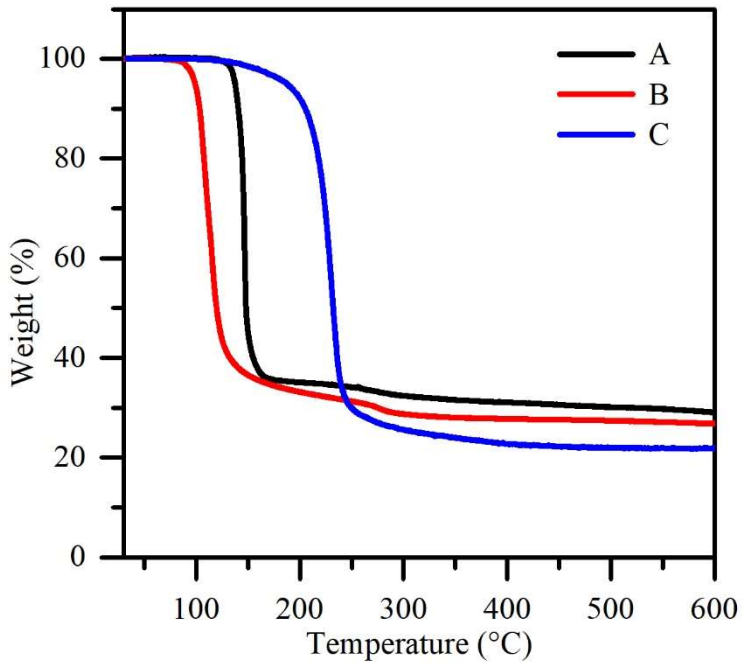

Figure 4.4 TGA curves of **A:** $Zn(S_2COEt)_2$, **B:** 2-MePy·$Zn(S_2COEt)_2$ and **C:** $Zn(S=C(NMe)_2NCH(Me)_2)_2$.

Thermal decomposition of $Zn(S_2COEt)_2$ [Mw= 307.76 g/mol], 2-MePy·$Zn(S_2COEt)_2$ [Mw = 400.89 g/mol] and $Zn(S=C(NMe)_2NCH(Me)_2)_2$ [Mw = 355.87 g/mol] was determined by thermogravimetric analysis and these results are shown in Figure 4.4.

2-MePy·Zn($S_2COEt)_2$ presented a sharp and significantly lower decomposition temperature than the other complexes with an initial weight loss at 100 °C. Final decomposition occurred at around 300 °C to leave a stable residue close to that expected for ZnS around 28.75 wt%. Zn($S_2COEt)_2$ displayed a thermal decomposition profile similar to 2-MePy·Zn($S_2COEt)_2$but with an initial decomposition temperature slightly higher than 2-MePy·Zn($S_2COEt)_2$ at around 130 °C. A final stable residue of 31.87 wt%, which was slightly higher than that expected for ZnS, was achieved at around 330 °C most likely due to incomplete decomposition of the precursor or incomplete elimination of some impurities. Zn($S=C(NMe)_2NCH(Me)_2)_2$ presented the highest thermal decomposition temperature, starting to decompose at a temperature around 140 °C before complete decomposition had been achieved around 415 °C with a stable weight percentage of that expected for ZnS of around 22.63 wt%. From the results of the TGA investigation, the approximate deposition temperatures were identified to undertake the AACVD of ZnS thin films with all three precursors.

4.3 ZnS thin film depositions

Table 4.3 Deposition conditions used to deposit ZnS thin films.

Variable	Detail
Precursor	Zn($S_2COEt)_2$
Precursor concentration	0.3 M
Substrate	SiCO Pilkington glass
Solvent	Toluene (C_7H_8)
Deposition time	60 min
Deposition temperature	150 - 200 °C
Deposition atmosphere	Nitrogen
Reactor type	Cold-wall

Variable	Detail
Precursor	2-MePy·Zn($S_2COEt)_2$
Precursor concentration	0.3 M
Substrate	SiCO Pilkington glass
Solvent	Toluene

Variable	Detail
Deposition time	60 min
Deposition temperature	100 - 250 °C
Deposition atmosphere	Nitrogen
Reactor type	Cold-wall

Variable	Detail
Precursor	$Zn(S{=}C(NMe)_2NCH(Me)_2)_2$
Precursor concentration	0.15 M
Substrate	SiCO Pilkington glass
Solvent	Toluene
Deposition time	60 min
Deposition temperature	150 - 300 °C
Deposition atmosphere	Nitrogen
Reactor type	Cold-wall

$Zn(S_2COEt)_2$, 2-MePy·$Zn(S_2COEt)_2$ and $Zn(S{=}C(NMe)_2NCH(Me)_2)_2$ were employed as single source precursors for ZnS thin film fabrication. The thin film deposition conditions are presented in Table 4.3. All deposited films were analysed and the results are discussed in the next section.

4.4 Appearance of deposited films

The appearance of all the deposited films is shown in Table 4.4. Most of films were transparent and possessed a gradient rainbow colour as a result of interference effects, which became more pronounced as the deposition temperature was increased. The films deposited at higher temperatures presented a slightly opaque appearance in comparison to those fabricated at lower deposition temperatures. At the same deposition temperature of 200 °C, for example, the film deposited from $Zn(S{=}C(NMe)_2NCH(Me)_2)_2$ presented a highly transparent appearance whereas the film deposited from 2-MePy·$Zn(S_2COEt)_2$ was opaque. All the deposited films passed the Scotch Tape test, which confirmed that they were well adhered to the substrate. The XRD, Raman and EDS analysis discussed below confirmed that all of the deposited films were ZnS.

Table 4.4 Appearance of all deposited films from $Zn(S_2COEt)_2$, 2-MePy·$Zn(S_2COEt)_2$ and $Zn(S{=}C(NMe)_2NCH(Me)_2)_2$ at various deposition temperatures.

Deposition temperature (°C)	**Precursor**		
	$Zn(S_2COEt)_2$]	**2-MePy· $Zn(S_2COEt)_2$**	**$Zn(S{=}C(NMe)_2$ $NCH(Me)_2)_2$**
100	-	 Amorphous	-
150	 Amorphous	 Cubic zinc blende ZnS	 Amorphous
200	 Cubic zinc blende ZnS	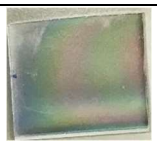 Cubic zinc blende ZnS	 Amorphous
250	-	 Cubic zinc blende ZnS	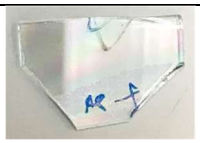 Hexagonal wurtzite ZnS
300	-	-	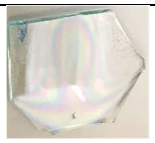 Hexagonal wurtzite ZnS

4.5 Crystallinity

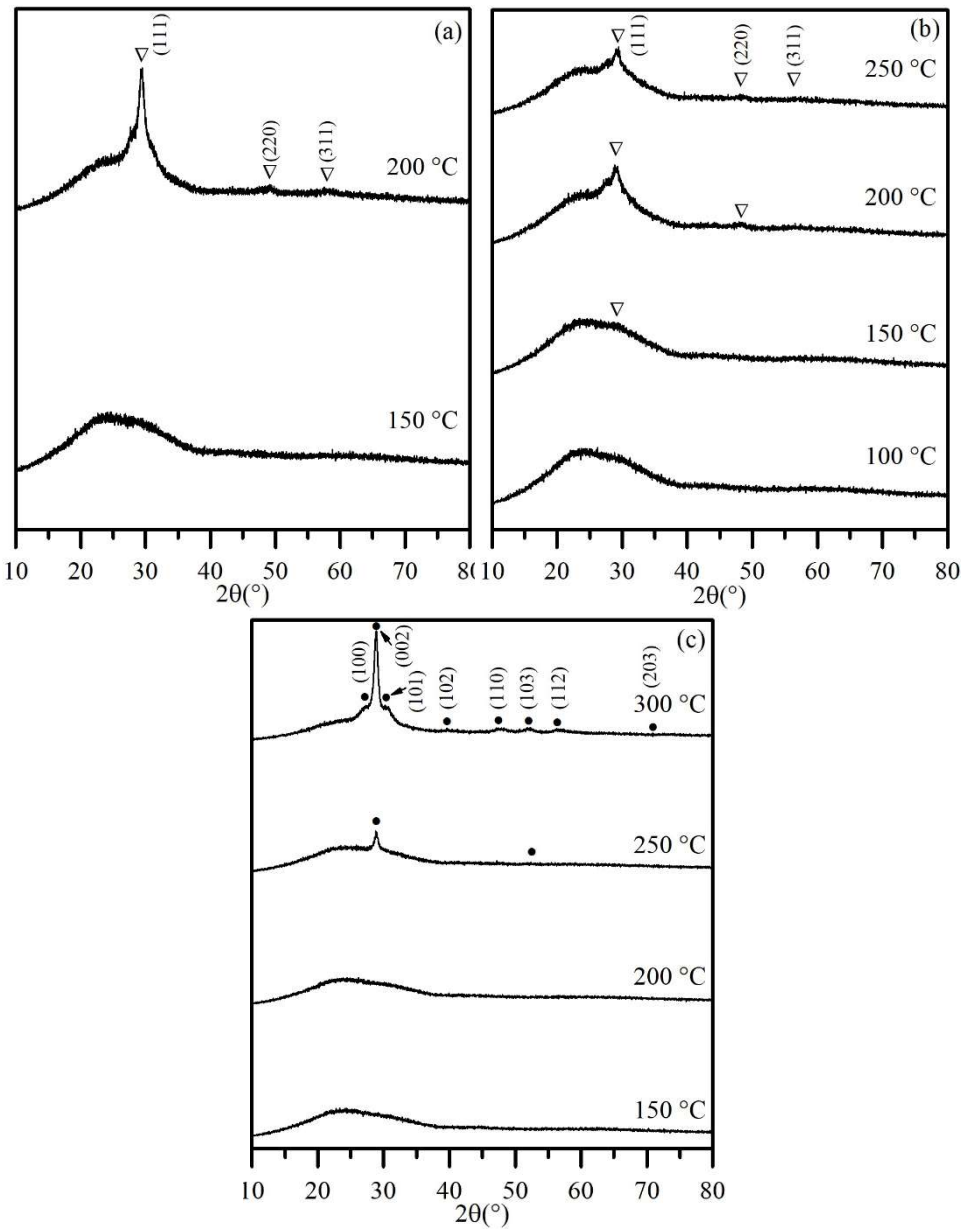

Figure 4.5 XRD patterns of films deposited from (a) $Zn(S_2COEt)_2$ and (b) 2-MePy·$Zn(S_2COEt)_2$ and (c) $Zn(S{=}C(NMe)_2NCH(Me)_2)_2$ at various deposition temperatures. (∇: Cubic zinc blende ZnS, JCPDS: 03-065-0309), (●: Hexagonal wurtzite ZnS, JCPDS: 01-075-1534).

All the deposited films were examined by powder X-ray diffraction analysis and the resultant XRD patterns are shown in Figure 4.5. $Zn(S_2COEt)_2$ provided an amorphous film at a deposition temperature of 150 °C but a crystalline film at 200 °C. The crystalline films exhibited three diffraction maxima which perfectly matched the cubic

zinc blende ZnS phase (JCPDCS 03-065-0309). The peaks presented at 2θ values of 29.39°, 48.98° and 58.26° index to the (111), (220) and (311) crystalline planes, respectively.

2-MePy·Zn($S_2COEt)_2$ also provided the cubic zinc blende phase but at a lower deposition temperature than Zn($S_2COEt)_2$ (Figure 4.5 (b)). The (111) peak of the ZnS phase was initially observed at 150 °C at a 2θ value of 29.38°. On increasing the temperature, the number and intensity of the peaks increased at 2θ values close to those exhibited by the zinc blende films deposited from Zn($S_2COEt)_2$. The XRD patterns of the films prepared from 2-MePy·Zn($S_2COEt)_2$ comprised very broad and low-intensity peaks in comparison to the films from Zn($S_2COEt)_2$. This is due to the deposited films from 2-MePy·Zn($S_2COEt)_2$ comprising smaller crystallite sizes than the films deposited from Zn($S_2COEt)_2$, Table 4.5.

Films which were fabricated from Zn($S=C(NMe)_2NCH(Me)_2)_2$ displayed the contrasting wurtzite phase, which could be observed at a deposition temperature of 250 °C. On raising the deposition temperature to 300 °C, the XRD pattern of the deposited film presented peaks which perfectly indexed to a wurtzite ZnS with a reference code 01-075-1534. The crystallite size of the deposited films was increased by around 2.65 times when the deposition temperature was increased from 250 °C to 300 °C (Table 4.5).

Table 4.5 Estimated crystallite sizes of deposited films.

Deposition temperature (°C)	**Estimated crystallite size (nm)**		
	Cubic Zinc blend *hkl* (111)		**Hexagonal wurtzite *hkl* (002)**
	Zn($S_2COEt)_2$	**2-MePy·Zn($S_2COEt)_2$**	**Zn($S=C(NMe)_2NCH(Me)_2)_2$**
100	-	amorphous	-
150	amorphous	6	amorphous
200	39	25	amorphous
250	-	10	9
300	-	-	25

4.6 Raman spectroscopy analysis

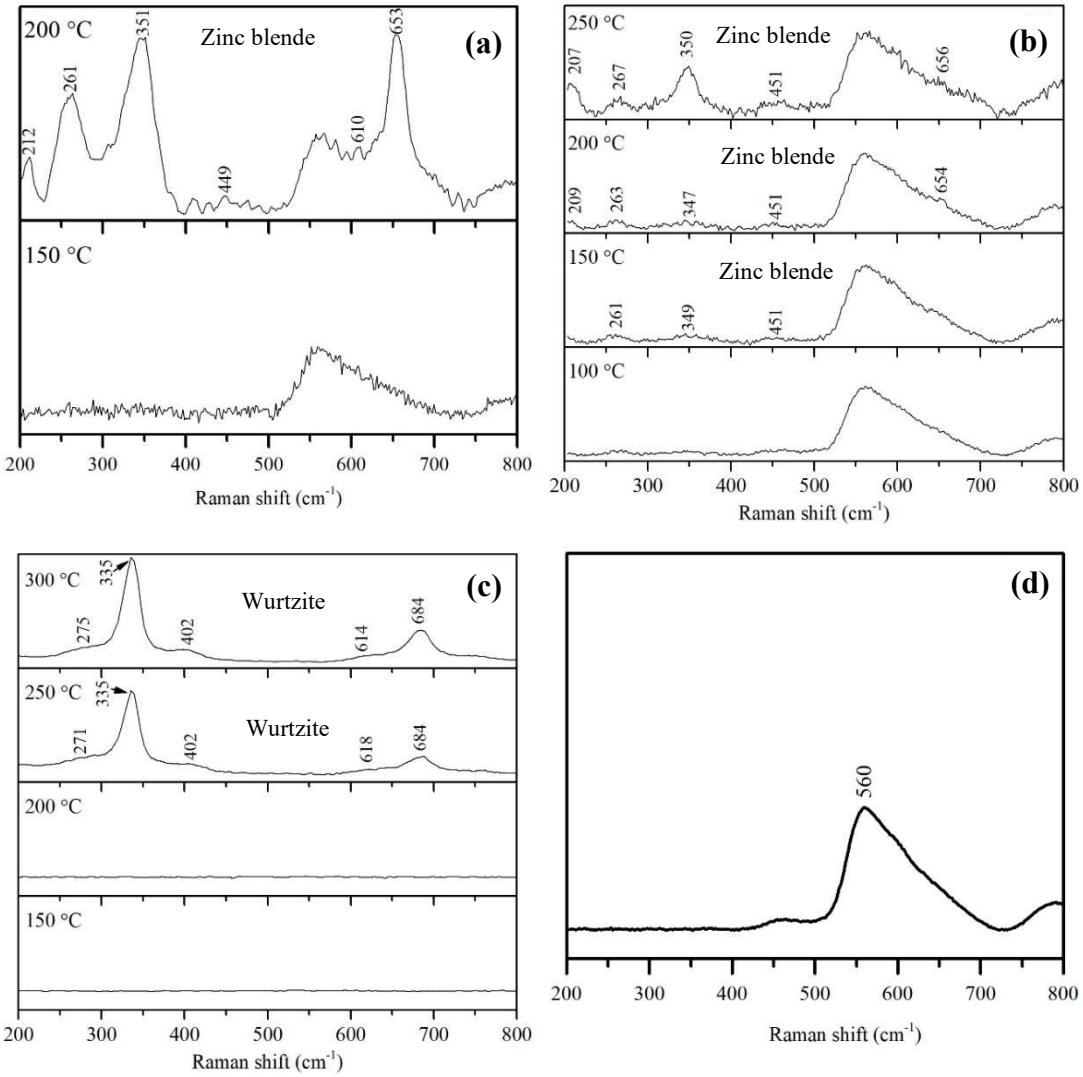

Figure 4.6 Raman spectra of films deposited from (a) $Zn(S_2COEt)_2$ (b) 2-MePy·$Zn(S_2COEt)_2$ (c) $Zn(S{=}C(NMe)_2NCH(Me)_2)_2$ at various deposition temperatures and (d) Pilkington SiCO glass.

Raman spectroscopy was performed on all deposited films at room temperature and the results are presented in Figure 4.6. The Raman spectra are in agreement with the XRD results of Figure 4.5 and confirm that $Zn(S_2COEt)_2$ and 2-MePy·$Zn(S_2COEt)_2$ provided cubic zinc blende ZnS, while $Zn(S{=}C(NMe)_2NCH(Me)_2)_2$ produced a wurtzite ZnS.

Figure 4.6 (a) shows the Raman spectra of deposited films from $Zn(S_2COEt)_2$ at deposition temperatures of 150 and 200 °C. The film deposited at 150 °C did not display any vibrations which could be assigned to either cubic or hexagonal ZnS, while

the film deposited at 200 °C presented seven narrow peaks at 212, 261, 351, 449, 610 and 653 cm^{-1}. These latter peaks match closely to the literature and can be assigned to zinc blende-type ZnS, Table 4.6.

The Raman spectra of films deposited from 2-MePy·$Zn(S_2COEt)_2$ show a similar profile as those from $Zn(S_2COEt)_2$ at 200 °C, Figure 4.6 (b). At the same deposition temperature (200 °C), however, the film deposited from $Zn(S_2COEt)_2$ possessed Raman peaks which were sharper and stronger than those displayed by the films from 2-MePy·$Zn(S_2COEt)_2$. This can be attributed to the higher crystallinity of the film and is consistent with Figure 4.5(a), (b) and Table 4.5. Furthermore, similar relationships have been reported by Xuqiang Hao ,et.al.[54]

Films deposited from $Zn(S{=}C(NMe)_2NCH(Me)_2)_2$ provided Raman spectra (Figure 4.6 (c)) which were different from those provided by both $Zn(S_2COEt)_2$ and 2-MePy·$Zn(S_2COEt)_2$. Five characteristic peaks at 271-275, 335, 402, 614-618 and 684 cm^{-1} fit well with those of wurtzite ZnS, which have been reported in literature and summarized in Table 4.6. This assignment is also consistent with the XRD analysis in Figure 4.5 (c). The vibrational modes of all the observed Raman spectral peaks of all deposited films are assigned in Table 4.6.

Table 4.6 Raman shifts of deposited thin films from $Zn(S_2COEt)_2$, 2-MePy·$Zn(S_2COEt)_2$ and $Zn(S{=}C(NMe)_2NCH(Me)_2)_2$ and their assignments.

Precursor	Raman shift (cm^{-1}) this work	Reference Raman shift (cm^{-1})	Assignment
$Zn(S_2COEt)_2$	212	219[55]	2LA
	263	262[56]	2(0) at W
	351	351,[56] 352,[55] 350[57]	T_2(LO)
	449	448,[55] 451[56]	LO+LA
	610	612,[55] 619.88[56]	2TO
	653	653,[58] 665[55]	2LO
2-MePy·$Zn(S_2COEt)_2$	207	219[55]	2LA
	267	262[56]	2(0) at W

Precursor	Raman shift (cm^{-1}) this work	Reference Raman shift (cm^{-1})	Assignment
$Zn(S=C(NMe)_2NCH(Me)_2)_2$	350	351,[56] 352,[55] 350[57]	T_2(LO)
	451	448,[55] 451[56]	LO+LA
	656	653,[58] 665[55]	2LO
	275	273,[59] 276,[60] 275,[56] 274[54]	TO
	335	335,[61] 335,[62] 338[63]	SO
	402	402,[56] 402.35[64]	TA+TO
	614	618[56],612[55],615[61],617[65]	2TO
	684	680[56],673[61]	2LO

LA: Longitudinal acoustic, TO: Transverse optic, LO: Longitudinal optic and SO: Surface optic

4.7 Compositional analysis

The composition of all the deposited ZnS films was investigated and estimated by EDS analysis and the analytical data are shown in Table 4.7. Zn and S were detected in all the deposited films and the atomic % of both elements increased with increasing deposition temperatures. In contrast, atomic % of O, Si, Mg, Na and Ca from the SiCO substrate decreased with raising deposition temperature due to the increasing film thickness on the substrate surface, which affected the penetration depth of the X-rays. In addition, it can be clearly seen that increasing film thickness is a result of rising deposition temperature by assessment of the cross-section SEM micrographs shown in Figures 4.13, 4.14 and 4.15.

The carbon content, which was detected in all the deposited films, possibly results from the precursors themselves or the solvent employed during deposition. The films which were prepared from 2-MePy·$Zn(S_2COEt)_2$ presented an increasing atomic % of carbon with the increasing deposition temperature, whilst the atomic % of carbon of

the films deposited from $Zn(S_2COEt)_2$ was observed to decrease slightly on raising the deposition temperature.

The atomic % of C in films from $Zn(S=C(NMe)_2NCH(Me)_2)_2$, however, was difficult to predict as the EDS analysis indicated that the carbon content decreased in raising the deposition temperature from 150 °C to 200 °C, while the film deposited at 250 °C presented a significantly lower carbon content than all other temperatures. This included the film deposited at the higher temperature of 300 °C, which displayed an insignificant carbon content.

Table 4.7 Summary of the EDS elemental analysis for ZnS films deposited onto Pilkington SiCO glass substrates from $Zn(S_2COEt)_2$ **(A)**, 2-MePy·$Zn(S_2COEt)_2$ **(B)** and $Zn(S{=}C(NMe)_2NCH(Me)_2)_2$ **(C)** at various deposition temperatures for 1 hour. Average atomic % from 3 measured areas.

Precursor	Deposition temperature (°C)	Atomic %							
		Zn	S	O	C	Si	Mg	Na	Ca
A	150	18.14±0.45	12.31±0.20	34.75±2.10	17.20±2.71	5.79±1.02	0.40±0.10	11.41±0.32	0
	200	31.17±0.87	28.01±1.87	10.49±0.75	16.89±1.62	0.07±0.16	0	13.37±0.57	0
B	100	6.12±0.95	6.91±1.18	40.38±2.06	8.13±1.37	25.96±1.03	1.60±0.14	8.39±0.12	2.52±0.18
	150	12.21±3.46	14.74±4.42	30.38±5.32	9.98±1.65	20.76±3.52	1.21±0.22	8.77±0.27	1.95±0.27
	200	25.63±2.67	31.58±3.77	11.90±3.44	10.58±1.48	9.77±4.02	0.36±0.26	9.30±0.01	0.90±0.23
	250	30.27±2.65	37.77±3.55	7.24±1.35	11.57±3.79	3.85±2.22	0.07±0.13	8.78±0.73	0.45±0.21
C	150	0.60±0.14	0.56±0.14	49.16±0.81	6.20±0.38	29.76±0.41	2.10±0.07	8.28±0.09	2.90±0.10
	200	0.82±0.12	1.16±0.08	48.98±0.40	5.11±0.60	30.52±0.43	2.02±0.07	8.33±0.11	3.07±0.07
	250	19.78±0.97	27.84±1.52	12.46±0.82	16.21±1.05	12.25±0.80	0.56±0.12	9.67±0.45	1.21±0.04
	300	32.62±0.31	45.40±0.62	2.33±0.27	8.66±.1.23	0.21±0.09	0	10.77±0.58	0

Table 4.8 Summary of the ratio of Zn and S contents on the deposited films from $Zn(S_2COEt)_2$ **(A)**, 2-MePy·$Zn(S_2COEt)_2$ **(B)** and $Zn(S{=}C(NMe)_2NCH(Me)_2)_2$ **(C)** at different disposition temperatures.

Deposition temperature (°C)	Atomic ratio					
	A		B		C	
	Zn	S	Zn	S	Zn	S
100	-	-	1	1.13	-	-
150	1	0.68	1	1.21	1	0.93
200	1	0.90	1	1.23	1	1.41
250	-	-	1	1.25	1	1.41
300	-	-	-	-	1	1.39

The atomic ratios between Zn and S for all deposited films are summarised and presented in Table 4.8. From this summary, it is apparent that all precursors provided an atomic ratio of Zn and S close to the stoichiometry of ZnS (1:1). Furthermore, it was found that increasing temperatures lead to more sulphur-rich films. At the same deposition temperature of 200 °C, $Zn(S_2COEt)_2$ provided a ratio close to a stoichiometry of 1 : 1 (1 : 0.90). In addition, this investigation of the EDS analysis confirms that all deposited films are ZnS, supporting the deductions drawn from the XRD and Raman analysis.

4.8 Surface and cross-section morphology

4.8.1 Surface morphology

The morphology of all the deposited films was examined using FESEM and AFM analysis. Figures 4.7, 4.8 and 4.9 illustrate the FESEM surface micrographs of the films deposited from $Zn(S_2COEt)_2$, 2-MePy·$Zn(S_2COEt)_2$ and $Zn(S{=}C(NMe)_2NCH(Me)_2)_2$, respectively. All precursors provided a good coverage of the substrate surface when the deposition temperature was increased.

The FESEM micrograph (Figure 4.7 (a)) of the film deposited from $Zn(S_2COEt)_2$ at 150 °C comprises some particles spread over the substrate surface but without complete coverage. When the deposition temperature is increased to 200 °C, however,

agglomerations of rounded particles appeared, which spread across the entirety of the substrate surface, (Figure 4.7 (b)). The crystalline zinc blende phase of ZnS was apparent at this temperature, while this deposition temperature also provided a smoother surface to the deposited film than the material deposited at 150 °C, Table 4.9.

Films deposited from 2-MePy·Zn($S_2COEt)_2$ at deposition temperatures of 100 and 150 °C displayed similar features with some particles sparsely scattered over the substrate surface (Figures 4.8 (a) and (b)). In contrast, at a deposition temperature at 200 °C, the film appears to be continuous and to comprise numerous agglomerated rounded particles across the substrate surface. This observation coincides with the observation of crystalline cubic ZnS found at this temperature, (Figure 4.8 (c)). A further increase of the deposition temperature to 250 °C provided much smaller and more uniform particles than the deposition temperature at 200 °C, Figure 4.8 (d). This may be due to faster evaporation of the precursor droplets after their introduction into the deposition chamber. The data shown in Table 4.9 also demonstrate that the surface roughness of the film deposited at 200 °C displays the highest value of around 20 nm, whereas the roughness value rapidly decreases to around 7.90 nm when the deposition temperature has reached 250 °C. In addition, these data are consistent with the decrease in crystallite size shown in Table 4.5.

Figure 4.9 displays the surface morphology of the films deposited from Zn(S=C($NMe)_2$NCH($Me)_2)_2$ at various deposition temperatures. The FESEM micrographs in Figures 4.9 (a) and (b) reveal that the films deposited at 150 and 200 °C display very flat surfaces with low values of surface roughness of only around 2.63 - 6.54 nm. Coinciding with the appearance of crystalline wurtzite ZnS at a deposition temperature of 250 °C, it can be clearly seen that the substrate is covered by uniform nanoparticles which are evenly dispersed over the substrate surface, Figure 4.9 (c). Moreover, at 300 °C, Figure 4.9 (d), the size of the nanoparticles is further increased and they agglomerate together. At this point, the surface roughness also increased from around 6.54 nm at a deposition temperature of 250 °C to 14.59 nm at 300 °C.

At the same deposition temperature of 200 °C, Zn($S_2COEt)_2$ and 2-MePy·Zn($S_2COEt)_2$ provided films which possessed a similar appearance, however,

the particles comprising the deposited film from 2-MePy·Zn($S_2COEt)_2$ are smaller than those from Zn($S_2COEt)_2$. On the other hand, Zn(S=C($NMe)_2NCH(Me)_2)_2$ provided a planar film with the lowest surface roughness value.

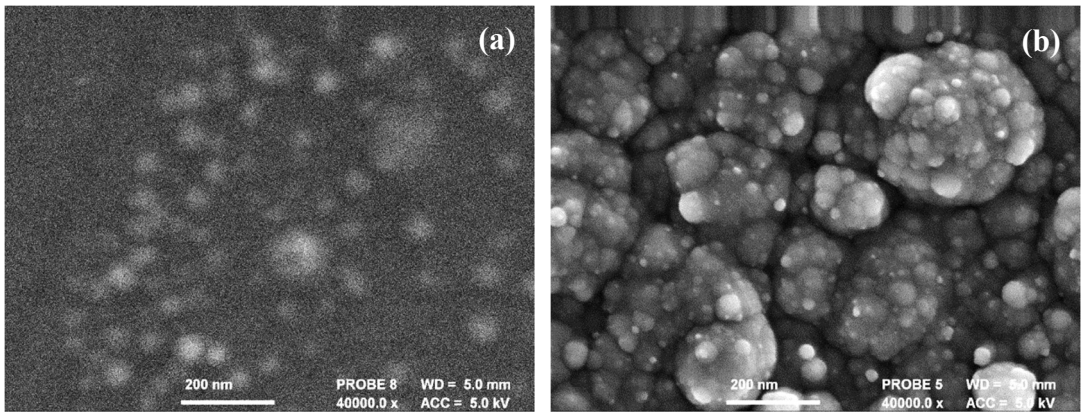

Figure 4.7 FESEM micrographs of the film deposited from Zn($S_2COEt)_2$ with the deposition temperature at (a) 150 °C (b) 200 °C.

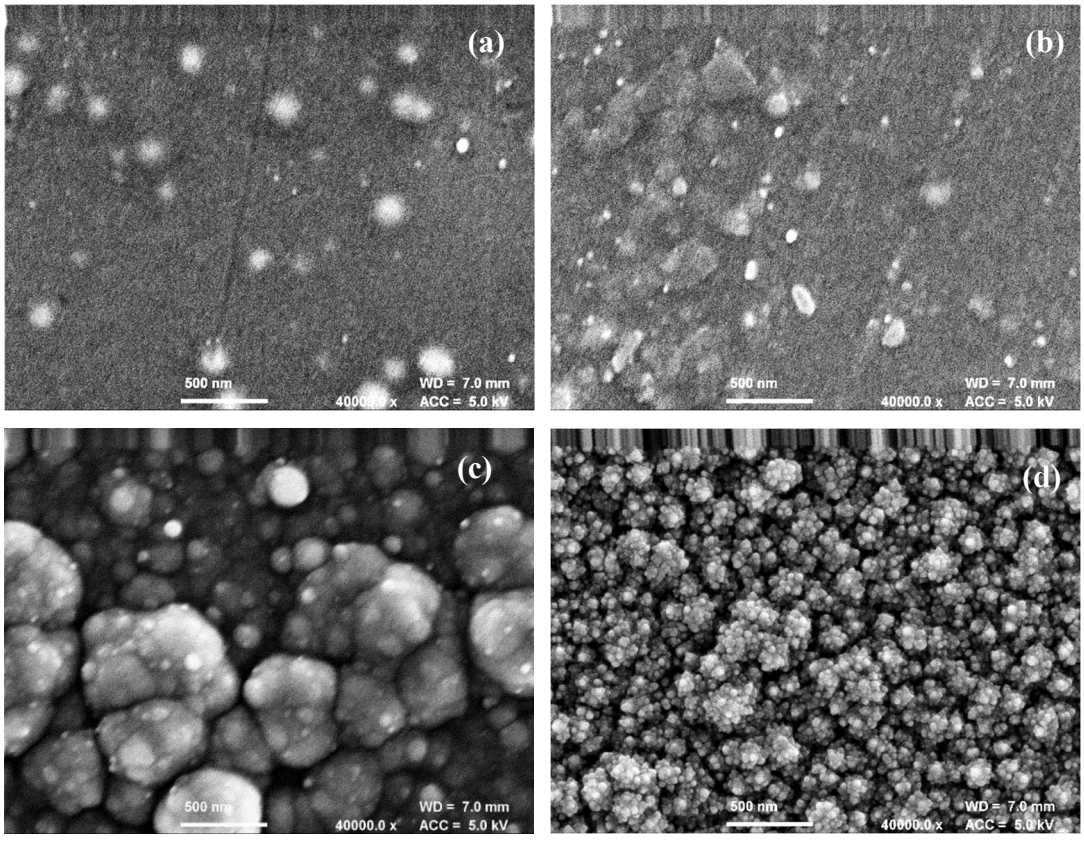

Figure 4.8 FESEM micrographs of the film deposited from 2-MePy·Zn($S_2COEt)_2$ with the deposition temperature at (a) 100 °C (b) 150 °C (c) 200 °C and (d) 250 °C.

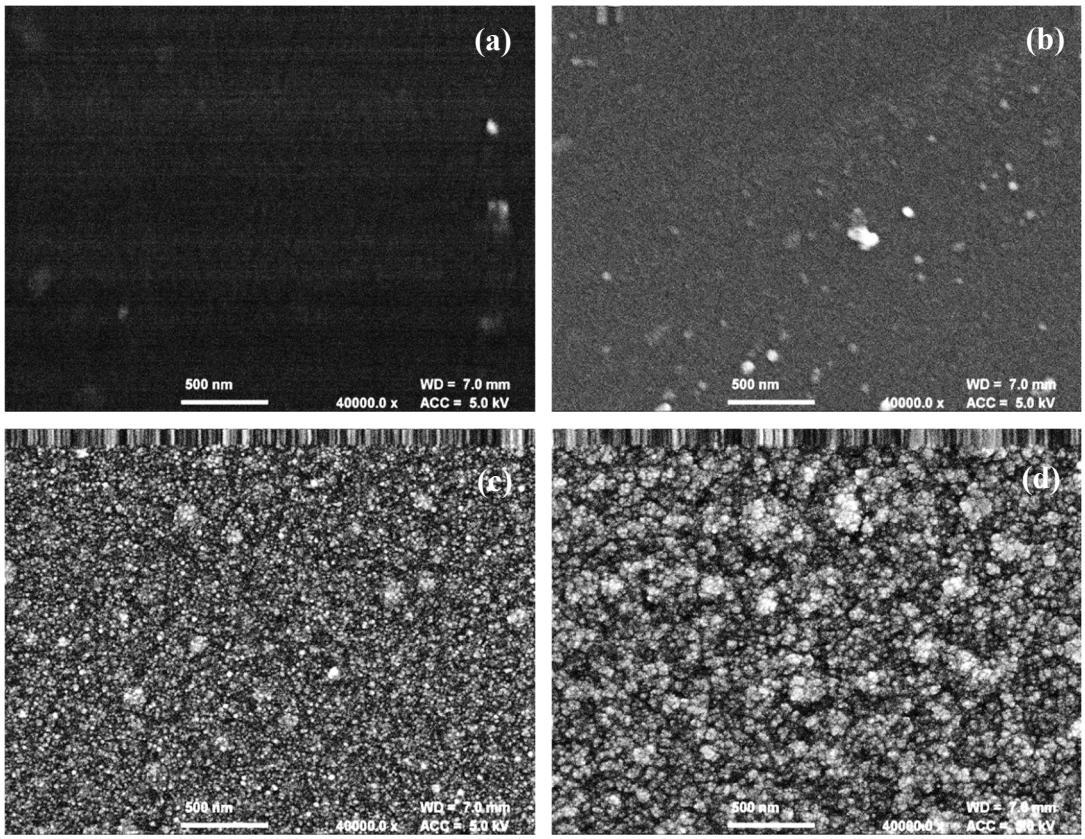

Figure 4.9 FESEM micrographs of the film deposited from $Zn(S{=}C(NMe)_2NCH(Me)_2)_2$ with the deposition temperature at (a) 150 °C (b) 200 °C (c) 250 °C and (d) 300 °C.

Table 4.9 Average surface roughness of all deposited film $Zn(S_2COEt)_2$, 2-MePy·$Zn(S_2COEt)_2$ and $Zn(S{=}C(NMe)_2NCH(Me)_2)_2$ at various deposition temperature. Average atomic % from 3 measured areas.

Deposition temperature (°C)	**Average surface roughness (nm), area measurement: 5 μm**		
	$Zn(S_2COEt)_2$	2-MePy· $Zn(S_2COEt)_2$	$Zn(S{=}C(NMe)_2NCH(Me)_2)_2$
100	-	6.14 ± 0.54	-
150	21.15 ± 10.52	11.03 ± 5.10	2.63 ± 0.27
200	12.41 ± 1.55	20.05 ± 3.39	6.54 ± 2.12
250	-	7.90 ± 4.25	7.02 ± 2.32
300	-	-	14.59 ± 2.25

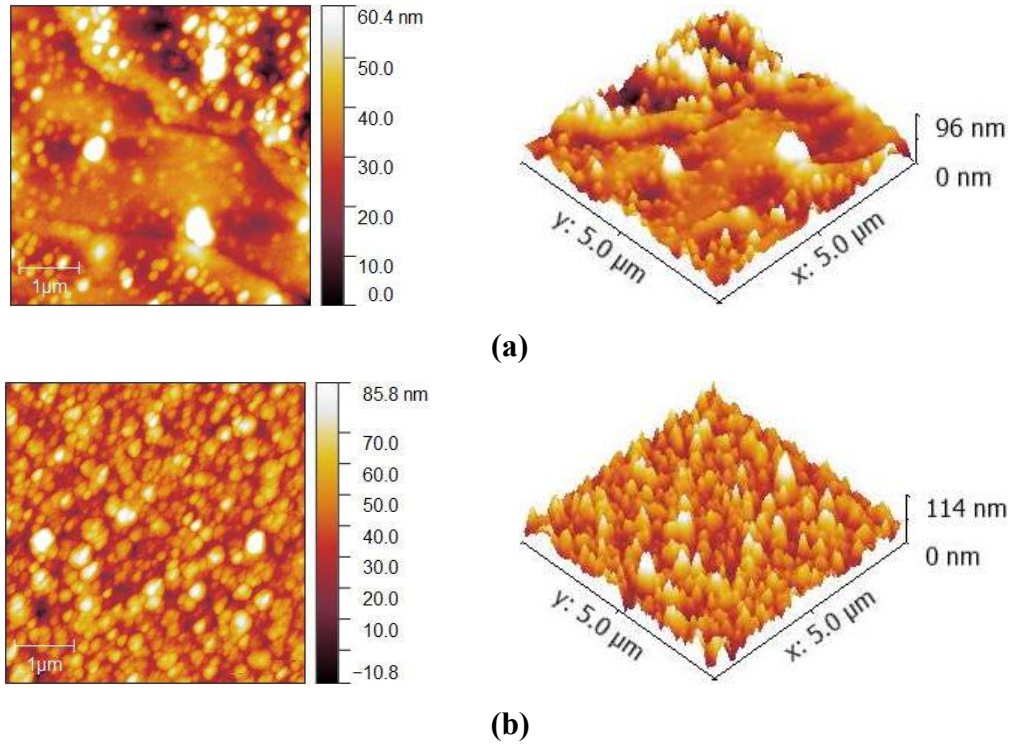

Figure 4.10 AFM images of films deposited from $Zn(S_2COEt)_2$ with the deposition temperature at (a) 150 °C (b) 200 °C.

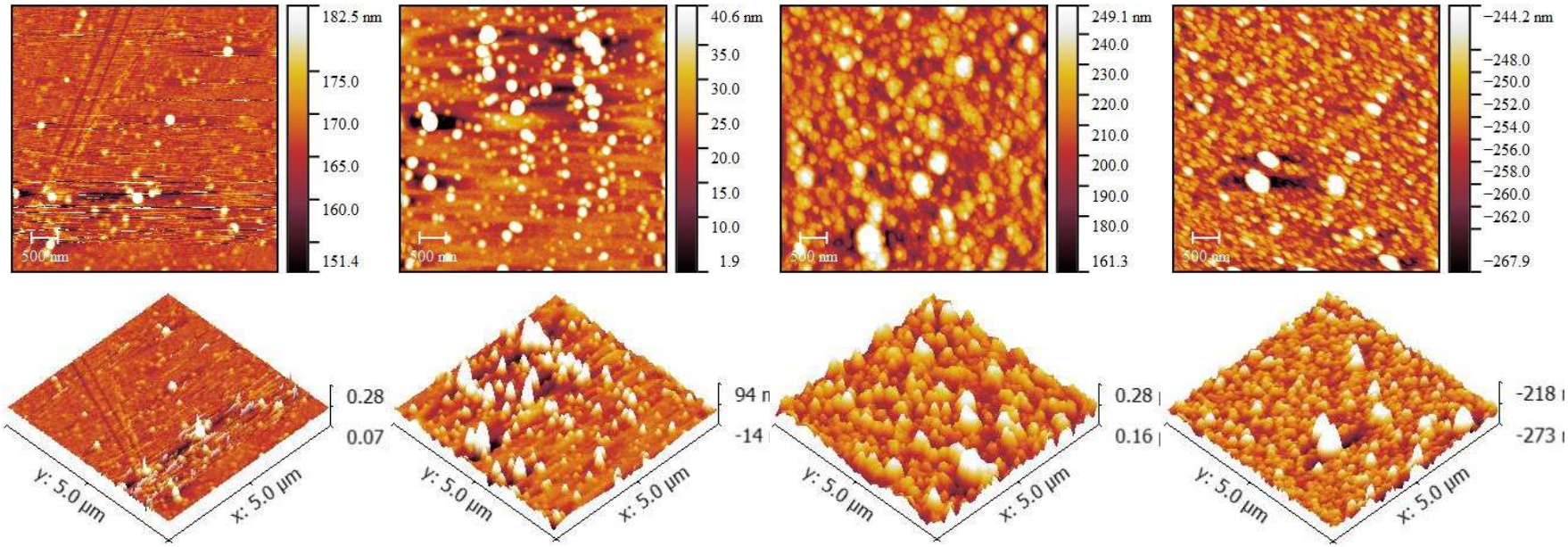

(a) (b) (c) (d)

Figure 4.11 AFM images of films deposited from 2-MePy·Zn($S_2COEt)_2$ with the deposition temperature at (a) 100 °C (b) 150 °C (c) 200 °C and (d) 250 °C.

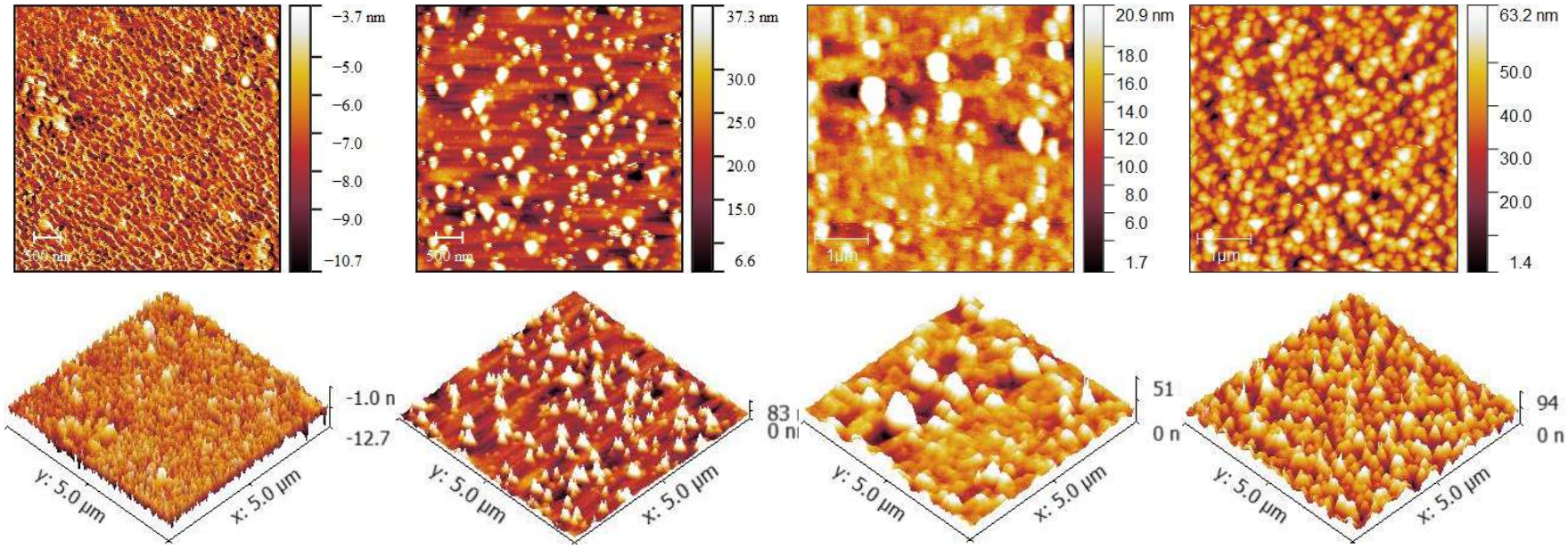

(a) (b) (c) (d)

Figure 4.12 AFM images of films deposited from $Zn(S{=}C(NMe)_2NCH(Me)_2)_2$ with the deposition temperature at (a) 150 °C (b) 200 °C (c) 250 °C and (d) 300 °C.

4.8.2 Cross-section morphology

Figures 4.13, 4.14 and 4.15 present the cross-sectional morphology of the deposited films from precursors $Zn(S_2COEt)_2$, 2-MePy·$Zn(S_2COEt)_2$ and $Zn(S{=}C(NMe)_2NCH(Me)_2)_2$ respectively. All three precursors provided increasing film thicknesses with increasing deposition temperature (Table 4.10) and all of the deposited films comprised compact and uniform appearances. In addition, Table 4.11 presents the estimated growth rate values of the films deposited from all three precursors. The deposition rate was calculated by using the thickness of the deposited films per deposition time (60 min) at each deposition temperature.

Table 4.10 Average thickness for the film deposited from $Zn(S_2COEt)_2$ **(A)**, 2-MePy·$Zn(S_2COEt)_2$ **(B)** and $Zn(S{=}C(NMe)_2NCH(Me)_2)_2$ **(C)**. Average thickness from 3 measured areas.

Deposition termperature (°C)	Average thickness (nm)		
	A	B	C
100	-	33.97 ± 2.39	-
150	91.32 ± 9.61	179.84 ± 4.47	58.53 ± 2.72
200	351.48 ± 7.15	316.54 ± 10.96	71.52 ± 3.91
250	-	554.13 ± 16.85	349.88 ± 6.54
300	-	-	443.96 ± 9.98

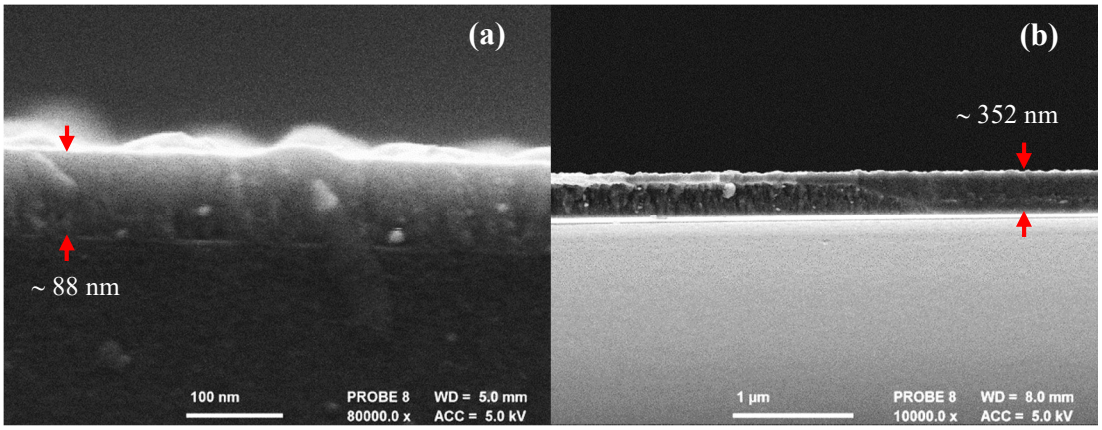

Figure 4.13 Cross-section micrographs of the film deposited from $Zn(S_2COEt)_2$ with the deposition temperature at (a) 150 °C (b) 200 °C.

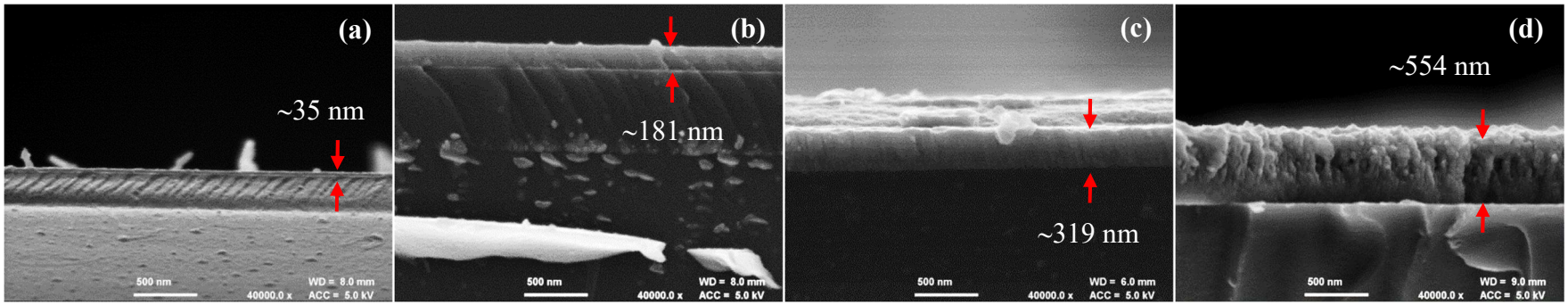

Figure 4.14 Cross-section micrographs of the film deposited from 2-MePy·Zn($S_2COEt)_2$ with the deposition temperature at (a) 100 °C (b) 150 °C (c) 200 °C and (d) 250 °C.

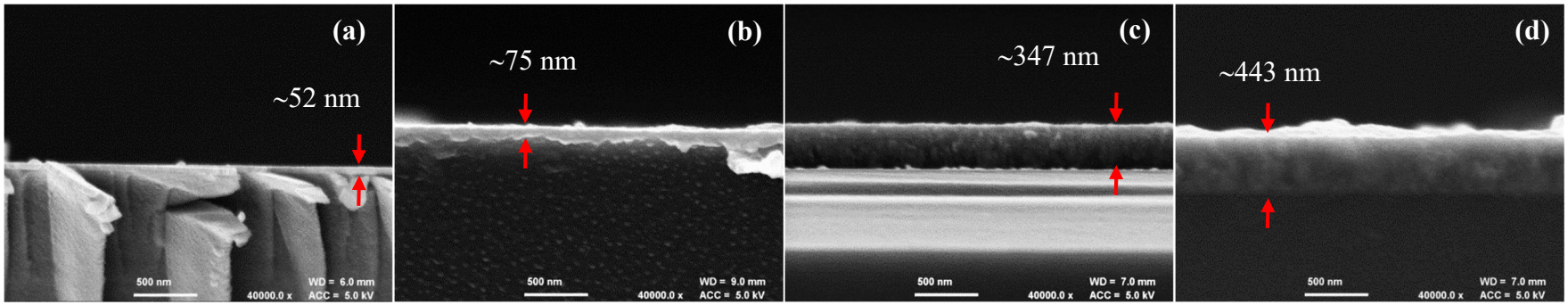

Figure 4.15 Cross-section micrographs of the film deposited from Zn(S=C$(NMe)_2$NCH$(Me)_2)_2$ with the deposition temperature at (a) 150 °C (b) 200 °C (c) 250 °C and (d) 300 °C.

Table 4.11 Average growth rate values for the film deposited from $Zn(S_2COEt)_2$ **(A)**, 2-MePy·$Zn(S_2COEt)_2$ **(B)** and $Zn(S{=}C(NMe)_2NCH(Me)_2)_2$ **(C)**.

Deposition termperature (°C)	Growth rate (nm/min)		
	A	**B**	**C**
100	-	0.57 ± 0.04	-
150	1.52 ± 0.16	3.00 ± 0.07	0.98 ± 0.05
200	5.86 ± 0.12	5.28 ± 0.18	1.19 ± 0.65
250	-	9.24 ± 0.28	5.83 ± 0.10
300	-	-	7.40 ± 0.17

$Zn(S_2COEt)_2$ provided thin film with a thickness of 88 nm at a deposition temperature 150 °C, whereas at 200 °C, the film deposited much more rapidly to provide a higher thickness of 352 nm, 4 times that provided by the lower deposition temperature, (Figure 4.13). In addition, the average growth rate at 200 °C was 5.86 ± 0.12 nm/min whereas at 150 °C this value is only 1.52 ± 0.16 nm/min, Table 4.11.

Cross-section morphologies of the deposited films prepared from 2-MePy·$Zn(S_2COEt)_2$ are displayed in Figure 4.14. All FESEM micrographs indicate continuous and dense layers of deposited material. The lowest deposition temperature at 100 °C provided a film with the lowest thickness at 35 nm, whilst the highest deposition temperature 250 °C provided a thicker film of 554 nm. The surface roughness of both films, however, did not change significantly; 6.14 nm for the film deposited at 100 °C and 7.90 nm for the film deposited at 250 °C. The films deposited between 100 and 200 °C exhibited a microstructure which was dense, continuous and homogeneous, Figure 4.14 (a)-(c). In contrast, the film deposited at 250 C° possessed some voids which evolved from within the bulk of the film. Moreover, columns with tight grain boundaries also appeared, Figure 4.14 (d). These morphologies can be explained by surface diffusion phenomena and a grain growth mechanism (columnar growth or Stranski-Krastanov growth) operating during the deposition process.[66] As such, the morphologies are not desirable, however, for applications such as thin film solar cells, which require a void-free and compact morphology.[67–69]

Figure 4.15 displays the cross-section FESEM micrographs of the film deposited from the $Zn(S{=}C(NMe)_2NCH(Me)_2)_2$. The cross-section images revealed that all of the deposited films were also dense, uniform and continuous across the substrate surface as well as void and crack -free. The film with the lowest deposition temperature at 150 °C possessed the lowest film thickness of 52 nm. The film thickness again increased with increasing temperature up to the highest temperature of 300 °C, which provided a film thickness of 443 nm. The film thickness increased sharply from 75 nm at 200 °C to 347 nm at 250 °C with a rapid increase of the growth rate from 1.19 ± 0.65 nm to 5.83 ± 0.10 nm/min (Table 4.10 and Figure 4.17).

The growth rate values of the three precursors present a similar increasing trend with the increasing deposition temperatures. At the same deposition temperature of 200 °C, $Zn(S_2COEt)_2$ provided the highest deposition growth rate, while 2-MePy·$Zn(S_2COEt)_2$ provided the lowest growth rate. In addition, $Zn(S_2COEt)_2$ at this temperature provided a film which displayed the highest thickness of around 352 nm whereas the films deposited from the 2-MePy·$Zn(S_2COEt)_2$ and $Zn(S{=}C(NMe)_2NCH(Me)_2)_2$ provided the films of 319 and 75 nm, respectively.

It should be noted, however, that deposition from $Zn(S{=}C(NMe)_2NCH(Me)_2)_2$ was performed with a lowest concentration of the precursor solution of 0.15 M, whilst the films deposited from $Zn(S_2COEt)_2$ and 2-MePy·$Zn(S_2COEt)_2$ both utilised 0.3 M solution concentrations.

Activation energies (E_a)

$$lnk = -\frac{E_a}{RT} + lnA$$

Where:

E_a is the activation energy

κ is a rate constant

A is a pre-exponential factor

R is the gas constant (8.314 J/mol/K)

T is a deposition temperature (Kelvin)

Slope of the Arrhenius plot is $-\frac{E_a}{RT}$

The activation energy (E_a) for the film deposition can be calculated by using an Arrhenius plot of the ln [growth rate (nm/min)] versus 1000/T (K^{-1}). All activation

energies calculated from the thin films deposited are indicated in Table 4.12 and Figure 4.16.

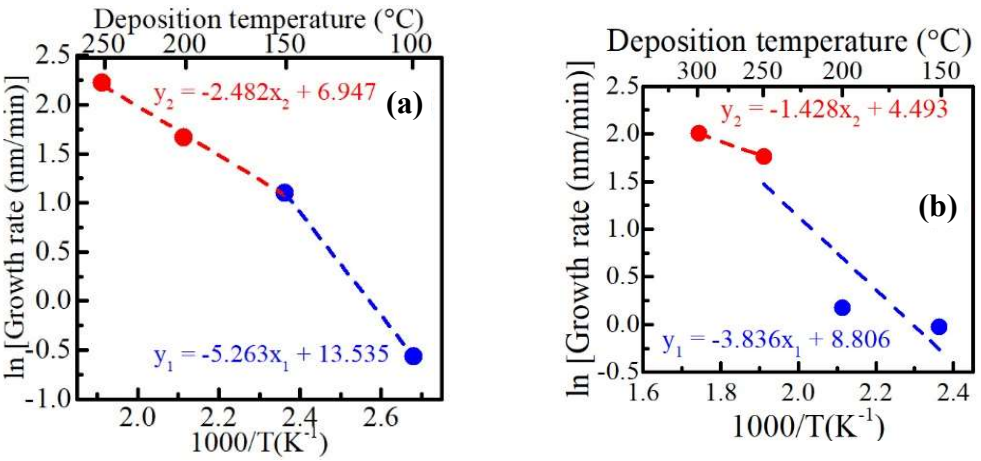

Figure 4.16 Arrhenius plots; (a) the films deposited from 2-MePy·Zn($S_2COEt)_2$ (b) the deposited films from Zn(S=C($NMe)_2$NCH($Me)_2)_2$.

Table 4.12 Activation energy values for the films deposited from 2-MePy·Zn($S_2COEt)_2$ and Zn(S=C($NMe)_2$NCH($Me)_2)_2$.

Precursor	Activation energy		Deposition temperature range (°C)
	E_a	(kJ.mol^{-1})	
2-MePy·Zn($S_2COEt)_2$	E_{a1}	43.74	100-150
	E_{a2}	20.63	150-250
Zn(S=C($NMe)_2$NCH($Me)_2)_2$	E_{a1}	31.88	150-250
	E_{a2}	11.87	250-300

In all the precursor deposition routes, the onset of observable crystalline films (Figure 4.5), corresponded with a rapid increase in the thickness of the deposited films. The observation of slow growing amorphous materials at lower deposition temperatures can be explained by the onset of different crystalline thin film formation mechanisms above a certain threshold temperature. Films deposited 2-MePy·Zn($S_2COEt)_2$ and Zn(S=C($NMe)_2$NCH($Me)_2)_2$ were selected to calculate an activation energy for the deposition processes.

The Arrhenius plot provided by the films deposited from 2-MePy·Zn($S_2COEt)_2$ in Figure 4.16 (a), allows the discrimination of two activation energies over two deposition temperature ranges. Between 100 and 150 °C, the activation energy (E_{a1}) is equal to 43.7 kJ/mol while across the higher temperature range of 150 to 250 °C the activation energy (E_{a2}) is equal to 20.6 kJ/mol. Consideration of these results implies that deposition occurs in two different temperature-controlled regimes. Within the lower temperature range (100-150°C), it is suggested that film growth is surface-reaction limited or kinetically controlled, whilst in the higher temperature regime (150-250 °C) deposition is mass transport limited. Similar effects have been observed and investigated previously in the literature.[70–72]

The growth rate analysis of $Zn(S{=}C(NMe)_2NCH(Me)_2)_2$ provided an Arrhenius plot with a similar appearance to that supplied by 2-MePy·Zn($S_2COEt)_2$, again occupying two regime deposition temperature ranges. The first presents across the temperature range 150-250 °C, with E_{a1} equal to 31.9 kJ/mol, whilst in the range 250-300 °C E_{a2} is estimated to be 11.9 kJ/mol.

It can be clearly seen that the activation energy at the higher temperature (E_{a2}) is significantly lower than at the lower temperature (E_{a1}). This observation is consistent with the observed increase of growth rate at these increasing deposition temperatures.

4.9 Optical properties

The optical properties of all the films were investigated by UV/Vis spectroscopy and the energy band gaps of the films were determined by Tauc plots. Transmission spectra of all the deposited films are shown in Figure 4.19.

All films deposited from the Zn($S_2COEt)_2$ provided a transmittance between 68 and 83 % in the visible light region, Figure 4.19 (a). In addition, the film deposited at 200 °C was slightly less transparent than the film deposited at 150 °C, while the film deposited at 200 °C presented an oscillation graph pattern which is attributed to the variation of the thickness of the film.

The % transmittance of the films deposited from 2-MePy·Zn($S_2COEt)_2$ are displayed in Figure 4.19 (b). The film deposited at 100 °C displays a transmission over 77 % across the visible region, whereas the film deposited at 150 °C presents a high

transparency of over 80% between wavelengths of 390 and 575 nm but which drops to between 80 % and 71 % at wavelengths between 575 and 800 nm. The films deposited at 200 and 250 °C present a similar profile over the visible region but the film deposited at 200 °C displays a % transmittance around 72 to 83 %, which is higher than the film deposited from 250 °C (60 to 77 %). The overview of the % transmittance of the films deposited from 2-MePy·Zn($S_2COEt)_2$ presents a decreasing trend with an increasing deposition temperature, which could be possibly due to an increase of crystallinity, grain boundaries and thickness of the deposited films.

Figure 4.19 (c) illustrates transmission spectra of films deposited from Zn(S=C($NMe)_2NCH(Me)_2)_2$. It can be clearly seen that increasing deposition temperatures provide a decrease in % transparency. This may again be rationalized in in a similar manner to the films deposited from 2-MePy·Zn($S_2COEt)_2$. These films displayed a % transmittance over 70 % in the visible region.

A comparison of the transmittance of films deposited from all three precursors at 200 °C is presented in Figure 4.19 (d). The film deposited from Zn(S=C($NMe)_2NCH(Me)_2)_2$ provides a higher % transmittance than those deposited from Zn($S_2COEt)_2$ and 2-MePy·Zn($S_2COEt)_2$, which may again be a consequence of the lower precursor solution concentration utilised during the AACVD process. The films deposited from Zn($S_2COEt)_2$, 2-MePy·Zn($S_2COEt)_2$ consist of numerous particles across their surfaces (Figure 4.7 (b) and Figure 4.8 (c)), whereas the film deposited from Zn(S=C($NMe)_2NCH(Me)_2)_2$ was flat and featureless. The amorphous nature of the films deposited from Zn(S=C($NMe)_2NCH(Me)_2)_2$ may also, therefore, be a source of it higher % transmittance, as the crystalline films deposited from Zn($S_2COEt)_2$ and 2-MePy·Zn($S_2COEt)_2$ comprise numerous and more light scattering grain boundaries.

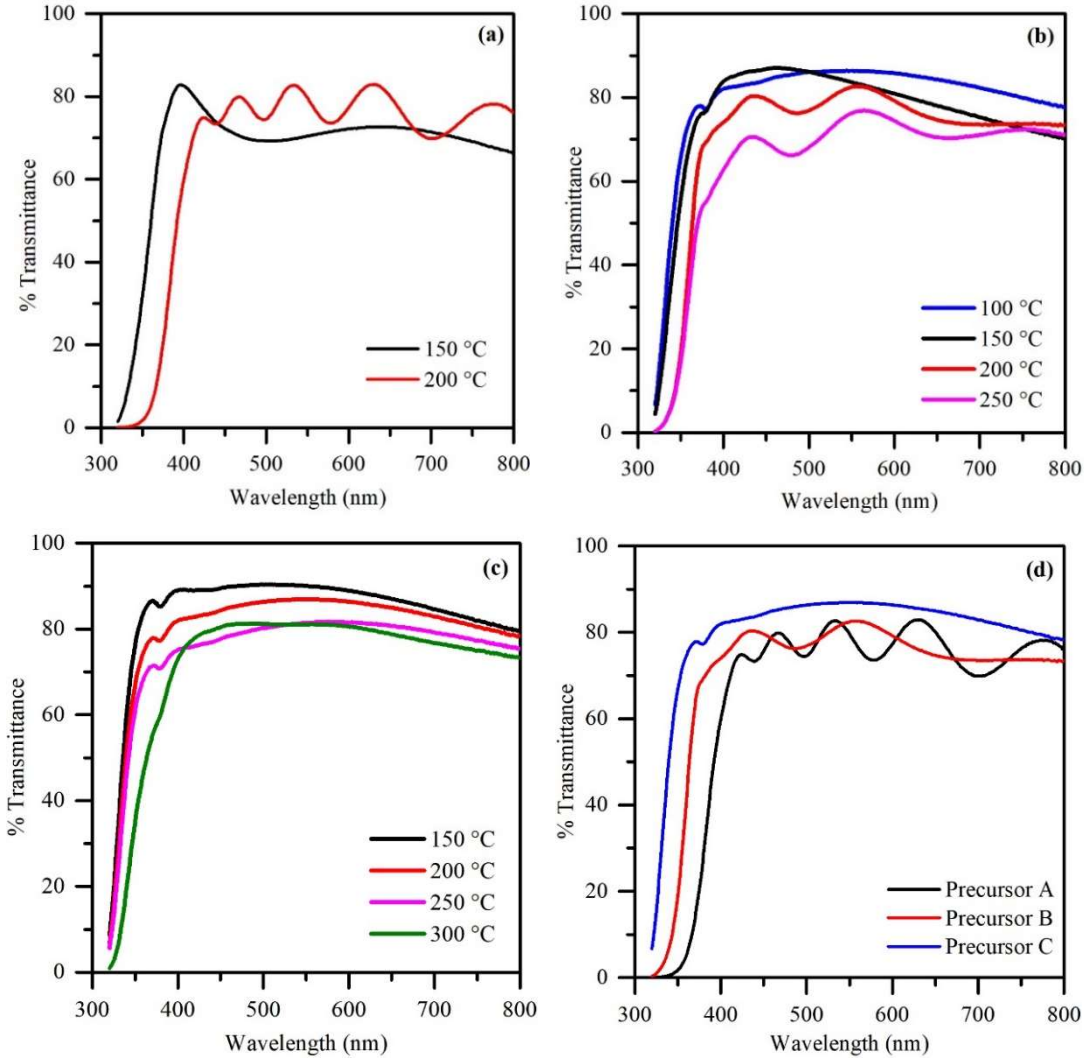

Figure 4.17 Transmission spectra of the films deposited from the precursors (a) $Zn(S_2COEt)_2$, (b) 2-MePy·$Zn(S_2COEt)_2$ and (c) $Zn(S{=}C(NMe)_2NCH(Me)_2)_2$ with various deposition temperatures. (d) is a comparison graph of the films deposited $Zn(S_2COEt)_2$ **(A)**, 2-MePy·$Zn(S_2COEt)_2$ **(B)** and $Zn(S{=}C(NMe)_2NCH(Me)_2)_2$ **(C)** at 200 °C.

Band gap energies

The direct band gap of the deposited films can be calculated via a Tauc plot and the resultants are presented in Figures 4.20 (a)-(c). All the deposited films display approximate band gaps that are similar to values in the literature for ZnS.[10,17,18,22,29,30,62,73]

Figure 4.20 (d) indicates a clear relationship between the observed band gaps and deposition temperature for all three precursors. It can be clearly seen that the band gap

values decrease with increasing deposition temperature. The onset of greater crystallinity, more numerous grain boundaries and film thickness with changing deposition temperature, therefore, apparently affects both the film transmission and absorption behaviour of the deposited films. An overview of the observed band gaps, thickness, crystallite size and roughness values of the all films deposited from all three precursors are presented in Table 4.12.

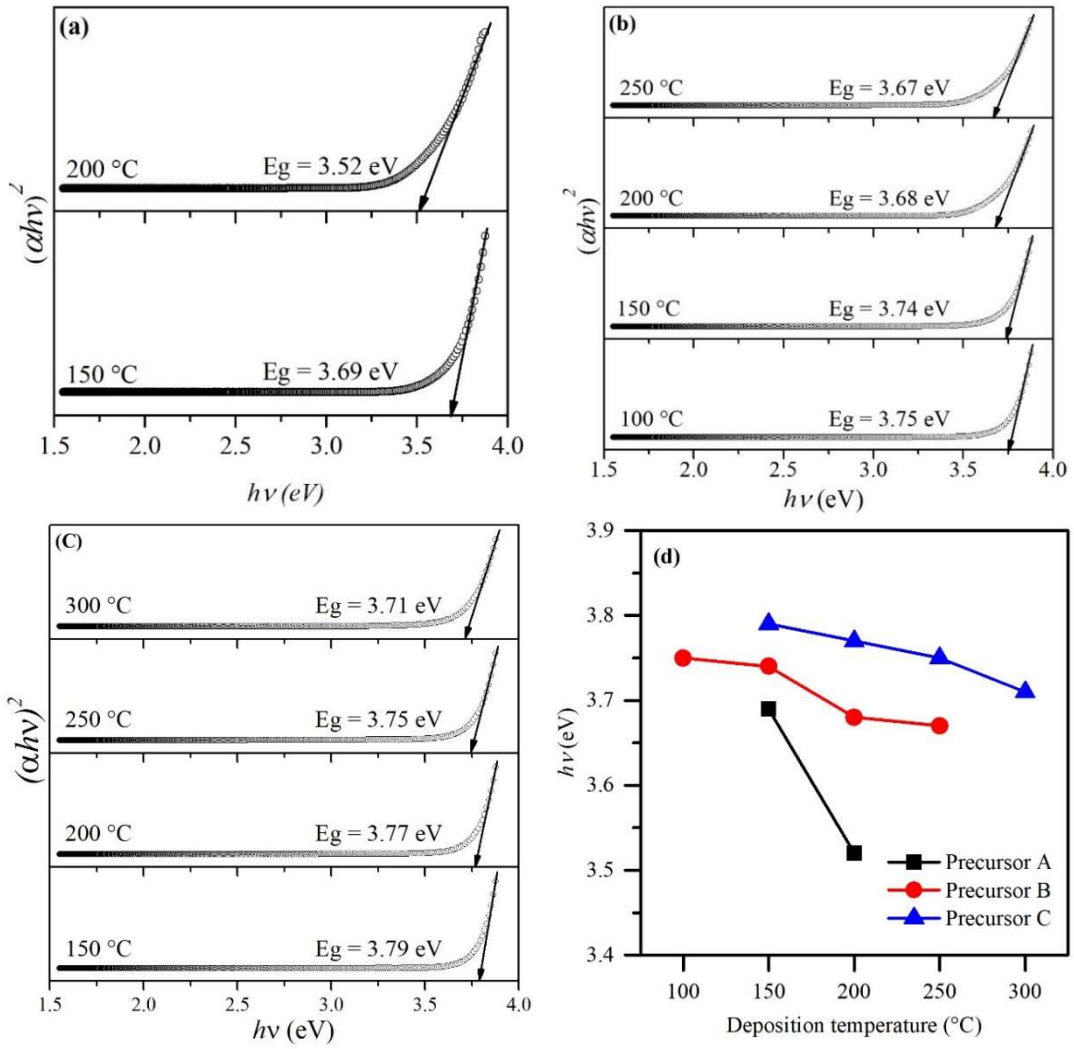

Figure 4.18 Band gaps of the films deposited from (a) $Zn(S_2COEt)_2$ **(A)** (b) 2-MePy·$Zn(S_2COEt)_2$ **(B)** and (c) $Zn(S{=}C(NMe)_2NCH(Me)_2)_2$ **(C)**. (d) is a comparison between the band gap values and the deposition temperatures of the films deposited from all three precursors.

Table 4.13 An overview of the band gap, film thickness, estimated crystallite size and roughness values of the films deposited from Zn(S2COEt)2, 2-MePy·Zn(S2COEt)2 and Zn(S=C(NMe)2NCH(Me)2)2 at various deposition temperatures.

Deposition temperature (°C)	$Zn(S_2COEt)_2$ Crystal structure: Zinc blende				$2\text{-MePy}\cdot Zn(S_2COEt)_2$ Crystal structure: Zinc blende				$Zn(S=C(NMe)_2NCH(Me)_2)_2$ Crystal structure: Wurtzite			
	Band gap (eV)	Average Thickness (nm)	Estimated crystallite size (nm)	Average roughness (nm)	Band gap (eV)	Average Thickness (nm)	Estimated Crystallite size (nm)	Average roughness (nm)	Band gap (eV)	Average Thickness (nm)	Estimated Crystallite size (nm)	Average roughness (nm)
100	-	-	-	-	3.75	33.97 ±2.39	AP	6.14± 0.54	-	-	-	-
150	3.69	91.32 ±9.61	AP	21.15± 10.52	3.74	179.84 ±4.47	5.73	11.03± 5.10	3.79	58.83 ±2.72	AP	2.63 ±0.27
200	3.52	351.48 ±7.15	39	12.41± 1.55	3.68	316.54 ±10.96	25.38	20.05± 3.39	3.77	71.52 ±3.91	AP	6.54 ±2.12
250	-	-	-	-	3.67	554.13 ±16.85	9.81	7.90± 4.25	3.75	349.88 ±6.54	9.39	7.02 ±2.32
300	-	-	-	-	-	-	-	-	3.71	443.96 ±9.98	24.97	14.59 ±2.25

AP = Amorphous phase

4.10 Conclusion

This chapter has described the achievement of ZnS thin film fabrication on Pilkington SiCO glass substrates using the single source of $Zn(S_2COEt)_2$, 2-MePy $Zn(S_2COEt)_2$ and $Zn(S{=}C(NMe)_2NCH(Me)_2)_2$ via AACVD.

Analysis of the deposited films by XRD and Raman spectroscopy revealed that the three single source precursor systems could provide different crystalline phases of ZnS thin films. $Zn(S_2COEt)_2$ and 2-MePy $Zn(S_2COEt)_2$ allowed the deposition of cubic zinc blende ZnS, whereas $Zn(S{=}C(NMe)_2NCH(Me)_2)_2$ provided hexagonal wurtzite ZnS films. EDS investigations revealed that all of the deposited films provided atomic ratios of Zn:S close to 1:1, and were highly transparent at visible wavelengths with bandgaps around 3.52 - 3.79 eV. This is a promising feature for many applications.

2-MePy $Zn(S_2COEt)_2$ allowed the deposition of crystalline ZnS thin films at the lowest deposition temperature of 150 °C. For deposition performed at 200 °C, $Zn(S_2COEt)_2$ provided a higher thin film growth rate than 2-MePy $Zn(S_2COEt)_2$ and $Zn(S{=}C(NMe)_2NCH(Me)_2)_2$ of around 5.28 nm/min. This precursor also provided the largest crystallite size and a very low surface roughness value.

Arrhenius analysis of the film growth rates associated with deposition performed by 2-MePy $Zn(S_2COEt)_2$ and **C** that revealed the apparent activation energies decreased at higher deposition temperatures and resulted in enhanced growth rates. The consequent increase in film thickness, however, appeared to have only limited impact on the atomic composition of Zn and S in the deposited films.

Reference

1 P. Dolcet, C. Maurizio, M. Casarin, L. Pandolfo, S. Gialanella, D. Badocco, P. Pastore, A. Speghini and S. Gross, *Eur. J. Inorg. Chem.*, 2015, **2015**, 706–714.

2 B. Gilbert, B. H. Frazer, H. Zhang, F. Huang, J. F. Banfield, D. Haskel, J. C. Lang, G. Srajer and G. De Stasio, *Phys. Rev. B*, 2002, **66**, 245205-1–6.

3 P. O'Brien and R. Nomura, *J. Mater. Chem.*, 1995, **5**, 1761–1773.

4 F. A. La Porta, J. Andrés, M. S. Li, J. R. Sambrano, J. A. Varela and E. Longo, *Phys. Chem. Chem. Phys.*, 2014, **16**, 20127–20137.

5 D. Moore and Z. L. Wang, *J. Mater. Chem.*, 2006, **16**, 3898–3905.

6 L. Yin and Y. Bando, *Nat. Mater.*, 2005, **4**, 721–722.

7 S. P. Patel, J. C. Pivin, V. V. Siva Kumar, A. Tripathi, D. Kanjilal and L. Kumar, *Vacuum*, 2010, **85**, 307–311.

8 S. Kasap and P. Capper, *Springer Handbook of Electronic and photonic Materials*, Springer Science: New York, 2006.

9 O. K. Echendu, A. R. Weerasinghe, D. G. Diso, F. Fauzi and I. M. Dharmadasa, *J. Electron. Mater.*, 2013, **42**, 692–700.

10 K. Nagamani, P. Prathap, Y. Lingappa, R. W. Miles and K. T. R. Reddy, *Phys. Procedia*, 2012, **25**, 137–142.

11 S. Song and Q. Gao, *J. Appl. Phys.*, 2006, **99**, 106107-1–3.

12 R. Vishwakarma, *J. Theor. Appl. Phys.*, 2015, **9**, 185–192.

13 R. Vishwakarma, *Ukr. J. Phys.*, 2017, **62**, 422–431.

14 G. Wang, B. Huang, Z. Li, Z. Lou, Z. Wang, Y. Dai and M.-H. Whangbo, *Sci. Rep.*, 2015, **5**, 1–7.

15 M. Scocioreanu, M. Baibarac, I. Baltog, I. Pasuk and T. Velula, *J. Solid State Chem.*, 2012, **186**, 217–223.

16 Z.-G. Chen, L. Cheng and J. Zou, *CrystEngComm*, 2011, **13**, 5885–5890.

17 A. Wei, J. Liu, M. Zhuang and Y. Zhao, *Mater. Sci. Semicond. Process.*, 2013, **16**, 1478–1484.

18 Y.-G. Yoon and I.-H. Choi, *J. Korean Phys. Soc.*, 2013, **63**, 1609–1614.

19 H. Ke, S. Duo, T. Liu, Q. Sun, C. Ruan, X. Fei, J. Tan and S. Zhan, *Mater. Sci. Semicond. Process.*, 2014, **18**, 28–35.

20 T. Toyama, T. Hama, D. Adachi, Y. Nakashizu and H. Okamoto, *Nanotechnology*, 2009, **20**, 1–5.

21 Y. He, H. F. Wang and X. P. Yan, *Chem. - A Eur. J.*, 2009, **15**, 5436–5440.

22 R. John and S. Sasi Florence, *Chalcogenide Lett.*, 2010, **7**, 269–273.

23 Z. Deng, L. Tong, M. Flores, S. Lin, J. X. Cheng, H. Yan and Y. Liu, *J. Am. Chem. Soc.*, 2011, **133**, 5389–5396.

24 E. Mohagheghpour, M. Rabiee, F. Moztarzadeh, M. Tahriri, M. Jafarbeglou, D. Bizari and H. Eslami, *Mater. Sci. Eng. C*, 2009, **29**, 1842–1848.

25 C. S. Hwang and I. H. Cho, *Bull. Korean Chem. Soc.*, 2005, **26**, 1776–1782.

26 L. E. Brus, *J. Chem. Phys.*, 1984, **80**, 4403–4409.

27 A. Torabi and V. N. Staroverov, *J. Phys. Chem. Lett.*, 2015, **6**, 2075–2080.

28 M. A. Osman, A. A. Othman, W. A. El-Said, A. G. Abd-Elrahim and A. A. Abu-Sehly, *J. Phys. D. Appl. Phys.*, 2016, **49**, 1–15.

29 J. Liu, A. Wei and Y. Zhao, *J. Alloys Compd.*, 2014, **588**, 228–234.

30 L. Zhou, N. Tang and S. Wu, *Surf. Coatings Technol.*, 2013, **228**, 146–149.

31 M. A. Buckingham, A. L. Catherall, M. S. Hill, A. L. Johnson and J. D. Parish, *Cryst. Growth Des.*, 2017, **17**, 907–912.

32 A. L. Johnson, M. S. Hill, G. Kociok-Köhn, K. C. Molloy and A. L. Sudlow, *Inorg. Chem. Commun.*, 2014, **49**, 8–11.

33 C. S. Lai, Y. X. Lim, T. C. Yap and E. R. T. Tiekink, *CrystEngComm*, 2002, **4**, 596–600.

34 E. R. T. Tiekink, *Crystals*, 2018, **8**, 1–32.

35 M. Akhtar, N. Revaprasadu, M. A. Malik and J. Raftery, *Mater. Sci. Semicond. Process.*, 2015, **30**, 368–375.

36 J. R. Castro, K. C. Molloy, Y. Liu, C. S. Lai, Z. Dong, T. J. White and E. R. T. Tiekink, *J. Mater. Chem.*, 2008, **18**, 5399–5405.

37 B. D. Barreca, A. Gasparotto, C. Maragno, E. Tondello and C. Sada, *Chem. Vap. Depos.*, 2004, **10**, 229–236.

38 D. Barreca, E. Tondello, D. Lydon, T. R. Spalding and M. Fabrizio, *Chem. Vap. Depos.*, 2003, **9**, 93–98.

39 J. M. Clark, G. Kociok-Köhn, N. J. Harnett, M. S. Hill, R. Hill, K. C. Molloy, H. Saponia, D. Stanton and A. Sudlow, *Dalt. Trans.*, 2011, **40**, 6893–6900.

40 K. R. Chaudhari, S. Dey, A. P. Wadawale and V. K. Jain, *J. Organomet. Chem.*, 2016, **813**, 119–124.

41 N. Alam, M. S. Hill, G. Kociok-Köhn, M. Zeller, M. Mazhar and K. C. Molloy, *Chem. Mater.*, 2008, **20**, 6157–6162.

42 T. Ito, *Acta Crystallogr. Sect. E Struct. Reports Online*, 2002, **58**, m517–m518.

43 J. R. Thompson, University of Bath, 2016.

44 C. Voss, Y.-J. Chang, S. Subramanian, S. O. Ryu, T.-J. Lee and C.-H. Chang, *J. Electrochem. Soc.*, 2004, **151**, C655–C660.

45 I. J. Gonzalez-Panzo, P. E. Martin-Varguez and A. I. Oliva, *J. Electrochem. Soc.*, 2014, **161**, D761–D767.

46 K. Patel, V. Kheraj, D. V Shah, C. J. Panchal and N. G. Dhere, *J. Alloys Compd.*, 2016, **663**, 842–847.

47 L. P. Mgabi, B. S. Dladla, M. A. Malik, S. S. Garje, J. Akhtar and N. Revaprasadu, *Thin Solid Films*, 2014, **564**, 51–57.

48 P. K. Nair, M. T. S. Nair, O. Gomezdaza and R. A. Zingaro, *J. Electrochem. Soc*, 1993, **140**, 1085–1089.

49 I. Y. Ahmet, M. S. Hill, A. L. Johnson and L. M. Peter, *Chem. Mater.*, 2015, **27**, 7680–7688.

50 M. J. Moloto, N. Revaprasadu, P. O'Brien and M. A. Malik, *J. Mater. Sci. Mater. Electron.*, 2004, **15**, 313–316.

51 T. Mandal, V. Stavila, I. Rusakova, S. Ghosh and K. H. Whitmire, *Chem. Mater.*, 2009, **21**, 5617–5626.

52 M. B. Harkness, E. Alvarado, A. C. Badaj, B. C. Skrela, L. Fan and G. G. Lavoie, *Organometallics*, 2013, **32**, 3309–3321.

53 K. Ramasamy, M. A. Malik, P. O'Brien and J. Raftery, *Dalt. Trans.*, 2010, **39**, 1460–1463.

54 A. Krol, A. Hoffmann and J. Gutowski, *Phys. Rev. B*, 1988, **38**, 946–948.

55 W. G. Nilsen, *Phys. Rev.*, 1969, **182**, 838–850.

56 Y. C. Cheng, C. Q. Jin, F. Gao, X. L. Wu, W. Zhong, S. H. Li and P. K. Chu, *J. Appl. Phys.*, 2009, **106**, 123505-1–5.

57 J. Serrano, A. Cantarero, M. Cardona, N. Garro, R. Lauck, R. E. Tallman, T. M. Ritter and B. A. Weinstein, *Phys. Rev. B - Condens. Matter Mater. Phys.*, 2004, **69**, 014301-1–11.

58 M. Scocioreanu, M. Baibarac, I. Baltog, I. Pasuk and T. Velula, *J. Solid State Chem.*, 2012, **186**, 217–223.

59 O. Brafman and S. S. Mitra, *Phys. Rev.*, 1968, **171**, 931–934.

60 J. Schneider and R. D. Kirby, *Phys. Rev. B*, 1972, **6**, 1290–1294.

61 Q. Xiong, J. Wang, O. Reese, L. C. L. Y. Voon and P. C. Eklund, *Nano Lett.*, 2004, **4**, 1991–1996.

62 J. H. Kim, H. Rho, J. Kim, Y. J. Choi and J. G. Park, *J. Raman Spectrosc.*, 2012, **43**, 906–910.

63 M. Lin, T. Sudhiranjan, C. Boothroyd and K. P. Loh, *Chem. Phys. Lett.*, 2004, **400**, 175–178.

64 X. Hao, Y. Wang, J. Zhou, Z. Cui, Y. Wang and Z. Zou, *Appl. Catal. B*

Environ., 2018, **221**, 302–311.

65 Y. Ebisuzaki and M. Nicol, *J. Phys. Chem. Solids*, 1971, **33**, 763–766.

66 M. Ling and C. Blackman, *Phys. Status Solidi Curr. Top. Solid State Phys.*, 2015, **12**, 869–877.

67 I. Y. Kim, J. Y. Lee, U. V. Ghorpade, M. P. Suryawanshi, D. S. Lee and J. H. Kim, *J. Alloys Compd.*, 2016, **688**, 12–17.

68 J. Chantana, K. Suzuki and T. Minemoto, *Sol. Energy Mater. Sol. Cells*, 2017, **168**, 207–213.

69 Y. M. Ko, R. B. V. Chalapathy, L. Larina and B. T. Ahn, *CrystEngComm*, 2017, **19**, 5764–5773.

70 M. Banerjee, N. B. Srinivasan, H. Zhu, S. J. Kim, K. Xu, M. Winter, H. W. Becker, D. Rogalla, T. De Los Arcos, D. Bekermann, D. Barreca, R. A. Fischer and A. Devi, *Cryst. Growth Des.*, 2012, **12**, 5079–5089.

71 W. Daranfed, M. S. Aida, N. Attaf, J. Bougdira and H. Rinnert, *J. Alloys Compd.*, 2012, **542**, 22–27.

72 S. Biira, P. L. Crouse, H. Bissett, T. T. Hlatshwayo, J. H. van Laar and J. B. Malherbe, *J. South. African Inst. Min. Metall.*, 2017, **117**, 931–938.

73 Z. Q. Li, J. H. Shi, Q. Q. Liu, Z. A. Wang, Z. Sun and S. M. Huang, *Appl. Surf. Sci.*, 2010, **257**, 122–126.

Chapter 5:

Experimental

5.1 General experimental procedure

5.1.1 Chemicals and solvents

All starting chemicals and solvents were purchased from Sigma-Aldrich, Fisher Scientific and Alfa Aesar or Acros.

5.1.2 Substrate preparation

The following substrates were used in the experiments:

- SiCO coated float and FTO glasses were supplied by NSG Group, UK,
- Silicon (100) wafers were supplied by PI-KEM Limited, UK
- Microscope slide glass supplied by VWR, UK

The substrates were cleaned by using detergent, deionized water, acetone and isopropanol, respectively, in an ultrasonic bath, prior to being dried under N_2 with a fast flow rate. The substrates were further cleaned with an oxygen plasma under a low pressure (0.1 bar) for 20 minutes immediately before use

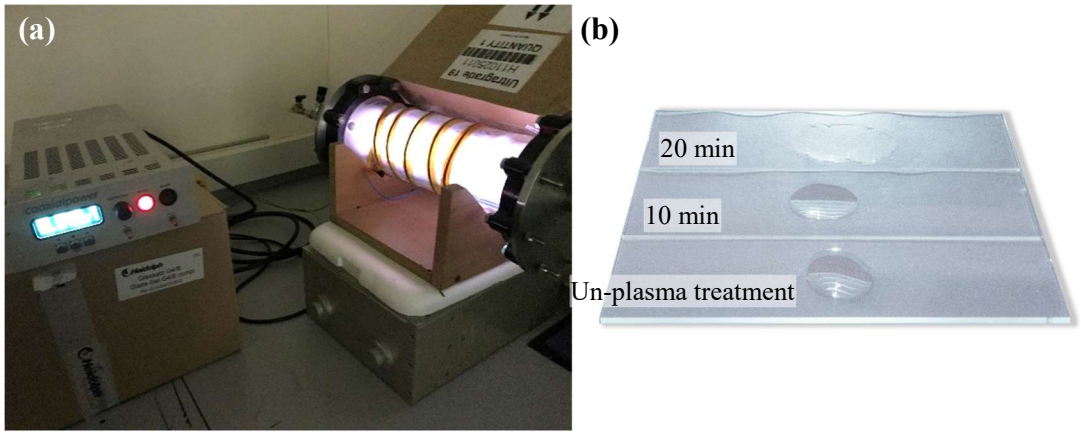

Figure 5.1 (a) Oxygen plasma cleaning equipment (b) sample substrates before and after oxygen plasma treatment with 10 and 20 min.

5.1.3 Aerosol Assisted Chemical Vapour Deposition (AACVD) procedure

The stainless steel bubbler and sealed nut were used as a precursor container for the thin film deposition was attached to the AACVD apparatus comprising a TSI generator 3076 constant output atomizer. The substrates were put into the deposition chamber under a nitrogen gas flow for 20 min to remove any air (O_2, CO_2 and or N_2) from the system. The nitrogen gas pressure was set at 20 psi. The hot wall or cold wall furnace was switched on to reach the desired deposition temperature and allowed to equilibrate for 20 min. To start the deposition, the bypass valve was closed and the inlet valve connected to the TSI generator was opened to produce the precursor aerosol. This was then transported to the reaction chamber for the required deposition time. The inlet and outlet valves of the bubbler were then shut and the bypass valve to the nitrogen carrier gas was opened when the furnace was turned off. The samples were left to cool down to a room temperature before removal from the chamber.

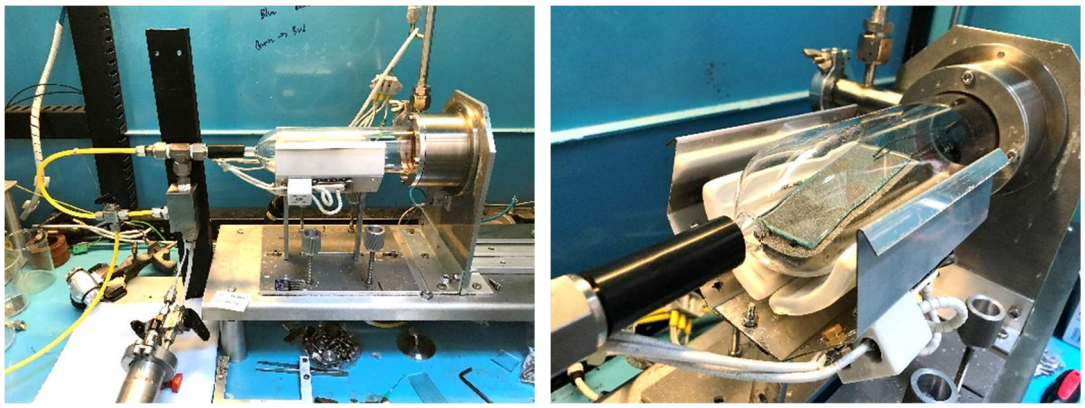

Figure 5.2 AACVD with the cold wall furnace reactor.

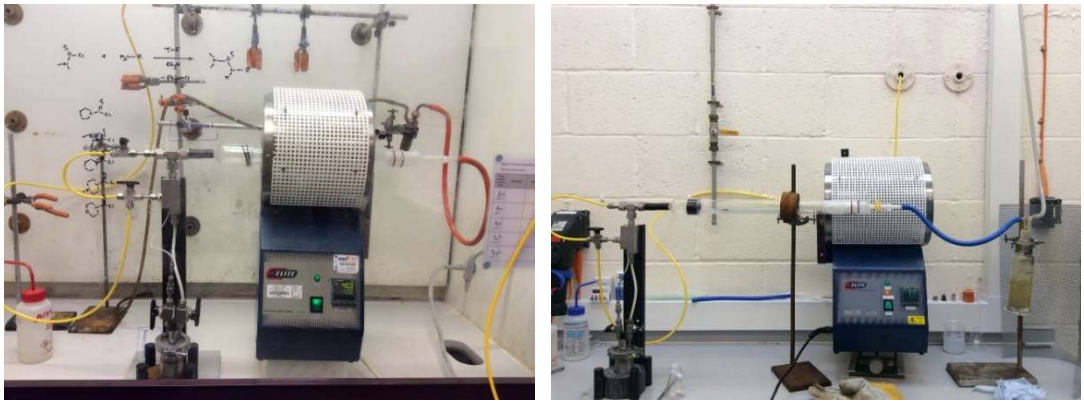

Figure 5.3 AACVD with the hot wall furnace reactor.

5.1.4 Spin coating procedure

A spin coater, model WS-650HZB-23NPP/UD3 from the Laurell technologies corporation, was used to form the deposited film. The spin coater was set up with a speed of 1500 rpm for 30 seconds. Sample substrates were mounted on the sample holder and the precursor was dropped to cover the substrate surface using a pipette. The spin coated substrate was transferred to a hot plate, which was heated at 120 °C to evaporate an organic solvent for 15 min in a fume hood. The samples were then left to cool down to a room temperature and the spin coat cycle was repeated 5 or 15 times to increase a film thickness.

5.1.5 Thermogravimetric Analysis (TGA)

Thermogravimetric data were recorded using a Perkin Elmer TGA 4000^{TM} quartz microbalance instrument. The RYRIS Version 10.1 instrument managing and analysis software was used to analyze the resultant data. Samples were prepared in crucible ceramic pans or sealed aluminium pans for an air sensitive sample. TGAs were performed under a continuous furnace purge of nitrogen gas with a flowrate of 20 mL min^{-1}. The furnace was heated from 30 °C to the target temperature with a ramp rate of 5 °C min^{-1}. Mass measurements were recorded every second and converted to a percentage measurement by reference to the initial mass of the samples.

5.1.6 Powder X-ray Diffractometry (PXRD)

PXRD data of all deposited films were collected using a Bruker D8 Advance (Cu-Kα radiation, λ = 1.5418 Å). PXRD was used to identify the crystalline and amorphous phases of the deposited films and information on the crystallite size was estimated by using the Scherrer Equation. The collected data were analyzed and processed by the X'pert high score software to determine the crystalline and structure phases by searching the internal reference database.

5.1.7 Atomic Force Microscopy (AFM)

AFM analysis was performed on the deposited films by using Nanosurf® easyScan 2 FlexAFM system instrument with Budget Sensors Contact-G tips. Nanosurf C3000 and Gwyddion software were used to process and analyse the roughness, 2D and 3D AFM images of the deposited films.

5.1.8 UV-Visible Spectroscopy

UV-Vis transmittance spectra were collected using the PerkinElmer® LAMBDA 750/650 UV/Vis and UV/Vis/near-IR spectrophotometer. Measurements were recorded with a wavelength 2500 to 320 nm.

5.1.9 Raman Spectroscopy Analysis

Raman spectra were collected using a Renishaw in Via Raman microscope with a 532 nm laser and the collected data were processed and analysed via Renishaw WiRE and originPro 2015 software.

5.1.10 Scanning Electron Microscopy (SEM)

SEM was performed on the deposited films by using a Field Emission Scanning Electron Microscope 6301F (FE-SEM). The samples were mounted onto an aluminium SEM sample holder with a conductive carbon tape attached on the top and bottom of the sample surface to increase the conductivity and to prevent charging by electron accumulation. Before measurement, the samples were stored in a vacuum chamber to desiccate for 24 hours at 35 °C. The sample surfaces were coated with a

sputtered chromium film of 5 nm to provide a conductive surface. SEM images of the deposited films were captured with various magnifications and analysed by using the Image J software.

5.1.11 Energy-dispersive X-ray spectroscopy (EDS)

EDS spectra were recorded using a JEOL 6480 LV SEM with High sensitivity Oxford INCA X-Act SDD X-ray detector and NICA Wave software was used to process the spectrum data. The samples were mounted onto the aluminium stubs and stored in a vacuum chamber for 24 hours at 35 °C before measurement.

5.1.12 Single Crystal X-ray diffraction analysis

Single crystal X-ray crystallography of the crystal complex in chapter 3 was performed on a New Xcalibur, EosS2 diffractometer at 150 K. Using Olex2, the structure was solved with the olex2. Solve structure solution program using Charge Flipping and refined with the ShelXL and refinement package using Least Squares minimisation.

5.2 Experimental for Chapter 2

5.2.1 Copper thin film deposition

Spin coating of $Cu(NO_3)_2{\cdot}3H_2O$

$Cu(NO_3)_2{\cdot}3H_2O$ (1.21 g) was dissolved in 100 ml ethanol, methanol or distilled water to form 0.05 M of the precursor solution, which was stirred until the solution had turned clear blue for 1 hour. The cleaned Pilkington SiCO glass substrates with a dimension 2.5 × 2.5 cm^2 were mounted onto the substrate holder in the spin coater. The precursor solution was dropped onto the substrate surface by using a pipette and the spin coater was turned on with a spinning speed of 1500 rpm for 30 seconds. The substrate was then transferred to a hot plate and dried at 120 °C for 15 min. The deposition cycle by the spin coater was repeated 5 times. Finally, the dried films were annealed in air or argon at temperatures between 300 - 600 °C for 1 hour.

AACVD of $Cu(NO_3)_2 \cdot 3H_2O$

Metallic copper films

The precursor was prepared by dissolving $Cu(NO_3)_2 \cdot 3H_2O$ (1.21 g) in 100 ml ethanol, methanol or distilled water to form a 0.05 M solution, which was stirred for 1 hour until the solution had turned clear blue. The precursor solution was transferred to a stainless steel bubbler and sealed shut. The stainless steel bubbler was connected to the TSI generator 3076 constant output atomizer and the procedure described in 5.1.3 was followed utilizing the hot-wall furnace. The deposition temperature was varied between 300 and 600 °C and the deposition time was 1 hour to produce the metallic copper films. Cleaned Pilkington SiCO glass (2.5×15 cm^2) was used as substrate throughout this thin film deposition process.

Copper oxide films

The metallic copper films from the deposition temperature at 300 °C using methanol as a solvent were annealed under an air atmosphere for 1 hour with the temperature range 100 - 600 °C resulting in the transformation of the shiny metallic copper films to the brownish-red or black oxide.

5.2.2 Nickel oxide thin film deposition

Spin coating of $Ni(NO_3)_2 \cdot 6H_2O$

$Ni(NO_3)_2 \cdot 6H_2O$ (1.45 g) was dissolved in 100 ml of ethanol, methanol or distilled water to form a 0.05 M solution of the precursor. The green solution was stirred for 1 hour until it was clear before being used in the spin coating deposition process. Pilkington SiCO glass, cleaned by following the substrate preparation in the described in 5.1.2, with a dimension 2.5 × 2.5 cm^2 were used as substrates. The substrates were mounted on the sample holder in the spin coater and the precursor was dropped onto the substrate surface by using a pipette. Then the spin coater was turned on with a speed at 1500 rpm for 30 seconds. The grey deposited films were annealed under air or an argon atmosphere in the temperature range 300 - 600 °C for 1 hour causing the grey films to become transparent.

AACVD of $Ni(NO_3)_2 \cdot 6H_2O$

$Ni(NO_3)_2 \cdot 6H_2O$ (1.45 g) was dissolved in 100 ml of ethanol, methanol or distilled water to form a 0.05 M of the precursor solution. The precursor was transferred to the stainless steel bubbler, which was sealed shut and attached to the TSI generator 3076 constant output atomizer. The hot wall deposition process followed the AACVD procedure in 5.1.3. Cleaned Pilkington SiCO glasses 2.5×15 cm^2 were used as the substrates. Deposition temperatures in the range 300 - 600 °C were employed for a deposition time of 1 hour. Cooling to room temperature provided shiny metallic nickel films.

Deposition of nickel oxide film and combustion processing technique

Precursors in this section were prepared with the recipes in Table 5.1, which were stirred for 1 hour until a clear green solution was obtained. The precursor was transferred to the stainless steel bubbler, which was attached to the TSI generator 3076 constant output atomizer for the deposition process following the AACVD procedure described in 5.1.3. The cold-wall reactor was used throughout these experiments at deposition temperatures between 225 and 400 °C and for 1 hour. Finally, the substrates were allowed to cool to a room temperature providing the transparent deposited films..

Table 5.1 Precursor recipes for the deposition of nickel oxide film and combustion processing technique.

Precursor code name	The recipe in 100 ml of the precursor solution			
	$Ni(NO_3)_2 \cdot 6H_2O$	Urea	Ammonium nitrate	Solvent
N1	0.1 M (2.91 g)	-	-	Ethanol
N2	0.1 M (2.91 g)	0.1 M (0.60 g)	-	Ethanol
N3	0.1 M (2.91 g)	-	0.1 M (0.80 g)	Ethanol

Deposition of the N3 precursor

The N3 precursor in Table 5.1 was used to deposit and investigate for the deposition of nickel oxide thin films on the cleaned FTO substrates. The deposition process followed the AACVD procedure described in 5.1.3 at deposition temperatures

between 275 and 400 °C and for 1 hour. After the deposition step, the FTO substrates (2.5×15 cm^2) were left to cool down to room temperature before removal from the chamber.

5.2.3 Lanthanum oxide thin film deposition

Spin coating of $La(NO_3)_2{\cdot}6H_2O$

$La(NO_3)_2{\cdot}6H_2O$ (1.08 g) and CH_4N_2O (0.15 g) were dissolved in 100 ml of ethanol or distilled water to form 0.05 M of the precursor solution, which was stirred for 1 hour before use in the deposition process. Cleaned Pilkington SiCO glass substrates with the dimension 2.5 × 2.5 cm^2 were mounted onto the sample holder in the spin coater and the precursor was dropped onto the substrate surface. The spin coater was turned on with a speed of 1500 rpm for 30 seconds. The substrate was transferred to a heated hot plate at a temperature of 120 °C and was left to evaporate the organic solvent for 15 min before cooling down to a room temperature. The cycle of the spin-coated process was repeated 5 times to increase the thickness of the deposited film. The white film was annealed under an air or argon atmosphere with a temperature between 300 °C and 600 °C for 1 hour.

AACVD of $La(NO_3)_2{\cdot}6H_2O$

A 0.05 – 0.5 M precursor solution was prepared by dissolving $La(NO_3)_2{\cdot}6H_2O$ (2.17 - 21.65 g) in ethanol or distilled water 100 ml, which was stirred for 1 hour. The precursor was transferred to a stainless steel bubbler, which was sealed shut and attached to the TSI generator 3076 constant output atomizer. The hot-wall furnace was used as a reactor and cleaned Pilkington SiCO glass and microscope slide glass were used as the substrates in thee experiments. The AACVD deposition followed the procedure in 5.1.3 with deposition temperatures over the range 300-600 °C and for 1 hour. After the deposition step, the samples were left to cool down to room temperature before removal from the reactor.

5.2.4 Praseodymium oxide thin film deposition

Spin coating of $Pr(NO_3)_3 \cdot 6H_2O$

$Pr(NO_3)_3 \cdot 6H_2O$ (1.09 g) and CH_4N_2O (0.15 g) were dissolved in 100 ml of ethanol or water to form a 0.05 M solution of the precursor system, which was stirred for 1 hour. 2.5×2.5 cm^2 cleaned Pilkington SiCO glass substrates were mounted onto the sample holder in the spin coater and the precursor solution was dropped onto the substrate surface. The spin coater was turned on with a speed 1500 rpm for 30 seconds before the substrate was transferred to a hot plate at a temperature of 120 °C. The sample was left to evaporate the organic solvent for 15 min and the spin coating process cycle was repeated 5 times to increase a film thickness. Finally, the white films were annealed under air or argon atmosphere in temperature range 300 °C to 600 °C for 1 hour before being left to cool down to room temperature.

AACVD of $Pr(NO_3)_3 \cdot 6H_2O$

$Pr(NO_3)_3 \cdot 6H_2O$ (21.75 g) was dissolved in a 100 ml of methanol to form a 0.5 M precursor solution. The precursor solution was transferred into a stainless steel bubbler and it was connected to the TSI generator 3076 constant output atomizer. A hot-wall furnace was used as a reactor and cleaned microscope glass slides were used as substrates in these experiments. The AACVD deposition followed the procedure in 5.1.3 between temperatures of 330 and 600 °C. The deposition time was 1 hour. The amorphous films deposited at 330 - 600 °C annealed under a nitrogen atmosphere in the deposition chamber for 1 hour at 600 °C to induce a phase transformation from an amorphous phase to a crystalline phase.

5.3 Experimental for Chapter 3

5.3.1 Lanthanum nickel oxide thin film deposition by using AACVD and hot-wall reactor.

The precursor solutions used in this section followed the recipes listed in Table 5.2 with a volume of 100 ml. The stainless steel bubbler was filled with the precursor

solution and attached to the TSI generator 3076 constant output atomizer. The deposition procedure followed the AACVD protocol described in 5.1.3 under the deposition conditions shown in Table 5.2. The hot wall reactor was used for the deposition in this section.

5.3.2 Lanthanum nickel oxide thin film deposition by using AACVD and cold-wall reactor.

The LNR11 precursor solution system (Table 5.2) was used to deposit the films on FTO glass substrates (2.5×15 cm^2). Ethanol was used as a solvent and the cold-wall furnace was used as a reactor in this section. The deposition temperature was varied between 250 and 500 °C for a deposition time of 1 hour utilizing the AACVD procedure described in 5.1.3.

Table 5.2 Summary of conditions for AACVD experiments to deposit lanthanum nickel oxide films via a hot wall reactor.

Precursor system	Ratio			Precursor concentration (M)	Solvent	Substrate	Deposition condition		Annealing in air	
	$La(NO_3)_3 \cdot 6H_2O$	$Ni(NO_3)_2 \cdot 6H_2O$	NH_4NO_3				Temp. (°C)	Time (min)	Temp. (°C)	Time (min)
LNR11	1	1	-	0.1-0.5	• Ethanol • Methanol • Water	• Pilkington SiCO glass :2.5×15 cm^2 • FTO: 2.5×15 cm^2 • Si wafer: 2.5×2.5 cm^2	150-600	20-60	300-600	60
LNR12	1	2	-							
LNR13	1	3	-							
LNR14	1	4	-							
LNR15	1	5	-							
LNR21	2	1	-							
LNR31	3	1	-							
LNR41	4	1	-							
LN R51	5	1	-							
LNAR111	1	1	1	0.2						
LNAR112	1	1	2							
LNAR115	1	1	5							
LNAR1110	1	1	10							

5.3.3 Lanthanum nickel oxide thin film deposition by using spin coating.

Table 5.3 Precursor recipes for the deposition in this section.

Precursor system	Ratio		CH_3COOH (vol %)	Precursor concentration (M)	Solvent
	$La(NO_3)_3 \cdot 6H_2O$	$Ni(NO_3)_2 \cdot 6H_2O$			
LNR11	1 (4.33 g)	1 (2.91 g)	-	0.2	Ethanol
LNR11-AA5	1(4.33 g)	1 92.91 g)	5	0.2	Ethanol

The 100 ml of the precursor were prepared from the recipes in Table 5.3. Pilkington SiCO glass with a dimension 2.5×2.5 cm^2 was used as a substrate. The substrate was mounted onto the sample holder in a spin coater and the precursor solution was dropped onto the substrate surface. The spin coater was turned on with a speed of 1500 rpm for 30 seconds before the substrate dried on a hot plate at 150 °C for 15 min. The spin coating deposition cycle was repeated 15 times to increase the film thickness. The grey as-deposited films were annealed in air with the temperature between 300 and 600 °C for 1 hour before being allowed to cool room temperature.

5.3.4 Lanthanum nickel oxide thin film deposition with various vol. % of an acetic acid by a spin coating technique.

Table 5.4 Precursor recipes for the deposition in this section.

Precursor system	Ratio		CH_3COOH (vol %)	Precursor concentration (M)	Solvent
	$La(NO_3)_3 \cdot 6H_2O$	$Ni(NO_3)_2 \cdot 6H_2O$			
LNR11	1 (4.33 g)	1 (2.91 g)	0	0.2	Ethanol
LNR11-AA5	1	1	5	0.2	Ethanol
LNR11-AA10	1	1	10	0.2	Ethanol
LNR11-AA15	1	1	15	0.2	Ethanol
LNR11-AA20	1	1	20	0.2	Ethanol
LNR11-AA30	1	1	30	0.2	Ethanol

Precursor solutions were prepared from the recipes in Table 5.4. The Pilkington SiCO glass (2.5×2.5 cm^2) used as a substrate this section was mounted onto a sample holder in a spin coater. The precursor solution was dropped by using a pipette onto the substrate surface before the spin coater was turned on at 1500 rpm for 30 seconds. The substrate was transferred to a hot plate at 150 °C to evaporate the organic solvent for 15 min. The spin coating deposition cycle was then repeated 5 times to increase the thickness of the deposited film before the transparent light-brown or grey films were annealed under an air atmosphere for 1 hour and at a temperature of 600 °C to provide transparent light-brown or light-black films.

5.3.5 Single crystal from lanthanum nitrate and nickel nitrate in an acetic acid solution

$La(NO_3)_3{\cdot}6H_2O$ (4.33 g) and $Ni(NO_3)_2{\cdot}6H_2O$ (2.91 g) were dissolved in 100 ml acetic acid to form 0.2 M of the precursor solution, which was stirred until the solution had turned clear green for 1 hour. Then the solution was allowed to slowly and completely evaporate at room temperature and after that, the light-green crystal was generated.

5.4 Experimental for Chapter 4

Zn(S_2COEt)2, 2-MePy Zn($S_2COEt)_2$ and Zn($SC(NMe)_2NCH(Me)_2)_2$ were used as the precursors for ZnS thin film fabrication in this chapter. Zn(S_2COEt)2, 2-MePy Zn($S_2COEt)_2$ and Zn($SC(NMe)_2NCH(Me)_2)_2$ were synthesized by Nicolò Maria Magnini, Dr Andrew Johnson and James Parish, respectively.

Precursor solutions were prepared as described in Table 5.5. As all precursors are oxygen sensitive, the precursor solution was prepared and transferred to a stainless steel bubbler then sealed shut in a glove box to eliminate oxygen. The bubbler was attached to the TSI generator 3076 constant output atomizer and the AACVD procedure followed as described in 5.1.3 and under the deposition conditions shown in Table 5.5. The coated substrates from each precursor were left to cool to room temperature before removal from the reactor.

To avoid the light induced precursor decomposition during the deposition process, aluminium foil was wrapped around the reactor and deposition chamber as shown in Figure 5.5.

Table 5.5 Summary of the deposition conditions for ZnS thin film fabrication via AACVD.

Precursor	Conc. (M)	Solvent	Volume (ml)	Substrate	Deposition temperature (°C)	Deposition time (min)	Reactor type
[A] $Zn(S_2COEt)_2$	0.30 (9.23g)	Toluene	100	Pilkington SiCO glass	150, 200	60	Cold-wall
[B] 2-MePy $Zn(S_2COEt)_2$	0.30 (12.03 g)	Toluene	100	Pilkington SiCO glass	100, 150, 200, 250	60	Cold-wall
[C] $Zn(SC(NMe)_2NCH(Me)_2)_2$	0.15 (5.34 g)	Toluene	100	Pilkington SiCO glass	150, 200, 250, 300	60	Cold-wall

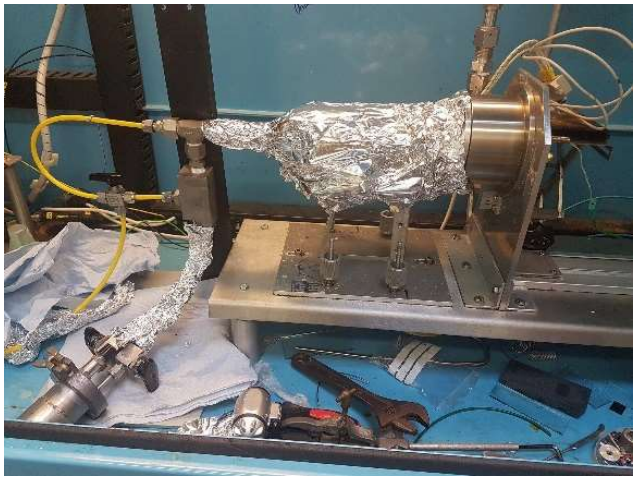

Figure 5.4 Aluminum foil was used to wrap the reactor during the deposition process to prevent light-induced decomposition.

Chapter 6:

Future work

6.1 Aerosol Assisted Chemical Vapour Deposition (AACVD)

The AACVD results presented in this thesis highlight that it is a fascinating technique for thin film fabrication. The AACVD experiments, however, also highlight that thin film production is affected by many parameters. There remain, therefore, numerous features that need further experiments to study and to understand AACVD.

Example factors or parameters:

- Deposition temperature and time
- Deposition position in the chamber which suitable to provide a desired deposited film.
- Gas pressure and atmosphere
- The position of the heating plate or furnace which provide a proper temperature in the deposition chamber
- Type of substrate
- The direction of the droplet precursor flows
- Precursor droplet size
- The character of precursor flow such as a laminar flow, the turbulent of the droplet precursor flow
- The concentration of the precursor solution
- The fresh or aged precursor or more than 24 hours
- The cooling temperature rate in the deposition chamber and on the sample substrate
- The angle of graphite supporters
- Etc.

Here below are some examples of the factors or parameters that can affect the deposited films and can be varied to improve the quality of deposition of the desired thin film material.

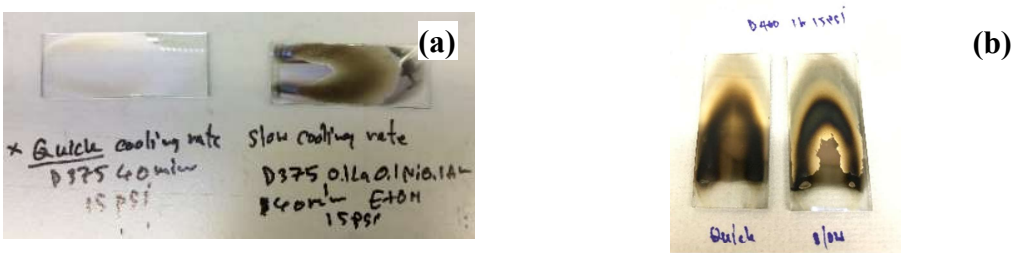

Figure 6.1 These samples are prepared with the different cooling rate. Those on the left in (a) and (b) were prepared with a rapid cooling rate and those on the right in (a) and (b) were prepared from a slow cooling rate.

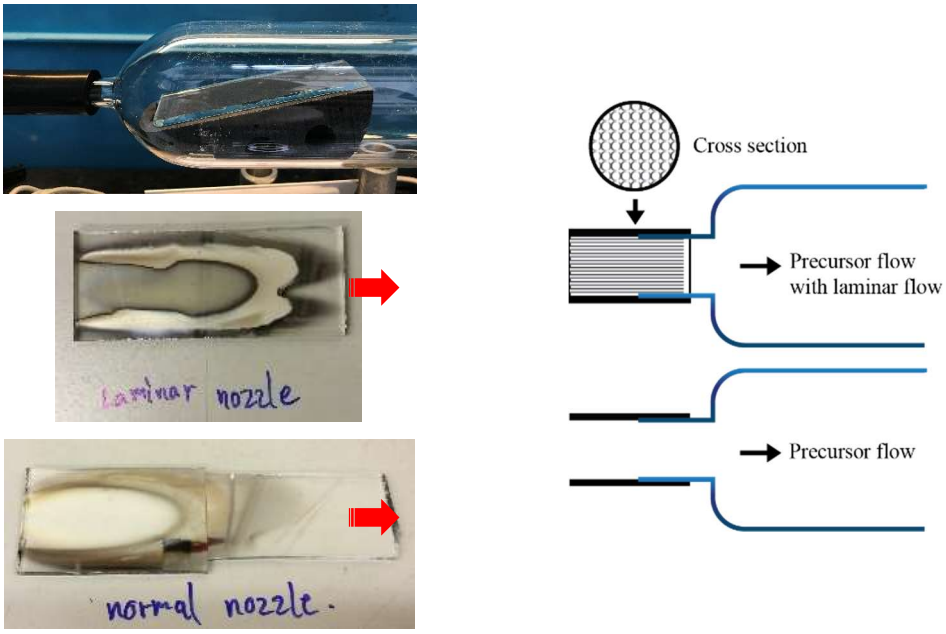

Figure 6.2 Deposited films were prepared with the different type of nozzle.

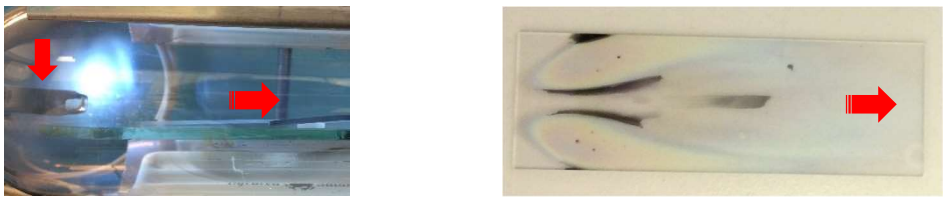

Figure 6.3 Left is an insertion nozzle and right is sample resultant.

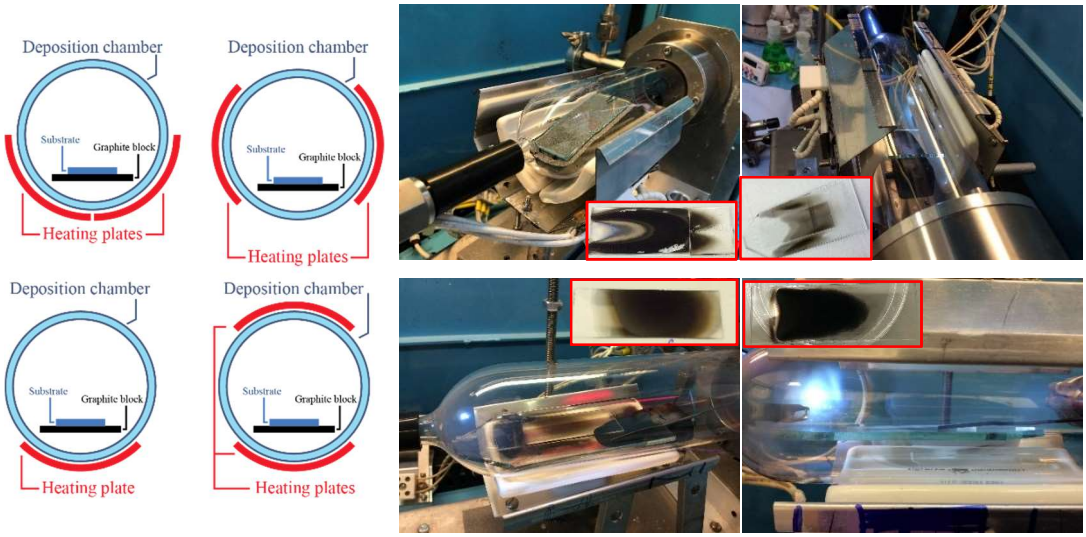

Figure 6.4 Different position of the heating plate for the cold wall reactor.

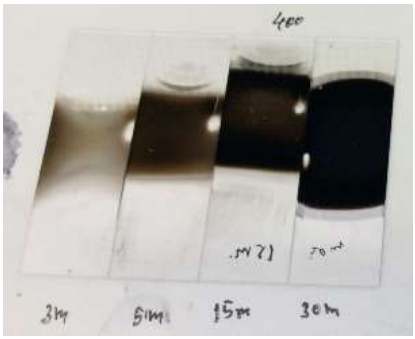

Figure 6.5 The deposition at 400 °C with the different deposition time. Left to right is 3, 5, 15 and 30 min.

Figure 6.6 The graphite supporter for the substrates.

Although omitted from this thesis, copper-nickel metal alloy thin films have also been demonstrated and investigated by using simple metal nitrates via AACVD at 600 °C (Figures 6.1 and 6.2). Also of interest, therefore, is the further potential of the AACVD technique to be applied to the fabrication of metal alloy films from simple binary metal nitrate solutions.

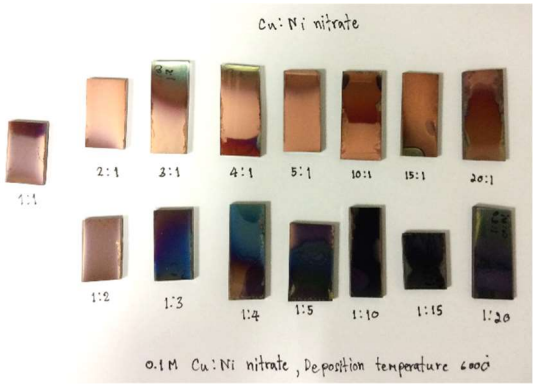

Figure 6.7 Appearance of deposited film from copper nitrate and nickel nitrate with various ratios via AACVD technique.

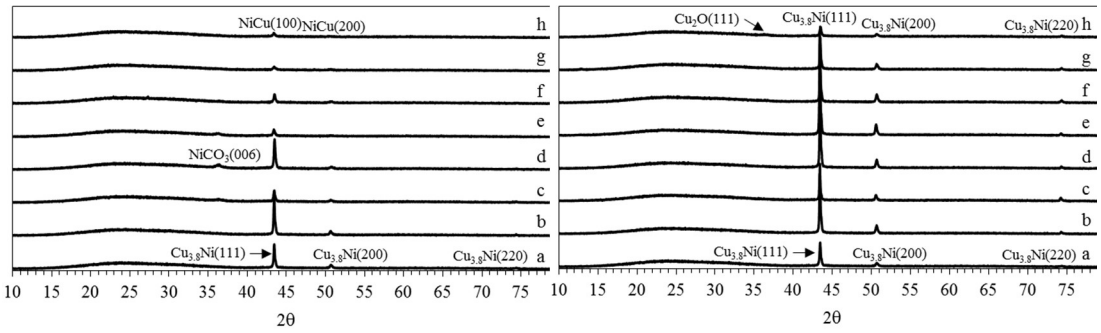

copper nitrate and nickel nitrate ratio (a) 1:1, (b) 1:2, (c) 1:3, (d) 1:4, (e) 1:5, (f) 1:10, (g) 1:15 and (h) 1:20.

copper nitrate and nickel nitrate ratio (a) 1:1, (b) 2:1, (c) 3:1, (d) 4:1, (e) 5:1, (f) 10:1, (g) 15:1 and (h) 20:1.

Figure 6.8 XRD patterns of copper-nickel alloy thin film grown from simple metal nitrate precursor via the AACVD technique.

6.2 Chapter 2: Deposition of Binary oxide thin films

The results described in Chapter 2 indicated that simple metal-nitrate based precursor solutions can enable the deposition of the binary oxide thin films via spin-coating or AACVD. The further study of other metal oxide thin film materials, such as MnO, ZnO, TiO or MgO, that are otherwise quite challenging to prepare may also be achievable from this simple metal nitrate based protocol.

The achievement of the cooperation of simple metal nitrate precursor and the combustion technique to produce nickel oxide thin films by using AACVD at deposition temperatures as low as 250 °C in one step implies that this process may be similarly applied to the fabrication of other oxide thin films to reduce their high deposition temperatures; for example, MgO typically requires 400 – 600 °C or higher,[1,2] while MnO requires temperatures in excess of 450 °C.[3–5] Materials which display a low-melting temperature such as plastic or polymers (including bio-polymers) can also be investigated as substrates. Moreover, multi-layer thin film deposition is may be readily developed for use in various applications such as in solar cells.[6–8]

The XRD results presented in Figure 3.22 (chapter 3) indicated the disappearance of the monoclinic $La_2O_2CO_3$ phase when an additional proportion of acetic acid was increased over 10 vol. %. At this point, it is interesting to further investigate the use of acetic acid in lanthanum oxide thin film fabrication for preventing or eliminating the reaction between lanthanum oxide film and ambient carbon dioxide ambient to form the $La_2O_2CO_3$ phase.

6.3 Chapter 3: Deposition of Ternary oxide thin films

Chapter 3 presented the achievement of $LaNiO_3$ thin film fabrication using the spin coating technique with precursor recipes which contained additional equivalents of acetic acid. $LaNiO_3$ thin film deposition via AACVD, however, could not be achieved due to time constraints. Thus, the precursor systems which have been successfully applied to the spin coating process should be studied in further AACVD experiments.

Additional volumes of acetic acid in the precursor solutions were found to exert significant effects on the properties and character of the lanthanum nickel oxide thin film, decreasing thickness and roughness, increasing transmission as well as providing improvements in the observed ratio of La/Ni close to 1:1 and the conductivity of the deposited film. Thus, an investigation into the influence of additional acetic acid volumes during $LaNiO_3$ film deposition could be applied to a further study by the AACVD technique. Furthermore, further study into the use water as an environmentally friendly solvent should be pursued for the thin film deposition.

In addition, the electrical and conductivity properties of all the deposited $LaNiO_3$ films require further investigation but will need the design of appropriate equipment and experiments. Moreover, the conductivity and catalytic performance of $LaNiO_3$ at various temperatures or under a modified atmosphere may uncover further interesting potential for exploitation in applications such as solid oxide cells (SOFCs) and polymer electrolyte membrane fuel cells (PEMFCs).

Further ternary oxides based on lanthanum may also be pursued to form thin film materials such as $LaMnO_3$, $LaFeO_3$ and $LaCoO_3$, which display properties useful for clean-energy technologies such as fuel cells, water electrolysis and as highly efficient electrocatalysts.

6.4 Chapter 4: Deposition of Zinc sulphide thin films

Chapter 4 focused on ZnS thin film deposition from the complex precursors $Zn(S_2COEt)_2$, 2-MePy $Zn(S_2COEt)_2$ and $Zn(S{=}C(NMe)_2NCH(Me)_2)_2$. $Zn(S_2COEt)_2$ and 2-MePy $Zn(S_2COEt)_2$ provided cubic zinc blende ZnS thin film whereas $Zn(S{=}C(NMe)_2NCH(Me)_2)_2$ yielded wurtzite ZnS thin film. Further studies should investigate the origin of this crystal structure phase transformation between cubic zinc blende ZnS and wurtzite ZnS, particularly when the deposition temperature is increased.

The ZnS thin film from the $Zn(S{=}C(NMe)_2NCH(Me)_2)_2$ precursor at a deposition temperature of 250 °C presented a strong fluorescent character under Raman spectroscopic analysis. The FESEM 6.1 indicated that this film comprised well compacted nanoparticles on its surface which may be contributing to a quantum dot property.[9–13] The quantum dot properties of all the deposited ZnS thin films are, thus, of interest for further study or measurement.

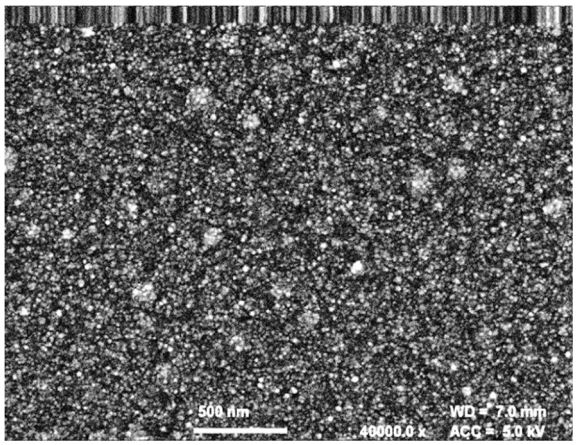

Figure 6.9 FESEM micrographs of the deposited film from 250 °C.

References

1 H. Güney and D. İskenderoğlu, *Ceram. Int.*, 2018, **44**, 7788–7793.

2 X. Fu, G. Wu, S. Song, Z. Song, X. Duo and C. Lin, *Appl. Surf. Sci.*, 1999, **1448**, 223–228.

3 X. Q. Yu, Y. He, J. P. Sun, K. Tang, H. Li, L. Q. Chen and X. J. Huang, *Electrochem. commun.*, 2009, **11**, 791–794.

4 F. Mattelaer, P. M. Vereecken, J. Dendooven and C. Detavernier, *Chem. Mater.*, 2015, **27**, 3628–3635.

5 S. Thirumalairajan, K. Girija, M. Sudha, P. Maadeswaran and J. Chandrasekaran, *Optoelectron. Adv. Mater. Commun.*, 2008, **2**, 779–781.

6 R. S. Dubey, K. Jhansirani and S. Singh, *Results Phys.*, 2017, **7**, 77–81.

7 S. R. Wenham, M. A. Green, S. Edmiston, P. Campbell, L. Koschier, C. B. Honsberg, A. B. Sproul, D. Thorpe, Z. Shi and G. Heiser, *IEEE*, 1994, **Dec. 5-9**, 1234–1241.

8 S. R. Wenham, M. A. Green, S. Edmiston, P. Campbell, L. Koschier, C. B. Honsberg, A. B. Sproul, D. Thorpe, Z. Shi and G. Heiser, *Sol. Energy Mater. Sol. Cells*, 1996, **41**, 3–17.

9 M. Y. Nadeem and W. Ahmed, *Turk J Phy*, 2000, **24**, 651–659.

10 J. Cheng, D. Fan, H. Wang, B. Liu, Y. Zhang and H. Yan, *Semicond. Sci. Technol*, 2003, **18**, 676–679.

11 D. Segets, *KONA Powder Part. J.*, 2016, **33**, 48–62.

12 S. O. Jeon and J. Y. Lee, *J. Ind. Eng. Chem.*, 2011, **17**, 105–108.

13 N. P. Huse, A. S. Dive, D. S. Upadhye, S. B. Bagul, K. P. Gattu and R. Sharma, *Ferroelectrics*, 2017, **519**, 170–177.

Appendix

Table 1 Crystal data and structure refinement for single crystal complex from LNR11 precursor system

Identification code	e18msh3
Empirical formula	$H_8La_{0.33}N_2Ni_{0.5}O_{10}$
Formula weight	271.74
Temperature/K	150.01(10)
Crystal system	trigonal
Space group	R-3
a/Å	11.0276(4)
b/Å	11.0276(4)
c/Å	34.1048(17)
α/°	90
β/°	90
γ/°	120
Volume/Å^3	3591.8(3)
Z	18.00006
ρ_{calc}g/cm^3	2.261
μ/mm^{-1}	3.067
F(000)	2430.0
Crystal size/mm^3	0.294 × 0.149 × 0.144
Radiation	MoKα (λ = 0.71073)
2Θ range for data collection/°	7.168 to 54.902
Index ranges	$-14 \leq h \leq 12$, $-14 \leq k \leq 14$, $-44 \leq l \leq 27$
Reflections collected	9606
Independent reflections	1826 [R_{int} = 0.0193, R_{sigma} = 0.0138]
Data/restraints/parameters	1826/8/131
Goodness-of-fit on F^2	1.058
Final R indexes [I>=2σ (I)]	R_1 = 0.0136, wR_2 = 0.0323
Final R indexes [all data]	R_1 = 0.0156, wR_2 = 0.0332
Largest diff. peak/hole / e Å^{-3}	0.37/-0.27

The asymmetric unit in **e18msh3** comprises 1/3 of a lanthanum centre coordinated in a bidentate manner to two nitrate anions (via O1, O2, O4 and O5), 1/3 of a nickel centre (Ni1) coordinated to 2 water ligands (via O7 and O8) and 1/6 of a nickel

coordinated to one water ligand (based on O9). The water hydrogens were located, but ultimately included at calculated positions with restrained O-H distances of 0.98Å and free U_{iso} values.

The gross structure is dominated by a dense hydrogen-bonded network, which involves all water hydrogen atoms.

Table 2 Fractional Atomic Coordinates ($\times 10^4$) and Equivalent Isotropic Displacement Parameters ($Å^2 \times 10^3$) for e18msh3. U_{eq} is defined as 1/3 of of the trace of the orthogonalised U_{IJ} tensor.

Atom	***x***	***y***	***z***	**U(eq)**
Ni1	6667	3333	4048.1(2)	9.11(7)
O7	5061.6(10)	3179.6(11)	4387.6(3)	13.2(2)
O8	6748.8(12)	4913.8(11)	3707.5(3)	17.8(2)
Ni2	10000	10000	5000	8.99(9)
O9	9956.6(11)	8469.5(11)	4645.3(3)	15.4(2)
O10	8291.3(12)	7687.1(12)	3970.9(3)	17.9(2)
La1	3333	6667	4156.3(2)	6.52(5)
N1	2952.9(12)	4131.3(12)	3678.5(4)	11.1(2)
N2	5478.3(12)	6345.9(12)	4673.7(4)	10.2(2)
O1	2200.7(11)	4001.3(11)	3976.7(3)	13.6(2)
O2	3841.7(11)	5374.6(11)	3576.3(3)	16.2(2)
O3	2821.2(12)	3106.6(11)	3500.1(3)	20.0(2)
O4	4902.2(11)	5589.3(10)	4372.9(3)	12.5(2)
O5	5081.2(11)	7204(1)	4769.2(3)	12.8(2)
O6	6366.4(11)	6232.1(11)	4863.0(3)	17.1(2)

Table 3 Anisotropic Displacement Parameters ($Å^2×10^3$) for e18msh3. The Anisotropic displacement factor exponent takes the form: $-2\pi^2[h^2a^{*2}U_{11}+2hka^*b^*U_{12}+\ldots]$.

Atom	U_{11}	U_{22}	U_{33}	U_{23}	U_{13}	U_{12}
Ni1	9.96(10)	9.96(10)	7.43(16)	0	0	4.98(5)
O7	16.0(5)	13.3(5)	12.2(5)	0.0(4)	2.3(4)	8.7(4)
O8	22.2(6)	15.8(6)	15.5(6)	-0.3(4)	-6.5(5)	9.7(5)
Ni2	9.08(13)	9.08(13)	8.8(2)	0	0	4.54(7)
O9	20.0(6)	14.1(5)	14.1(5)	-2.1(4)	-2.9(4)	10.1(5)
O10	21.6(6)	24.1(6)	14.0(6)	-0.8(5)	-0.1(5)	15.8(5)
La1	6.84(6)	6.84(6)	5.86(7)	0	0	3.42(3)
N1	11.5(6)	11.3(6)	10.3(6)	-1.5(5)	-0.6(5)	5.7(5)
N2	10.2(6)	9.9(6)	10.0(6)	1.3(5)	-0.3(5)	4.7(5)
O1	13.6(5)	12.7(5)	11.4(5)	-1.3(4)	4.3(4)	4.2(4)
O2	16.9(5)	10.3(5)	14.4(6)	-0.3(4)	5.6(4)	1.6(4)
O3	27.8(6)	14.1(5)	19.5(6)	-4.5(4)	4.3(5)	11.5(5)
O4	16.5(5)	13.1(5)	10.7(5)	-3.4(4)	-3.9(4)	9.4(4)
O5	17.4(5)	12.0(5)	12.7(5)	-2.9(4)	-1.8(4)	10.2(4)
O6	16.0(5)	19.6(6)	19.0(6)	-2.1(4)	-7.7(4)	11.5(5)

Table 4 Bond Lengths for e18msh3.

Atom	Atom	Length/Å	Atom	Atom	Length/Å
Ni1	$O7^1$	2.0500(10)	La1	$O2^8$	2.6564(11)
Ni1	O7	2.0499(10)	La1	O2	2.6564(10)
Ni1	$O7^2$	2.0500(10)	La1	$O2^9$	2.6564(11)
Ni1	$O8^1$	2.0584(11)	La1	$O4^8$	2.6469(10)
Ni1	$O8^2$	2.0584(11)	La1	O4	2.6469(10)
Ni1	O8	2.0584(11)	La1	$O4^9$	2.6469(10)
Ni2	$O9^3$	2.0574(10)	La1	$O5^8$	2.7008(10)
Ni2	$O9^4$	2.0574(10)	La1	$O5^9$	2.7008(10)
Ni2	$O9^5$	2.0574(10)	La1	O5	2.7007(10)
Ni2	$O9^6$	2.0574(10)	N1	O1	1.2743(15)
Ni2	$O9^7$	2.0574(10)	N1	O2	1.2720(16)

Ni2	O9	2.0575(10)	N1	O3	1.2264(16)
La1	O1[8]	2.6275(10)	N2	O4	1.2737(15)
La1	O1	2.6275(10)	N2	O5	1.2680(15)
La1	O1[9]	2.6275(10)	N2	O6	1.2305(16)

[1]1-Y,+X-Y,+Z; [2]1+Y-X,1-X,+Z; [3]1-Y+X,+X,1-Z; [4]2-X,2-Y,1-Z; [5]+Y,1-X+Y,1-Z; [6]2-Y,1+X-Y,+Z; [7]1+Y-X,2-X,+Z; [8]1-Y,1+X-Y,+Z; [9]+Y-X,1-X,+Z

Table 5 Bond Angles for e18msh3.

Atom	**Atom**	**Atom**	**Angle/°**	**Atom**	**Atom**	**Atom**	**Angle/°**
O7[1]	Ni1	O7	91.23(4)	O1[8]	La1	O5	129.37(3)
O7[1]	Ni1	O7[2]	91.23(4)	O1	La1	O5[9]	129.37(3)
O7	Ni1	O7[2]	91.23(4)	O1[9]	La1	O5[9]	108.29(3)
O7	Ni1	O8	93.41(4)	O1	La1	O5[8]	66.00(3)
O7[2]	Ni1	O8	84.42(4)	O1	La1	O5	108.29(3)
O7	Ni1	O8[2]	173.71(4)	O1[9]	La1	O5[8]	129.37(3)
O7[1]	Ni1	O8[2]	84.43(4)	O1[8]	La1	O5[9]	66.00(3)
O7[1]	Ni1	O8	173.71(4)	O2[9]	La1	O2	70.62(4)
O7[2]	Ni1	O8[2]	93.41(4)	O2[8]	La1	O2[9]	70.62(4)
O7[2]	Ni1	O8[1]	173.71(4)	O2[8]	La1	O2	70.62(4)
O7[1]	Ni1	O8[1]	93.41(4)	O2[9]	La1	O5[9]	112.04(3)
O7	Ni1	O8[1]	84.42(4)	O2	La1	O5[8]	110.80(3)
O8[2]	Ni1	O8[1]	91.28(4)	O2[8]	La1	O5	177.22(3)
O8[2]	Ni1	O8	91.28(4)	O2	La1	O5	112.04(3)
O8	Ni1	O8[1]	91.28(4)	O2	La1	O5[9]	177.22(3)
O9[3]	Ni2	O9[4]	91.05(4)	O2[8]	La1	O5[8]	112.04(3)
O9[4]	Ni2	O9[5]	180.0	O2[9]	La1	O5	110.80(3)
O9[6]	Ni2	O9[4]	91.05(4)	O2[8]	La1	O5[9]	110.80(3)
O9[7]	Ni2	O9[4]	88.95(4)	O2[9]	La1	O5[8]	177.22(3)
O9[3]	Ni2	O9	180.0	O4	La1	O2[9]	108.46(3)
O9[3]	Ni2	O9[7]	91.05(4)	O4	La1	O2	66.82(3)
O9[7]	Ni2	O9[5]	91.05(4)	O4	La1	O2[8]	134.46(3)
O9[6]	Ni2	O9	91.05(4)	O4[9]	La1	O2	134.46(3)
O9[5]	Ni2	O9	91.05(4)	O4[8]	La1	O2[8]	66.82(3)
O9[4]	Ni2	O9	88.95(4)	O4[9]	La1	O2[9]	66.82(3)

O9[7]	Ni2	O9	88.95(4)	O4[8]	La1	O2	108.46(3)
O9[3]	Ni2	O9[5]	88.95(4)	O4[9]	La1	O2[8]	108.46(3)
O9[3]	Ni2	O9[6]	88.95(4)	O4[8]	La1	O2[9]	134.46(3)
O9[6]	Ni2	O9[5]	88.95(4)	O4[9]	La1	O4[8]	112.531(19)
O9[6]	Ni2	O9[7]	180.0	O4[9]	La1	O4	112.531(19)
O1[8]	La1	O1[9]	114.735(17)	O4[8]	La1	O4	112.530(19)
O1[8]	La1	O1	114.735(17)	O4	La1	O5[9]	111.10(3)
O1[9]	La1	O1	114.736(17)	O4[9]	La1	O5[8]	111.10(3)
O1	La1	O2[8]	72.73(3)	O4[9]	La1	O5[9]	47.74(3)
O1[8]	La1	O2[9]	72.73(3)	O4[9]	La1	O5	70.39(3)
O1[8]	La1	O2[8]	48.40(3)	O4	La1	O5[8]	70.39(3)
O1	La1	O2[9]	116.09(3)	O4	La1	O5	47.74(3)
O1[9]	La1	O2[9]	48.40(3)	O4[8]	La1	O5	111.10(3)
O1[9]	La1	O2	72.73(3)	O4[8]	La1	O5[8]	47.74(3)
O1[9]	La1	O2[8]	116.09(3)	O4[8]	La1	O5[9]	70.39(3)
O1	La1	O2	48.40(3)	O5	La1	O5[8]	66.51(4)
O1[8]	La1	O2	116.09(3)	O5[9]	La1	O5[8]	66.51(4)
O1	La1	O4	67.34(3)	O5	La1	O5[9]	66.51(4)
O1[9]	La1	O4[8]	177.06(3)	O2	N1	O1	116.58(11)
O1	La1	O4[9]	177.06(3)	O3	N1	O1	121.44(12)
O1[8]	La1	O4[8]	67.34(3)	O3	N1	O2	121.98(12)
O1[9]	La1	O4	65.28(3)	O5	N2	O4	116.78(11)
O1	La1	O4[8]	65.28(3)	O6	N2	O4	121.16(12)
O1[8]	La1	O4	177.06(3)	O6	N2	O5	122.06(12)
O1[8]	La1	O4[9]	65.28(3)	N1	O1	La1	98.14(8)
O1[9]	La1	O4[9]	67.34(3)	N1	O2	La1	96.81(8)
O1[9]	La1	O5	66.00(3)	N2	O4	La1	98.89(7)
O1[8]	La1	O5[8]	108.29(3)	N2	O5	La1	96.45(8)

[1]1-Y,+X-Y,+Z; [2]1+Y-X,1-X,+Z; [3]2-X,2-Y,1-Z; [4]2-Y,1+X-Y,+Z; [5]+Y,1-X+Y,1-Z; [6]1-Y+X,+X,1-Z; [7]1+Y-X,2-X,+Z; [8]+Y-X,1-X,+Z; [9]1-Y,1+X-Y,+Z

Table 6 Hydrogen Bonds for e18msh3.

D	H	A	d(D-H)/Å	d(H-A)/Å	d(D-A)/Å	D-H-A/°
O7	H7A	O4	0.87	1.90	2.7498(14)	165.1
O7	H7B	O5[1]	0.97	1.97	2.8993(15)	157.9
O8	H8A	O8[2]	0.86	2.37	3.0663(19)	138.1
O8	H8B	O10	0.88	1.95	2.8020(16)	162.5
O9	H9A	O10	0.86	1.98	2.7970(16)	159.2
O9	H9B	O6[3]	0.86	2.11	2.9468(15)	164.7
O10	H10A	O2[4]	0.85	2.30	3.0478(16)	147.3
O10	H10A	O3[5]	0.85	2.39	2.9934(16)	129.0
O10	H10B	O1[6]	0.85	2.02	2.8530(15)	164.1

[1]1-X,1-Y,1-Z; [2]1/3-Y+X,-1/3+X,2/3-Z; [3]1-Y+X,+X,1-Z; [4]1/3+Y,2/3-X+Y,2/3-Z; [5]1+Y-X,1-X,+Z; [6]1-Y,1+X-Y,+Z

Table 7 Hydrogen Atom Coordinates (Å×10^4) and Isotropic Displacement Parameters (Å^2×10^3) for e18msh3.

Atom	*x*	*y*	*z*	U(eq)
H7A	5162	4007	4367	43(6)
H7B	4968	2811	4652	47(7)
H8A	6007	4596	3566	70(9)
H8B	7089	5803	3769	64(8)
H9A	9279	8183	4480	59(8)
H9B	9838	7770	4786	33(6)
H10A	8747	7917	3757	41(6)
H10B	7731	8007	3975	46(7)

Experimental

Single crystals of $H_8La_{0.33}N_2Ni_{0.5}O_{10}$ [e18msh3] were []. A suitable crystal was selected and [] on a New Xcalibur, EosS2 diffractometer. The crystal was kept at 150.01(10) K during data collection. Using Olex2 [1], the structure was solved with the olex2.solve [2] structure solution program using Charge Flipping and refined with the ShelXL [3] refinement package using Least Squares minimisation.

Dolomanov, O.V., Bourhis, L.J., Gildea, R.J, Howard, J.A.K. & Puschmann, H. (2009), J. Appl. Cryst. 42, 339-341.

Bourhis, L.J., Dolomanov, O.V., Gildea, R.J., Howard, J.A.K., Puschmann, H. (2015). Acta Cryst. A71, 59-75.

Sheldrick, G.M. (2015). Acta Cryst. C71, 3-8.

Crystal structure determination of [e18msh3]

Crystal Data for $H_{7.999973}La_{0.333332}N_{1.999993}Ni_{0.499998}O_{9.999967}$ (M =271.74 g/mol): trigonal, space group R-3 (no. 148), a = 11.0276(4) Å, c = 34.1048(17) Å, V = 3591.8(3) Å^3, Z = 18.00006, T = 150.01(10) K, μ(MoKα) = 3.067 mm^{-1}, *Dcalc* = 2.261 g/cm^3, 9606 reflections measured (7.168° ≤ 2Θ ≤ 54.902°), 1826 unique (R_{int} = 0.0193, R_{sigma} = 0.0138) which were used in all calculations. The final R_1 was 0.0136 (I > 2σ(I)) and wR_2 was 0.0332 (all data).

Refinement model description

Number of restraints - 8, number of constraints - unknown.

Details:

1. Restrained distances
O10-H10B = O10-H10A = O9-H9A = O9-H9B = O8-H8B = O8-H8A = O7-H7A = O7-H7B 0.98 with sigma of 0.005
2.a Free rotating group:O10(H10A,H10B)
2.b Rotating group: O7(H7A,H7B), O8(H8A,H8B), O9(H9A,H9B)

This report has been created with Olex2, compiled on 2017.08.10 svn.r3458 for OlexSys. Please let us know if there are any errors or if you would like to have additional features.